

VILNIAUS UNIVERSITETAS
GAMTOS TYRIMŲ CENTRAS
KLAIPĖDOS UNIVERSITETAS

Rasa Janušaitė

Priekrantės sėklių dinamikos tyrimai
nuotolinio stebėjimo metodais (Kuršių
nerijos Baltijos jūros priekrantės
pavyzdžiu)

DAKTARO DISERTACIJA

Gamtos mokslai,
Fizinė geografija (N 006)

VILNIUS 2022

Disertacija rengta 2018–2022 metais Gamtos tyrimų centre.

Mokslinis vadovas – dr. Darius Jarmalavičius (Gamtos tyrimų centras, gamtos mokslai, fizinė geografija, N 006).

Mokslinis konsultantas – dr. Laurynas Jukna (Vilniaus universitetas, gamtos mokslai, fizinė geografija, N 006).

Gynimo taryba:

Pirmininkas – prof. dr. Egidijus Rimkus (Vilniaus universitetas, gamtos mokslai, fizinė geografija, N 006).

Nariai:

prof. dr. Albertas Bitinas (Gamtos tyrimų centras, gamtos mokslai, geologija, N 005);

doc. dr. Ilya Buynevich (Templio universitetas, gamtos mokslai, geologija, N 005);

akad. dr. Jūratė Kriauciūnienė (Lietuvos energetikos institutas, technologijos mokslai, aplinkos inžinerija, T 004);

prof. dr. Edvinas Stonevičius (Vilniaus universitetas, gamtos mokslai, fizinė geografija, N 006).

Disertacija ginama viešame Gynimo tarybos posėdyje 2022 m. gruodžio 2 d. 11 val. Gamtos tyrimų centro konferencijų salėje, 101 kab. Adresas: Akademijos g. 2, 101 kab., Vilnius, Lietuva, tel. + 370 527 29 257; el. paštas sekretoriatas@gamtc.lt

Disertaciją galima peržiūrėti Gamtos tyrimų centro, Klaipėdos universiteto, Vilniaus universiteto bibliotekose ir VU interneto svetainėje adresu:

<https://www.vu.lt/naujienos/ivykiu-kalendorius>

VILNIUS UNIVERSITY
NATURE RESEARCH CENTRE
KLAIPĖDA UNIVERSITY

Rasa Janušaitė

Investigation of Nearshore Sandbar Dynamics Using Remote Sensing Methods (on the Example of the Baltic Sea's Nearshore in the Curonian Spit)

DOCTORAL DISSERTATION

Natural Sciences,
Physical Geography N 006

VILNIUS 2022

The dissertation was prepared between 2018 and 2022 at the Nature Research Centre.

Academic supervisor – Dr. Darius Jarmalavičius (Nature Research Centre, Natural Sciences, Physical Geography, N 006).

Academic consultant – Dr. Laurynas Jukna (Vilnius University, Natural Sciences, Physical Geography, N 006).

This doctoral dissertation will be defended in a public meeting of the Dissertation Defence Panel:

Chairman – Prof. Dr. Egidijus Rimkus (Vilnius University, Natural Sciences, Physical Geography, N 006).

Members:

Prof. Dr. Albertas Bitinas (Nature Research Centre, Natural Sciences, Geology, N 005),

Assoc. Prof. Dr. Ilya Buynevich (Temple University, Natural Sciences, Geology, N 005),

Acad. Dr. Jūratė Kriauciūnienė (Lithuanian Energy Institute, Technologies, Environmental Engineering, T 004),

Prof. Dr. Edvinas Stonevičius (Vilnius University, Natural Sciences, Physical Geography, N 006).

The dissertation shall be defended at a public meeting of the Dissertation Defence Panel at 11 a. m. on December 2, 2022 in Meeting Room 101 of the Nature Research Centre.

Address: 2 Akademijos Str., Vilnius, Lithuania

Phone No.: +37052729257; e-mail: sekretoriatas@gamtc.lt

The text of this dissertation can be accessed through the libraries of Nature Research Centre, Klaipėda University and Vilnius University, as well as on the website of Vilnius University:

www.vu.lt/lt/naujienos/ivykiu-kalendorius

SANTRUMPOS

Santrumpa	Reikšmė anglų kalba	Reikšmė lietuvių kalba
CEOФ	<i>Complex Empirical Orthogonal Function Analysis</i>	Kompleksinė empirinė ortogonalių funkcijų analizė
ESA	<i>European Space Agency</i>	Europos kosmoso agentūra
ISODATA	<i>Iterative Self-Organizing Data Analysis</i>	Nekontroliuojamos klasifikacijos algoritmas
m/mén.	<i>Metres per month</i>	Metrai per mėnesį
NASA	<i>National Aeronautics and Space Administration</i>	JAV Nacionalinė aeronautikos ir kosmoso administracija
NBB region	<i>Sandbar behaviour region</i>	Panašiomis sėklių elgsenos ypatybėmis pasižymintis priekrantės ruožas
NDWI	<i>Normalized Difference Water Index</i>	Normalizuoto skirtumo vandens rodiklis
NIR	<i>Near-infrared</i>	Artimasis infraraudonasis spektras
NOM	<i>Net offshore migration</i>	Ijūrinės migracijos ciklas
p	<i>Significance level</i>	Reikšmingumo lygmuo
RBPI	<i>Relative Bathymetric Position Index</i>	Santykinis batimetrinės padėties rodiklis
RMSE	<i>Root Mean Square Error</i>	Vidutinė kvadratinė paklaida
R ²	<i>Coefficient of determination</i>	Determinacijos koeficientas
T _r	<i>Bar cycle return period</i>	Sėkliaus ciklo pasikartojimo rodiklis

TURINYS

PUBLIKACIJŲ SĄRAŠAS	8
AUTORĖS INDÉLIS PUBLIKACIJOSE	9
TYRIMŲ REZULTATŲ APROBAVIMAS	10
ĮVADAS	11
1. TYRIMŲ MEDŽIAGA IR METODIKA	18
1.1. Tyrimų rajonas ir naudoti duomenys	18
1.2. Priekrantės séklių identifikavimo palydoviniuose vaizduose ir duomenų paruošimo analizei metodika	20
1.3. Duomenų analizės metodika	23
2. TYRIMŲ REZULTATAI	26
2.1. Priekrantės séklių identifikavimo palydoviniuose vaizduose metodikos tikslumas	26
2.2. Priekrantės séklių struktūra ir dinamika	28
2.2.1. Priekrantės séklių morfologinė struktūra	28
2.2.2. Priekrantės séklių kaita skersai kranto	29
2.2.3. Priekrantės séklių morfodinaminiai ypatumai	31
2.2.4. Priekrantės séklių kaita, paveikta žmogaus veiklos	33
2.2.5. Panašia séklių struktūra ir dinamika pasižymintys priekrantės ruožai	34
2.3. Priekrantės séklių dinamiką lemiantys veiksniųai	35
2.4. Priekrantės séklių dinamikos įtaka kranto raidai	38
3. TYRIMŲ REZULTATŲ APTARIMAS	41
IŠVADOS	46
SUMMARY	48
LITERATŪROS SĄRAŠAS	61
PADĖKA	71
CURRICULUM VITAE	72
PUBLIKACIJŲ KOPIJOS	73

PUBLIKACIJŲ SĄRAŠAS

Daktaro disertacija yra paremta toliau pateiktomis publikacijomis, paskelbtomis tarptautiniuose mokslo žurnaluose, turinčiuose cituojamumo rodiklį *Clarivate Analytics Web of Science (CA WoS)* duomenų bazėje:

- I. **Janušaitė R.**, Jukna L., Jarmalavičius D., Pupienis D., Žilinskas G. 2021. A novel GIS-Based approach for automated detection of nearshore sandbar morphological characteristics in optical satellite imagery. *Remote Sensing*, 13 (11): 2233. <https://doi.org/10.3390/rs13112233> (Q1, IF 5.349)
- II. **Janušaitė R.**, Jarmalavičius D., Jukna L., Žilinskas G., Pupienis D. 2022. Analysis of interannual and seasonal nearshore bar behaviour observed from decadal optical satellite data in the Curonian Spit, Baltic Sea. *Remote Sensing*, 14 (14): 3423. <https://doi.org/10.3390/rs14143423> (Q1, IF 5.349)
- III. Žilinskas G., **Janušaitė R.**, Jarmalavičius D., Pupienis D. 2020. The impact of Klaipėda Port entrance channel dredging on the dynamics of coastal zone, Lithuania. *Oceanologia*, 62, 489–500. <https://doi.org/10.1016/j.oceano.2020.08.002> (Q2, IF 2.526)
- IV. **Janušaitė R.**, Jarmalavičius D., Pupienis D., Žilinskas G., Jukna L. 2021. Nearshore sandbar switching episodes and their relationship with coastal erosion at the Curonian Spit, Baltic Sea. *Oceanologia*, <https://doi.org/10.1016/j.oceano.2021.11.004> (Q2, IF 2.526)

AUTORĖS INDĖLIS PUBLIKACIJOSE

Autorės indėlis į daktaro disertaciją įtrauktose publikacijose:

- I PUBLIKACIJA: R. Janušaitė pasiūlė tyrimo idėją, sukūrė pasiūlytą algoritmą, apdorojo palydovinę informaciją, prisdėjo prie algoritmo tikslumui vertinti skirtų batimetriniių matavimų, atliko algoritmo validavimą, parengė publikacijos tekštą ir iliustracijas.
- II PUBLIKACIJA: R. Janušaitė pasiūlė tyrimo idėją, sudarė analizei skirtą palydoviniais duomenimis pagrįstą priekrantės sėklių charakteristikų duomenų bazę, adaptavo tyime taikytą metodiką palydoviniams duomenims, atliko duomenų statistinę analizę, parengė publikacijos tekštą ir iliustracijas.
- III PUBLIKACIJA: R. Janušaitė įskaitmenino istorinę-kartografinę medžiagą, atliko istorinių-kartografinių ir batimetinių duomenų GIS analizę, parengė dalį publikacijos iliustracijų ir lentelių.
- IV PUBLIKACIJA: R. Janušaitė pasiūlė tyrimo idėją, suformulavo tyime taikytą metodiką, identifikavo priekrantės sėklių persirikiavimo epizodus ir atliko jų analizę, atliko duomenų statistinę analizę, parengė publikacijos tekštą ir iliustracijas.

TYRIMŲ REZULTATŲ APROBAVIMAS

Autorė pristatė pagrindinius daktaro disertacijos rezultatus penkiose tarptautinėse ir dviejose nacionalinėse konferencijose:

1. **Janušaitė R.**, Karaliūnas V., Bevainis L. 2018. Nuotolinių metodų panaudojimas jūros priekrantės sėklių tyrimuose. Konferencija CartoCon2018, VU mokslinės komunikacijos ir informacijos centras, Vilnius, 2018 m. lapkričio 30 d.
2. **Janušaitė R.**, Karaliūnas V., Bevainis L. 2019. Application of remote sensing methods in research of nearshore sandbars. 77th International Scientific Conference of University of Latvia: Geodynamics and geospatial research, Riga, Latvia, 3rd March 2019, Conference abstracts and papers, p. 25.
3. **Janušaitė R.**, Jarmalavičius D., Karaliūnas V., Jukna L., Žilinskas G., Pupienis D. 2019. The influence of multiple sandbar system behavior on coastal erosion and accretion. 12th Baltic Sea Science Congress, Stockholm, Sweden, 19–23 August 2020, Abstracts, p. 144.
4. **Janušaitė R.**, Jarmalavičius D., Pupienis D., Žilinskas G., Karaliūnas V. 2020. Sandbar switching as a factor controlling coastal erosion during storm events, Curonian Spit, Lithuania. 3rd Baltic Earth Conference: Earth system changes and Baltic Sea coasts, 2–3 June 2020, Conference proceedings, p. 99–100.
5. **Janušaitė R.**, Jarmalavičius D., Karaliūnas V., Jukna, L., Žilinskas G., Pupienis D. 2020. Jūros priekrantės sėklių morfodinamikos įtaka Kuršių nerijos kranto raidai (Preilos pavyzdžiu). Jūros ir krantų tyrimai 2020: 13-oji nacionalinė jūros mokslų ir technologijų konferencija. Klaipėdos universitetas, Klaipėda, 2020 m. spalio 7–9 d. Konferencijos medžiaga, p. 74–77.
6. **Janušaitė R.**, Jarmalavičius D., Jukna L. 2021. Examining the potential of medium resolution satellite imagery for high frequency observation of nearshore sandbars. Coastal Dynamics 2021, Delft, Netherlands, 28 June–2 July 2021.
7. **Janušaitė R.**, Jarmalavičius D., Jukna L., Žilinskas G., Pupienis D. 2022. Evaluation of seasonal and interannual nearshore sandbar morphodynamics using optical satellite remote sensing. Fourth ICES PICES Early Career Scientists Conference, St. John's, Newfoundland, Canada, 17–21 July, 2022.

IVADAS

Mokslinė problema

Priekrantės sėkliai – išilgai kranto nutišę povandeniniai smėlio gūbriai, suformuoti bangų ir priekrantės srovį, aptinkami smėlėtų jūrų, vandenynų ir didelių ežerų pakrantėse iki 10 m gylio (Múnera ir kt., 2014; Price ir kt., 2014; Ruessink ir kt., 2003; Rutten ir kt., 2018; Van Enckevort ir Ruessink, 2003a). Šios gūbriškos reljefo formos pradėtos tirti XIX a. viduryje (de Beaumont, 1845), tačiau jų tyrimai įgavo pagreitį tik XX a. viduryje (King ir Williams, 1949; Shepard, 1950). Per beveik šimtmetį siekiančią intensyvių sėklių tyrimų istoriją sukaupta gausybė žinių apie jų morfologiją (Aleman ir kt., 2015; Gelfenbaum ir Brooks, 2003; Greenwood ir Davidson-Arnott, 1979; Lippmann ir Holman, 1990; Price ir Ruessink, 2011; Short ir Aagaard, 1993; Van Enckevort ir kt., 2004; Wright ir Short, 1984), formavimąsi (Aagaard ir kt., 2008; Boczar-Karakiewicz ir Davidson-Arnott, 1987; Caballeria ir kt., 2002; Falqués ir kt., 2000; Holman ir Bowen, 1982; King ir Williams, 1949; Sallenger ir Howd, 1989) ir dinamiką (Gallagher ir kt., 1998; Gijsman ir kt., 2021; Hoefel ir Elgar, 2003; Melito ir kt., 2020; Plant ir kt., 1999; Ruessink ir kt., 2003; Ruessink ir Kroon, 1994; Rutten ir kt., 2018; Tátui ir kt., 2016; Van Enckevort ir Ruessink, 2003a; Vidal-Ruiz ir Ruiz de Alegria-Arzaburu, 2019).

Nustatyta, kad priekrantės sėkliai susidaro kaip vieno ar kelių sėklių sistemos ir pasižymi didele formų įvairove, nuo orientuotų lygiagrečiai su krantu iki įstrižų ar skersų krantui, nuo tiesių iki gerokai išlenktų pusmėnulio formų (Wijnberg ir Kroon, 2002). Manoma, jog tiesūs sėkliai susidaro ties bangų gožos tašku, kur susitinka ir nusėda kranto ir jūros link nukreipti nešmenų srautai (Roelvink ir Stive, 1989; Sallenger ir Howd, 1989; Thornton ir kt., 1996), o pusmėnulio formų susidarymas yra grindžiamas grįztamaisiais ryšiais tarp jūros dugno reljefo ir hidrodinaminių bei litodinaminių procesų priekrantėje (Caballeria ir kt., 2002; Falqués ir kt., 2008, 1996).

Priekrantės sėklių kaita tiriant jų dinamiką dažnai skaidoma į du komponentus:

- sėklių judėjimą skersai kranto nusakančių išilgai kranto vientisą (dvidimensi (2D)) komponentą (Larson ir Kraus, 1994; Melito ir kt., 2020; Plant ir kt., 1999; Ruessink ir kt., 2009; Van Enckevort ir Ruessink, 2003a);
- sėklių formos kaitą ir judėjimą išilgai kranto nusakančių tridimensi (3D) komponentą (Rutten ir kt., 2018; Van Enckevort ir kt., 2004; Van Enckevort ir Ruessink, 2003b).

Gausybėje priekrantės sėklių kaitos skersai kranto tyrimų analizuota jų migracija kranto ir jūros link (Gallagher ir kt., 1998; Hoefel ir Elgar, 2003;

Larson ir Kraus, 1994; Melito ir kt., 2020; Plant ir kt., 1999; Van Enckevort ir Ruessink, 2003a; Vidal-Ruiz ir Ruiz de Alegría-Arzaburu, 2019). Šiuose tyrimuose XX a. antroje pusėje nusistovėjo suvokimas, kad įprastai sėkliai migruoja tolyn nuo kranto kai yra didelė bangų energija, o kranto link – kai bangų energija maža (Aubrey, 1979; Gallagher ir kt., 1998; Sallenger ir kt., 1985). XX a. dešimtajame dešimtmetyje pastebėta, jog, taikant daugiametę laiko skalę, priekrantės sėkliai klostosi pagal trijų stadijų ijūrinės migracijos ciklo modelį, t. y. susidaro nedideliu atstumu nuo kranto, migruoja tiek kranto, tiek jūros link, o pagal daugiametę laiko skalę ijūrinė migracija viršija įkrantinę, todėl priekrantės sėkliai palaipsniui tolsta nuo kranto, kol galiausiai, pasiekę tam tikrą gylį, sunyksta (Ruessink ir Kroon, 1994). Šis reiškinys fiksuotas daugelyje smėlėtų krantų su keliagubo sėkliaus sistemomis (Aleman ir kt., 2017; Grunnet ir Hoekstra, 2004; Kuriyama, 2002; Ruessink ir kt., 2003; Shand ir kt., 1999; Tātui ir kt., 2016; Yuhi ir Okada, 2011). Nustatyta ijūrinės migracijos ciklo trukmė varijuoja nuo vienerių metų (Kuriyama, 2002) iki poros dešimtmecčių (Ruessink ir Kroon, 1994).

Priekrantės sėklių formos kaita ir judėjimas išilgai kranto analizuoti šių povandeninių gūbrių morfodinamikos tyrimuose. Kertinį sėklių kaitą paaiskinančių morfodinaminį modelį, skirtą viengubo sėkliaus sistemoms, XX a. devintajame dešimtmetyje pasiūlė australai (Wright ir Short, 1984). Vėliau šis modelis buvo modifikuotas ir pritaikytas dvigubiems bei trigubiems sėkliams (Aagaard, 1991; Short, 1992; Short ir Aagaard, 1993). Pagal šį modelį, priklausomai nuo bangavimo sąlygų, priekrantės sėkliai vystosi aukštesnių (tiesėja) ir žemesnių (vystosi ritmiškos pusmėnulio formos) raidos stadijų link (Aleman ir kt., 2015; Price ir Ruessink, 2011; Wright ir Short, 1984).

Vis dėlto mokslinėje literatūroje aprašyta nemažai į šio modelio rėmus netelpančių priekrantės sėkliams būdingų morfodinaminių reišinių, tarp kurių sėklių morfologinis „poravimasis“ (Castelle ir kt., 2010a, 2010b; Price ir kt., 2014; Ruessink ir kt., 2007; Van de Lageweg ir kt., 2013), išsitiesinimas (Contardo ir Symonds, 2015; Garnier ir kt., 2013) ar persirikiavimas (Aleman ir kt., 2017; Shand ir kt., 2001; Walstra ir kt., 2016; Wijnberg ir Wolf, 1994). Pastarasis apibūdina iš kelių sėklių susidariusioms sistemoms būdingą reiškinį, kai dėl netolygaus vystymosi išilgai kranto sėkliai praranda vientisumą, prisišlieja prie kito arčiau arba toliau nuo kranto esančio sėkliaus ir pradeda klostytis jo vietoje (Shand ir kt., 2001). Tokie morfologinės struktūros pokyčiai kelių sėklių sistemose sutrikdo įprastą šių darinių kaitą ijūrinės migracijos ciklo metu.

Priekrantės sėklių tyrimų tematikos įvairovė lemia ir jų tyrimui taikomų metodų, tarp kurių yra įvairūs natūriniai, eksperimentiniai ir nuotolinių tyrimų

metodai, gausą. Vienos pirmųjų įžvalgų apie priekrantės sėklių susidarymą ir kaitą padarytos atliekant laboratorinius eksperimentus (Bowen ir Inman, 1971; Dyhr-Nielson ir Sorensen, 1970; Keulegen, 1948; King ir Williams, 1949; Roelvink ir Stive, 1989). Sėklių dinamikos tyrimuose visą šių formų pažinimo laikotarpį nuolat naudoti dideliu tikslumu pasižyminčių, tačiau itin imlių ištekliams ir nuo oro sąlygų labai priklausomų batimetrinijų matavimų duomenys (Aleman ir kt., 2013; Di Leonardo ir Ruggiero, 2015; Gijsman ir kt., 2021; Kuriyama, 2002; Larson ir Kraus, 1994; Plant ir kt., 1999; Pruszak ir kt., 1997; Ruessink ir Kroon, 1994; Tātui ir kt., 2016; Vidal-Ruiz ir Ruiz de Alegria-Arzaburu, 2019; Wijnberg ir Terwindt, 1995). Kokybinius sėklių tyrimo metodų šuolis įvyko XX a. pabaigoje amerikiečiams pasiūlius vaizdo kameromis pagrįstą priekrantės sėklių stebėsenos metodą (Lippmann ir Holman, 1989), kuris daug prisišėjo prie šių povandeninių formų morfodinamikos pažinimo (Armaroli ir Ciavola, 2011; Lippmann ir Holman, 1990; Ojeda ir kt., 2011; Parlagreco ir kt., 2019; Price ir Ruessink, 2011; Shand ir kt., 2001; Van de Lageweg ir kt., 2013; Van Enckevort ir kt., 2004; Van Enckevort ir Ruessink, 2003b). Nors stebėsena vaizdo kameromis teikia itin dažno periodiškumo ir didelio tikslumo duomenis sėklių tyrimams, šis metodas apsiriboja trumpu kelių kilometrų ilgio priekrantės ruožų stebėsena, jam reikia specifinės įrangos ir nuolatinio jos palaikymo (Román-Rivera ir Ellis, 2019).

Tobulėjant technologijoms, vis daugiau galimybių sėklių tyrimams atveria optiniai Žemės stebėsenos palydovai, kurių duomenys yra tinkami nuolatinei dažno periodiškumo priekrantės sėklių stebėsenai ilguose kranto ruožuose atlikti. Išnaudojant palydovinių technologijų teikiamas galimybes, pastaruoju metu pasaulinėje mokslinėje spaudoje publikuoti pavieniai tyrimai, pagrįsti palydovinių vaizdų panaudojimu priekrantės sėklių pažinimui (Athanasios ir kt., 2018; Do ir kt., 2021; Lafon ir kt., 2004; Román-Rivera ir kt., 2020; Tātui ir Constantin, 2020). Tačiau dėl palydovinių vaizdų ir juos fiksuojančių jutiklių kokybinių ypatybių, vaizdų apdorojimo procedūrų specifikos ir povandeninių formų analizės metodų tokio pobūdžio duomenyse trūkumo kol kas žengiami tik pirmieji priekrantės sėklių pažinimo iš optinių palydovinių vaizdų žingsniai.

Apibendrinant pasaulinių mokslinių tyrimų patirtį, galima teigti, kad, nors priekrantės sėklių tyrimų yra gausu, vis dar trūksta žinių apie šių sėklių dinamiką ilguose kranto ruožuose, neapsiribojančiuose kelių kilometrų atkarjomis, ir jų sąveiką su krante vykstančiais procesais. O dėl metodologinės bazės trūkumo palydovinės Žemės stebėsenos teikiamos galimybės néra visiškai išnaudojamos sėklių tyrimų spragų užpildymui. Taip pat svarbu pabrėžti, kad Lietuvos Baltijos jūros priekrantėje sėklių tyrimų

tematika sulaukia itin nedaug mokslo bendruomenės dėmesio. Iki šiol nėra tirti sėklių daugiametės kaitos dėsningumai, nėra nustatytos jų morfometriniai bruožų kaitos išilgai kranto priežastys, taip pat nėra kaip reikiant ištirta šių povandeninių formų sąveika su krante vykstančiais procesais.

Disertacijos rengimo metu atliktu tyrimu motyvacija yra pagrįsta pirmiau aptartomis mokslinėmis problemomis: 1) priekrantės sėklių identifikavimo ir analizės palydoviniuose vaizduose metodų trūkumu; 2) keliagubo sėkliaus sistemų ištirtumo ilguose kranto ruožuose trūkumu; 3) menku priekrantės sėklių dinamikos ištirtumu Lietuvos Baltijos jūros krantuose; 4) krantotvarkai svarbių žinių apie priekrantės sėklių ir kranto raidos sąveiką ribotumu.

Objektas, tikslas ir uždaviniai

Šio darbo tyrimų objektas – priekrantės sėklių dinamika. Tyrimų teritorija – Lietuvos Kuršių nerijos dalies Baltijos jūros priekrantė.

Darbo tikslas – sukurti priekrantės sėklių geodinamikos bei morfologijos optinių nuotolinių tyrimų metodologinę bazę ir remiantis ja nustatyti sėklių kaitos dėsningumus.

Darbo uždaviniai:

1. Sukurti ir validuoti priekrantės sėklių identifikavimo bei analizės palydoviniuose vaizduose metodologiją.
2. Įvertinti Kuršių nerijos jūros priekrantės sėklių dinamikos skersai kranto ypatumus.
3. Įvertinti Kuršių nerijos jūros priekrantės sėklių morfodinamikos ypatumus.
4. Nustatyti Kuršių nerijos jūros priekrantės sėklių dinamiką lemiančius veiksnius.
5. Įvertinti Kuršių nerijos jūros priekrantės sėklių įtaką kranto raidai.

Ginami teiginiai

1. Didelės ir vidutinės skiriamosios gebos (3–15 m) optiniai palydoviniai vaizdai yra tinkamas duomenų šaltinis tiksliai nustatyti priekrantės sėklių morfologinėms charakteristikoms.
2. Sėklių morfologinę struktūrą apibūdinantys rodikliai, pagrįsti optinių palydovinių vaizdų informacija, yra tinkama batimetrinių ir vaizdo stebėsenos duomenų alternatyva priekrantės sėklių migracijos skersai kranto dėsningumų kiekybiniam vertinimui.
3. Kuršių nerijos jūros priekrantės sėklai klostosi pagal smėlėtiems krantams būdingą ijjūrinės migracijos ciklo modelį. Šio ciklo trukmė

- išilgai Kuršių nerijos jūros priekrantės yra nevienoda ir ilgėja pietų kryptimi.
4. Kuršių nerijos jūros priekrantės sėkliams būdingas keliagubo sėkliaus sistemoje vykstantis persirikiavimo reiškinys, o šio reiškinio susidarymas periodiškai pasikartoja tose pačiose priekrantės zonose.
 5. Svarbiausi veiksniai, lemiantys sėklių kaitos skirtumus išilgai Kuršių nerijos Baltijos jūros priekrantės, yra sėklių zonas gylis bei sėklių dydis ir bangų sklidimo kryptis, aukštis bei periodas.
 6. Priekrantės sėklių persirikiavimo reiškiniu būdingi priekrantės morfologiniai pokyčiai turi įtakos kranto erozijos procesams, o tarp smėlio kiekiečių pokyčių krante ties priekrantės sėklių persirikiavimo zonomis ir už jų ribų egzistuoja reikšmingi skirtumai.

Naujumas ir aktualumas

Priekrantės sėklių pažinimas yra svarbus krantotvarkine-krantosaugine, ekologine bei socialine prasmėmis. Šios povandeninės reljefo formos turi didžiules smėlio atsargas ir yra neatsiejama litodinaminių, morfodinaminių bei hidrodinaminių procesų kranto zonoje dalis (Cohn ir kt., 2017; Phillips ir kt., 2017; Robin ir kt., 2014; Tātui ir kt., 2013). Priekrantės sėklai atlieka gamtinio bangolaužio funkciją – sulaiko dalį bangų energijos ir taip saugo krantą nuo ardos (Dubarbier ir kt., 2015; Fernández-Mora ir kt., 2015; Plant ir kt., 2001; Sallenger ir kt., 1985). Su jų morfologine struktūra yra glaudžiai susijusi priekrantės srovių cirkuliacija, o nuo pastarosios itin priklauso maisto medžiagų, teršalų bei žuvų išteklių pasiskirstymas priekrantėje (Camara ir kt., 2018; Elgar ir kt., 2001; Holzhauer ir kt., 2019) ir jūroje besimaudančių poilsiautojų saugumas (Brighton ir kt., 2013; Castelle ir kt., 2016). Dėl šių priežasčių priekrantės sėklių sistemas ir jos dinaminių ypatybių pažinimas yra būtinas parenkant optimalias krantosaugos bei krantotvarkos priemones, užtikrinant poilsiautojų saugumą rekreacinėse jūros kranto zonose ar tiriant ekologines jūros priekrantės problemas.

Lietuvos Baltijos jūros priekrantės sėklių dinamika iki šiol mažai ištirta. Nors sovietmečiu buvo atlikta nemažos apimties darbų (Jankevičiūtė, 1962; Stauskaitė, 1965; Jankevičiūtė-Močkienė, 1965; Kirlys ir kt., 1969, 1974a, 1974b; Žaromskis, 1974; Kirlys, Močiekienė, 1975), parengtas Lietuvos Baltijos jūros krantų geologinis atlasas (Baltijos jūros..., 2004), detalizuojantis tuometinę priekrantės sėklių struktūrą, taip pat yra pavienių tyrimų, atliktu nepriklausomos Lietuvos laikotarpiu (Gelumbauskaite, 2003; Žaromskis ir Gulbinskas, 2010; Žilinskas ir Jarmalavičius, 2007), šie darbai neatskleidžia dinamiškos priekrantės sėklių prigimties, jų kaitos dėsningumų ir priežasčių, taip pat jų sąveikos su krantu. Be to, dauguma pasaulyje pripažintų ir šių

gūbriškų formų kaitą paaiškinančių koncepcijų nėra taikytos ar patvirtintos Lietuvos Baltijos jūros priekrantėje. Šiame darbe pirmą kartą kiekybiškai įvertintos sėklių dinaminės ypatybės pagal sezoninę ir tarpmetinę laiko skales (**II publikacija**) ir apibūdinti jiems būdingi morfodinaminiai reiškiniai išilgai Lietuvos Kuršių nerijos jūros kranto (**IV publikacija**). Taip pat pirmą kartą pasaulinėje mokslinių tyrimų praktikoje pastebėtas niekada anksčiau neužfiksotas ir neaprašytas ryšys tarp priekrantės sėkliams būdingo persirikiavimo reiškinio ir kranto erozijos (**IV publikacija**).

Minėtiems reiškiniams tirti naudota atliktu tyrimu metu sudaryta Kuršių nerijos jūros priekrantės sėklių morfologinių charakteristikų, nustatytų iš palydovinių vaizdų, duomenų bazė. Jos sudarymas pagrįstas originaliu darbo autorės sukurtu automatizuotu algoritmu, skirtu šioms charakteristikoms identifikuoti optiniuose palydoviniuose vaizduose (**I publikacija**). Pasiūlytas algoritmas validuotas remiantis doktorantūros metu naujai surinktu natūrinių duomenų rinkiniu, periodiškai atliekant batimetrinius matavimus Lietuvos Kuršių nerijos dalies Baltijos jūros priekrantėje 17 skersinių pjūvių (iš viso 6 matavimai). Pasaulyje egzistuoja tik keletas metodikų, skirtų priekrantės sėklių identifikavimui palydoviniuose vaizduose (Román-Rivera ir kt., 2020; Tātui ir Constantin, 2020), tačiau sukurtais algoritmas yra unikalus tuo, kad, priešingai nei kituose darbuose aprašomi algoritmai, leidžia identifikuoti visą aibę priekrantės sėklių morfologinių charakteristikų, kurios gali būti taikomos skirtinėse sėklių tyrimų kryptyse. Darbų, kuriuose remiantis palydovine informacija analizuojama priekrantės sėklių kaita, taip pat trūksta, todėl disertacijoje, adaptavus tradicinius sėklių tyrimo metodus palydoviniams duomenims, atskleidžiamos jų dinamikos ypatybės ir parodomos neišnaudotos Žemės stebėjimo palydovų teikiamos galimybės šioje krantų geomorfologijos srityje (**II publikacija**).

Rezultatų reikšmė

Daktaro disertacijoje pasiūlyta priekrantės sėklių identifikavimo ir dinamikos analizės palydoviniuose vaizduose metodologija (**I publikacija**) pasižymi dideliu pritaikomumu: 1) ji pritaikoma (validuota) bent su keturiais skirtinės erdinės skiriamosios gebos palydoviniai jutikliai; 2) identifikuojama sėklių morfologines charakteristikas dideliu tikslumu, nepriklausomai nuo testuotų palydovų jutiklių savybių; 3) buvo kuriamas taip, kad tinkamai veiktu su visomis priekrantės sėklių morfologinėmis formomis, todėl yra taikytina kitoms smėlėtomis priekrantėms. Tai leidžia taikyti erdvėlaikinę priekrantės sėklių struktūros analizę ilguose kranto ruožuose, pakeičiant tradicinius daug išteklių reikalaujančius tyrimų metodus laiko ir finansinius išteklius taupančia alternatyva, ypač priekrantėse, kuriose šie

povandeniniai gūbriai nebuvvo tirti dėl duomenų trūkumo. Disertaciniame darbe sukurta sėklių duomenų bazė, kurioje nurodytos Kuršių nerijos jūros priekrantės sėklių morfologinės charakteristikos (**I-II publikacijos**) sudaro priealaidas atlikti tolesnius šių formų morfodinamikos tyrimus, neapsiribojančius disertacijoje pateiktomis publikacijomis.

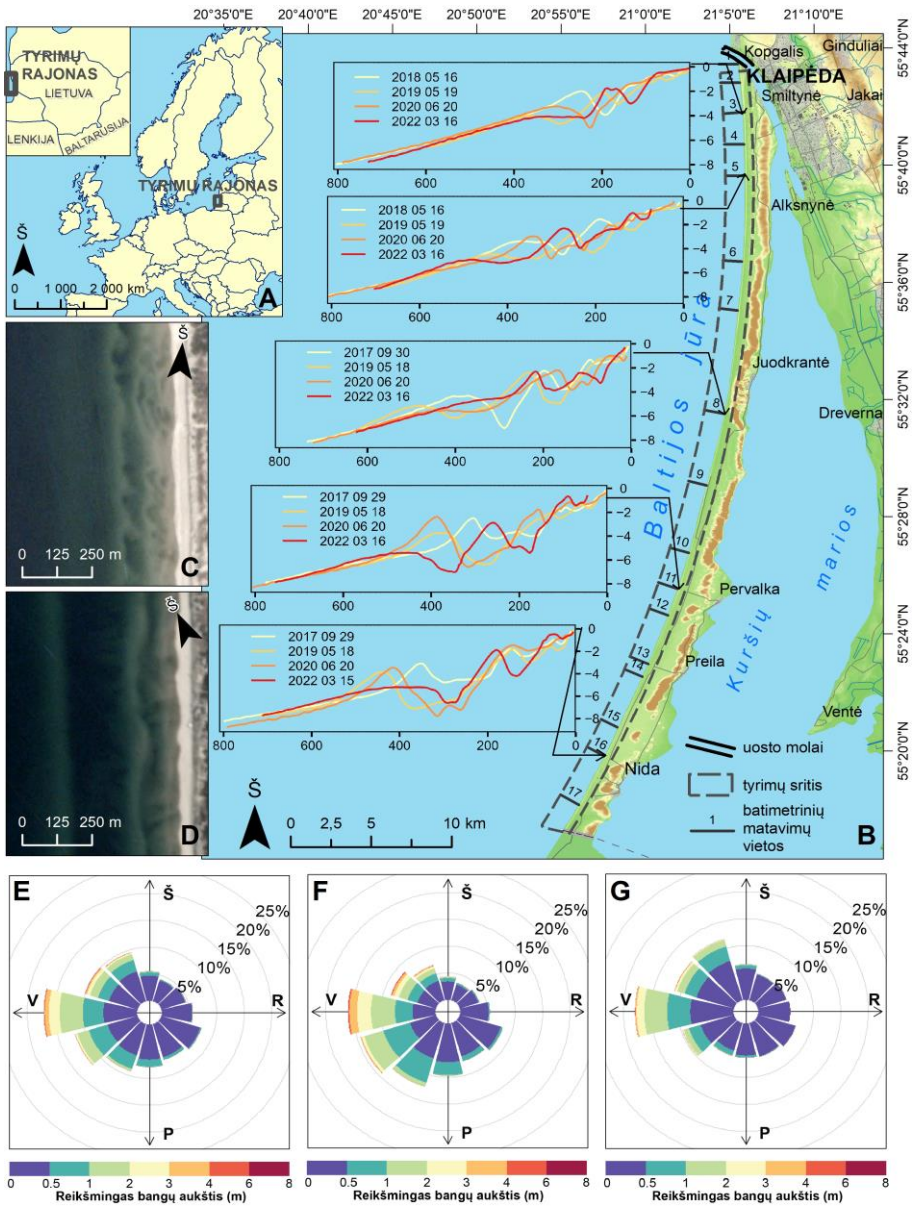
Priekrantės sėklių dinamikos ir jų ryšio su krante vykstančiais procesais vertinimas (**II-IV publikacijos**) prisideda prie visapusiško kranto zonos, kartu ir Kuršių nerijos, pažinimo ir sudaro priealaidas priimti informacija pagrįstus sprendimus krantotvarkoje. Atliktas Kuršių nerijos jūros priekrantės sėklių migracijos ir jos cikliškumo vertinimas (**III publikacija**) sudaro priealaidas prognozuoti sėklių elgseną išilgai Kuršių nerijos Baltijos jūros priekrantės. Darbe nustatytas ryšys tarp priekrantės sėklių persiriikiavimo epizodų ir kranto erozijos (**IV publikacija**) gali prisidėti prie kranto ardos procesų prognozavimo, probleminių ruožų identifikavimo ir savalaikio prevencinių krantosaugos priemonių pritaikymo.

1. TYRIMŲ MEDŽIAGA IR METODIKA

1.1. Tyrimų rajonas ir naudoti duomenys

Daktaro disertacijoje atliktų tyrimų rajonas apima 51 km ilgio Lietuvos Kuršių nerijos dalies jūros priekrantės ir kranto atkarą nuo Kopgalio iki Nidos (1 pav.). Tyrimai buvo atliki Baltijos jūros priekrantėje iki 8 m gylio ir paplūdimyje bei kopagūbryje.

Tyrimų teritorija yra nepotvyninė aplinka, kurioje vyrauja bangų ir priekrantės srovių veikla. Kuršių nerijos Baltijos jūros priekrantėje vyrauja vakarinių krypčių (V, PV, ŠV) bangos, kurių vidutinis reikšmingas aukštis tirtu laikotarpiu siekė 0,5 m (1 pav., E). Kuršių nerijos Baltijos jūros priekrantė pasižymi sezominiais bangų režimo skirtumais, todėl čia galima išskirti didelės bangų energijos (spalio–kovo mėnesiai) ir mažos bangų energijos (balandžio–rugsėjo mėnesiai) sezonus. Tirtu laikotarpiu reikšmingas bangų aukštis spalio–kovo mėnesiais Kuršių nerijoje siekė nuo 0 iki 8,3 m (vidutiniškai 0,7 m) (1 pav., F), o balandžio–rugsėjo mėnesiais nuo 0 iki 5,6 m (vidutiniškai 0,4 m) (1 pav., G).



1 pav. Tyrimų rajonas Lietuvos Kuršių nerijos dalyje: tyrimų rajono vieta (A); tyrimų rajono konfigūracija, batimetriinių matavimų vietos ir batimetriinių profilių pavyzdžiai (B); „PlanetScope“ palydovinių vaizdų pavyzdžiai su priekrantės sėkliais ties Smiltyne (C) ir Nida (D); Kuršių nerijos Baltijos jūros priekrantės bangų rožės 2009–2021 m. (E–G): visus metus (E), spalį–kovą (F) ir balandį–rugsėjį (G). Bangų rožės sudarytos remiantis valandiniais „Copernicus“ Baltijos jūros bangų reanalizės duomenimis (rezoliucija 2 x 2 km) arčiausiai kranto linijos esančiose gardelėse (E.U. Copernicus..., 2022).

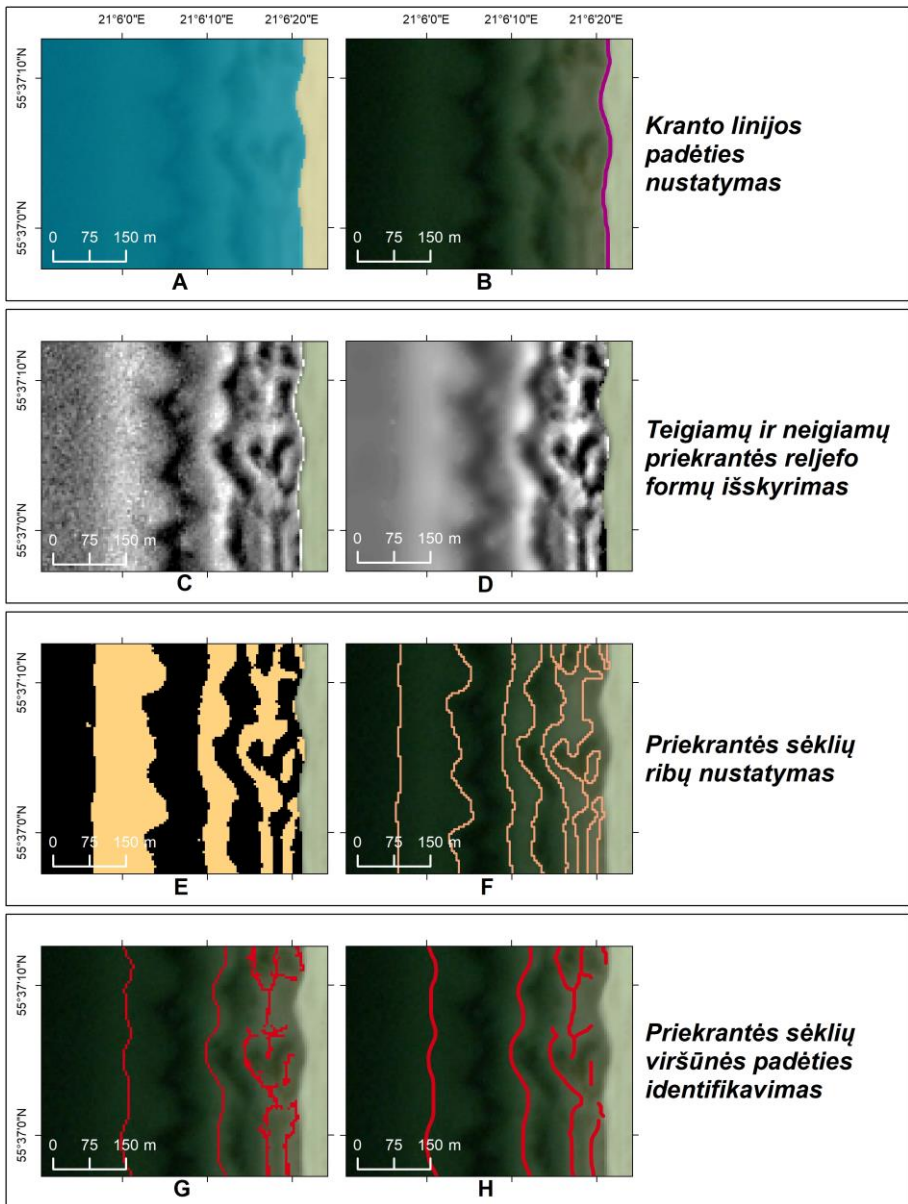
Disertacijoje naudojami optinio bei akustinio nuotolinio stebėjimo, kranto niveliacijos ir kitų šaltinių duomenys, iš kurių:

1. 2009–2021 m. laikotarpio optiniai palydoviniai vaizdai, užfiksuoti „PlanetScope“ (3 m) ir „RapidEye“ (5 m) jutiklių (**I**, **II**, **IV publikacijos**).
2. Batimetrių matavimų, kurie buvo atliekami 17 skersinių pjūvių, išsidėsčiusių išilgai Kuršių nerijos Baltijos jūros priekrantės kas 1–5 km (1 pav., A), duomenys. Matavimai buvo atliekami du kartus per metus (rudenį ir pavasarij) 2017–2022 m. (**I**, **II publikacijos**).
3. Gamtos tyrimų centro Geoaplinkos tyrimų laboratorijos mokslininkų kartą per metus atliekamų topografinių kranto matavimų duomenys (**IV publikacija**).
4. Istorinių-kartografinių šaltinių ir įvairiaisiais laikotarpiais Klaipėdos uosto prieigose surinkti batimetriniai duomenys (**III publikacija**). Tokio pobūdžio duomenų naudojimą šioje publikacijoje nulėmė tai, kad Klaipėdos uosto hidrotechniniai statiniai buvo pradėti statyti XIX a., todėl, siekiant įvertinti priekrantės pokyčius, paveiktus uosto statybos, buvo reikalingi ilgo laikotarpio duomenys, prieinami tik istoriniuose-kartografiniuose šaltiniuose.

1.2. Priekrantės sėklių identifikavimo palydoviniuose vaizduose ir duomenų paruošimo analizei metodika

Priekrantės sėklių morfodinamikos tyrimams sururta originali šių formų identifikavimo ir dinamikos analizės metodologija, skirta didelės ir vidutinės erdinės skiriamosios gebos (3–15 m) daugiaspektriams palydoviniams vaizdams (**I publikacija**). Joje priekrantės sėklių identifikavimas yra pagrįstas daugiažingsniu algoritmu, sudarytu iš keturių pagrindinių veiksmų blokų. Atliekant šiuos veiksmus nustatomos skirtingesnios šių povandeninių smėlių gūbrių morfoliginės charakteristikos, svarbios šių formų tyrimui.

Pirmojo veiksmų bloko tikslas – atskirti povandeninę kranto zonas dalį nuo sausumos (2 pav., A, B) (**I publikacija, 8–9 p.**). Jo metu, panaudojus artimojo infraraudonojo spektro kanalą (angl. *near-infrared* (NIR)) ir normalizuoto vandens skirtumo spektrinį rodiklį (angl. *Normalized Difference Water Index* (NDWI)) kaip įvesties sluoksnius ISODATA klasterizavimo algoritmui, sururiamas binarinis rastras su vandens ir sausumos paviršiais (2 pav., A). Jo pagrindu išskiriama kranto linija (2 pav., B). Toliau darbas tęsiamas tik su tais pikseliais, kurie priskirti vandens paviršiaus klasei.



2 pav. Pasiūlyto priekrantės sėklių morfologinių charakteristikų identifikavimo palydoviniuose vaizduose algoritmo pagrindiniai veiksmų blokai ir jų išvesties sluoksnių pavyzdžiai: A – binarinis vandens ir sausumos paviršių rastras; B – identikuota kranto linijos padėtis; C – daugiaskalio RBPI rodiklio rastras; D – daugiaskalio RBPI rastras po erdvinio filtravimo; E – binarinis rastras su sėkliais ir kitais paviršiais; F – nustatytos priekrantės sėklių ribos; G – nustatyta pirminė sėklių viršūnės padėtis; H – nustatyta galutinė sėklių viršūnės padėtis.

Antrasis veiksmų blokas skirtas teigiamų (sékliai) ir neigiamų (tarpsékliai) priekrantės reljefo formų identifikavimui (2 pav., C, D) (**I publikacija, 9–14 p.**). Joms atskirti naudojamas santykinis batimetrinės padėties rodiklis (angl. *Relative Bathymetric Position Index* (RBPI)). Tai vienos reljefo metrika, parodanti, ar analizuojamo pikselio gylis yra didesnis, ar mažesnis negu vidutinė gylio reikšmė kaimynystėje (slankiajame lange), ir normalizuota pagal minimalias bei maksimalias gylio reikšmes kaimynystėje (Janušaitė ir kt., 2021; Newman ir kt., 2018). Teigiamos RBPI rodiklio reikšmės indikuja iškilius dugno reljefo formas, o neigiamos – dubias. Šiam rodikliui apskaičiuoti įprastai naudojamos gylio reikšmės, tačiau kuriant algoritmą buvo pasiūlyta, kad jos gali būti pakeistos paviršiaus atspindžio reikšmių regimojo spektro kanaluose kombinacija.

RBPI rodiklio rezultatas labai priklauso nuo naudojamos kaimynystės dydžio: kaimynystė, kai pikselių skaičius mažas, tinka išskirti smulkiausias reljefo formas, o kai pikselių skaičius didelis – stambias (**I publikacija, 10 p., 4 pav.**). Priekrantės sékliai yra labai nevienodo dydžio ir formos sudėtingumo, o šios ypatybės labai kinta didėjant sékliaus atstumui nuo kranto (Short ir Aagaard, 1993; Van Enckevort ir kt., 2004; Wijnberg ir Kroon, 2002). Tarkim, Kuršių nerijoje ijūrinio sékliaus plotis gali siekti 90–400 m, vidurinio 50–250 m, o įkrantinio 20–200 m (Janušaitė, 2018). Dėl šių priežasčių kaimynystės dydžio parinkimas yra sudėtinga problema. Šiai problemai spręsti buvo pasiūlytas RBPI rodiklio skaičiavimo būdas, sujungiantis skirtinę pikselių skaičių turinčias kaimynystes, didinant jų apimtį, didėjant pikselio atstumui nuo kranto linijos (**I publikacija, 11–12 p., 5 pav.**) Šis daugiaskalis RBPI skaičiavimo būdas leidžia išsaugoti visą priekrantės séklių dydžių ir formų įvairovę (2 pav., C).

Santykinai homogeniški vandens paviršiai palydoviniuose vaizduose dažnai pasižymi mažu signalo ir triukšmo santykiumi. Ši problema itin ryški „PlanetScope“ ir „RapidEye“ jutiklių vaizduose (Houborg ir McCabe, 2018; Leach ir kt., 2019; Sadeh ir kt., 2021, 2019), todėl gautas daugiaskalio RBPI rastrinis sluoksnis pasižymi ryškiu atsitiktiniu triukšmu (2 pav., C). Šiai problemai spręsti pasitelktas erdvinis filtravimas, pritaikius pirmiau pristatytą daugiaskalį metodą, didinant filtro dydį, didėjant pikselio atstumui nuo kranto (**I publikacija, 14 p.**). Daugiaskalio RBPI rastrinis sluoksnis, iš kurio pašalintas triukšmas (2 pav., D), yra galutinis antrojo priekrantės séklių identifikavimo etapo rezultatas.

Trečiasis veiksmų blokas yra skirtas priekrantės séklių ribų, t. y. jų ploto, išskyrimui (2 pav., E, F) (**I publikacija, 14–15 p.**). Tam RBPI rastrinis sluoksnis yra suklasifikuojamas į binarinį rastrą, kuriame išskirtos séklių ir kitų paviršių klasės (2 pav., E). Jeigu gautame rezultate yra sékliams

klaidingai priskirtų priekrantės plotų, jie yra pašalinami taikant atrankos operacijas, paremtas sėklių dydžio ir atstumo nuo kranto kombinacijų kriterijais.

Ketvirtasis veiksmų blokas yra skirtas priekrantės sėklių viršunių padėties identifikavimui (2 pav., G, H), panaudojant išskirtas jų ribas (2 pav., F) ir daugiaskalio RBPI rastrus, iš kurių pašalintas triukšmas (2 pav., D) (**I publikacija, 15–18 p.**). Sėklių viršūnėmis laikomi maksimalios RBPI rodiklio reikšmės pikseliai. Jie yra identifikuojami trimis kryptimis (V–R, ŠR–PV, ŠV–PR), kurios leidžia nustatyti sėkliaus viršūnės padėtį, kad ir kokia bebūtų sėkliaus forma ir viršūnės orientacija kranto atžvilgiu (2 pav., G) (**I publikacija, 15–17 p., 8 pav.**). Pavieniai pikseliai negali reprezentuoti sėkliaus viršūnės, todėl, siekiant pašalinti klaidingai identifikuotus viršūnių pikselius ir nustatyti galutinę viršūnės padėtį (2 pav., H), buvo sukurtas ir pasiūlytas viršūnės pikselių artumu pagrįstas erdvinis filtras (**I publikacija, 17–18 p., 8 pav.**).

Įgyvendinus visą aprašytą algoritmą gaunami išvesties sluoksniai, kuriuose saugoma kranto linijos padėtis (1) (2 pav., B), daugiaskalis RBPI rodiklis, indikuojantis priekrantės dugno reljefo formas (2) (2 pav., D), sėklių ribos (plotai) (3) (2 pav., F) ir viršūnių padėtis (4) (2 pav., H).

Algoritmas buvo įgyvendintas naudojant 145 datų „PlanetScope“ ir „RapidEye“ jutiklių vaizdus, užfiksuotus 2009–2021 m., o gautų duomenų pagrindu sudaryta Kuršių nerijos jūros priekrantės sėklių morfologinių charakteristikų duomenų bazė. Kuršių nerijos jūros priekrantės sėklių dinamikos analizė buvo atliekama naudojant 1 071 skersinį pjūvį (profilį), kurie buvo išsidėstę kas 50 m (**II publikacija**). Profiliams buvo sudarytos dvi duomenų bazės, paremtos iš palydovinių vaizdų nustatytomis charakteristikomis. Pirmoji apima šiuos rodiklius: sėkliaus atstumą nuo vidutinės kranto linijos, sėkliaus eilės numerį sėklių sekoje ir sėklių skaičių, o antroji – RBPI rodiklio reikšmių laiko eilutes kiekvienam profiliui. Sėkliaus padėtis kranto atžvilgiu (eilės numeris sėklių sekoje) apibrėžta pagal jo atstumą nuo kranto: toliausiai nuo kranto esantis sėklius laikytas pirmu, antras labiausiai nuo kranto nutolęs – antru, o arčiausiai kranto esantis sėklius – *n*-uoju.

1.3. Duomenų analizės metodika

Atliekant Kuršių nerijos jūros priekrantės sėklių dinamikos ir jos ryšio su kranto raida analizę, buvo:

1. Ivertinti priekrantės sėklių migracijos skersai kranto tempai pagal skirtingas laiko skales (sezoninę ir tarpmetinę) 2011–2021 m. (**II**

publikacija). Šiam vertinimui buvo naudojamos mėnesinių priekrantės sėklių atstumo nuo kranto rodiklių laiko eilutės. Sezoninė laiko skalė išskaidyta į mažos bangų energijos (balandis–rugsėjis) ir didelės bangų energijos (spalis–kovas) sezonus. Tarpmetiniai ir sezoniai sėklių migracijos greičiai nustatyti naudojant jų atstumo nuo kranto laiko eilučių slankiuosius vidurkius, kurių laiko imtys yra skirtingo dydžio, ir jų pirmo laipsnio išvestines (**II publikacija, 6–7 p.**). Analogiška metodika jau ne kartą taikyta vertinant sėklių dinamiką pagal batimetrinius ir stebėsenos vaizdo kameromis gautus duomenis (Melito ir kt., 2020; Van Enckevort ir Ruessink, 2003a), todėl gautus rezultatus galima palyginti su kitų smėlėtų pasaulio krantų rezultatais.

2. Ivertintas priekrantės sėklių migracijos skersai kranto cikliškumas (**II publikacija**). Jam nustatyti buvo atlikta kompleksinė empirinių ortogonalų funkcijų analizė (angl. *Complex Orthogonal Function Analysis* (CEOF)), o kaip jos rezultatas nustatytas sėkliaus ciklo pasikartojimo periodas (angl. *bar cycle return period* (T_r)), kuris apibūdina laiko tarpą tarp dviejų išūrinio sėkliaus degeneracijų (Ruessink ir kt., 2003) išilgai Kuršių nerijos Baltijos jūros kranto. Tradiciškai CEOF analizėje naudojami batimetriniai priekrantės skersiniai profiliai (Ruessink ir kt., 2003; Tātui ir kt., 2016) buvo pakeisti šiame darbe pasiūlyto daugiaskalio RBPI rodiklio laiko eilutėmis priekrantės skersiniuose profiliuose (**II publikacija, 7–8 p.**).
3. Ivertintas priekrantės sėklių persirikiavimo reiškinys 2009–2021 m. (**IV publikacija**). Tam palydoviniuose vaizduose buvo identifikuotos Kuršių nerijos jūros priekrantės sėklių persirikiavimo zonas, jų pirmojo ir paskutinio pastebėjimo datos, erdvinis pasikartojimas, atlikta vizualioji priekrantės morfologinių pokyčių eigos persirikiavimo zonose analizė (**IV publikacija, 4 p.**).
4. Išskirti panašia priekrantės sėklių elgsena pasižymintys priekrantės ruožai (**II publikacija**). Tam atlikta klasterinė analizė, pritaikius mišrų k. vidurkių ir hierarchinio klasterizavimo metodą, o klasterinei analizei naudotos 36 charakteristikos, apibūdinančios priekrantės sėklių morfologinę struktūrą ir dinamiką skersai kranto, nustatytos atlikus pirmo ir antro punktų vertinimus (**II publikacija, 8–9 p.**).
5. Ivertinta antropogeninės veiklos paveikta priekrantės dugno reljefo kaita Klaipėdos uosto prieigose nuo XIX a. (**III publikacija**). Ji buvo pagrįsta skirtinę laikotarpių istorinių-kartografinių bei batimetrinų duomenų GIS analize ir kranto zonos pokyčių vertinimu 11 topobatimetinių skersinių profilių abipus uosto molų (**III publikacija, 490 p.**).

6. Įvertinti priekrantės sėklių kaitą lemiantys veiksniai (**II–IV publikacijos**). Priekrantės sėklių dinamikos ypatumai buvo siejami su sėklių zonas morfometrija, hidrodinamika ir bendra kranto konfigūracija. Jų sąsajoms įvertinti buvo atliekama tiesinė regresinė ir logistinė regresinė analizės.
7. Įvertintas priekrantės sėklių persirikiavimo ir kranto kaitos ryšys 2009–2021 m. (**IV publikacija**). Atliekant šį vertinimą buvo analizuojami kranto linijos padėties ir smėlio kieko krante pokyčiai sėklių persirikiavimo zonose ir už jų ribų, remiantis palydoviniais ir topografinių matavimų duomenimis, pagal tarpmetinę laiko skalę ir audrų metu. Ryšiu ivertinti buvo atliekama tiesinė regresinė analizė ir statistinis hipotezių testavimas (**IV publikacija, 4 p.**).

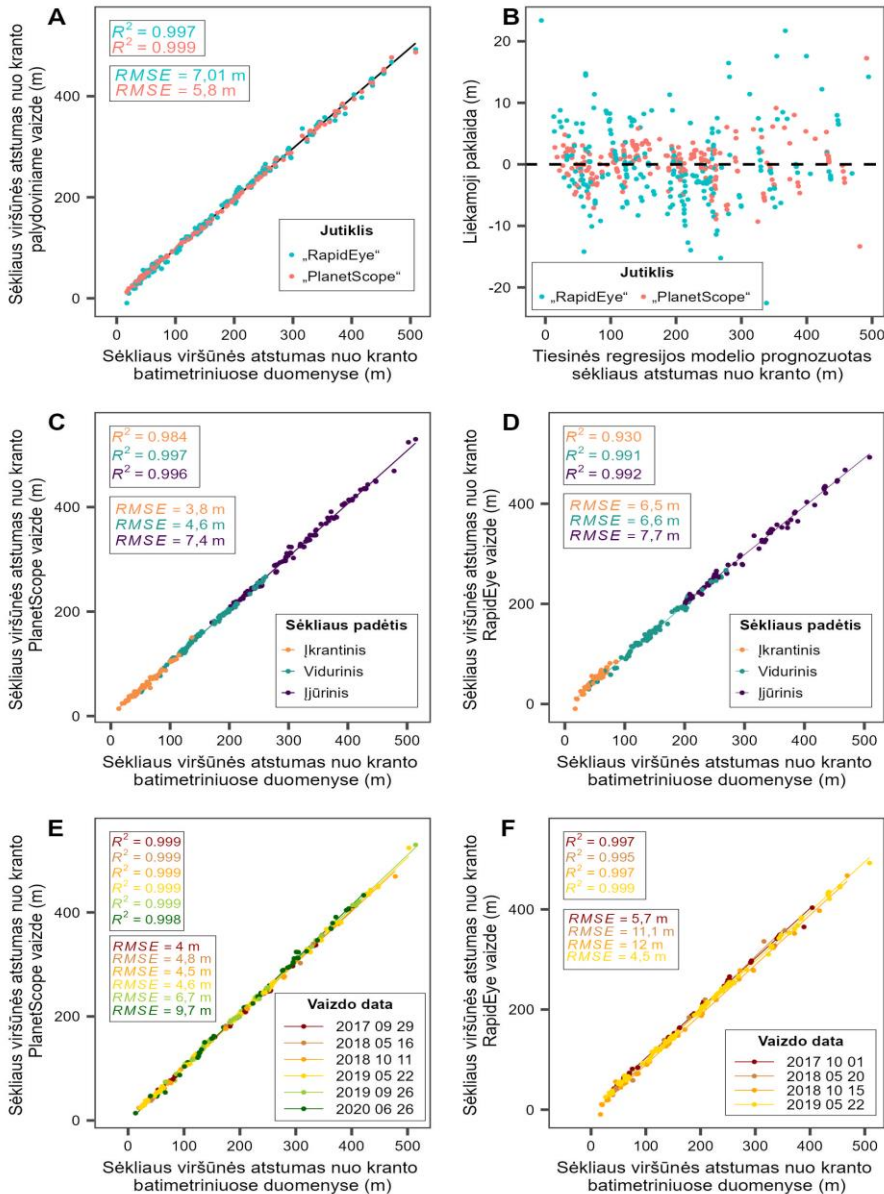
2. TYRIMŲ REZULTATAI

2.1. Priekrantės sėklių identifikavimo palydoviniuose vaizduose metodikos tikslumas

Siekiant įvertinti priekrantės sėklių identifikavimo palydoviniuose vaizduose metodikos tikslumą, atliktas jų viršūnės padėties, nustatytos iš palydovinių ir batimetrinij matavimų duomenų, palyginimas (**I publikacija, 19–20, 22, 23–25 p.**).

Tikslumas esant mažai bangų energijai. Palyginimui mažos bangų energijos sąlygomis naudoti šešių datų batimetrinij matavimų, kurių atlikimo data nuo palydovinio vaizdo užfiksavimo datos skyrėsi 0–6 dienomis, duomenys. Iš viso palygintos 553 poros viršūnių taškų, identifikuotų „PlanetScope“ ir „RapidEye“ jutiklių vaizduose, ir batimetriniuose duomenyse. Nustatyta vidutinė kvadratinė paklaida (angl. *root mean square error (RMSE)*) „PlanetScope“ ir „RapidEye“ jutikliams atitinkamai siekė 5,8 m ir 7,0 m (3 pav., A), tačiau skirtingomis vaizdo fiksavimo datomis variavo nuo 4,0 iki 12,0 m (3 pav., E, F). Didžiausios paklaidos buvo aptiktos tomis datomis, kai dienų skirtumas tarp vaizdo fiksavimo ir batimetrinij matavimų datų buvo didžiausias, todėl didesnės paklaidų reikšmės gali būti nulemtos priekrantėje įvykusiu pokyčiu (**I publikacija, 19–20 p.**).

„RapidEye“ vaizduose identifikuota sėklių viršūnių padėtis pasižymėjo didesne paklaidų amplitude negu identifikuota „PlanetScope“ vaizduose (3 pav., B). Paklaidų amplitudė taip pat šiek tiek didėjo, didėjant sėkliaus atstumui nuo kranto (3 pav., B). Tai patvirtina ir viršūnės padėties tikslumo skirtumai, kai sėkliaus padėtys skersai kranto yra skirtinges: tiksliausiai buvo identifikuojama įkrantinio sėkliaus padėtis, o mažiausiai tiksliai – ijjūrinio (3 pav., C, D).



3 pav. Tiesinis ryšys ir vidutinės kvadratinės paklaidos tarp „PlanetScope“ (A, C, E) ir „RapidEye“ (A, D, F) palydoviniuose vaizduose pasiūlyto algoritmo identifikuotų priekrantės séklių viršūnių taškų ir viršūnių taškų, nustatytų iš batimetriinių matavimų duomenų, priklausomai nuo jutiklio (A), sékliaus padėties skersai kranto (C, D) ir vaizdo užfiksavimo datos (E, F). B grafike pateikiamos liekamosios paklaidos tarp remiantis A grafike pavaizduotu regresiniu modeliu nustatyti viršūnių padėcių ir batimetriiniuose duomenyse identifikuotų viršūnių padėcių.

Pasiūlytas algoritmas validuotas ir su Europos kosmoso agentūros (ESA) „Sentinel-2“ MSI (erdvinė skiriamoji geba 10 m) bei Šiaurės Amerikos kosmoso agentūros (NASA) „Landsat-8“ OLI (panchromatinio kanalo erdvinė skiriamoji geba 15 m) palydovų vaizdais, kurie yra laisvai prieinami ir nemokami visiems naudotojams. Nustatyta, kad, nesant bangavimo, sėklių viršūnės „Sentinel-2“ MSI vaizduose buvo identifikuojamos su $RMSE = 4,5$ m, o „Landsat-8“ OLI – $RMSE = 7,5$ m (**I publikacija, 23–24 p., 12 pav.**). Sie rezultatai rodo, kad, nors šių jutiklių vaizdų erdvinė raiška prastesnė, sėklių viršūnių padėtis juose gali būti nustatoma panašiu tikslumu kaip ir „PlanetScope“ bei „RapidEye“ vaizduose.

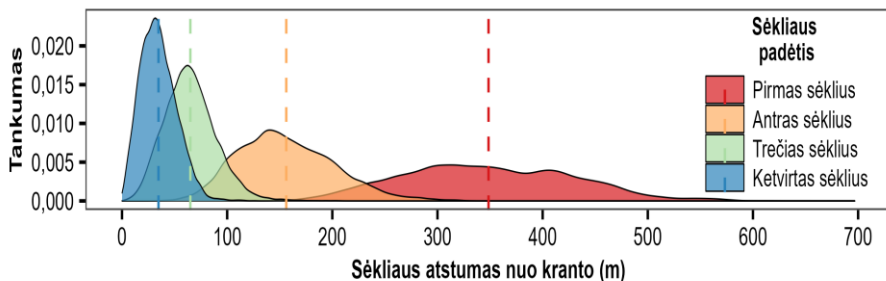
Tikslumas esant didelei bangų energijai. Metodo tikslumas esant ryškiam bangavimui buvo įvertintas palyginus sėklių viršūnių padėti „Sentinel-2“ MSI ir „Landsat-8“ OLI vaizduose su batimetrinį matavimų duomenimis. Nustatyta, kad sėklių viršūnių padėties tikslumas, kai bangų energija yra didelė, sumažėjo 3–4 kartus ir „Sentinel-2“ MSI bei „Landsat-8“ OLI vaizduose atitinkamai siekė 18,9 ir 22,9 m (**II publikacija, 23, 25 p., 13 pav.**).

Metodo taikymo limitai. Metodo taikymas tiriant sėklus yra nulemtas aplinkos charakteristikų vaizdo fiksavimo metu (vandens skaidrumas, debesuotumas, bangų energija) ir pačių sėklių charakteristikų (dydžio, gylio, formos išraiškingumo). Dėl didelių paklaidų esant aukštoms bangoms metodą rekomenduojama taikyti tik tada, kai palydoviniame vaizde nėra matomų gožtančių bangų. Degeneracijos stadijoje esantys ir formos išraiškingumu nepasižymintys ijūriniai sėkliai, kurių viršūnė yra didesniame negu 6 m gylyje, taip pat kartais lieka neaptiktii, todėl metodo taikymas yra ribojamas ir sėklių viršūnės gylio (**I publikacija, 21–22 p.**).

2.2. Priekrantės sėklių struktūra ir dinamika

2.2.1. Priekrantės sėklių morfologinė struktūra

Kuršių nerijos jūros priekrantei būdinga trigubo ir keturgubo sėkliaus sistema. Tai patvirtina ir 2009–2021 m. situacija, kai 85 % tirtų priekrantės skersinių profilių sėklių skaičiaus moda buvo trys, o 13 % – keturi sėkliai. Ijūrinis (pirmas) sėkliai nuo kranto vidutiniškai buvo nutolęs 349 m, antras 156 m, trečias ir ketvirtas sėkliai atitinkamai 65 ir 35 m (4 pav.), tačiau šios charakteristikos buvo labai nevienodos išilgai Kuršių nerijos Baltijos jūros priekrantės. Vidutinis sėklių zonos plotis Kuršių nerijoje siekė 512 m ir išilgai kranto varijavo tarp 340 ir 700 m (**II publikacija, 9–10 p., 5 pav.**).



4 pav. Kuršių nerijos jūros priekrantės sėklių viršūnių atstumo nuo kranto reikšmių pasiskirstymo 2009–2021 m., atsižvelgiant į jų padėtį skersai kranto, reikšmių tankio diagrama.

2.2.2. Priekrantės sėklių kaita skersai kranto

Priekrantės sėklių kaita skersai kranto įvertinta atlikus jų įkrantinės ir ižūrinės migracijos tempų pagal skirtinges laiko skales ir jos cikliškumo analizes (**II publikacija, 10–16 p.**).

Sezoninė laiko skalė. Mažos bangų energijos sezono metu (balandži–rugsėji) vidutinis sėklių migracijos greitis analizuotuose profiliuose kito nuo 0,1 iki 7,0 m/mėn., tai priklausė nuo sėkliaus padėties skersai kranto ir migracijos krypties (1 lentelė) (**II publikacija, 12 p., 9 pav.**). Didelės bangų energijos sezono metu (spalį–kovą) vidutinis sėklių migracijos greitis varijavo nuo 0,1 iki 13,4 m/mėn. (1 lentelė) (**II publikacija, 13–14 p., 8 pav.**). Vidutinis sezominis sėklių migracijos greitis didėjo, didėjant sėklių atstumui nuo kranto linijos (1 lentelė), todėl tiek mažos, tiek didelės bangų energijos sezono metu pirmas sėkliai pasižymėjo didžiausiu vidutiniu migracijos skersai kranto greičiu, o trečias bei ketvirtas sėkliai – mažiausiu (1 lentelė) (**II publikacija, 12–14 p., 8–9 pav.**). Taip pat tiek mažos, tiek didelės bangų energijos sezono metu antro–ketvirto sėklių vidutinis įkrantinės migracijos greitis viršijo vidutinį ižūrinės krypties migracijos greitį (1 lentelė). Priešingai negu kitiems sėklams, pirmam (ižūriniam) sėklui buvo būdingas beveik identiškas vidutinis ižūrinės ir įkrantinės migracijos greitis mažos bangų energijos sezono metu ir didesnis vidutinis ižūrinės krypties migracijos greitis didelės bangų energijos sezono metu (1 lentelė) (**II publikacija, 12–13 p.**).

1 lentelė. Kuršių nerijos priekrantės sėklių migracijos skersai kranto greitis pagal skirtingas laiko skales. Min. ir Maks. – vidutinė migracijos greičio reikšmė skersiniame profilyje, kuriame vidutinis migracijos greitis iš analizuotų 1 071 profilio atitinkamai buvo mažiausias ir didžiausias; Vid. – visų analizuotų skersinių profilių vidutinė migracijos greičio reikšmė. Migracijos greičiai lentelėje nurodyti m/mėn.

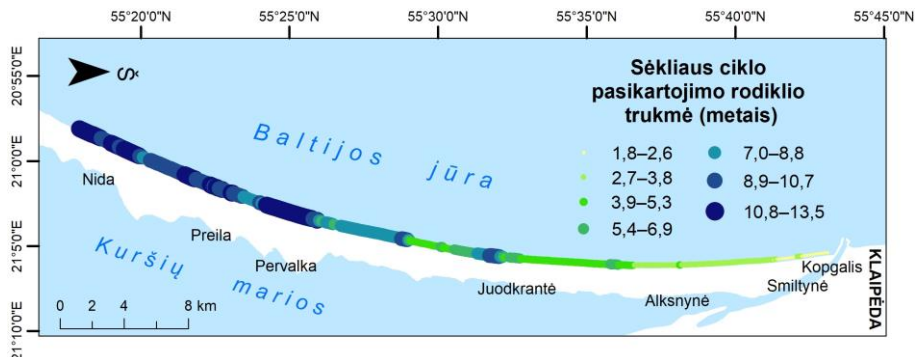
Sėkliaus padėtis	Migracijos kryptis	Laiko skalė									
		Tarpmetinė			Sezoninė (balandis–rugsėjis)			Sezoninė (spalis–kovas)			
		Min.	Vid.	Maks.	Min.	Vid.	Maks.	Min.	Vid.	Maks.	
1 sėklius	Jūros link	2,6	5,4	9,7	1,6	3,6	6,1	0,7	6,7	12,9	
	Kranto link	0,3	4,9	11,0	1,0	3,5	7,0	0,1	5,5	13,4	
2 sėklius	Jūros link	1,3	3,4	6,3	1,2	2,9	5,1	0,1	4,4	8,4	
	Kranto link	0,4	3,1	6,1	0,9	3,4	6,0	0,1	4,7	11,4	
3 sėklius	Jūros link	0,5	2,4	4,4	0,9	2,4	4,3	0,4	3,3	6,0	
	Kranto link	0,5	2,2	4,2	1,4	3,0	4,9	0,2	3,4	6,8	
4 sėklius	Jūros link	0,4	2,4	5,5	0,1	2,1	4,8	0,1	2,5	6,8	
	Kranto link	0,1	1,9	4,9	0,1	2,4	5,3	0,1	2,7	7,0	

Tarpmetinė laiko skalė. Pagal tarpmetinę laiko skalę vidutinis sėklių migracijos greitis analizuotuose profiliuose siekė 0,1–11,0 m/mėn., priklausomai nuo sėkliaus padėties skersai kranto ir migracijos krypties (1 lentelė) (**II publikacija, 10–11 p., 6 pav.**). Didžiausiu migracijos skersai kranto greičiu pasizymėjo pirmas sėklius (vidutiniškai 4,9–5,4 m/mėn.) (1 lentelė), o lėčiausiai migravo trečias ir ketvirtas sėkliai (vidutiniškai 1,9–2,4 m/mėn.) (1 lentelė) (**II publikacija, 11–12 p.**). Vidutinis įjūrinės migracijos greitis pagal tarpmetinę laiko skalę viršijo vidutinį įkrantinės migracijos greitį, kad ir kokia būtų buvusi sėkliaus padėtis skersai kranto (1 lentelė).

Migracijos skersai kranto greičio pagal tarpmetinę ir sezoninę laiko skales palyginimas. Didžioji dalis analizuotų profilių pasizymėjo didžiausiu vidutiniu sėklių migracijos skersai kranto greičiu pagal sezoninę laiko skalę didelės bangų energijos sezono metu ir mažiausiu vidutiniu greičiu mažos bangų energijos sezono metu. Toks migracijos greičio pasiskirstymas yra nulemtas sezoninių bangų aukščio skirtumų, aptartą 1.1 poskyryje. Vidutinis migracijos skersai kranto greitis pagal tarpmetinę laiko skalę buvo mažesnis negu didelės bangų energijos sezono metu, bet didesnis negu mažos bangų energijos sezono metu. Šios tendencijos buvo būdingos visiems sėkliams nuo pirmo iki ketvirto (**II publikacija, 14–15 p., 9 pav.**)

Daugiametė laiko skalė. Pastebėta, kad, taikant daugiametę laiko skalę, keliagubo sėkliaus sistema Kuršių nerijos jūros priekrantėje vystosi pagal

olandų mokslininkų pasiūlytą modelį, kurį apibūdina įjūrinės migracijos ciklas (Ruessink ir Kroon, 1994). Sėkliai susidaro nedideliu atstumu nuo kranto, migruodami skersai kranto palaipsniui tolsta nuo jo, kol galiausiai įjūrinis sėkliai išnyksta iš priekrantės profilio, o antrasis sėkliai įgauna „antrajį kvėpavimą“ ir pradeda sparčiai vystytis bei tolti nuo kranto. Šio ciklo trukmę apibūdina įjūrinio sėklių ciklo pasikartojimo rodiklis (T_r). Nustatyta, kad vidutinė šio rodiklio reikšmė Kuršių nerijoje yra 6,7 m., tačiau išilgai kranto ji labai nevienoda ir kinta nuo 1,8 m. iki 13,5 m. (5 pav.) (II publikacija, 15 p.).



5 pav. Priekrantės sėklių ciklo pasikartojimo rodiklio (T_r) trukmė Lietuvos Kuršių nerijos dalies Baltijos jūros priekrantėje.

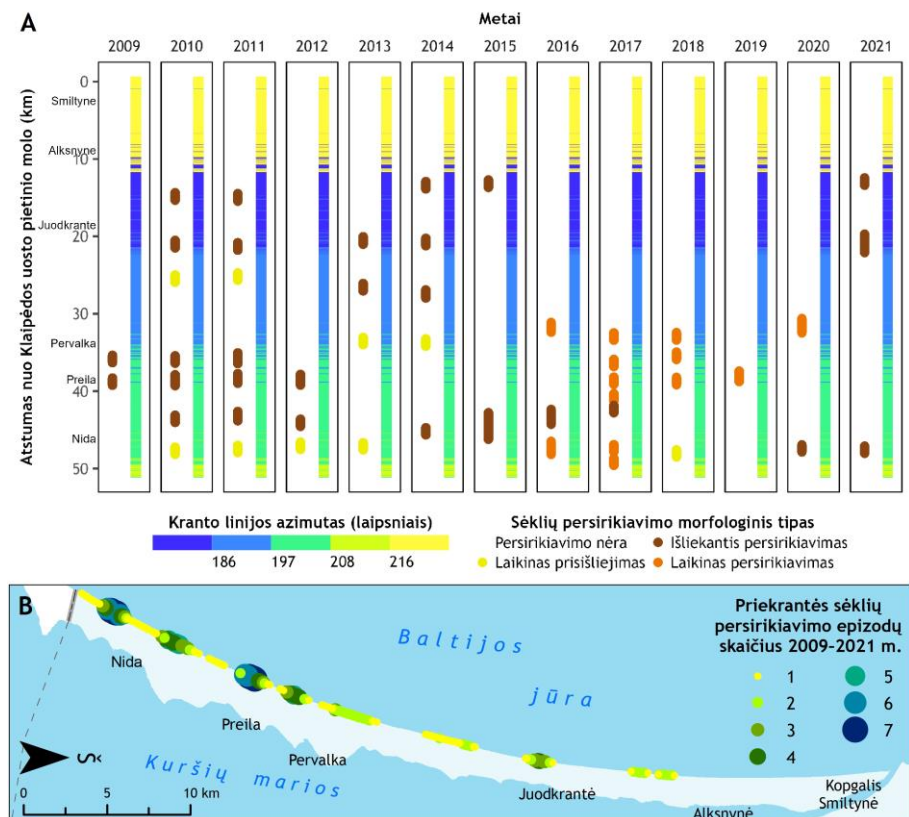
Kaitos skersai kranto skirtumai išilgai Kuršių nerijos jūros priekrantės. Sėklių migracijos skersai kranto greitis išilgai Kuršių nerijos jūros priekrantės buvo labai netolygus. Tieki pagal tarpmetinę, tieki pagal sezoninę laiko skales priekrantės sėkliai šiaurinėje Kuršių nerijos dalyje pasižymėjo didesniu migracijos skersai kranto greičiu, o pietinėje nerijos dalyje jie judėjo lėčiau (II publikacija, 11, 12, 14 p., 6–8 pav.). Sėklių ciklo pasikartojimo rodiklio trukmė taip pat ilgėjo iš šiaurės į pietus (5 pav.) ir atitiko sėklių migracijos skersai kranto greičio nevienodumo išilgai nerijos priekrantės tendencijas.

2.2.3. Priekrantės sėklių morfodinaminiai ypatumai

Darbe 2009–2021 m. laikotarpiu analizuotas vienas iš kelių sėklių susidariusioms priekrantės sėklių sistemoms būdingų morfodinaminių reiškiniių – sėklių persirikiavimas, kurio metu dėl netolygaus sėklių vystymosi išilgai kranto jis praranda vientisumą, atitrūkės jo galas prisišlieja prie kito arčiau arba toliau nuo kranto esančio sėklių ir ima vystytis jo vietoje (Shand ir kt., 2001; Wijnberg ir Wolf, 1994) (IV publikacija).

Persirikiavimo epizodų trukmė. Analizuotu 2009–2021 m. laikotarpiu Kuršių nerijoje užfiksuoti 27 priekrantės sėklių persirikiavimo epizodai. Jų trukmė varijavo nuo dviejų mėnesių iki ketverių metų, o vidutiniškai persirikiavimo epizodas truko 14 mėnesių (**IV publikacija, 5 p., 1 lentelė**).

Persirikiavimo susidarymo vietos. Tipiškai sėklių persirikiavimo epizodai vyko šešiose Kuršių nerijos jūros priekrantės atkarpose, kurių pirmoju buvo ties Alksnyne, į pietus nuo jos persirikiavimo epizodų skaičius didėjo, o priekrantės atkarpoje tarp Kopgalio ir Alksnynės persirikiavimo epizodų 2009–2021 m. nebuvo užfiksuota (6 pav., B). Didžiausias persirikiavimo epizodų skaičius 2009–2021 m. užfiksotas ties Preila ir pietine Nidos dalimi (7 epizodai) (6 pav., B) (**IV publikacija, 5 p.**).



6 pav. A – priekrantės sėklių persirikiavimo zonas ir kranto linijos orientacija 2009–2021 m. Kranto linijos azimutas grafike yra nustatyta pagal vidutinę 2009–2021 m. kranto linijos padėtį ir yra vienodos visuose subgrafikuose. B – 2009–2021 m. užfiksotų priekrantės sėklių persirikiavimo epizodų pasikartojimas išilgai Kuršių nerijos jūros priekrantės.

Persirikiavimo morfologiniai tipai. Atlikus vizualiają persirikiavimo epizodų eigos analizę 2009–2021 m., buvo išskirti trys persirikiavimo morfologiniai tipai, būdingi Kuršių nerijai: 1) kai sėklius užima kito arčiau arba toliau nuo kranto esančio sėkliaus vietą ir toliau joje vystosi (išliekantis persirikiavimas, 44 % persirikiavimo atvejų); 2) kai sėklius užima kito arčiau arba toliau nuo kranto esančio sėkliaus vietą, tačiau po kurio laiko grįžta į pirminę padėtį (laikinas persirikiavimas, 41 % persirikiavimo atvejų); 3) kai sėklius laikinai prisijungia prie kito sėkliaus, tačiau nesivysto jo vietoje (laikinas prisišlejimas, 15 % persirikiavimo atvejų) (**IV publikacija, 5–6 p., 3 pav.**). Skirtingų persirikiavimo morfologinių tipų susidarymo vietas 2009–2021 m. pažymėtos 6 pav., A.

Priekrantės sėklių persirikiavimas yra svarbus, nes turi įtakos priekrantės hidrodinamikai iki kelerių metų. Be to, pasikartojančių persirikiavimo epizodų zonas dažnai įvardijamos kaip pereinamosios zonas tarp skirtingomis morfodinaminėmis ypatybėmis pasižymintių priekrantės ruožų (Walstra ir kt., 2016; Wijnberg ir Terwindt, 1995).

2.2.4. Priekrantės sėklių kaita, paveikta žmogaus veiklos

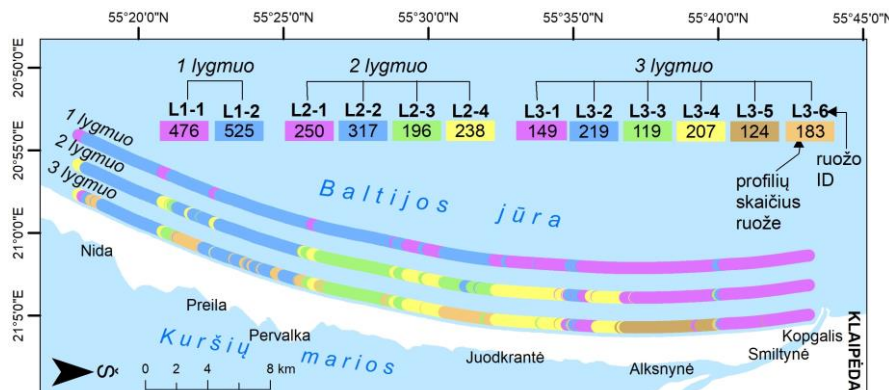
Nors didžioji Lietuvos Kuršių nerijos jūros priekrantės dalis reprezentuoja žmogaus nepaveiktus sėklių kaitos procesus, trumpas priekrantės ruožas šiaurinėje nerijos dalyje ties Kopgaliu yra veikiamas Klaipėdos uosto hidrotechninių statinių, todėl atlikta detali šio ruožo kaitos analizė nuo uosto molų statybos pradžios iki šių dienų (**III publikacija**). Klaipėdos uosto molų statyba, jų konfigūracijos bei ilgio kaita ir iplaukos kanalo gilinimo darbai lėmė ir priekrantės dugno reljefo struktūros kaitą distaliniame Kuršių nerijos gale du pastaruosius šimtmecius. Dėl to priekrantės raidą šioje uosto įtakos zonoje būtų galima suskirstyti į keletą etapų: 1) iki uosto molų statybos, kai jūros priekrantėje distaliniame nerijos gale buvo susiformavusi sekluma (**III publikacija, 491 p.**); 2) uosto molų statybos, kai pastačius pietinį uosto molą (1847–1902 m.) ši sekluma prisišlejo prie kranto, lemdama didelę kranto akumuliaciją (**III publikacija, 492 p.**); 3) iplaukos kanalo gilinimo (1902–2000 m.), kai tiek krante, tiek jūros priekrantėje vyravo erozijos procesai (**III publikacija, 495 p.**); 4) uosto molų rekonstrukcijos (nuo 2002 m.) (**III publikacija, 496–497 p.**). Pastaruoju laikotarpiu ties pietiniu uosto molu yra susiklostęs dvigubas sėklius, susidaręs iš lėkštos 220–270 m ilgio ir 70–100 m pločio seklumos, kuri piečiau išsišakoja į 2–3 nedidelius sėkliukus ir periodiškai prisišleja prie kranto arba suformuoja negilų tarpsėklį, ir neryškios ijjūrinio sėkliaus, išplatėjančio ir išryškėjančio pietų kryptimi, užuomazgos. Panaši priekrantės sėklių struktūra buvo dar iki uosto molų

rekonstrukcijos ir pailginimo darbų (2001–2002 m.) 1963 ir 1998 m. darytuose ortofotografiniuose žemėlapiuose, todėl galima teigti, kad dabartinė sėklių struktūra seklioje jūros priekrantėje šalia pietinio molo susiformavo dar uosto iplaukos kanalo gilinimo etape.

2.2.5. Panašia sėklių struktūra ir dinamika pasižymintys priekrantės ruožai

Atlikus klasterinę 36 Kuršių nerijos jūros priekrantės sėklių morfologinių ir dinaminių charakteristikų, apibūdinančių jų kaitą ir struktūrą skersai kranto, analizę, buvo išskirti panašiomis šių rodiklių ypatybėmis pasižymintys priekrantės ruožai (**II publikacija, 16–18 p.**). Naudotos charakteristikos yra pateiktos 2 lentelėje. Ruožai išskirti trijuose lygmenyse, nuo pirmo lygmens, atskleidžiančio labiausiai apibendrintus ruožus, pasižyminčius panašia priekrantės sėklių elgsena aukščiausiame lygmenyje, iki trečio lygmens, identifikuojančio stambesnio mastelio priekrantės sėklių elgsenos ruožus. Šis lygmuo atskleidžia sėklių struktūros ir vystymosi ypatybių skirtumus aukščiausio lygmens ruožų viduje (7 pav., 2 lentelė).

Aukščiausiaiame lygmenyje buvo išskirti du stambiausi priekrantės sėklių elgsenos ruožai: greitesniais sėklių migracijos tempais, trumpesne įjūrinės migracijos ciklo trukme, arčiau kranto esančiais sėkliais ir didesniu jų skaičiumi pasižymintis šiaurinis ir priešingomis charakteristikomis pasižymintis pietinis (7 pav., 2 lentelė). Žemesniuose lygmenyse išryškėjo pereinamasis centrinis priekrantės sėklių elgsenos ruožas, tačiau jis savo charakteristikomis yra labai nevienalytis ir pietinė jo dalis yra artimesnė pietiniams ruožui, o šiaurinė – šiauriniams (7 pav., 2 lentelė).



7 pav. Panašia sėklių struktūra ir dinamika pasižyminčių Kuršių nerijos jūros priekrantės ruožų (klasterių) erdvinis išsidėstymas. Juos apibūdinančios charakteristikos pateikiamas 2 lentelėje.

2 lentelė. Vidutinės priekrantės sėklių struktūrą ir dinamiką apibūdinančią rodiklių reikšmės išskirtuose panašia sėklių elgsena pasižymintuose Kuršių nerijos jūros priekrantės ruožuose. Ruožų lygmenys, identifikacinių kodų ir juos žymintios spalvos atitinka 7 pav. pavaizduotus ruožus. Paryškintos rodiklių reikšmės lentelėje žymi reikšmes, didesnes negu visos Kuršių nerijos vidurkis, o paprastu šriftu užrašyti reikšmės – mažesnes. Spalvos perėjimas nuo rožinės iki violetinės rodo rodiklio reikšmių didėjimą.

Panašia sėklių elgsena pasižymintis priekrantės ruožas																
Lygmuo				1 lygmuo				2 lygmuo				3 lygmuo				
Ruožo identifikacinis kodas			LI-1	LI-2	L2-1	L2-2	L2-3	L2-4	L3-1	L3-2	L3-3	L3-4	L3-5	L3-6		
Sėklių atstumas nuo kranto (m)	Kranto link	Jūros link														
Sėklių atstumas nuo kranto (m)	4	3	2	1	4	3	2	1	4	3	2	1	4	3	2	1
Sėklių zonas	430,5	364,1	314,5	354,0	380,0	349,4	300,0	357,0	398,5	348,7	333,2	353,4				
Sėklių zonos plotis (m)	156,1	155,1	151,9	146,3	168,5	161,1	145,3	145,0	175,4	161,5	158,4	155,2				
Sėklių skaičiaus moda	70,2	59,2	72,4	54,5	66,2	67,7	68,7	53,6	67,7	67,7	75,4	60,4				
Sėklių ciklo pasikartojimo periodas (m.)	35,6	33,1	34,8	31,8	35,0	36,7	34,2	30,7	35,4	36,1	35,4	35,2				

2.3. Priekrantės sėklių dinamiką lemiantys veiksniai

Sėklių kaitą skersai kranto ir jos skirtumus išilgai kranto lemiantys veiksniai. 2.2.4 poskyryje aptarta, kad sėklių kaita trumpoje nerijos atkarpoje ties Kopgaliu yra veikiama Klaipėdos uosto statinių, tačiau likusioje Lietuvos Kuršių nerijos dalyje vyrauja žmogaus veiklos nepaveikti sėklių kaitos

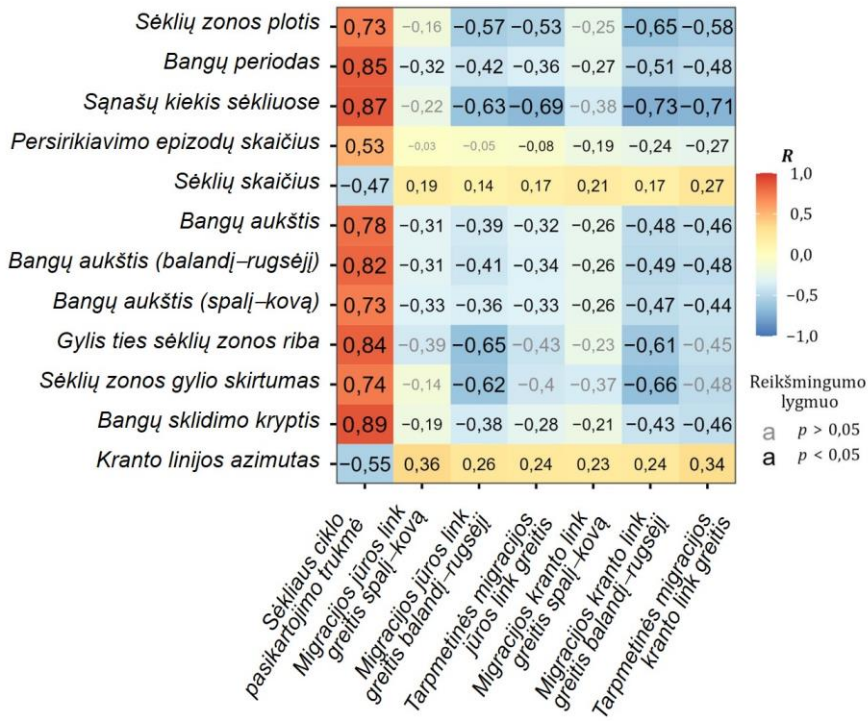
procesai. Darbe pastebėta, jog priekrantės sėkliai migruoja lėčiau, o sėkliaus ciklo pasikartojimo periodas (T_r) ilgėja Kopgalio–Nidos kryptimi (5, 7 pav.). Šią tendenciją išilgai nerijos kranto paaiškina sėklių dinaminių rodiklių ir juos galimai lemiančių veiksnių tiesinės regresinės analizės rezultatai (8 pav.) (**II publikacija, 19–20 p.**). Remiantis šios analizės rezultatais, skiriami šie sėkliaus ciklo pasikartojimo periodo trukmę lemiantys rodikliai:

- *Bangų charakteristikos.* Nustatytas stiprus ($R = 0,73\text{--}0,89$) ir patikimas ($p < 0,05$) koreliacinis ryšys rodo, kad ilgesnė sėkliaus ciklo pasikartojimo periodo trukmę lemia įstriža krantui bangų sklidimo kryptis, ilgesnis bangų periodas ir didesnis bangų aukštis (8 pav.).
- *Sėklių ir sėklių zonos charakteristikos.* Nustatytas stiprus ($R = 0,73\text{--}0,87$) ir patikimas ($p < 0,05$) koreliacinis ryšys rodo, jog ilgesnė sėkliaus ciklo pasikartojimo periodo trukmę lemia didesnis sėklių zonas plotis ir sąnašų kiekis sėkliuose ir didesnis gylis ties sėklių zonas riba bei didesnis gylio skirtumas tarp įkrantinės ir ijjūrinės sėklių zonas ribų (8 pav.). Taip pat nustatytas vidutinio stiprumo patikimas koreliacinis ryšys tarp T_r ir sėklių skaičiaus bei sėklių persirikiavimo epizodų skaičiaus rodo šiu rodiklių svarbą T_r trukmei (8 pav.).
- *Kranto konfigūracija.* Nustatytas vidutinio stiprumo koreliacinis ryšys ($R = 0,55$; $p < 0,05$) rodo, jog T_r trukmei įtakos turi ir kranto linijos orientacija (8 pav.).

Šie rezultatai rodo, kad gilesnėje ir platesnėje sėklių zonoje, kur sėkliai didesni, T_r yra ilgesnis negu siauresnėje ir seklesnėje sėklių zonoje, kur sėkliai mažesni, bet didesnis jų skaičius. Įstrižai kranto sklindančios, aukštesnės ir ilgesnio periodo bangos lemia ilgesnę ijjūrinės migracijos ciklo trukmę negu žemesnės, dažnesnės, statmenos krantui bangos (**II publikacija, 19 p.**).

Koreliacinis ryšys tarp sėklių migracijos greičio skersai kranto ir galimai ją lemiančių veiksnių buvo silpnesnis negu sėkliaus ciklo pasikartojimo rodiklio atveju. Vidutinio stiprumo ir stiprus koreliacinis ryšys nustatytas tik su sėklių zoną ir sėklių dydį apibūdinančiais rodikliais (8 pav.). Šie rezultatai rodo, jog gilesnėje ir platesnėje sėklių zonoje, kur sėkliai didesni, jie skersai kranto migruoja lėčiau.

Kadangi šiaurinė Kuršių nerijos dalis pasižymi siauresne ir seklesne sėklių zona, kurioje didesnis sėklių skaičius, o bangos čia yra šiek tiek žemesnės, dažnesnės ir į krantą ritasi statmeniau negu pietinėje nerijos dalyje (**II publikacija, 20 p., 12 pav.**), šie rodikliai nulemia T_r trukmės ir sėklių migracijos skersai kranto greičio skirtumus šiaurinėje ir pietinėje Kuršių nerijos jūros priekrantės dalyse.



8 pav. Pirsono tiesinės koreliacijos koeficientai tarp Kuršių nerijos jūros priekrantės séklių dinamiką apibūdinančiu rodikliu ir potencialiai juos lemiančiu veiksniu (bangų, séklių bei kranto konfigūracijos rodiklių) ir jų statistinis reikšmingumas.

Séklių persirikiavimo epizodų susidarymą lemiantys veiksniai. Atliekant priekrantės séklių persirikiavimo zonų analizę pastebėta, kad šios zonas tipiškai formuoja ties skirtinges kranto linijos orientacijos lūžio taškais (6 pav., A). Taip pat, remiantis ankstesnių tyrimų rezultatais, daryta prieleda, jog persirikiavimo reiškiniai susiformuoja palankios sąlygos yra susijusios su stipriomis išilginėmis srovėmis ir įstrižia krantui bangų energija (Aleman ir kt., 2017; Shand ir kt., 2001). Šių veiksniai Kuršių nerijoje svarbai įvertinti sudarytas logistinės regresijos modelis, įtraukiantis kranto linijos orientaciją ir bangų sklidimo kampą kaip nepriklausomuosius kintamuosius ir persirikiavimo susidarymą kaip priklausomąjį kintamąjį. Gautas modelis ($y = -29,1082 + 0,4330x + 0,0689z$; čia y – priekrantės séklių susidarymo tikimybė; x – bangų sklidimo kryptis; z – kranto linijos azimutas) leidžia prognozuoti persirikiavimo susidarymą Kuršių nerijos jūros priekrantėje, kai determinacijos koeficientas $R^2 = 0,57$ (**IV publikacija, 13 p., 11 pav.**), o tai rodo šių rodiklių svarbą susidarančius priekrantės séklių persirikiavimui.

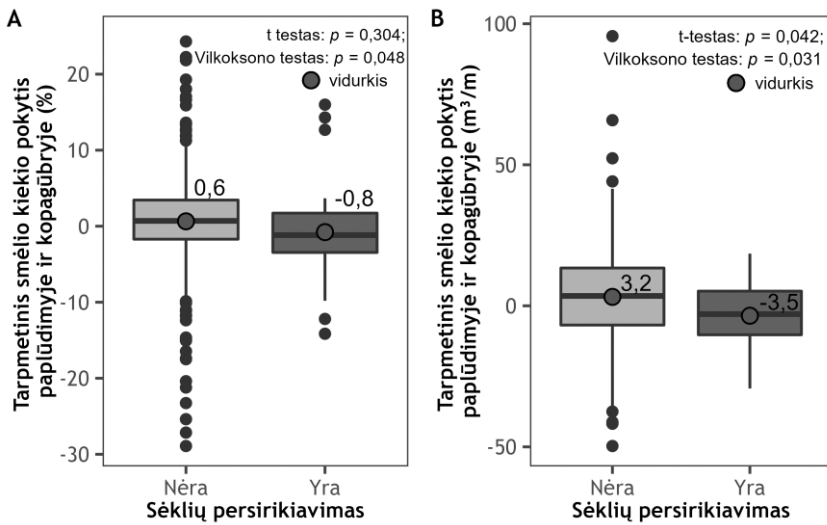
Tiek sėklių migraciją skersai kranto, tiek jų persirikiavimą lemiančių veiksnių analizės rezultatai rodo, jog kranto linijos orientacija ir jos sąveika su vyraujančiais hidrodinaminiais procesais yra svarbūs Kuršių nerijos jūros priekrantės sėklių raidai bei struktūrai (**II, IV publikacijos**).

2.4. Priekrantės sėklių dinamikos įtaka kranto raidai

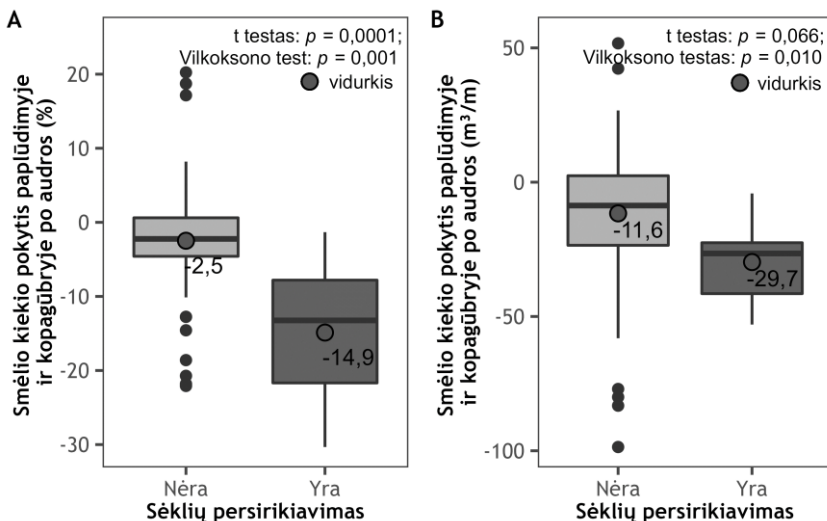
Tarp priekrantės ir kranto nuolat vyksta smėlio apykaita, todėl procesai povandeniniame šlaite ir sausuminėje kranto dalyje yra neatsiejami (Cohn ir kt., 2017; Phillips ir kt., 2017; Robin ir kt., 2014; Tātui ir kt., 2013). Disertacijos rengimo metu pirmą kartą pasaulinėje krantų geomorfologijos tyrimų praktikoje pastebėtas ryšys tarp priekrantės sėklių persirikiavimo epizodų ir kranto raidos šio reiškinio paveiktoje jo zonoje (**IV publikacija, 5–11 p.**).

Kranto linijos pokyčiai ties priekrantės sėklių persirikiavimo zonomis. Atlikus kranto linijos padėties pokyčių analizę persirikiavimo epizodų metu, 26 iš 27 identifikuotų Kuršių nerijos jūros priekrantės sėklių persirikiavimo zonų užfiksuotas kranto linijos atsitraukimas, siekës iki 49 m (vidutiniškai 14 m) (**IV publikacija, 5–8 p., 5 pav.**). Iprastu atveju kranto linija persirikiavimo epizodo metu atsitraukė į sausumą, o priekrantėje atsikūrus įprastai sėklių struktūrai, kranto linijos padėtis irgi grižo į pirminę padėtį.

Tarpmetiniai smėlio kieko pokyčiai krante ties sėklių persirikiavimo zonomis ir už jų ribų. Palyginus vidutinius tarpmetinius smėlio kieko pokyčius krante persirikiavimo zonose ir už jų ribų pastebėta, jog krantui persirikiavimo zonose buvo būdinga nedidelė arda, o už jų ribų – nedidelė akumuliacija (9 pav.) (**IV publikacija, 7–8 p.**). T testo rezultatai rodo, kad tarp vidutinių kranto smėlio kieko pokyčių, vertintų kubiniais metrais, persirikiavimo zonose ir už jų ribų buvo statistiškai reikšmingas skirtumas ($p < 0,05$) (9 pav., B), tačiau dėl itin didelio išskirčių skaičiaus tarp vidutinių kranto smėlio kieko pokyčių, vertintų procentais, persirikiavimo zonose ir už jų ribų, skirtumas nebuvo statistiškai reikšmingas ($p > 0,05$) (9 pav., A). Kad sumažėtų išskirčių įtaka rezultatams, buvo atliktas smėlio kieko pokyčių krante persirikiavimo zonose ir už jų ribų medianų palyginimas (Vilkoksono testas). Jo rezultatai rodo, kad abiem atvejais (tieki pokyčius vertinant kubiniais metrais, tiek procentais) tarp smėlio kieko pokyčių krante persirikiavimo zonose ir už jų ribų buvo statistiškai reikšmingas skirtumas ($p < 0,05$) (9 pav.).



9 pav. Paplūdimio ir kopagūbrio smėlio kieko pokyčių pagal tarpmetinę laiko skalę palyginimas priekrantės séklių persirikiavimo zonose ir už jų ribų.



10 pav. Paplūdimio ir kopagūbrio smėlio kieko pokyčių audrų metu palyginimas priekrantės séklių persirikiavimo zonose ir už jų ribų.

Audrų nulemti smėlio kieko pokyčiai krante séklių persirikiavimo zonose ir už jų ribų. Taip pat užfiksuota, kad stiprių audrų nulemti smėlio praradimai krante vidutiniškai buvo didesni persirikiavimo zonose negu už jų ribų (10 pav.) (**IV publikacija, 8–9 p.**). T testo rezultatai rodo, kad skirtumas tarp vidutinių audrų nulemtų smėlio kieko pokyčių krante (vertintų kubiniais metrais) persirikiavimo zonose ir už jų ribų nebuvo statistiškai reikšmingas (p

$> 0,05$) (10 pav., B). Tokie rezultatai yra nulemti smėlio kiekio atsargų Kuršių nerijos krante skirtumų. Šiaurinė nerijos dalis pasižymi didžiausiu smėlio kiekiu krante, todėl absolutiniai smėlio kiekio pokyčiai krante audrų metu čia būna didžiausi, nors persirikiavimo epizodai šiai nerijos daliai ir nėra būdingi. Dėl to buvo palyginti vidutiniai procentiniai smėlio kiekio pokyčiai krante ir šiuo atveju tarp vidutinių smėlio kiekio pokyčių krante persirikiavimo zonose ir už jų ribų nustatytas statistiškai reikšmingas skirtumas ($p < 0,05$) (10 pav., A). Vilkoksono testo rezultatai rodo, kad tarp smėlio kiekio pokyčių krante persirikiavimo zonose ir už jų ribų medianų abiem vertinimo atvejais egzistavo statistiškai reikšmingas skirtumas ($p < 0,05$) (10 pav.).

Priekrantės ir kranto pokyčių analizė individualiose persirikiavimo zonose. Atlikus nuodugnias trijų persirikiavimo epizodų atvejo analizes (**IV publikacija, 9–11 p.**), tarp smėlio kiekio pokyčių krante persirikiavimo epizodo metu ir persirikiavimo nulemto ijūrinio sėkliaus atstumo nuo kranto pokyčių nustatytas stiprus koreliacinis ryšys ($R = 0,75\text{--}0,86$ (prilausomai nuo atvejo); $p < 0,05$), o tarp kranto linijos ir ijūrinio sėkliaus padėčių pokyčių nustatytas vidutinio stiprumo koreliacinis ryšys ($R = 0,49\text{--}0,59$ (prilausomai nuo atvejo); $p < 0,05$). Visais analizuotais persirikiavimo epizodų atvejais smėlio kiekis krante buvo sumažėjęs, kranto linija atsitraukusi, o ijūrinis sėkliaus – priartėjęs prie kranto.

Šiame poskyryje aptarti rezultatai rodo, kad persirikiavimo epizodų metu šio reiškinio paveiktose zonose kranto linija yra linkusi atsitraukti, o smėlio kiekis paplūdimyje bei kopagūbryje – sumažėti.

3. TYRIMU REZULTATU APTARIMAS

Šiame darbe Kuršių nerijos Baltijos jūros priekrantės pavyzdžiu sukurta ir validuota sėklių identifikavimo ir analizės palydoviniuose vaizduose metodologija atskleidžia dar neišnaudotas Žemės stebėjimo palydovų galimybes šių iškilių povandeninių reljefo formų morfologinių tyrimų srityje (**I publikacija**). Sukurtas algoritmas leidžia gauti patikimus didelio tikslumo duomenis ir didesnį sėklių rodiklių skaičių, todėl yra pranašesnis už esamas panašaus pobūdžio metodikas (Román-Rivera ir kt., 2020; Tātui ir Constantin, 2020) (**I publikacija, 21 p.**). Pasiūlytas metodas yra pritaikytas didelei priekrantės sėklių morfologinių formų įvairovei, todėl gali būti taikomas ir kituose smėlėtuose krantuose. Šiam tikslui užtektų modifikuoti daugiaskalio RBPI skaičiavimui ir erdviniam filtravimui taikomus kaimynysčių dydžius, atsižvelgiant į vietines sėklių dydžio charakteristikas.

Nustatyta, kad pritaikius pasiūlytą metodiką priekrantės sėklių viršūnės gali būti identifikuojamos su 5,8 m, 7,0 m, 4,9 m ir 7,5 m vidutine kvadratinė paklaida atitinkamai „PlanetScope“ (3 m), „RapidEye“ (5 m), „Sentinel-2“ MSI (10 m) ir „Landsat-8“ OLI (15 m) palydovinių jutiklių vaizduose. Kadangi nustatytos vidutinės kvadratinės paklaidos dydis „PlanetScope“ ir „RapidEye“ vaizduose atitinka 1,4–1,9 pikselio dydžio, tai rodo, kad įprastai sėkliaus viršūnė šiuose vaizduose identifikuojama gretimame pikselių nuo realios jų padėties, o „Sentinel-2“ MSI ir „Landsat-8“ OLI vaizduose, kuriuose vidutinė kvadratinė paklaida atitinka apie 0,5 pikselio, sėkliaus viršūnės padėtis nustatoma tame pikselių, kuriamo yra reali jos padėtis.

Nustatytos vidutinės kvadratinės paklaidos taip pat rodo, kad tiek didelės skiriamosios gebos (3–5 m) komercinių palydovų vaizduose, tiek vidutinės skiriamosios gebos (10–15 m) nemokamos prieigos palydovinių jutiklių vaizduose priekrantės sėklių viršūnė gali būti identifikuojama labai panašiu tikslumu. To priežastis gali lemti palydovinių jutiklių vaizdų kokybės skirtumai. Ankstesni tyrimai rodo, kad „PlanetScope“ ir „RapidEye“ jutiklių vaizdai pasižymi didesniu signalo ir triukšmo santykiu negu „Sentinel-2“ MSI ir „Landsat-8“ OLI jutiklių vaizdai (Houborg ir McCabe, 2018; Kudela ir kt., 2019; Leach ir kt., 2019; Sadeh ir kt., 2021), todėl galima daryti prielaidą, jog identifikuojant priekrantės sėklus palydoviniuose vaizduose geresnė palydovinio jutiklio fiksuojamų vaizdų kokybė gali atsverti prastesnes vaizdų erdvinių raiškos charakteristikas.

Nustatyti viršūnių padėties palydoviniuose vaizduose skirtumai skirtingomis vaizdo fiksavimo datomis ir sėkliaus padėtims skersai kranto rodo, kad metodo tikslumas priklauso nuo specifinių sąlygų priekrantėje ir sėkliaus ypatybių vaizdo fiksavimo metu. Nustatyti skirtumai tarp skirtingu

sėklių padėčių tikslumo gali būti nulemti sėklių gylio ir jų formos ypatumų. Iškrantiniai bei viduriniai sėkliai aptinkami mažesniuose gyliuose negu ijūrinis ir dažniausiai pasižymi didesniu formos išraiškingumu bei tiksliau išreikšta viršūnės padėtimi, o didesniame gylyje esantys ijūriniai sėkliai dažnai pasižymi lėkštesne bei mažiau išreikšta viršūnės padėtimi (1 pav., B), o tai lemia itin mažus paviršiaus atspindžio skirtumus tarp gretimų pikselių palydoviniame vaizde ir mažiau tiksliai nustatomą ijūrinio sėkliaus padėtį (**I publikacija, 20 p.**).

Darbe taip pat atskleista, kad pasiūlytas daugiaskalis santykinis batimetrinės padėties rodiklis (RBPI) yra tinkamas ne tik sėkliaus viršūnės padėties nustatymui, bet gali būti naudojamas ir kaip batimetrinį priekrantęs pjūvių alternatyva cikliškai priekrantęs sėklių elgsenai vertinti (**II publikacija**). Pritaikius šį rodiklį CEOF analizei, nustatyta, kad priekrantęs sėkliai Kuršių nerijoje vystosi pagal ijūrinės migracijos ciklo modelį (Ruessink ir Kroon, 1994). Ši ciklą apibūdinančio sėkliaus ciklo pasikartojimo periodo trukmę (T_r) Kuršių nerijoje varijuoja nuo 1,8 iki 13,5 m.

Pagrindžiant tyrimų metu gautus rezultatus, svarbu pabrėžti, kad nors ijūrinės migracijos cikliškumo vertinimui darbe naudota laiko eilutės trukmė buvo artima nustatyta maksimaliai T_r trukmei, tačiau ankstesni batimetrine informacija pagrįsti tyrimai rodo, jog CEOF analizė leidžia apskaičiuoti T_r trukmę naudojant duomenų laiko eilutę, kurios trukmė yra artima nustatytais T_r trukmei (Aleman ir kt., 2013; Tātui ir kt., 2016) (**II publikacija, 21 p.**). Taip pat reikėtų atkreipti dėmesį į tai, kad sėklių vystymosi cikliškumas yra gamtinis procesas, priklausantis nuo analizuojamo laikotarpio hidrodinaminių sąlygų, todėl T_r trukmė toje pačioje vietoje kiekvieno ciklo atveju gali variuoti, o ribota laiko eilutės trukmė lemia cikliškumo apibrėžtį, būdingą analizuojamam laikotarpiui. Dėl to šiame darbe pirmą kartą Kuršių nerijai nustatyta T_r trukmė leidžia susidaryti sėklių vystymosi skirtumų išilgai Kuršių nerijos Baltijos jūros priekrantęs vaizdą, o ilgesnės RBPI rodiklio laiko eilutės naudojimas leistų patikslinti T_r rodiklio trukmę, remiantis didesne pasikartojuusių ciklų imtimi.

Darbe pasiūlyto sėklių identifikavimo palydoviniuose vaizduose algoritmo nustatyta sėklių viršūnių atstumo nuo kranto laiko eilutės leidžia vertinti sėklių migraciją skersai kranto pagal tarpmetinę ir sezonię laiko skales (**II publikacija**). Pritaikius Van Enckevort ir Ruessink (2003a) pasiūlytą metodiką iš palydovinių vaizdų gautiems duomenims, nustatyta, kad vidutinis priekrantęs sėklių migracijos skersai kranto greitis 1 071 priekrantęs skersinių profilių pagal tarpmetinę laiko skalę varijuoja nuo 0,1 iki 11,0 m/mėn., o pagal sezonię laiko skalę nuo 0,1 iki 13,4 m/mėn. Nors kai kurios iš šiuos migracijos greičio intervalus patenkančios reikšmės yra mažesnės negu analizuotų

palydovinių duomenų erdvinė raiška (5 m) ir identifikuotos viršūnių padėties palydoviniuose vaizduose paklaidos, tai yra suvidurkintas nustatytų migracijos greičių, reikšmingų naudojant tarpmetinę ir sezonių laiko skales, rezultatas, kai nereikšmingi epizodiniai svyravimai yra pašalinti, nustatant sezoninius ir tarpmetinius laiko eilutės komponentus. Dėl šios priežasties gautos reikšmės yra mažesnės negu pirminis skirtumas tarp sėkliaus atstumo nuo kranto palyginus dviejų datų duomenis. Tarkim, 2011–2021 m. vidutinis absolitus ijūrinio sėkliaus atstumo nuo kranto pokytis, remiantis epizodiniais svyravimais tarp dviejų mėnesių vaizdų, visuose profiliuose siekė 19,4 m (standartinis nuokrypis 33,8 m), o šio rodiklio vidurkis skirtinguose profiliuose varijavo nuo 7,6 m iki 68,7 m, todėl visais atvejais viršijo analizuotą palydovinių vaizdų pikselio dydį (5 m) ir vidutines kvadratinės paklaidas. Tai rodo gautų rezultatų patikimumą.

Gauti rezultatai rodo, kad priekrantės sėklių migracijos skersai kranto greitis priklauso nuo sėkliaus eilės numerio sėklių sekoje: pirmas (ijūrinis) sėkliai pasižymėjo didžiausiu migracijos greičiu, o ketvirtas – mažiausiu. Toks migracijos greičio pasiskirstymas tarp sėklių gali būti nulemtas to, kad ijūrinį sėklių pasiekia didžiausia energija pasižyminti bangos, o gožtančių ties sėkliais bangų energija mažėja su kiekvienu arčiau kranto esančiu sėklumi (Alexander ir Holman, 2004). Be to, ijūrinio sėkliaus padėtis apriboja kitų arčiau kranto esančių sėklių judėjimą. Panašus migracijos greičio pasiskirstymas tarp sėklių buvo aptiktas ir kituose smėlėtuose krantuose (Melito ir kt., 2020; Van Enckevort ir Ruessink, 2003a). Vis dėlto sėklių tyrimų praktikoje yra fiksuota ir kitokių migracijos greičio pasiskirstymo tarp sėklių padėties skersai kranto atvejų (Larson ir Kraus, 1993; Goulart ir Calliari, 2013), todėl šiai ypatybei nustatyti skirtingose vietovėse turėtų būti atliekamas detalus sėklių migracijos vertinimas (**II publikacija, 18 p.**).

Pagal tarpmetinę laiko skalę visų sėklių ijūrinės migracijos greitis viršijo įkrantinės migracijos greitį, o tai lemia, kad pagal daugiametę laiko skalę Kuršių nerijoje matoma pirmiau aptarta ijūrinės migracijos ciklo modeliui būdinga sėklių elgsena (**II publikacija, 18 p.**). Ijūrinės migracijos ciklas pietryčių Baltijos jūros priekrantėje užfiksuotas ir kiekybiškai įvertintas pirmą kartą. Tai svarbu, nes šis rezultatas rodo, kad ijūrinės migracijos modelis yra taikytinas ir šiame regione.

Pagal sezonių laiko skalę ijūrinio sėkliaus migracijos jūros link tempai viršijo migracijos kranto link greitį didelės bangų energijos sezono metu, o mažos bangų energijos sezono metu ijūriniam sėklui buvo būdingas beveik identiškas migracijos kranto ir jūros link greitis. Kiti sėkliai tiek didelės, tiek mažos bangų energijos sezono metu migravo greičiau kranto negu jūros link. Sezoniniai priekrantės sėklių padėties svyravimai spalio–kovo mėnesiais

viršijo sezoninius balandžio–rugsėjo mėnesių ir tarpmetinius sėklių padėties svyra vimus, o tai rodo, kad didžiausi sėklių padėties skersai kranto pasikeitimai Kuršių nerijoje vyksta spalio–kovo mėnesiais (**II publikacija, 18 p.**).

Atliktų tyrimo rezultatai rodo, kad priekrantės sėkliai išilgai Kuršių nerijos Baltijos jūros priekrantės vystosi nevienodai: priekrantės sėklų migracijos skersai kranto greitis mažėja, o sėklius ciklo pasikartojimo periodo trukmė ilgėjo nuo Kopgalio link Nidos (**II publikacija**). Didžiausias priekrantės sėklių persirikiavimo epizodų skaičius taip pat buvo fiksuojamas priekrantės atkarpoje tarp Pervalkos ir Nidos, o atkarpoje tarp Kopgalio ir Alksnynės persirikiavimo epizodų nebuvo užfiksuota (**IV publikacija**). Tai rodo reikšmingus sėklių elgsenos skirtumus tarp šiaurinės ir pietinės Kuršių nerijos dalių. Dėl Kuršių nerijai būdingos vyraujančios vakarų–pietvakarių bangų sklidimo krypties ir šiaurinei nerijos daliai būdingos šiaurės vakarų–pietryčių krypties kranto konfigūracijos bangos į krantą čia dažniau ritasi statmenai. Kadangi maksimalus sėklių migracijos skersai kranto greitis yra fiksuojamas esant statmenoms krantui bangoms (Dubarbier ir kt., 2015), šiaurinė nerijos dalis pasižymi didesniu sėklių migracijos skersai kranto greičiu ir stipresne skersine nešmenų pernaša. Dėl pietinės nerijos dalies kranto linijai būdingos šiaurės rytų–pietvakarių krypties konfigūracijos bangos į krantą čia dažniau ritasi įstrižai, o tai lemia palankesnes sąlygas išilginių srovų susidarymui ir išilginės nešmenų pernašos vyksmui. Dėl šių priežasčių pietinėje nerijos dalyje yra lėtesni sėklių vystymosi skersai kranto tempai ir dažnesnis sėklių persirikiavimo epizodų vyksmas (**II publikacija, 20–21 p.; IV publikacija, 11 p.**). Tai patvirtina ankstesnių tyrimų rezultatai, kurie rodo, jog palankiausios sąlygos persirikiavimui susidaryti yra įstriža krantui bangų energija ir stiprios išilginės srovės (Aleman ir kt., 2017; Shand ir kt., 2001). Šiame darbe pastebėta, kad persirikiavimo epizodams formuotis palankios sąlygos, be šių veiksniių, apima ir skirtingos kranto linijos orientacijos sandūros taškus, o tai papildo anksčiau atlirktytų tyrimų rezultatus.

Nors priekrantės sėklių persirikiavimas pirmą kartą buvo pastebėtas prieš beveik tris dešimtmečius (Shand ir kt., 2001; Wijnberg ir Wolf, 1994), kaip šis reiškinys veikia kranto raidą, niekada anksčiau nebuvo tirta. Šiame darbe pirmą kartą pastebėta, kad priekrantės sėklių persirikiavimo zonose smėlio kiekis krante dažnai sumažėja, o kranto linija – atsitraukia (**IV publikacija**). Tai rodo, jog priekrantės sėklių persirikiavimas vaidina svarbų vaidmenį kranto raidoje. Šio ryšio priežastys gali būti dvejopos: 1) sėklių persirikiavimo nulemti priekrantės morfologiniai pokyčiai sutrikdo įprastus hidrodinaminius bei litodinaminius procesus priekrantėje, o tai lemia įprastos smėlio apykaitos tarp priekrantės ir kranto sutrikdymą; 2) priekrantės sėklių persirikiavimas

dažnai lemia lokalų sėklių zonas susiaurėjimą. Kadangi priekrantės sėklai atlieka gamtinių bangolaužių vaidmenį (Dubarbier ir kt., 2015; Fernández-Mora ir kt., 2015; Plant ir kt., 2001; Price ir kt., 2014), šiam barjerui išnykus ar sumažėjus, priekrantėje išsklaidomos bangų energijos kiekis taip pat sumažėja, o krantą pasieka didesnės energijos bangos, lemiančios didesnę jo ardą (**IV publikacija, 12–13 p.**). Šie rezultatai atskleidžia priekrantės sėklių persirikiavimo svarbą kranto raidai ir parodo, kad potencialių sėklių persirikiavimo vietų nustatymas galėtų būti naudojamas potencialių kranto erozijos taškų identifikavimui.

IŠVADOS

1. Nustatyta, kad pritaikius darbe pasiūlytą metodologiją priekrantės sėklių viršūnės didelės ir vidutinės (3–15 m) erdvinės raiškos „PlanetScope“, „RapidEye“, „Sentinel-2“ MSI ir „Landsat-8“ OLI palydovinių jutiklių vaizduose gali būti identifikuojamos su 4,9–7,5 m vidutine kvadratinė paklaida. Gautos viršūnės padėties tikslumas priklauso nuo vaizdo ypatybių, bangavimo sąlygų, sėkliaus atstumo nuo kranto bei gylio ir palydovinio jutiklio kokybinių charakteristikų.
2. Darbo rezultatai rodo, kad palydovine informacija pagrįstos sėklių viršūnių padėties laiko eilutės yra tinkamos kiekybiniam priekrantės sėklių migracijos skersai kranto vertinimui, pagrįstam vaizdo stebėsenos duomenims taikoma metodika, o darbe pasiūlytas daugiaskalis santykinis batimetrinės padėties rodiklis (RBPI) yra tinkama batimetriinių priekrantės pjūvių alternatyva cikliškai priekrantės sėklių elgsenai vertinti.
3. Remiantis 2011–2021 m. palydovine informacija nustatyta, kad, taikant daugiametę laiko skalę, Kuršių nerijos jūros priekrantės sėkliai vystosi pagal išjūrinės migracijos ciklo modelį, kurį apibūnančio sėkliaus ciklo pasikartojimo rodiklio vidutinė trukmė Kuršių nerijoje siekia 6,7 m. Apskaičiuota šio rodiklio trukmė ilgėja Kopgalio–Nidos kryptimi nuo 1,8 iki 13,5 metų.
4. Nustatyta, kad 2011–2021 m. 98 % Lietuvos Kuršių nerijos dalies jūros priekrantės buvo būdinga trigubo ir keturgubo sėkliaus sistema, kurią sudarančių sėklių vidutinis migracijos skersai kranto greitis skirtinguose priekrantės profiliuose pagal tarpmetinę ir sezonię laiko skales siekė nuo 0,1 iki 13,4 m/mėn. Priekrantės sėkliai šiaurinėje Kuršių nerijos dalyje pasižymėjo didesniu vidutiniu migracijos skersai kranto greičiu negu pietinėje jos dalyje.
5. Nustatyta, kad sėkliaus ciklo pasikartojimo rodiklio (T_r) trukmė pasižymėjo stipriu koreliaciniu ryšiu ($R = 0,73\text{--}0,89$; $p < 0,05$) su bangų aukščiu, periodu bei sklidimo kryptimi, sąnašų kiekiu sėkliuose, sėklių zonas gyliu bei pločiu, o šių rodiklių vidutinių reikšmių didėjimas iš Kuršių nerijos šiaurės į pietus lėmė T_r trukmės ilgėjimą ta pačia kryptimi.
6. Priekrantės sėklių migracijos skersai kranto greitis pasižymėjo vidutinio stiprumo ir stipriu koreliaciniu ryšiu ($R = 0,53\text{--}0,73$; $p < 0,05$) tik su sąnašų kiekiu sėkliuose, sėklių zonas pločiu ir gyliu, todėl sėklių migracijos jūros ir kranto link tempai 2011–2021 m. buvo nulemti sėklių dydžio bei gylio rodiklių, o šių rodiklių vidutinių reikšmių didėjimas iš

Kuršių nerijos šiaurės į pietus lėmė didesnį vidutinį sėklių migracijos greitį šiaurinėje nerijos dalyje negu pietinėje.

7. Šiaurinė Kuršių nerijos Baltijos jūros priekrantės dalis ties Kopgaliu yra veikiama Klaipėdos uosto hidrotechninių statinių, tai rodo greta pietinio uosto molo susiformavusi likusiai nerijos daliai nebūdinga priekrantės sėklių struktūra, susidariusi iš lėkštos seklumos, piečiau išsišakojančios į 2–3 nedidelius sėklius.
8. Kuršių nerijoje 2009–2021 m. užfiksuoti 27 priekrantės sėklių persirikiavimo epizodai, kurių vidutinė trukmė siekė 14 mėnesių, todėl tipiškas persirikiavimo epizodas turėjo įtakos priekrantės hidrodinamikai bei litodinamikai pagal tarpmetinę laiko skalę. Sėklių persirikiavimo epizodai pasižymėjo salyginai stabiliomis periodiško susidarymo vietomis, būdingomis priekrantės atkarpai nuo Alksnynės iki Nidos. Šios vietas sutapo su pereinamaisiais ruožais, esančiais ties skirtingos kranto orientacijos sandūra, ir įstrižomis krantui bangomis.
9. Nustatyta, kad pagal tarpmetinę laiko skalę krantas priekrantės sėklių persirikiavimo zonose pasižymėjo nedidele arda, o už persirikiavimo zoną ribų – nedidele akumuliacija. Audrų metu krantas ties persirikiavimo zonomis buvo apardomas labiau negu už jų ribų. Remiantis Vilkoksono testo rezultatais, tiek tarp tarpmetinių, tiek tarp audrų nulemtų smėlio kiekiejų pokyčių krante medianų persirikiavimo zonose ir už jų ribų buvo statistiškai reikšmingas skirtumas ($p < 0,05$). Tai rodo, kad tarp priekrantės sėklių persirikiavimo epizodų ir kranto erozijos yra ryšys.

SUMMARY

INTRODUCTION

Nearshore sandbars are elongated underwater sand ridges formed by waves and nearshore currents, found on the sandy shores of seas, oceans, and large lakes at depths of up to 10 m (Múnera et al., 2014; Price et al., 2014; Ruessink et al., 2003; Rutten et al., 2018; Van Enckevort and Ruessink, 2003a). The importance of nearshore sandbar studies arises from the fact that these ridges contain large reservoirs of sand that play a major role in sediment exchange between the submerged and dry beach (Cohn et al., 2017; Phillips et al., 2017; Robin et al., 2014; Tătui et al., 2013). They are also of primary importance for the persistence of sandy beaches as they constitute a natural barrier that safeguards beaches by causing wave dissipation through wave breaking (Dubarbier et al., 2015; Fernández-Mora et al., 2015; Plant et al., 2001; Sallenger et al., 1985). Sandbar morphologies exhibit high alongshore variability, affecting the nearshore hydrodynamics and rip current circulation that is related to the distribution of sediments, pollutants, or biota and might be dangerous for swimmers (Brighton et al., 2013; Camara et al., 2018; Castelle et al., 2016; Elgar et al., 2001; Holzhauer et al., 2019). All this determines the need for understanding the behaviour of nearshore sandbars in coastal geomorphology, coastal prediction, coastal management, ecology, and other related socioeconomic sectors.

The first studies of nearshore sandbars date back to the middle of the 19th century (de Beaumont, 1845), but intensive research has only been conducted since the middle of the 20th century (King and Williams, 1949; Shepard, 1950). During this time, plenty of knowledge was collected on the formation (e.g., Caballeria et al., 2002; Holman and Bowen, 1982; King and Williams, 1949; Sallenger and Howd, 1989), dynamics (e.g., Gallagher et al., 1998; Gijsman et al., 2021; Hoefel and Elgar, 2003; Plant et al., 1999; Ruessink and Kroon, 1994), and morphology (e.g., Lippmann and Holman, 1990; Price and Ruessink, 2011; Wright and Short, 1984) of nearshore sandbars.

Nearshore sandbars have been found to develop as single or multiple sandbar systems and exhibit a wide range of shapes (Wijnberg and Kroon, 2002). In response to hydrodynamic forcing, nearshore sandbars might migrate offshore and onshore (Gallagher et al., 1998; Hoefel and Elgar, 2003). In the 1990s, nearshore sandbars were observed to exhibit multi-annual cyclic behaviour incorporating net offshore migration (NOM) (Ruessink and Kroon, 1994). During the NOM cycle, sandbars generate near the shoreline, move offshore across the nearshore, and decay at the outer nearshore boundary.

In addition to cross-shore migration, nearshore sandbars demonstrate three-dimensional behaviour studied through changes in their shape. A morphodynamic beach state model explaining the three-dimensional behaviour of sandbars was introduced by Australian scientists in the 1980s (Wright and Short, 1984). Many morphodynamic phenomena characteristic of nearshore sandbars have been also observed, including morphological coupling (Castelle et al., 2010a), straightening (Garnier et al., 2013), or sandbar switching (Shand et al., 2001).

However, despite considerable research on understanding the behaviour of nearshore sandbars, there is still a lack of knowledge on sandbar dynamics over large spatial extents with alongshore lengths greater than a few kilometres, as well as on the interaction between nearshore sandbar dynamics and coastal evolution.

Furthermore, the behaviour of nearshore sandbars along the Lithuanian Baltic Sea coast has received little attention from the scientific community, especially over the last three decades. Most of the widely accepted concepts explaining the behaviour of these submerged forms have never been confirmed or applied on the Lithuanian Baltic Sea coast, and it is unknown how nearshore sandbars evolve and interact with coastal processes in this coastal region.

The other and no less important side of nearshore sandbar research refers to a methodological part of these studies. In almost a century of intensive nearshore sandbar research, numerous studies have used bathymetric (e.g., Gijsman et al., 2021; Larson and Kraus, 1994; Ruessink and Kroon, 1994; Wijnberg and Terwindt, 1995) or remotely sensed data acquired by video monitoring systems (e.g., Lippmann and Holman, 1990; Parlagreco et al., 2019; Price and Ruessink, 2011) to study the behaviour of nearshore sandbars. However, these techniques are either resource-intensive or limited in spatial or temporal extent. The emergence of optical Earth observation satellites offers a low-cost solution to study nearshore sandbars over large spatiotemporal extents (Román-Rivera and Ellis, 2019). The use of satellite imagery has only recently emerged in a few nearshore sandbar studies (Athanasios et al., 2018; Lafon et al., 2004; Román-Rivera et al., 2020; Tătui and Constantin, 2020), but the coastal research community still lacks methods specifically designed to extract and analyse nearshore sandbar data from satellite imagery. Therefore, only the first steps have been taken in exploitation of optical satellite remote sensing in the studies of nearshore sandbars.

Scientific problem

The motivation for the research carried out during the preparation of this thesis is based on the following scientific problems: (1) lack of methods for identifying and analysing nearshore sandbars in satellite imagery; (2) lack of knowledge about the multiple sandbar systems along coastal stretches longer than a few kilometres; (3) lack of understanding of nearshore sandbar dynamics along the Lithuanian Baltic Sea coast; and (4) lack of understanding of the interaction between nearshore sandbars and coastal evolution.

Research object, aim, and objectives

The object of this thesis is nearshore sandbar dynamics. The study area is the Baltic Sea nearshore of the Lithuanian part of the Curonian Spit.

The aim of this thesis is to develop and apply a methodological framework for optical remote sensing of the geodynamics and morphology of nearshore sandbars as a basis for the determination of dynamic features of nearshore sandbars.

Objectives:

1. To develop and validate a methodology for the identification and analysis of nearshore sandbars in satellite imagery;
2. To assess the characteristics of nearshore sandbar cross-shore dynamics in the Curonian Spit;
3. To assess the morphodynamic features of nearshore sandbars in the Curonian Spit;
4. To identify the factors influencing the dynamics of nearshore sandbars in the Curonian Spit;
5. To assess the influence of nearshore sandbar dynamics on coastal evolution in the Curonian Spit.

Defending arguments

1. High- to medium-resolution optical satellite imagery is a suitable data source for an accurate determination of the morphological characteristics of nearshore sandbars.
2. Satellite-derived indicators of the nearshore sandbar morphology are a suitable alternative to bathymetric and video monitoring data for quantifying the cross-shore migration of nearshore sandbars.
3. Nearshore sandbars in the Curonian Spit exhibit cyclic net offshore migration typical of sandy shores.

4. Nearshore sandbars in the Curonian Spit are characterised by the sandbar switching phenomenon observed in multiple sandbar systems.
5. The most important factors determining the differences in sandbar evolution along the Curonian Spit are sandbar zone depth and sandbar size, as well as the wave height, period, and direction of propagation.
6. Changes in nearshore morphology determined by sandbar switching affect coastal erosion; therefore, changes in the sand volume of the beach-foredune system within the sandbar switching zones and outside them are significantly different.

Novelty

The main novelties proposed in this thesis include:

1. Development and validation of a unique automated methodology for the extraction of multiple morphological characteristics of nearshore sandbars from optical satellite imagery (**Paper I**).
2. Adaptation of traditional analysis techniques used to study nearshore sandbar behaviour with bathymetric and video monitoring data to satellite-derived sandbar data, extracted using the proposed method (**Paper II**).
3. A new database based on decadal satellite data that describes the morphological characteristics of nearshore sandbars in the Curonian Spit (**Paper I, II**).
4. First quantification of the Curonian Spit nearshore sandbar cross-shore migration and first observation of well-known cyclic net offshore migration behaviour in the Southeastern Baltic Sea coast, allowing for a better understanding of sandbar behaviour in this coastal region (**Paper II**).
5. First determination of a link between the morphodynamic phenomenon of multiple sandbar systems (sandbar switching) and coastal erosion (**Paper IV**).

Applicability

The proposed methodology for the extraction of nearshore sandbars in satellite imagery works with at least four optical satellite sensors of different spatial resolutions, extracts the sandbar morphology with high accuracy, regardless of the sensor, and is designed to work with a variety of sandbar shapes (**Paper I**). This enables a spatiotemporal analysis of nearshore sandbars across large spatial extents on other sandy shores, replacing traditional resource-intensive data collection techniques with a cost-effective alternative.

The assessment of nearshore sandbar dynamics and its relation to coastal evolution (**Papers II–IV**) contributes to a comprehensive understanding of the processes in the coastal zone and provides a basis for informed coastal management decisions. The analysis of the cross-shore migration of sandbars and its cyclic nature in the Curonian Spit (**Paper II**) provides a foundation for predicting the behaviour of sandbars along the Baltic Sea coast of the Curonian Spit. The relationship between sandbar switching episodes and coastal erosion established in this thesis (**Paper IV**) may contribute to the prediction of coastal erosion hotspots.

1. MATERIALS AND METHODS

1.1. Study area and data

The study region of the thesis covers a 51 km stretch of the Lithuanian part of the Curonian Spit, from Kopgalis to Nida. The research was conducted along the Baltic Sea nearshore up to a depth of 8 m, as well as on the beach and foredune. The main data source used in this thesis are optical satellite imagery captured by PlanetScope and RapidEye sensors, covering the period from 2009 to 2021. Multiple bathymetric surveys performed during the preparation of this thesis along the Baltic Sea coast of the Curonian Spit, as well as topographic surveys and historical-cartographic data were also used.

1.2. Extraction of sandbar data from satellite images

A methodology for the automated extraction of nearshore sandbars in multispectral satellite images was developed (**Paper I**). It is a multi-step, GIS-based algorithm consisting of four main steps of execution:

1. *Shoreline extraction* (**Paper I, p. 8–9**). At this step, spectral indices and unsupervised classification techniques are used to binarize satellite images into submerged and subaerial coastal parts, and extract shoreline position based on reflective properties of water and land in the visible and near-infrared light spectrum.
2. *Identification of nearshore morphology* (**Paper I, p. 9–14**). At this step, positive and negative seabed topographies are distinguished based on a local relief metric – the Relative Bathymetric Position Index (RBPI) – indicating if a pixel value is lower or higher than the mean in the local neighbourhood, and normalised by the minimum and maximum values within the local neighbourhood. A multi-scale approach for calculating and filtering RBPI was designed and proposed to preserve both larger and

smaller scale sandbar morphologies and to reduce distortions caused by low signal-to-noise ratios over water surfaces in satellite images.

3. *Extraction of nearshore sandbars (Paper I, p. 14–15)*. At this step, criteria-based selection operations and unsupervised classification techniques are used to extract the boundaries of nearshore sandbars from filtered multi-scale RBPI images.
4. *Extraction of sandbar crests (Paper I, p. 15–18)*. At this step, variously oriented local neighbourhoods are used to derive primary sandbar crest positions, irrespectively to their shore-wise orientation. Then, a proximity-based filter is developed to remove falsely identified crest pixels.

After implementing the entire algorithm, outputs with shoreline position (1), multi-scale RBPI image (2), sandbar boundaries (3), and crestlines (4) are generated.

For the data analysis, the algorithm was implemented with 145 dates of PlanetScope and RadpidEye imagery. Based on satellite-derived data, a database with a time series of multiple sandbar morphological characteristics was created for the spatiotemporal analysis.

1.3. Analysis of satellite-derived and other sandbar data

Several assessments have been carried out to analyse the dynamics of nearshore sandbars and their relationship to coastal evolution in the Curonian Spit:

1. Evaluation of interannual and seasonal sandbar cross-shore migration rates using a decadal time series of monthly satellite-derived crest positions and their temporal derivatives in 1071 cross-shore profiles with 50-metre spacing (**Paper II**).
2. Evaluation of the duration of sandbar cycle return periods using 1071 RBPI-derived cross-shore profiles with 50-metre spacing and CEOF analysis (**Paper II**).
3. Evaluation of nearshore sandbar switching episodes, including their duration, reoccurrence, boundaries, and morphology, identified from satellite images (**Paper IV**).
4. Determination of sandbar behaviour regions on three spatial levels based on 36 satellite-derived morpho-temporal sandbar metrics and cluster analysis (**Paper II**).
5. Evaluation of anthropogenic changes in nearshore seabed topography in the vicinity of the Klaipėda Port jetties, using a GIS-analysis of historical-cartographical and bathymetric data (**Paper III**).

6. Identification of the factors determining nearshore sandbar behaviour, using linear and logistic regression analyses (**Papers II, IV**).
7. Evaluation of the relationship between sandbar switching episodes and coastal evolution, using topographic and satellite-derived data to assess coastal changes during sandbar switching episodes, as well as statistical hypothesis tests and linear regression analysis to examine the relationship (**Paper IV**).

2. RESULTS AND DISCUSSION

2.1. Accuracy of the proposed method

The accuracy of the proposed algorithm to extract sandbars from satellite images was assessed by comparing the satellite-derived sandbar crest positions with the ones derived from bathymetric surveys performed on six different dates (**Paper I, p. 19–20, 23–25**). Sandbar crests were derived from the images of four satellite sensors: PlanetScope (3 m), RapidEye (5 m), Sentinel-2 MSI (10 m), and Landsat-8 OLI (15 m). A very good agreement was found between satellite-derived and bathymetry-derived sandbar crest positions with $R^2=0.996\text{--}0.999$, depending on the sensor. The average root-mean-square error (*RMSE*) in images captured during low wave energy conditions was 5.8, 7.0, 4.9, and 7.5 m for PlanetScope, RapidEye, Sentinel-2 MSI, and Landsat-8 OLI sensors, respectively. However, under high wave energy conditions, the accuracy of satellite-derived crest positions dropped to *RMSE*=18.9–22.9 m, suggesting that only satellite images acquired under non-breaking wave conditions are suitable to study nearshore sandbars. The accuracy of the satellite-derived sandbar crest positions also depended on overall image quality on a specific date, sandbar cross-shore position, and depth. The results discussed in this section suggest that using the proposed method, sandbar crests may be derived from satellite images of commercial high-resolution sensors (3–5 m) and open-source medium-resolution sensors (10–15 m) with comparable accuracy. This can be determined by a lower signal-to-noise ratio in PlanetScope and RapidEye images than in Sentinel-2 MSI and Landsat-8 OLI (Houborg and McCabe, 2018; Kudela et al., 2019; Leach et al., 2019; Sadeh et al., 2021).

2.2. Morphology and dynamics of nearshore sandbars

2.2.1. Sandbar cross-shore dynamics

On an interannual timescale, the average sandbar cross-shore migration rates at 1071 profiles ranged from 0.1 to 11.0 m/month (**II paper, p. 10–12**). The first and second sandbars had the highest cross-shore migration rates (on average, 4.9–5.4 m/month), while the third and fourth sandbars migrated slower (on average, 1.9–2.4 m/month). The rates of offshore migration exceeded the rates of onshore migration in most of the Curonian Spit. During the low wave energy season, the nearshore sandbars migrated at an average rate of 0.1–7.0 m/month, while during the high wave energy season, sandbar migration rates within cross-shore profiles varied between 0.1 and 13.4 m/month (**II paper, p. 12–14**). The average speed of the seasonal sandbar migration increased with the increasing distance of the sandbars from the shoreline. The average rates of seasonal onshore migration of the second to fourth sandbars outpaced the average rates of seasonal offshore migration during both the low and high wave energy seasons. In contrast, the first (outer) sandbar exhibited higher average offshore migration rates than average onshore migration rates during the high wave energy season but had nearly identical average offshore and onshore migration rates during the low wave energy season. Both interannual and seasonal sandbar cross-shore migration rates increased from north to south of the Curonian Spit.

On a multi-annual timescale, nearshore sandbars in the Curonian Spit demonstrated cyclic offshore-directed behaviour according to the Dutch Net Offshore Migration (NOM) model proposed by Ruessink and Kroon (1994) (**II paper, p. 15–16**). They formed near the shoreline, migrated across the surf zone, and, on a multi-annual timescale, gradually moved further offshore, until the outer sandbar eventually decayed from the nearshore profile, while the second sandbar began to develop rapidly in its position. The duration of this cycle is characterised by the sandbar cycle return period (T_r). The average duration of the sandbar cycle return period in the Curonian Spit was found to be 6.7 years, but it varied significantly alongshore and increased from 1.8 to 13.5 years from north to south of the Curonian Spit. Although this analysis covers a period slightly shorter than the maximum estimated T_r in the Curonian Spit, the CEOF analysis enables such estimations and has been previously successfully applied in similar cases (Aleman et al., 2013; Tătui et al., 2016). However, the use of a longer time series of RBPI profiles, including a higher count of sandbar cycles, could enable a more accurate estimation of T_r duration.

2.2.2. Sandbar morphodynamics (switching)

Sandbar switching, also known as longshore realignment of nearshore sandbars, is a common morphodynamic phenomenon in multi-sandbar systems. It occurs when a sandbar becomes discontinuous longshore and on its discontinuous side attaches to a landward or seaward sandbar (Shand et al., 2001). Between 2009 and 2021, 27 sandbar switching episodes with an average duration of 14 months were observed in the Curonian Spit. Typically, they occurred in nearshore stretches from Alksnynė to Nida, with an increasing number of switching episodes in the southern direction (**Paper IV**, p. 5, 7). Three types of sandbar switching episodes based on their morphological evolution have been observed in the Curonian Spit (**Paper IV**, p. 5–6). Sandbar switching episodes are important, because the switching-related sandbar morphology affects the nearshore flow field and coastal evolution for up to several years. Sandbar switching zones are also often considered to be transitional zones between different sandbar behaviour regions (Walstra et al., 2016; Wijnberg and Terwindt, 1995).

2.2.3. Sandbar dynamics affected by anthropogenic activity

Although the majority of the Curonian Spit's nearshore represents natural sandbar evolution, the development of the nearshore morphology in the short nearshore sector at the distal end of the Curonian Spit was influenced by the construction of the Klaipėda port jetties, changes in their configuration and length, as well as the dredging of the port entrance channel (**Paper III**). The development of this nearshore sector over the last two centuries could be divided into several stages: before the construction of port jetties (**Paper III**, p. 491); the construction of port jetties (**Paper III**, p. 492); the intensive dredging of the port entrance channel (**Paper III**, p.495); and the reconstruction of port jetties (**Paper III**, p. 496–497). The current nearshore morphology at the distal end of the Curonian Spit, consisting of a wide flat shoal and a rudimentary outer sandbar, has been observed since the port entrance channel dredging stage and does not exhibit the typical dynamic patterns that characterise the rest of the Curonian Spit.

2.2.4. Sandbar behaviour regions

Cluster analysis was used to identify nearshore sandbar behaviour (NBB) regions that exhibit similar patterns of satellite-derived cross-shore temporal and morphological characteristics of a multiple sandbar system in the

Curonian Spit (**Paper II, p. 16–18**). The NBB regions were distinguished at three spatial levels, demonstrating alongshore differences in sandbar cross-shore behaviour from the most generalised large-scale level to a more detailed small-scale level. At the large-scale level, two NBB regions divide the Curonian Spit into northern and southern parts. The northern NBB region exhibits higher rates of sandbar cross-shore migration, shorter sandbar cycle return periods, a higher sandbar count, and sandbars located closer to the shoreline than the southern one. At the lower-scale levels, the transitional central sector, consisting of several NBB regions, emerges. However, it is very heterogeneous in its cross-shore characteristics, with its southern part exhibiting more similar features to the large-scale southern NBB region and its northern part being more comparable to the large-scale northern NBB region.

2.2.5. Factors determining nearshore sandbar dynamics

It was previously discussed that the coastal engineering structures of the Klaipėda port influence the sandbar evolution at the distal end of the Curonian Spit. However, sandbar behaviour in the rest of the Curonian Spit is determined by natural factors. Linear regression analysis demonstrated that sandbar cycle return periods (T_r) and sandbar migration rates are well-correlated with depth-related, sandbar-size-related, as well as wave-related parameters (**Paper II, p. 19–21**). In a wider and deeper sandbar zone with sandbars of larger volume, T_r is longer and sandbars migrate slower than in a shallower and narrower sandbar zone with smaller volume sandbars but a higher number of them. Shore-oblique and higher waves with longer periods determine longer sandbar cycle return periods than lower, more frequent, and shore-normal waves. Predominant wind directions from W and SW, as well as the shifting of the shoreline orientation from SW-NE to S-N, determine that oblique wave energy is more frequent in the southern part of the Curonian Spit. Therefore, sandbars here evolve slower than in the northern part.

It was also observed that in the Curonian Spit, sandbar switching episodes tend to occur at breakpoints of different shoreline compass angles. Previous studies have suggested that favourable conditions for the occurrence of sandbar switching are associated with strong longshore currents and oblique wave energy (Aleman et al., 2017; Shand et al., 2001). This thesis evaluated the importance of these factors and determined that by using the shoreline compass angle and wave obliquity as predictors, the occurrence of sandbar switching episodes in the Curonian Spit can be predicted with $R^2=0.57$ (**Paper IV, p. 11–13**).

The discussed results suggest that the interplay between shoreline orientation and small alongshore differences in predominant nearshore hydrodynamics, caused by the local wave climate, determine the morphology and evolution of the multi-sandbar system in the Curonian Spit (**Papers II, IV**).

2.2.6. The influence of sandbar dynamics on coastal evolution

Submerged and subaerial beaches form a feedback-based morphothodynamic system with a constant exchange of sediments between the beach and the nearshore; thus, the processes in the subaqueous and subaerial coastal domains are strongly related (Cohn et al., 2017; Phillips et al., 2017; Robin et al., 2014; Tătui et al., 2013). In this thesis, a connection between sandbar switching episodes and coastal erosion was observed for the first time worldwide. It was found that the shoreline typically retreats landward during the sandbar switching episode and recovers after it. In 26 of the 27 identified sandbar switching zones on the Curonian Spit, a shoreline retreat of up to 49 m was observed (**Paper IV, p. 5, 6, 8**). Interannual and storm-induced sand volume changes in the beach and foredune were compared inside and outside the sandbar switching zones. On the interannual timescale, the beach and foredune experienced a small average rate of erosion inside the sandbar switching episodes compared to locations outside the sandbar switching zones, which exhibited a small average rate of accretion (**Paper IV, p. 7–8**). On a storm-related timescale, a higher average rate of beach and foredune erosion was observed inside the sandbar switching zones than at locations outside of these zones (**Paper IV, p. 8–9**). Statistical hypothesis testing showed that the difference between the median sand volume changes in the beach-foredune system within the sandbar switching zones and outside them was statistically significant. The increased coastal erosion at sandbar switching locations could be related to an imbalance in typical beach-nearshore sediment exchange and a local diminishing of the sandbar zone, both caused by sandbar switching-induced changes in nearshore morphology and nearshore flow field (**Paper IV, p. 9–10, 12–13**).

CONCLUSIONS

1. Using an automated algorithm proposed in this thesis, sandbar crests are derived with an average root-mean-square-error of 4.9–7.5 m in images of high-medium (3–15 m) resolution from PlanetScope, RapidEye, Sentinel-2 MSI, and Landsat-8 OLI satellite sensors. The accuracy of satellite-derived sandbar crest position depends on the wave conditions, sandbar depth, and distance from the shoreline, as well as the quality of the satellite sensor.
2. It was demonstrated that a time series of satellite-derived sandbar crest positions is a suitable data source for the quantification of sandbar cross-shore migration, while the multi-scale Relative Bathymetric Position Index, proposed in this thesis, is a suitable alternative to bathymetric cross-shore profiles for the assessment of cyclic sandbar behaviour.
3. Based on decadal satellite-derived data, it was observed that sandbars in the Curonian Spit exhibit multi-annual cyclic offshore directed behaviour, and the average duration of the bar cycle return period in the Curonian Spit is 6.7 years. It was estimated that the duration of the bar cycle return period increases from Koggalis to Nida from 1.8 to 13.5 years.
4. A triple-quadruple sandbar system, with an average interannual and seasonal sandbar cross-shore migration rates ranging from 0.1 to 13.4 m/month in different cross-shore profiles, was observed in 98% of the Curonian Spit from 2011 to 2021. Sandbars in the northern part of the Curonian Spit exhibited higher cross-shore migration rates than those in the southern part.
5. The duration of bar cycle return periods (T_r) was found to be strongly correlated ($R=0,73\text{--}0,89$; $p<0,05$) with wave height, period and direction of propagation, as well as with sandbar volume and the depth and width of the sandbar zone. The increase in the average values of these rates from the north to the south of the Curonian Spit determined an increase in the duration of T_r in the same direction.
6. The rates of sandbar cross-shore migration had moderate and strong correlation rates ($R=0,53\text{--}0,73$; $p<0,05$) with sandbar volume, and the depth and width of the sandbar zone only. Thus, sandbar offshore and onshore migration rates in 2011–2021 were determined by the characteristics of the sandbar size and depth. The increase in the average values of these rates from the north to the south of the Curonian Spit determined the higher cross-shore migration rates in the northern part of the Curonian Spit than in the southern part.

7. The nearshore morphology at the distal end of the Curonian Spit is affected by the Klaipėda port jetties. It is evidenced by the formation of the sandbar morphology, which is uncharacteristic of the rest of the Curonian Spit and consists of a flat shallow shoal branching off to the south into 2–3 small sandbars.
8. Between 2009 and 2021, 27 sandbar switching episodes with an average duration of 14 months were observed in the Curonian Spit. Therefore, a typical switching episode affected the nearshore flow field on an interannual time scale. Sandbar switching episodes reoccurred in quasi-stable locations along the Baltic Sea nearshore from Alksnynė to Nida. These locations coincided with the transitional zones between different shoreline orientations and oblique wave energy.
9. The results of this study revealed that on the interannual time scale, the beach-foredune system within the sandbar switching zones exhibited a small average rate of erosion, while the beach-foredune system outside the sandbar switching zones demonstrated a small average rate of accretion. On a storm-related time scale, the beach-foredune system exhibited higher rates of erosion within the sandbar switching zones than outside them. According to the results of the Wilcoxon test, the difference between median changes in the sand volume of the beach-foredune system within and outside sandbar switching zones on both interannual and storm-related time scales was statistically significant ($p<0,05$).

LITERATŪROS SĀRAŠAS

- Aagaard, T., 1991. Multiple-bar morphodynamics and its relation to low-frequency edge waves. *Journal of Coastal Research* 7, 801–813.
- Aagaard, T., Kroon, A., Hughes, M. G., Greenwood, B., 2008. Field observations of nearshore bar formation. *Earth Surface Processes and Landforms*, 33, 1021–1032. <https://doi.org/10.1002/esp.1599>
- Aleman, N., Certain, R., Robin, N., Barusseau, J.-P., 2017. Morphodynamics of slightly oblique nearshore bars and their relationship with the cycle of net offshore migration. *Marine Geology*, 392, 41–52. <https://doi.org/10.1016/j.margeo.2017.08.014>
- Aleman, N., Robin, N., Certain, R., Anthony, E. J., Barusseau, J. P., 2015. Longshore variability of beach states and bar types in a microtidal, storm-influenced, low-energy environment. *Geomorphology*, 241, 175–191. <https://doi.org/10.1016/j.geomorph.2015.03.029>
- Aleman, N., Robin, N., Certain, R., Barusseau, J.-P., Gervais, M., 2013. Net offshore bar migration variability at a regional scale: Inter-site comparison (Languedoc-Roussillon, France). *Journal of Coastal Research*, 165, 1715–1720. <https://doi.org/10.2112/si65-290.1>
- Alexander, P. S., Holman, R. A., 2004. Quantification of nearshore morphology based on video imaging. *Marine Geology*, 208, 101–111. <https://doi.org/10.1016/j.margeo.2004.04.017>
- Armaroli, C., Ciavola, P., 2011. Dynamics of a nearshore bar system in the northern Adriatic: A video-based morphological classification. *Geomorphology*, 126, 201–216. <https://doi.org/10.1016/j.geomorph.2010.11.004>
- Athanasiou, P., de Boer, W., Yoo, J., Ranasinghe, R., Reniers, A., 2018. Analysing decadal-scale crescentic bar dynamics using satellite imagery: A case study at Anmok beach, South Korea. *Marine Geology*, 405, 1–11. <https://doi.org/10.1016/j.margeo.2018.07.013>
- Aubrey, D.G., 1979. Seasonal patterns of onshore/offshore sediment movement. *Journal of Geophysical Research*, 84, 6347. <https://doi.org/10.1029/JC084iC10p06347>
- Baltijos jūros Lietuvos krantų geologinis atlasas*. 2004. Vilnius: Lietuvos geologijos tarnyba.
- Boczar-Karakiewicz, B., Davidson-Arnott, R.G.D., 1987. Nearshore bar formation by non-linear wave processes – A comparison of model results and field data. *Marine Geology*, 77, 287–304. [https://doi.org/10.1016/0025-3227\(87\)90118-6](https://doi.org/10.1016/0025-3227(87)90118-6)
- Bowen, A. J., Inman, D. L., 1971. Edge waves and crescentic bars. *Journal of*

- Geophysical Research*, 76, 8662–8671.
<https://doi.org/10.1029/JC076i036p08662>
- Brighton, B., Sherker, S., Brander, R., Thompson, M., Bradstreet, A., 2013. Rip current related drowning deaths and rescues in Australia 2004–2011. *Natural Hazards and Earth System Science*, 13, 1069–1075. <https://doi.org/10.5194/nhess-13-1069-2013>
- Caballeria, M., Coco, G., Falqués, A., Huntley, D. A., 2002. Self-organization mechanisms for the formation of nearshore crescentic and transverse sand bars. *Journal of Fluid Mechanics*, 465, 379–410. <https://doi.org/10.1017/S002211200200112X>
- Camara, E. M., Caramaschi, É. P., Di Dario, F., Petry, A. C., 2018. Short-term changes in two tropical coastal lagoons: Effects of sandbar openings on fish assemblages. *Journal of Coastal Research*, 341, 90–105. <https://doi.org/10.2112/jcoastres-d-16-00026.1>
- Castelle, B., Ruessink, B. G., Bonneton, P., Marieu, V., Bruneau, N., Price, T. D., 2010a. Coupling mechanisms in double sandbar systems. Part 2: Impact on alongshore variability of inner-bar rip channels. *Earth Surface Processes and Landforms*, 35, 771–781. <https://doi.org/10.1002/esp.1949>
- Castelle, B., Ruessink, B. G., Bonneton, P., Marieu, V., Bruneau, N., Price, T. D., 2010b. Coupling mechanisms in double sandbar systems. Part 1: Patterns and physical explanation. *Earth Surface Processes and Landforms*, 35, 476–486. <https://doi.org/10.1002/esp.1929>
- Castelle, B., Scott, T., Brander, R. W., McCarroll, R. J., 2016. Rip current types, circulation and hazard. *Earth-Science Reviews* 163, 1–21. <https://doi.org/10.1016/J.EARSCIREV.2016.09.008>
- Cohn, N., Ruggiero, P., De Vries, S., García-Medina, G., 2017. Beach growth driven by intertidal sandbar welding, in: *Coastal Dynamics 2017*. Helsingør, p. 12–16.
- Contardo, S., Symonds, G., 2015. Sandbar straightening under wind-sea and swell forcing. *Marine Geology*, 368, 25–41. <https://doi.org/10.1016/j.margeo.2015.06.010>
- De Beaumont E. 1845. *Lecons de Géologie Practique*. Paris.
- Di Leonardo, D., Ruggiero, P., 2015. Regional scale sandbar variability: Observations from the U.S. Pacific Northwest. *Continental Shelf Research*, 95, 74–88. <https://doi.org/10.1016/j.csr.2014.12.012>
- Do, J. D., Jin, J.-Y., Jeong, W. M., Lee, B., Kim, C. H., Chang, Y. S., 2021. Observation of nearshore crescentic sandbar formation during storm wave conditions using satellite images and video monitoring data. *Marine Geology*, 442, 106661.

- https://doi.org/10.1016/J.MARGEOP.2021.106661
- Dubarbier, B., Castelle, B., Marieu, V., Ruessink, G., 2015. Process-based modeling of cross-shore sandbar behavior. *Coastal Engineering*, 95, 35–50. https://doi.org/10.1016/j.coastaleng.2014.09.004
- Dyhr-Nielson, M., Sorensen, T., 1970. Some sand transport phenomena on coasts with bars. *Coastal Engineering Proceedings* 1, 54. https://doi.org/10.9753/icce.v12.54
- Elgar, S., Gallagher, E. L., Guza, R. T., 2001. Nearshore sandbar migration. *Journal of Geophysical Research: Oceans*, 106, 11623–11627. https://doi.org/10.1029/2000jc000389
- E.U. Copernicus Marine Service Information. Baltic Sea Wave Analysis and Forecast. https://doi.org/10.48670/moi-00011 (žiūrėta 2022-05-18)
- Falqués, A., Coco, G., Huntley, D. A., 2000. A mechanism for the generation of wave-driven rhythmic patterns in the surf zone. *Journal of Geophysical Research: Oceans*, 105, 24071–24087. https://doi.org/10.1029/2000jc900100
- Falqués, A., Dodd, N., Garnier, R., Ribas, F., MacHardy, L. C., Larroudé, P., Calvete, D., Sancho, F., 2008. Rhythmic surf zone bars and morphodynamic self-organization. *Coastal Engineering*, 55, 622–641. https://doi.org/10.1016/j.coastaleng.2007.11.012
- Falqués, A., Montoto, A., Iranzo, V., 1996. Bed-flow instability of the longshore current. *Continental Shelf Research*, 16, 1927–1964. https://doi.org/10.1016/0278-4343(96)00031-3
- Fernández-Mora, A., Calvete, D., Falqués, A., De Swart, H. E., 2015. Onshore sandbar migration in the surf zone: New insights into the wave-induced sediment transport mechanisms. *Geophysical Research Letters*, 42, 2869–2877. https://doi.org/10.1002/2014GL063004
- Gallagher, E. L., Elgar, S., Guza, R. T., 1998. Observations of sand bar evolution on a natural beach. *Journal of Geophysical Research: Oceans*, 103, 3203–3215. https://doi.org/10.1029/97jc02765
- Garnier, R., Falqués, A., Calvete, D., Thiébot, J., Ribas, F., 2013. A mechanism for sandbar straightening by oblique wave incidence. *Geophysical Research Letters*, 40, 2726–2730. https://doi.org/10.1002/grl.50464
- Gelfenbaum, G., Brooks, G. R., 2003. The morphology and migration of transverse bars off the west-central Florida coast. *Marine Geology*, 200, 273–289. https://doi.org/10.1016/S0025-3227(03)00187-7
- Gelumbauskaite, L. Ž., 2003. On the morphogenesis and morphodynamics of the shallow zone of the Kuršių Nerija (Curonian Spit). *Baltica*, 16, 37–42.

- Gijsman, R., Ruessink, B. G., Visscher, J., Schlurmann, T., 2021. Observations on decadal sandbar behaviour along a large-scale curved shoreline. *Earth Surface Processes and Landforms*, 46, 490–503. <https://doi.org/10.1002/ESP.5041>
- Goulart, E. S., Calliari, L. J., 2013. Medium-term morphodynamic behavior of a multiple sand bar beach. *Journal of Coastal Research*, 165, 1774–1779. <https://doi.org/10.2112/si65-300.1>
- Greenwood, B., Davidson-Arnott, R.G.D., 1979. Sedimentation and equilibrium in wave-formed bars: A review and case study. *Canadian Journal of Earth Sciences*, 16, 312–332. <https://doi.org/10.1139/e79-030>
- Grunnet, N. M., Hoekstra, P., 2004. Alongshore variability of the multiple barred coast of Terschelling, The Netherlands. *Marine Geology*, 203, 23–41. [https://doi.org/10.1016/S0025-3227\(03\)00336-0](https://doi.org/10.1016/S0025-3227(03)00336-0)
- Hoefel, F., Elgar, S., 2003. Wave-induced sediment transport and sandbar migration. *Science*, 299, 1885–1887. <https://doi.org/10.1126/science.1081448>
- Holman, R. A., Bowen, A. J., 1982. Bars, bumps, and holes' models for the generation of complex beach topography, *Journal of Geophysical Research*, 87, 457–468. <https://doi.org/10.1029/JC087iC01p00457>
- Holzhauer, H., Borsje, B. W., van Dalfsen, J. A., Wijnberg, K. M., Hulscher, S.J.M.H., Herman, P.M.J., 2019. Benthic species distribution linked to morphological features of a barred coast. *Journal of Marine Science and Engineering*, 8, 16. <https://doi.org/10.3390/jmse8010016>
- Houborg, R., McCabe, M. F., 2018. A Cubesat enabled Spatio-Temporal Enhancement Method (CESTEM) utilizing Planet, Landsat and MODIS data. *Remote Sensing of Environment*, 209, 211–226. <https://doi.org/10.1016/j.rse.2018.02.067>
- Jankevičiūtė S. 1962. Apie Baltijos jūros smėlio paplūdimio skersinio profilio dinamiką seklioje priekrantėje. *Geografijos metraštis*, 4, 369–381.
- Jankevičiūtė-Močkienė S. 1965. Jūros paplūdimio skersinio profilio ir litologinės sudėties įtaka plūsmo srauto litodinamikai. *Geografijos metraštis*, 6–7, 469–484.
- Janušaitė R. 2018. *Kuršių nerijos priekrantės seklių dinamikos įtaka paplūdimio rekreacinėms zonoms*. Vilnius: Vilniaus universitetas, Chemijos ir geomokslų fakultetas. Magistro darbas.
- Janušaitė, R., Jukna, L., Jarmalavičius, D., Pupienis, D., Žilinskas, G., 2021. A novel GIS-based approach for automated detection of nearshore sandbar morphological characteristics in optical satellite imagery. *Remote Sensing*, 13, 2233. <https://doi.org/10.3390/rs13112233>
- Keulegen, G. H., 1948. An experimental study of submarine sand bars. U.S.

- Beach Erosion Board, [Washington] :
<https://doi.org/10.5962/bhl.title.38103>
- King, C.A.M., Williams, W. W., 1949. The formation and movement of sand bars by wave action. *The Geographical Journal*, 113, 70.
<https://doi.org/10.2307/1788907>
- Kirlys V. 1974. Pietrytinės Baltijos jūros dalies litodinaminiai ir morfodinaminiai priekrantės bruožai. *Geografijos metraštis*, 13, 217–228.
- Kirlys V., Janukonis Z., Žaromskis R. 1974a. Baltijos jūros pietryčių sektoriaus priekrantės povandeninio šlaito viršutinės dalies morfodinaminės ypatybės (1. Kursių nerija). *Lietuvos TSR Mokslų akademijos darbai, B serija*, 6 (85), 153–164.
- Kirlys V., Janukonis Z., Žaromskis R. 1974b. Baltijos jūros pietryčių sektoriaus povandeninio šlaito viršutinės dalies morfodinaminės ypatybės (2. Pagrindinio kranto zonos priekrantė). *Lietuvos TSR Mokslų akademijos darbai, B serija*, 6 (85), 165–171.
- Kirlys V., Močiekienė S. 1975. Apie jūros priekrantės zonas ilgalaikių pakitimų pobūdį (3. Reljefo deformacijos intensyvumas). *Lietuvos TSR Mokslų akademijos darbai, B serija*, 4 (89), 161–168.
- Kirlys V., Stauskaitė R., Jankevičiūtė-Močiekienė S., Dolotovas J. 1969. Povandeninių sėklių dinamikos klausimu. *Lietuvos TSR Mokslų akademijos darbai, B serija*, 4 (59).
- Kudela, R. M., Hooker, S. B., Houskeeper, H. F., McPherson, M., 2019. The influence of signal to noise ratio of legacy airborne and satellite sensors for simulating next-generation coastal and inland water products. *Remote Sensing*, 11, 2071. <https://doi.org/10.3390/rs11182071>
- Kuriyama, Y., 2002. Medium-term bar behavior and associated sediment transport at Hasaki, Japan. *Journal of Geophysical Research: Oceans*, 107, 15–1. <https://doi.org/10.1029/2001jc000899>
- Lafon, V., De Melo Apoluceno, D., Dupuis, H., Michel, D., Howa, H., Froidefond, J. M., 2004. Morphodynamics of nearshore rhythmic sandbars in a mixed-energy environment (SW France): I. Mapping beach changes using visible satellite imagery. *Estuarine, Coastal and Shelf Science*, 61, 289–299. <https://doi.org/10.1016/j.ecss.2004.05.006>
- Larson, M., Kraus, N. C., 1993. Dynamics of longshore bars, in: Proceedings of the Coastal Engineering Conference. p. 2219.
<https://doi.org/10.1061/9780872629332.169>
- Larson, M., Kraus, N. C., 1994. Temporal and spatial scales of beach profile change, Duck, North Carolina. *Marine Geology*, 117, 75–94.
[https://doi.org/10.1016/0025-3227\(94\)90007-8](https://doi.org/10.1016/0025-3227(94)90007-8)

- Leach, N., Coops, N. C., Obrknezev, N., 2019. Normalization method for multi-sensor high spatial and temporal resolution satellite imagery with radiometric inconsistencies. *Computers and Electronics in Agriculture*, 164, 104893. <https://doi.org/10.1016/j.compag.2019.104893>
- Lippmann, T. C., Holman, R. A., 1990. The spatial and temporal variability of sand bar morphology. *Journal of Geophysical Research*, 95, 575–586. <https://doi.org/https://doi.org/10.1029/JC095iC07p11575>
- Lippmann, T. C., Holman, R. A., 1989. Quantification of sand bar morphology: A video technique based on wave dissipation. *Journal of Geophysical Research*, 94, 995–1011. <https://doi.org/https://doi.org/10.1029/JC094iC01p00995>
- Melito, L., Parlagreco, L., Perugini, E., Postacchini, M., Devoti, S., Soldini, L., Zitti, G., Liberti, L., Brocchini, M., 2020. Sandbar dynamics in microtidal environments: Migration patterns in unprotected and bounded beaches. *Coastal Engineering*, 161, 103768. <https://doi.org/10.1016/j.coastaleng.2020.103768>
- Múnera, S., Osorio, A. F., Velásquez, J. D., 2014. Data-based methods and algorithms for the analysis of sandbar behavior with exogenous variables. *Computers and Geosciences*, 72, 134–146. <https://doi.org/10.1016/j.cageo.2014.07.009>
- Newman, D. R., Lindsay, J. B., Cockburn, J.M.H., 2018. Evaluating metrics of local topographic position for multiscale geomorphometric analysis. *Geomorphology*, 312, 40–50. <https://doi.org/10.1016/j.geomorph.2018.04.003>
- Ojeda, E., Guillén, J., Ribas, F., 2011. Dynamics of single-barred embayed beaches. *Marine Geology*, 280, 76–90. <https://doi.org/10.1016/j.margeo.2010.12.002>
- Parlagreco, L., Melito, L., Devoti, S., Perugini, E., Soldini, L., Zitti, G., Brocchini, M., 2019. Monitoring for coastal resilience: Preliminary data from five Italian sandy beaches. *Sensors*, 19, 1854. <https://doi.org/10.3390/s19081854>
- Phillips, M. S., Harley, M. D., Turner, I. L., Splinter, K. D., Cox, R. J., 2017. Shoreline recovery on wave-dominated sandy coastlines: The role of sandbar morphodynamics and nearshore wave parameters. *Marine Geology*, 385, 146–159. <https://doi.org/10.1016/j.margeo.2017.01.005>
- Plant, N. G., Freilich, M. H., Holman, R. A., 2001. Role of morphologic feedback in surf zone sandbar response. *Journal of Geophysical Research: Oceans*, 106, 973–989. <https://doi.org/10.1029/2000JC900144>
- Plant, N. G., Holman, R. A., Freilich, M. H., Birkemeier, W. A., 1999. A

- simple model for interannual sandbar behavior. *Journal of Geophysical Research: Oceans*, 104, 15755–15776. <https://doi.org/10.1029/1999jc900112>
- Price, T. D., Ruessink, B. G., 2011. State dynamics of a double sandbar system. *Continental Shelf Research*, 31, 659–674. <https://doi.org/10.1016/j.csr.2010.12.018>
- Price, T. D., Ruessink, B. G., Castelle, B., 2014. Morphological coupling in multiple sandbar systems – A review. *Earth Surface Dynamics*, 2 (1), 309–321. <https://doi.org/10.5194/esurf-2-309-2014>
- Pruszak, Z., Różyński, G., Zeidler, R. B., 1997. Statistical properties of multiple bars. *Coastal Engineering*, 31, 263–280. [https://doi.org/10.1016/S0378-3839\(97\)00010-0](https://doi.org/10.1016/S0378-3839(97)00010-0)
- Robin, N., Certain, R., Bouchette, F., Anthony, E. J., Meulé, S., Aleman, N., 2014. Wave-driven circulation over a double nearshore bar system during storm conditions. *Journal of Coastal Research*, 70, 84–89. <https://doi.org/10.2112/si70-015.1>
- Roelvink, J. A., Stive, M.F.J., 1989. Bar-generating cross-shore flow mechanisms on a beach. *Journal of Geophysical Research*, 94, 4785–4800. <https://doi.org/10.1029/JC094iC04p04785>
- Román-Rivera, M. A., Ellis, J. T., 2019. A synthetic review of remote sensing applications to detect nearshore bars. *Marine Geology*, 408, 144–153. <https://doi.org/10.1016/j.margeo.2018.12.003>
- Román-Rivera, M. A., Ellis, J. T., Wang, C., 2020. Applying a rule-based object-based image analysis approach for nearshore bar identification and characterization. *Journal of Applied Remote Sensing*, 14, 044502. <https://doi.org/10.1117/1.jrs.14.044502>
- Ruessink, B. G., Coco, G., Ranasinghe, R., Turner, I. L., 2007. Coupled and noncoupled behavior of three-dimensional morphological patterns in a double sandbar system. *Journal of Geophysical Research: Oceans*, 112, C07002. <https://doi.org/10.1029/2006JC003799>
- Ruessink, B. G., Kroon, A., 1994. The behaviour of a multiple bar system in the nearshore zone of Terschelling, the Netherlands: 1965–1993. *Marine Geology*, 121, 187–197. [https://doi.org/10.1016/0025-3227\(94\)90030-2](https://doi.org/10.1016/0025-3227(94)90030-2)
- Ruessink, B. G., Pape, L., Turner, I. L., 2009. Daily to interannual cross-shore sandbar migration: Observations from a multiple sandbar system. *Continental Shelf Research*, 29, 1663–1677. <https://doi.org/10.1016/j.csr.2009.05.011>
- Ruessink, B. G., Wijnberg, K. M., Holman, R. A., Kuriyama, Y., van Enckevort, I.M.J., 2003. Intersite comparison of interannual nearshore bar behavior. *Journal of Geophysical Research: Oceans*, 108, 5–1.

- <https://doi.org/10.1029/2002jc001505>
- Rutten, J., Ruessink, B. G., Price, T. D., 2018. Observations on sandbar behaviour along a man-made curved coast. *Earth Surface Processes and Landforms*, 43, 134–149. <https://doi.org/10.1002/esp.4158>
- Sadeh, Y., Zhu, X., Chenu, K., Dunkerley, D., 2019. Sowing date detection at the field scale using CubeSats remote sensing. *Computers and Electronics in Agriculture*, 157, 568–580. <https://doi.org/10.1016/j.compag.2019.01.042>
- Sadeh, Y., Zhu, X., Dunkerley, D., Walker, J. P., Zhang, Y., Rosenstein, O., Manivasagam, V. S., Chenu, K., 2021. Fusion of Sentinel-2 and PlanetScope time-series data into daily 3 m surface reflectance and wheat LAI monitoring. *International Journal of Applied Earth Observation and Geoinformation*, 96, 102260. <https://doi.org/10.1016/j.jag.2020.102260>
- Sallenger, A. H., Holman, R. A., Birkemeier, W. A., 1985. Storm-induced response of a nearshore-bar system. *Marine Geology*, 64, 237–257. [https://doi.org/10.1016/0025-3227\(85\)90107-0](https://doi.org/10.1016/0025-3227(85)90107-0)
- Sallenger, A. H., Howd, P. A., 1989. Nearshore bars and the break-point hypothesis. *Coastal Engineering*, 14 (4), 301–313. [https://doi.org/10.1016/0378-3839\(89\)90009-4](https://doi.org/10.1016/0378-3839(89)90009-4)
- Shand, R. D., Bailey, D. G., Shepherd, M. J., 2001. Longshore realignment of shore-parallel sand-bars at Wanganui, New Zealand. *Marine Geology*, 179, 147–161. [https://doi.org/10.1016/S0025-3227\(01\)00223-7](https://doi.org/10.1016/S0025-3227(01)00223-7)
- Shand, R. D., Shepherd, M. J., Bailey, D. G., 1999. An inter-site comparison of net offshore bar migration characteristics and environmental conditions. *Journal of Coastal Research*, 15, 750–765.
- Shepard, F. P., 1950. Longshore-bars and longshore-troughs. *Beach Erosion Board Technical Memorandum*, 15, 1–31.
- Short, A. D., 1992. Beach systems of the central Netherlands coast: Processes, morphology and structural impacts in a storm driven multi-bar system. *Marine Geology*, 107. [https://doi.org/10.1016/0025-3227\(92\)90071-O](https://doi.org/10.1016/0025-3227(92)90071-O)
- Short, A. D., Aagaard, T., 1993. Single and multi-bar beach change models. *Journal of Coastal Research*, SI15, 141–157.
- Stauskaitė R. 1965. Jūros priekrantinės zonos povandeninio šlaito ir paplūdimio smėlių mineraloginė sudėtis ir litodinamika Nidos rajone. *Geografijos metraštis*, 6–7, 439–468.
- Tătui, F., Constantin, S., 2020. Nearshore sandbars crest position dynamics analysed based on earth observation data. *Remote Sensing of Environment*, 237, 111555. <https://doi.org/10.1016/j.rse.2019.111555>
- Tătui, F., Vespremeanu-Stroe, A., Preoteasa, L., 2013. The correlated

- behavior of sandbars and foredunes on a nontidal coast (Danube Delta, Romania). *Journal of Coastal Research*, 65, 1874–1879. <https://doi.org/10.2112/si65-317.1>
- Tătui, F., Vespremeanu-Stroe, A., Ruessink, G. B., 2016. Alongshore variability of cross-shore bar behavior on a nontidal beach. *Earth Surface Processes and Landforms*, 41, 2085–2097. <https://doi.org/10.1002/esp.3974>
- Thornton, E. B., Humiston, R. T., Birkemeier, W., 1996. Bar/trough generation on a natural beach. *Journal of Geophysical Research: Oceans*, 101, 12097–12110. <https://doi.org/10.1029/96JC00209>
- Van de Lageweg, W. I., Bryan, K. R., Coco, G., Ruessink, B. G., 2013. Observations of shoreline-sandbar coupling on an embayed beach. *Marine Geology*, 344, 101–114. <https://doi.org/10.1016/j.margeo.2013.07.018>
- Van Enckevort, I.M.J., Ruessink, B. G., 2003a. Video observations of nearshore bar behaviour. Part 1: Alongshore uniform variability. *Continental Shelf Research*, 23, 501–512. [https://doi.org/10.1016/S0278-4343\(02\)00234-0](https://doi.org/10.1016/S0278-4343(02)00234-0)
- Van Enckevort, I.M.J., Ruessink, B. G., 2003b. Video observations of nearshore bar behaviour. Part 2: Alongshore non-uniform variability. *Continental Shelf Research*, 23, 513–532. [https://doi.org/10.1016/S0278-4343\(02\)00235-2](https://doi.org/10.1016/S0278-4343(02)00235-2)
- Van Enckevort, I.M.J., Ruessink, B. G., Coco, G., Suzuki, K., Turner, I. L., Plant, N. G., Holman, R. A., 2004. Observations of nearshore crescentic sandbars. *Journal of Geophysical Research: Oceans*, 109, C06028. <https://doi.org/10.1029/2003JC002214>
- Vidal-Ruiz, J. A., Ruiz de Alegría-Arzaburu, A., 2019. Variability of sandbar morphometrics over three seasonal cycles on a single-barred beach. *Geomorphology*, 333, 61–72. <https://doi.org/10.1016/j.geomorph.2019.02.034>
- Walstra, D.-J., Wesselman, D., van der Deijl, E., Ruessink, G., 2016. On the intersite variability in inter-annual nearshore sandbar cycles. *Journal of Marine Science and Engineering*, 4, 15. <https://doi.org/10.3390/jmse4010015>
- Wijnberg, K. M., Kroon, A., 2002. Barred beaches. *Geomorphology*, 48, 103–120. [https://doi.org/10.1016/S0169-555X\(02\)00177-0](https://doi.org/10.1016/S0169-555X(02)00177-0)
- Wijnberg, K. M., Terwindt, J.H.J., 1995. Extracting decadal morphological behaviour from high-resolution, long-term bathymetric surveys along the Holland coast using eigenfunction analysis. *Marine Geology*, 126, 301–330. [https://doi.org/10.1016/0025-3227\(95\)00084-C](https://doi.org/10.1016/0025-3227(95)00084-C)

- Wijnberg, K. M., Wolf, F.C.J., 1994. Three-dimensional behaviour of a multiple bar system, in: *Proceedings of Coastal Dynamics'94*. ASCE, p. 59–73.
- Wright, L. D., Short, A. D., 1984. Morphodynamic variability of surf zones and beaches: A synthesis. *Marine Geology*, 56, 93–118. [https://doi.org/https://doi.org/10.1016/0025-3227\(84\)90008-2](https://doi.org/https://doi.org/10.1016/0025-3227(84)90008-2)
- Yuhi, M., Okada, M., 2011. Long-term field observations of multiple bar properties on an eroding coast. *Journal of Coastal Research*, 64, 860–864. <https://doi.org/10.2307/26482295>
- Žaromskis R. 1974. Povandeninių sėklių reljefingumo klausimu (Kuršių nerijos jūros priekrantės pavyzdžiu). *Geografijos metraštis*, 13, 229 – 236.
- Žaromskis, R., Gulbinskas, S., 2010. Main patterns of coastal zone development of the Curonian Spit, Lithuania. *Baltica*, 23, 149–156.
- Žilinskas, G., Jarmalavičius, D., 2007. Interrelation of morphometric parameters of the submarine shore slope of the Curonian Spit. Lithuania. *Baltica*, 20, 46–52.

PADĖKA

Pirmiausia norėčiau padėkoti savo darbo vadovui dr. Dariui Jarmalavičiui už visokeriopą pagalbą rengiant šitą darbą, nuo įžvalgų apie krante vykstančius procesus, dalinimosi duomenimis, batimetrinį matavimų organizavimo iki pagalbos tvarkant formalumus. Dėl to doktorantūros procesas buvo sklandus ir ramus.

Taip pat norėčiau padėkoti darbo konsultantui dr. Laurynui Juknai, kuris mane lydėjo nuo pirmųjų sėklių pažinimo žingsnių dar magistro studijų metu iki išskeltų tikslų įgyvendinimo doktorantūros studijų metu. Esu dėkinga už nuolatines ilgas diskusijas, kurių metu nuomonės dažnai nesutapdavo, bet visada padėdavo užgimti naujoms mintims ir nusibrėžti tolesnį kelią. Esu dėkinga už visų išskeltų idėjų palaikymą, entuziazmą ir nuolatinį moralinį palaikymą, kuris padėjo nepasiduoti šitame ilgame kelyje. Nuolatinis dalinimasis moksliniais atradimais ir nusivylimais buvo svarbi darbo rengimo dalis.

Dar norėčiau padėkoti publikacijų bendraautoriams doc. dr. Donatui Pupieniui ir dr. Gintautui Žilinskui už bendradarbiavimą ir pagalbą. Taip pat esu dėkinga visam krantotyrininkų kolektyvui už skirtą laiką, jėgas ir kitokią pagalbą atliekant batimetrinius matavimus Baltijos jūros priekrantėje. Nepaisant nemoriai nurimstančios jūros, nuolat gėstančio valties variklio ir kitų nenumatyty nesklandumų, visų entuziazmas leido surinkti vertingą duomenų rinkinį.

Galiausiai norėčiau padėkoti darbo recenzentams akad. dr. Jūratei Kriauciūnienei ir prof. dr. Edvinui Stonevičiui, kurių išsakyti pastebėjimai ir komentarai padėjo patobulinti galutinį darbo variantą.

Dékoju visiems besidomintiems priekrantės sėklių tyrimais ir skaitantiems šią disertaciją.

Ačiū.

CURRICULUM VITAE

Rasa Janušaitė gimė 1993 m. sausio 14 d. Tauragėje. 2012 m. baigė Tauragės „Versmės“ gimnaziją. 2012–2016 m. studijavo Vilniaus universiteto Gamtos mokslų fakultete, kur įgijo gamtinės geografijos kaip pagrindinės studijų krypties ir visuomeninės geografijos kaip gretutinės studijų krypties bakalauro laipsnį. 2016–2018 m. studijavo Vilniaus universiteto Chemijos ir geomokslų fakulteto Geomokslų institute, kur įgijo visuomeninės geografijos studijų krypties ir teritorijų planavimo magistro laipsnį. Rengdama magistro darbą, pradėjo gilinti žinias apie priekrantės morfodinaminius procesus. 2018 m. išstojo į jungtines Vilniaus universiteto, Gamtos tyrimų centro ir Klaipėdos universiteto fizinės geografijos doktorantūros studijas, kurių metu parengta ši disertacija.

PUBLIKACIJŲ KOPIJOS

I PUBLIKACIJA

A Novel GIS-Based Approach for Automated Detection of Nearshore Sandbar Morphological Characteristics in Optical Satellite Imagery

Janušaitė R., Jukna L., Jarmalavičius D., Pupienis D., Žilinskas G.
Remote Sensing, 2021, 13 (11): 2233.
DOI: <https://doi.org/10.3390/rs13112233>



Article

A Novel GIS-Based Approach for Automated Detection of Nearshore Sandbar Morphological Characteristics in Optical Satellite Imagery

Rasa Janušaitė ^{1,*}, Laurynas Jukna ², Darius Jarmalavičius ¹, Donatas Pupienis ¹ and Gintautas Žilinskas ¹

¹ Nature Research Centre, LT-08412 Vilnius, Lithuania; darius.jarmalavicius@gamtc.lt (D.J.); donatas.pupienis@gamtc.lt (D.P.); gintautas.zilinskas@gamtc.lt (G.Ž.)

² Institute of Geosciences, Vilnius University, LT-03100 Vilnius, Lithuania; laurynas.jukna@gf.vu.lt

* Correspondence: rasa.janusaitė@gamtc.lt

Abstract: Satellite remote sensing is a valuable tool for coastal management, enabling the possibility to repeatedly observe nearshore sandbars. However, a lack of methodological approaches for sandbar detection prevents the wider use of satellite data in sandbar studies. In this paper, a novel fully automated approach to extract nearshore sandbars in high–medium-resolution satellite imagery using a GIS-based algorithm is proposed. The method is composed of a multi-step workflow providing a wide range of data with morphological nearshore characteristics, which include nearshore local relief, extracted sandbars, their crests and shoreline. The proposed processing chain involves a combination of spectral indices, ISODATA unsupervised classification, multi-scale Relative Bathymetric Position Index (RBPI), criteria-based selection operations, spatial statistics and filtering. The algorithm has been tested with 145 dates of PlanetScope and RapidEye imagery using a case study of the complex multiple sandbar system on the Curonian Spit coast, Baltic Sea. The comparison of results against 4 years of in situ bathymetric surveys shows a strong agreement between measured and derived sandbar crest positions ($R^2 = 0.999$ and 0.997) with an average RMSE of 5.8 and 7 m for PlanetScope and RapidEye sensors, respectively. The accuracy of the proposed approach implies its feasibility to study inter-annual and seasonal sandbar behaviour and short-term changes related to high-impact events. Algorithm-provided outputs enable the possibility to evaluate a range of sandbar characteristics such as distance from shoreline, length, width, count or shape at a relevant spatiotemporal scale. The design of the method determines its compatibility with most sandbar morphologies and suitability to other sandy nearshores. Tests of the described technique with Sentinel-2 MSI and Landsat-8 OLI data show that it can be applied to publicly available medium resolution satellite imagery of other sensors.



Citation: Janušaitė, R.; Jukna, L.; Jarmalavičius, D.; Pupienis, D.; Žilinskas, G. A Novel GIS-Based Approach for Automated Detection of Nearshore Sandbar Morphological Characteristics in Optical Satellite Imagery. *Remote Sens.* **2021**, *13*, 2233. <https://doi.org/10.3390/rs13112233>

Academic Editors: Mohammad Firuz Ramli, Peter Redshaw and Andy Gibson

Received: 16 May 2021

Accepted: 3 June 2021

Published: 7 June 2021

Publisher's Note: MDPI stays neutral with regard to jurisdictional claims in published maps and institutional affiliations.



Copyright: © 2021 by the authors. Licensee MDPI, Basel, Switzerland. This article is an open access article distributed under the terms and conditions of the Creative Commons Attribution (CC BY) license (<https://creativecommons.org/licenses/by/4.0/>).

1. Introduction

Nearshore sandbars are elongated sandy ridges acting as natural barriers that safeguard subaerial beaches in many coastal environments [1,2]. These morphological features are deposited by waves and nearshore currents; they form in shallow waters up to 10 m depth along a wide range of environmental settings, from non-tidal to macrotidal regimes [1,3–5]. Sandbars vary in size, from tens of centimetres to six meters in height [6–8] and extend from tens of meters to tens of kilometres [7,9,10]. They exhibit diverse morphologies from longshore parallel to crescentic or transverse [5,11] and move in cross-shore and longshore directions, demonstrating daily, seasonal and inter-annual migration patterns [10,12]. Sedimentary and morphological connections exist between the evolution of subaerial coast and nearshore sandbars [13,14]. Because of such links and the complexity

of these structures, continuous observation of these dynamic subaqueous features is an important element of coastal monitoring.

To address the need for study and monitoring of sandbar morphodynamics, data of sandbar observations should enable the possibility to derive sandbar crest and identify sandbar shape. It should be possible to study those features over a range of longshore distances and time scales, from short-term to monthly and interannual, and data should be collected over a range of hydrodynamic conditions [15].

Traditionally acoustic and optical remote sensing techniques have been employed in the research of nearshore sandbars. Echo-sounding surveys of nearshore bottom have been performed to study sandbar dynamics and utilized in significant findings of sandbar behaviour [8,16–21]. However, besides being expensive and limited to sampling under calm weather, this technique often provides spatiotemporally sparse datasets and may be inaccurate in the shallowest nearshore areas. Optical remote sensing instruments—*aerial photography, video monitoring, bathymetric, topo-bathymetric or topographic LiDAR (light detection and ranging)*—are another group of methods utilized to study sandbar behaviour. The use of passively sensed aerial photography for sandbar research enabled studies in larger spatial extents and hardly accessible regions [9,22] but a sparse temporal frequency. Recently, active airborne LiDAR sensors have been employed in sandbar morphology and dynamics studies [23–26], but resource-intensive data collection and processing limit the applicability of this technique either in temporal frequency or spatial extent.

Since the 1980s, when a fixed video monitoring system hourly sampling nearshore region was established [27], it has become the state-of-the-art method to study sandbar morphodynamic behaviour [12,28–40]. During the last three decades, the pioneering Argus video monitoring system has made many advancements, and its network was expanded to many sites worldwide [15,41–43], including the development of other video monitoring systems [44–47]. Recently, the utilization of surf cameras was suggested as a cost-effective source for coastal monitoring [48,49]. Despite many advancements and the high temporal frequency, video monitoring systems are limited to short longshore distances and require maintenance.

The increasing availability of optical Earth observation satellite data opens new possibilities to study nearshore region in large spatial extents and has been successfully exploited in a wide range of coastal studies, including the derivation of shoreline [50–54] and nearshore bathymetry [55–58], but the potential of optical satellite remote sensing in the research of nearshore sandbars remains unemployed with only a few existing studies [59–63]. While such delay could be explained by poor spatiotemporal and spectral resolution of predecessors of current Earth observation satellites, present-day sensors produce higher spatial and spectral resolution imagery with a temporal frequency of days. It is a low-cost/free alternative to state-of-art methods for the evaluation of sandbar morphology, cross-shore and longshore movement with no need for data acquisition and instruments. However, the capabilities of optical satellite remote sensing to detect nearshore sandbars are limited to imagery with relatively clear water, clear sky and low wave energy periods with no breaking waves.

Previously, attempts were made to detect single and multiple nearshore sandbar systems in medium and high-resolution satellite imagery. In most cases, sandbar morphology was extracted manually to assess morphodynamic evolution of rhythmic sandbar system [59] and evaluate migration rates of multiple [60] and single [61] sandbar systems in interannual and decadal time scales. Manual sandbar crest extraction might be satisfactory for the local level case studies, but it is a too time-intensive task for larger coastal regions. Recently, Tátui and Constantin [62] suggested an automated algorithm for sandbar crest extraction in multispectral images based on finding peaks in cross-shore profiles extracted from multiplicated bands of the visible light spectrum. Román-Rivera, Ellis and Wang [63] proposed a semi-automated procedure to extract sandbars in very high-resolution satellite imagery using object-based classification. However, to this day, no approach based on Geo-

graphic Information System (GIS) and dealing with nearshore sandbars in multispectral satellite imagery has been suggested.

In this study, we present a fully automated GIS-based algorithm for the extraction of sandbar morphological characteristics in the imagery of PlanetScope and RapidEye sensors. To demonstrate the capabilities of the proposed methodology, a case study of sandy nearshore with a multiple sandbar system in the Curonian Spit, Baltic Sea is used.

The main contributions of the paper are: (1) a multi-step GIS workflow for multispectral satellite data processing dedicated to deriving nearshore morphology, including sandbars and their crestlines; (2) visual and quantitative assessment of satellite-derived sandbar data accuracy using *in situ* bathymetric dataset; (3) a discussion on strengths, limitations and applicability of the proposed algorithm and satellite-derived sandbar data with the addition of the promising performance of the proposed algorithm in application to Sentinel-2 MSI and Landsat-8 OLI imagery.

2. Materials and Methods

2.1. Study Area

The proposed algorithm has been tested in a sandy barrier—the Curonian Spit—separating Curonian Lagoon from the south-eastern Baltic Sea (Figure 1). The Curonian Spit politically is divided between Lithuania (51 km) and Russia (47 km); the Lithuanian part, stretching in the northeast from Nida settlement to Klaipėda port jetty, has been considered in this study. The coast of the Curonian Spit is a non-tidal (tidal range < 0.05 m) wave-dominated environment with predominant lower than 2.0 m waves approaching from western directions (NW, SW, W). The annual mean wave height at the Lithuanian Baltic Sea coast is 0.5–1 m [64]. Wave climate has a seasonal character with the occurrence of higher waves in autumn and winter (0.76 and 0.85 m) and lower waves in spring and summer (0.56 and 0.62 m) [65]. During storms, wave height may reach 4–6 m. Wave energy flux in a year of median wave intensity is equal to 1.21 kWh/m on average and depends on seasonality, reaching its maximum in winter (2.38 kWh/m) and minimum in summer (0.68 kWh/m) [65]. The net annual longshore sediment supply is directed northward. Subaerial coast is defined by 30–80 m wide beaches, composed of fine to medium sand and bordered by up to 16 m high foredune [66].

The nearshore is characterized by a gentle slope ($\tan\beta = 0.009\text{--}0.015$, up to 8 m water depth) with a multiple sandbar system consisting of 2–5 bars. The increasing number of sandbars and decreasing sandbar volume describe the variability of nearshore morphology from the southern to the northern end of the Curonian Spit. The sandbar zone with 10–400 m wide sandbars stretch from 250 to 750 m offshore. Sandbar crests rise 0.15–4.9 m above the trough in up to 5.6 m water depth over them. The sandbar system exhibits various morphologies from longshore straight to crescentic and shore-attached. According to Wright and Short [67], the morphology of inner bars are from the transverse bar and rip (TBR) to rhythmic bar and beach (RBB) and longshore bar and trough (LBT) states; outer bar morphology usually corresponds to longshore bar and trough (LBT) or dissipative (D) states. Complex sandbar morphologies complicate automated sandbar crest extraction in remote sensing images but also make the study area a suitable polygon to design and examine such an algorithm.

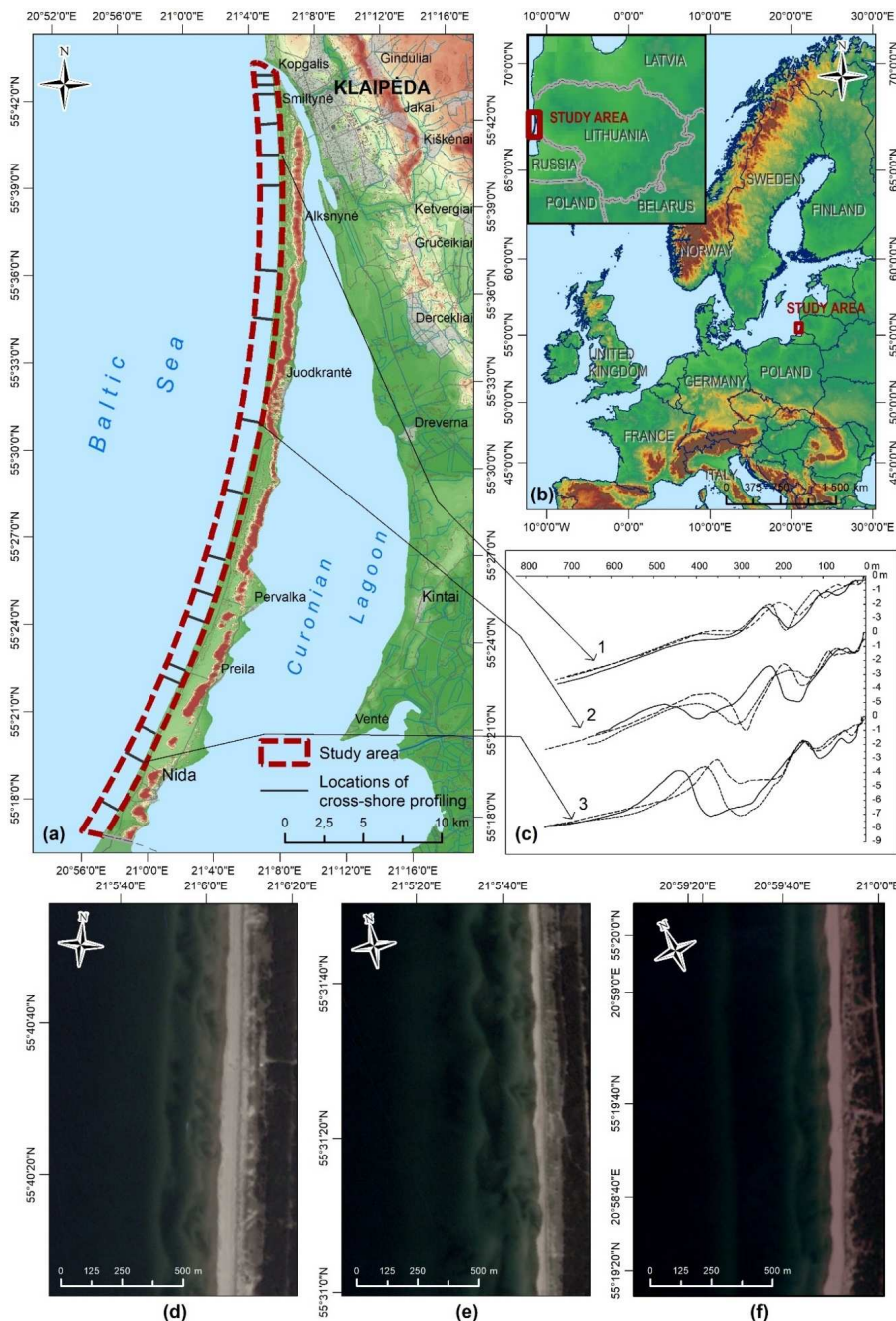


Figure 1. Study area: (a) a configuration of the study area and locations of nearshore cross-shore profiling used for algorithm validation; (b) the situation of the study area; (c) examples of nearshore cross-shore profiles at three different locations in the Curonian Spit; (d,e) examples of PlanetScope and RapidEye (f) imagery at the same locations as examples of cross-shore profiles (profile 1 corresponds to (d); 2-(e), 3-(f)).

2.2. Satellite Data

Multispectral imagery of PlanetScope and RapidEye sensors, provided by Planet Labs Inc. under the Education and Research program [68], were used in this study.

RapidEye satellite system is a constellation of five identical five-band multispectral sensors (Table 1), operated in 2009–2020. PlanetScope satellite system is a constellation, also known as the Dove satellite constellation, launched in 2017. It comprises multiple launches of groups of individual CubeSat satellites (total approx.130 satellites) with multispectral four-band sensors daily acquiring data of the entire Earth land surface. The wavelength of PlanetScope bands varies depending on satellite generation (Table 1). In this study, RapidEye Level 3A and PlanetScope Level 3B data products (Table 1), both radiometrically corrected and orthorectified with Ground Control Points (GCPs) and elevation model (DEM) to <10 m RMSE positional accuracy, were analysed. RapidEye Level 3A products are distributed as constant $25 \times 25 \text{ km}^2$ grid tiles. PlanetScope satellites collect imagery as overlapping framed scenes of size equal to $25 \times 11.5 \text{ km}^2$ or $25 \times 23 \text{ km}^2$, and scenes are not organized into a constant tiling grid system [69].

Table 1. Specifications of the RapidEye and PlanetScope sensors and products used in this study.

Constellation	Sensor Type	Revisit Time	Spatial Resolution	Wavelength Range (nm)	Utilized Product	Pixel Value
PlanetScope	four-band frame imager	daily	3 m	Blue: 455–515 ¹ (464–517) ² Green: 500–590 ¹ (547–585) ² Red: 590–670 ¹ (650–682) ² NIR: 780–860 ¹ (846–888) ²	PlanetScope Analytic Ortho Scene Product (Level 3B)	Surface reflectance
RapidEye	push-broom	5.5 days	5 m	Blue: 440–510 Green: 520–590 Red: 630–685 Red Edge: 690–730 NIR: 760–850	RapidEye Analytic Ortho Tile Product (Level 3A)	Surface reflectance

¹ first-generation satellites; ² second-generation satellites, launched starting in November 2018.

Both PlanetScope and RapidEye images were visually inspected, and only dates satisfying three criteria were selected. Criteria include cloud cover up to 20%, relatively clear water (sandbars are visible), no visible wave breaking over sandbars. Mean significant wave height on dates when selected images were acquired was 0–0.65 m (0.27 m on average), on dates used for algorithm validation between 0.07 and 0.4 m.

2.3. In Situ Data

Data of bathymetric surveys conducted with DualBeam Humminbird Helix 9 SI GPS echo-sounder, mounted on a shallow draft motor vessel, were used to validate sandbar crest position derived from satellite images. During surveys, dual beams of 200 kHz/20° and 83 kHz/60° were used. The echo-sounder blends returns from both frequency beams by starting with 83 kHz wide beam return (secondary source), dimming it, and then overlaying it with the 200 kHz narrow beam return (primary source). Echosounder has an integrated GPS/WAAS receiver, providing fast position fixes accurate within 2.5 m. Measurements were vertically corrected for water level fluctuation using data acquired with GNSS Topcon HiPer SR.

Bathymetric surveys are a result of cross-shore profiling along the Curonian Spit nearshore at 17 different locations with a spacing of 1–5 km (Figure 1). Surveys were performed in spring and autumn under low wave energy. Sandbar crests at six dates with 1–6 days difference between a bathymetric survey and image acquisition were compared with PlanetScope-derived crests and at four dates with 1–4 days difference with RapidEye-derived crests (Table 2).

Table 2. The dates of PlanetScope and RapidEye images used for sandbar crest extraction compared with the dates of bathymetric surveys used for accuracy evaluation of satellite-derived crest positions.

Constellation	Date of Image Acquisition	Date of Bathymetric Survey
PlanetScope	29 September 2017	29–30 September 2017
PlanetScope	16 May 2018	16 May 2018
PlanetScope	11 October 2018	12 October 2018
PlanetScope	22 May 2019	18–19 May 2019
PlanetScope	26 September 2019	26–27 September 2019
PlanetScope	26 June 2020	20 June 2020
RapidEye	1 October 2017	29–30 September 2017
RapidEye	20 May 2018	16 May 2018
RapidEye	15 October 2018	12 October 2018
RapidEye	22 May 2019	18–19 May 2019

2.4. Data Pre-Processing

Multiple scenes of analysed sensors cover the study area (RapidEye—4 scenes; PlanetScope—variable number of scenes). Scenes were composed into mosaics covering all of the study area prior to further processing and analysis. PlanetScope multi-band mosaics were resampled to 5 m/pixel spatial resolution using bilinear interpolation to eliminate the difference between PlanetScope and RapidEye sensors. Enhanced Lee filter with the kernel of 3x3 pixels (Section 2.5) was applied to RapidEye mosaics prior to processing to reduce noise-induced distortions.

2.5. Spatial Filtering

The quality of PlanetScope and RapidEye images used in this study suffers from low signal-to-noise ratios compared to other optical sensors [70–74]. By distorting the original signal, noise complicates the process of sandbar extraction and causes sandbar fragmentation during the procedure. To solve this problem, spatial filtering techniques—adaptive median, enhanced Lee, Kuan and Gaussian filters—applied at different stages of the sandbar extraction procedure are presented.

In this study, a modified version of the adaptive median filter suggested by Li and Fan [75] was applied (Figure 2). Filter reduces the variance of intensities in the image by replacing pixel value with a median value within the defined window surrounding the processing pixel. The window surrounding each pixel is variable, and it is determined whether the pixel is noisy in a current window prior to changing its value.

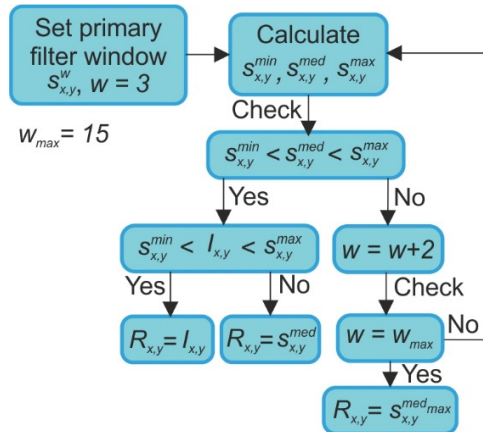


Figure 2. An adaptive median filter by Li and Fan [75]. $S_{x,y}^{min}$, $S_{x,y}^{med}$ and $S_{x,y}^{max}$ denote, minimum, median and maximum values of the pixel in the filter window $S_{x,y}^w$ centered at (x, y) with a window of size w ; w_{max} —maximum filter window; $I_{x,y}$ —primary value of pixel; $R_{x,y}$ —value of filtered pixel; $S_{x,y}^{med_{max}}$ —median value within w_{max} . Primary filter window w is set to 3×3 pixels and w_{max} to 15×15 . If it is determined that the pixel is not contaminated with noise within the 3×3 window, the primary pixel value is preserved. If the pixel is contaminated with noise, the filtering window is increased by 2 pixels. The procedure is repeated until the maximum window is reached.

The Enhanced Lee filter—introduced by [76] as an improvement of Lee filter [77] categorizes pixels into three classes: homogenous, heterogeneous and point target [76]. The distinction of classes relies on the image variation C_i , noise variation C_u and maximum noise variation C_{max} coefficients. In image $I_{x,y}$, the signal $R_{x,y}$ is expressed as in Equation (1):

$$R_{x,y} = \begin{cases} \overline{I_{x,y}}, & \text{for } C_i \leq C_u \\ I_{x,y} \times W_{x,y} + I_{x,y} \times (1 - W_{x,y}), & \text{for } C_u < C_i < C_{max} \\ I_{x,y}, & \text{for } C_i \geq C_{max} \end{cases} \quad (1)$$

where $W_{x,y}$ is weighting function.

The Kuan filter is an adaptive filter for speckle noise reduction introduced by Kuan et al. [78]. In the Kuan filter, a multiplicative model is transformed to a signal-dependent additive noise model and the pixel value is smoothed using an estimate from the local mean, variance and standard deviation (Equation (2)):

$$R_{x,y} = I_{x,y} \times W_{x,y} + I_{x,y} \times (1 - W_{x,y}) \quad (2)$$

where $W_{x,y}$ is weighting function.

Although the Enhanced Lee and Kuan filtering techniques are typically utilized to despeckle radar images, optical images used in this study portray a granular appearance different in nature but visually similar to multiplicative speckle radar noise, and local statistics filters effectively reduce such graininess and image fragmentation caused by it.

The Gaussian filter is a low-pass convolution filter, where an image $I_{x,y}$ is multiplicatively convolved by convolution matrix (kernel) K, which is a discrete approximation of the Gaussian function. In this study, a kernel of 5×5 pixels was used as in Equation (3).

$$K = \frac{1}{256} \begin{bmatrix} 1 & 4 & 6 & 4 & 1 \\ 4 & 16 & 24 & 16 & 4 \\ 6 & 24 & 36 & 24 & 6 \\ 4 & 16 & 24 & 16 & 4 \\ 1 & 4 & 6 & 4 & 1 \end{bmatrix} \quad (3)$$

2.6. Algorithm for Sandbar and Sandbar Crest Extraction

The proposed algorithm is divided into four stages of data processing and analysis. First, a shoreline is extracted, and a land-sea mask is created to discriminate the subaqueous domain with nearshore sandbars from the subaerial domain (the detailed procedure is discussed in Section 2.6.1). Second, multiple calculations are performed in the subaqueous domain to generate raster, representing nearshore bottom morphology, where sandbars and their crestlines might be identified easily (Section 2.6.2). Then, in a generated raster, boundaries of nearshore sandbars are defined, and sandbars are extracted (Section 2.6.3). Finally, sandbar crestlines are derived within previously defined boundaries (Section 2.6.4).

The algorithm was implemented in a GIS environment (ArcGIS Desktop 10.7). Maximum value pixels per transect was extracted via a script written in the R programming language. The script was made available as a tool in ArcGIS via an R-ArcGIS bridge.

2.6.1. Land-Sea Masking and Shoreline Extraction

The land-sea masking procedure is based on spectral differences between water and land in infrared bands where water absorbs most of the radiation. Many spectral indices for water retrieval have been introduced based on this reflective property [51,79–81]. Most of them are combinations of the visible light spectrum and near-infrared (NIR) or short-wave infrared (SWIR) wavelengths. Because PlanetScope and RapidEye sensors contain a limited number of bands with only near-infrared outside visible light spectrum, Normalized Difference Water Index (NDWI) [79] (requiring only green and near-infrared reflectance) was employed in water and land separation procedure. It was calculated using Equations (4) and (5) for PlanetScope and RapidEye sensors, respectively.

$$NDWI_{\text{PlanetScope}} = \frac{SR_2 - SR_4}{SR_2 + SR_4} \quad (4)$$

where SR_2 and SR_4 correspond to the surface reflectance of the green and near-infrared bands of the PlanetScope sensor.

$$NDWI_{\text{RapidEye}} = \frac{SR_2 - SR_5}{SR_2 + SR_5} \quad (5)$$

where SR_2 and SR_5 correspond to the surface reflectance of the green and near-infrared bands of the RapidEye sensor.

NDWI was designed with a 0 threshold to distinguish water and land, but this value varies depending on sensor and image properties. Although several methods have been tested for binarization of NDWI images (0 thresholding, Otsu thresholding), The Iterative Selforganizing Data Analysis Techniques Algorithm (ISODATA) was chosen to derive land-sea masks and delineate shoreline. NDWI and near-infrared band images were used as inputs for ISODATA unsupervised classification. Employing both NDWI and near-infrared band images gave more stable results in most instances compared to NDWI alone. The main steps of the land-sea masking and shoreline delineation procedure are shown in Figure 3.



Figure 3. A flowchart of the land-sea masking and shoreline derivation procedure used in this study.

2.6.2. Generation of Inputs for Sandbar and Sandbar Crest Extraction

In bands of the visible light spectrum, brighter pixels with larger reflectance values represent shallower underwater features. Therefore, surface reflectance values might be considered relatively representative of the bathymetric position. In geomorphology, a topographic position might be described by topographic indices, which compare the elevation of central pixel to elevations within the local neighbourhood, defined by window size [82]. These metrics are typically used for landform classification [83–86], but they deal with the same issue as this study—distinguishing positive landforms from negative or sandbars from troughs. The most applied metric of local topographic position is the Topographic Position Index (TPI), in marine geomorphology referred to as the Bathymetric Position Index (BPI) [87]. It is a signed unbounded absolute metric comparing the elevation of the central pixel with a mean elevation in a local neighbourhood. Similarly, the Relative Topographic Position Index (RTPI), which links central elevation with mean, minimum and maximum values within the local neighbourhood, was introduced. It is a signed metric accounting for elevation distribution, bounded by the interval (−1,1). As this paper deals with subaqueous features, it will be further referred to as the Relative Bathymetric Position Index (RBPI).

Both the BPI and the RBPI have been examined in this study. As surface reflectance decreases with increasing water depth and distance offshore, inner sandbars are represented by higher surface reflectance values than outer sandbars despite their height. Using an absolute metric as the BPI results in sinking outer sandbars because of a smaller difference between values in the local neighbourhood. Using a relative metric as the RBPI, which considers minimum and maximum values in the local neighbourhood, reduces distortions caused by water depth over sandbar crest and results in a better representation of nearshore morphology. Hence, the RBPI was chosen for further analysis. It was calculated separately for blue, green and red bands of PlanetScope and RapidEye imagery, using Equation (6) (based on Newman, Lindsay and Cockburn [82]).

$$RBPI = \begin{cases} \frac{SR - SR_{mean}}{SR_{mean} - SR_{min}} & \text{if } SR < SR_{mean} \\ \frac{SR - SR_{mean}}{SR_{max} - SR_{mean}} & \text{if } SR > SR_{mean} \end{cases} \quad (6)$$

where SR denotes surface reflectance of the processing pixel and SR_{mean} , SR_{min} and SR_{max} denote mean, minimum and maximum surface reflectance values in the local neighbourhood, respectively.

The RBPI depends on the size of the local neighbourhood. Choice of the window size determines the scale at which underwater landforms is distinguished: using small-sized window results in a detailed picture of smallest-scale underwater features and fragmented large-scale landforms (Figure 4b); large-sized window results in distinguished large-scale underwater landforms with small-scale features merged into the whole (Figure 4e). In multiple nearshore sandbar systems, spacing and scale of submerged sandbars increase in the offshore direction [5,35,88]. Therefore, the optimal size of the local neighbourhood for inner and outer sandbars diverges. To save all the information about inner and outer sandbars multiscale approach for RBPI calculation is implemented. The routine of this approach is presented below and in Figure 5.

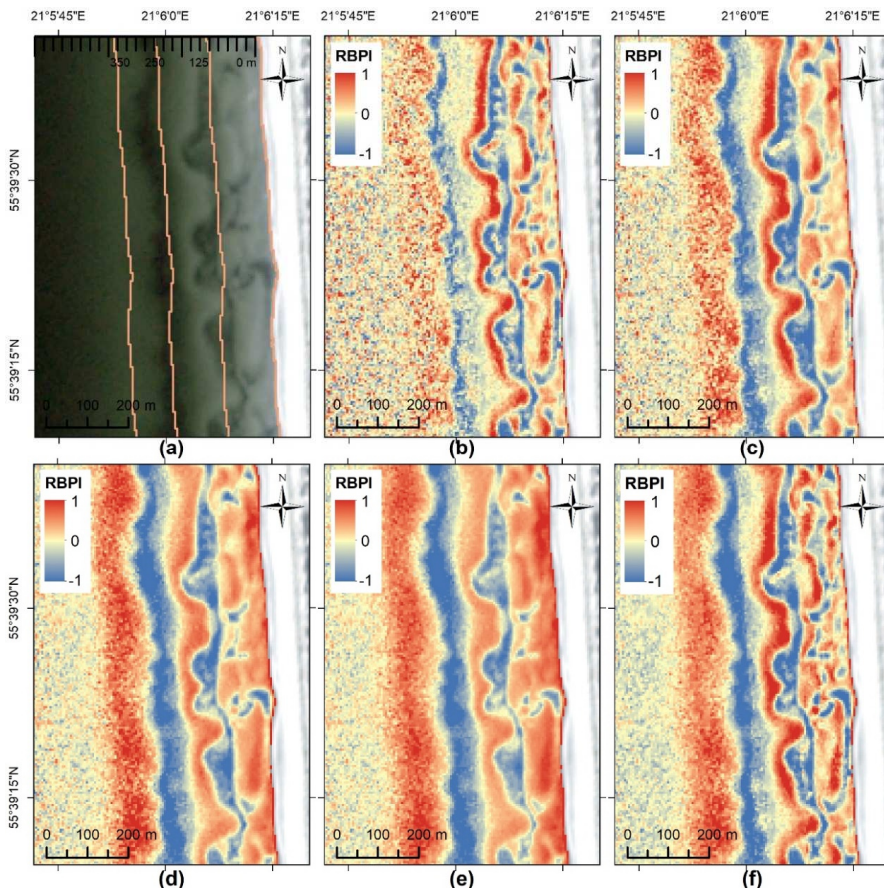


Figure 4. The Relative Bathymetric Position Index (RBPI) dependence on local neighbourhood size and multiscale approach solution: (a) nearshore cross-shore-distance-based sectors used in this study; (b–e) the mean RBPI in different size local neighbourhoods ((b) circle 3, 5, 7, 9; (c) circle 9, 11, 15; (d) circle 15, 19, 23, 31; (e) circle 23, 31, 39; (f) multiscale RBPI with the combination of (b–e) neighbourhoods in nearshore cross-shore-distance-based sectors.

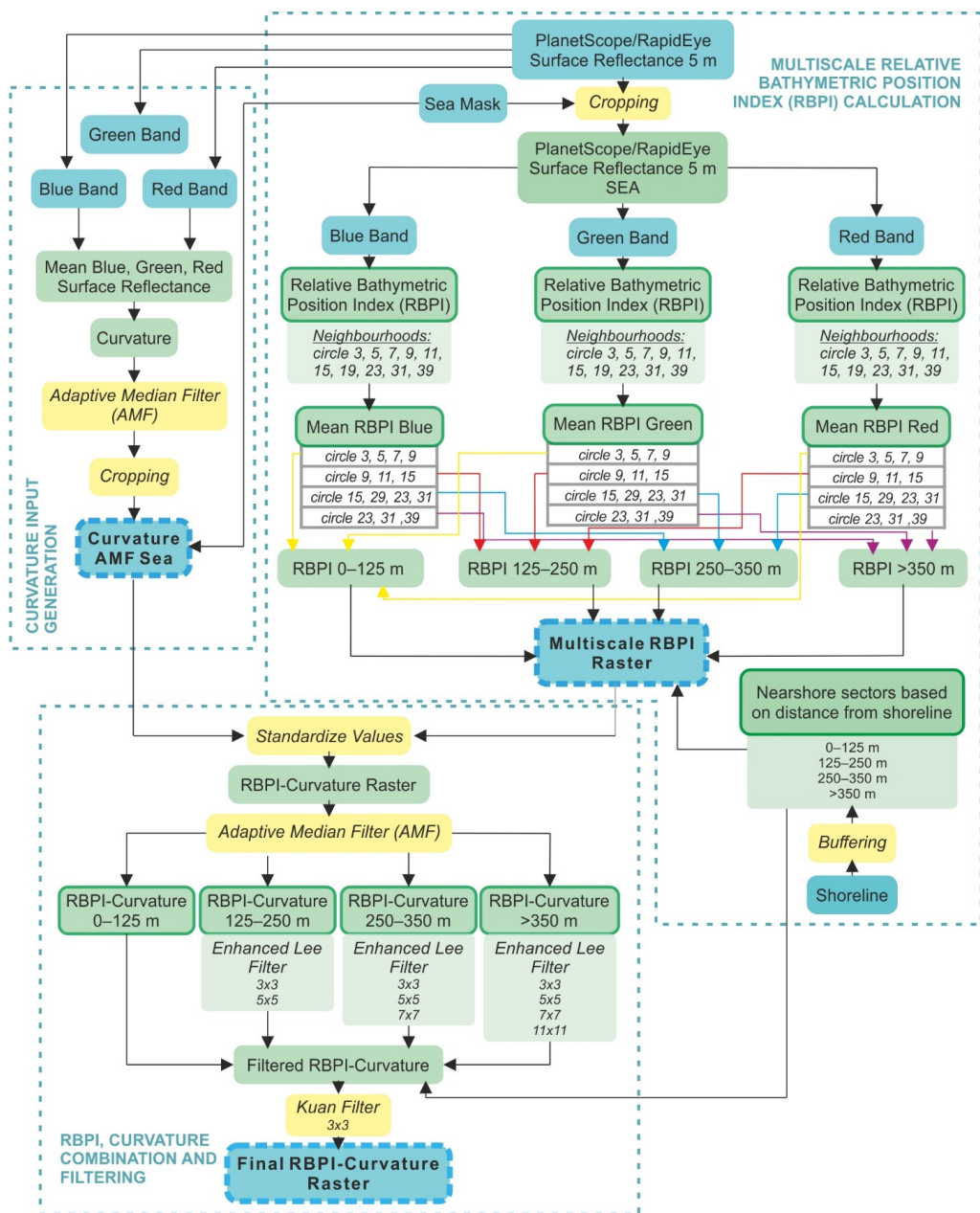


Figure 5. A flowchart of the generation of input for sandbar extraction: first, the multiscale Relative Bathymetric Position Index (RBPI) is computed, and the curvature output is created. Then, the multiscale RBPI and curvature outputs are combined and filtered with different size kernels based on nearshore cross-shore sectors for the final RBPI-Curvature raster creation. Numbers by the neighbourhoods/kernels are in pixels.

Procedure for the multiscale RBPI computation:

1. Nearshore zone is divided into fixed cross-shore sectors based on offshore distance (Figure 4a). The width and number of the cross-shore sectors are defined by prevailing features of the sandbar system in the study area.
2. RBPI values with 10 circle local neighbourhoods (Figure 5) are calculated for visible light bands. The motive for the choice of a circle neighbourhood instead of the traditional square was a continuous and smooth nature of nearshore sandbar shape.
3. The mean of RBPI values in local neighbourhoods of multiple sizes was calculated for each sector in each band of the visible light spectrum: from the mean of 3 smallest neighbourhoods for the sector closest to the shoreline to the mean of 3 largest neighbourhoods for the sector furthest offshore (Figure 5). Other measures of descriptive statistics have been tested, and the maximum value was considered instead of the mean, but it resulted in random noise generation.
4. Mean RBPI values in local neighbourhoods of multiple sizes for nearshore zone sectors in blue, green and red bands are summed using weighting coefficients. The selection of weighting coefficients was mainly governed by the penetrating capabilities of blue, green and red light and the quality of band images. In coastal waters, green light penetrates the water column the deepest [89], and the sandbar system is visible most sharply in its image. In contrast, longer red wavelengths are quickly absorbed by water, and only inner-middle sandbars are completely visible in their images, whereas the outer sandbar is often obscure. Blue wavelengths penetrate the water column deeper than red, but their images contain significant distortions caused by noise in both PlanetScope and RapidEye mosaics. Therefore, the largest coefficient of 0.6–0.8 was given to the green band; a coefficient of 0.1–0.3 was given to the red band; 0.1-to the blue band. The proportion of coefficients for green and red bands was differentiated based on nearshore cross-shore sectors: as distance offshore increases, the coefficient for green band increases. Final RBPI values for nearshore cross-shore sectors are calculated as in Equation (7):

$$\left\{ \begin{array}{ll} 0.1 \times \mu_{RBPIBlue} + 0.6 \times \mu_{RBPIGreen} + 0.3 \times \mu_{RBPIRed} & \text{if } D_{off} < 250 \text{ m} \\ 0.1 \times \mu_{RBPIBlue} + 0.7 \times \mu_{RBPIGreen} + 0.2 \times \mu_{RBPIRed} & \text{if } 250 \text{ m} < D_{off} < 350 \text{ m} \\ 0.1 \times \mu_{RBPIBlue} + 0.8 \times \mu_{RBPIGreen} + 0.1 \times \mu_{RBPIRed} & \text{if } D_{off} > 350 \text{ m} \end{array} \right. \quad (7)$$

where μ_{Blue} , μ_{Green} and μ_{Red} denote mean RBPI values in multiple sizes local neighbourhoods for blue, green and red bands of PlanetScope and RapidEye imagery, and D_{off} denotes the distance from the shoreline. The result is saved as a *multiscale RBPI Raster* (Figure 6b).

The multiscale RBPI is calculated only for the underwater part of an image. When there is no shore-attached sandbar, a step or a slight slope is a typical characteristic of foreshore. The upper slope of the foreshore is characterized by higher surface reflectance values than the lower one. When RBPI is calculated, it might be misclassified as a positive landform (sandbar). To solve this issue, the multiscale RBPI Raster is combined with a second-order derivative raster, which represents surface curvature (convexity and concavity). In the Curvature raster, the foreshore is a convex surface, and in combination with multiscale RBPI Raster, the Curvature raster submerges the misleadingly elevated upper slope of the beach face. The routine of Curvature generation and combination with the multiscale RBPI is described below and in Figure 5.

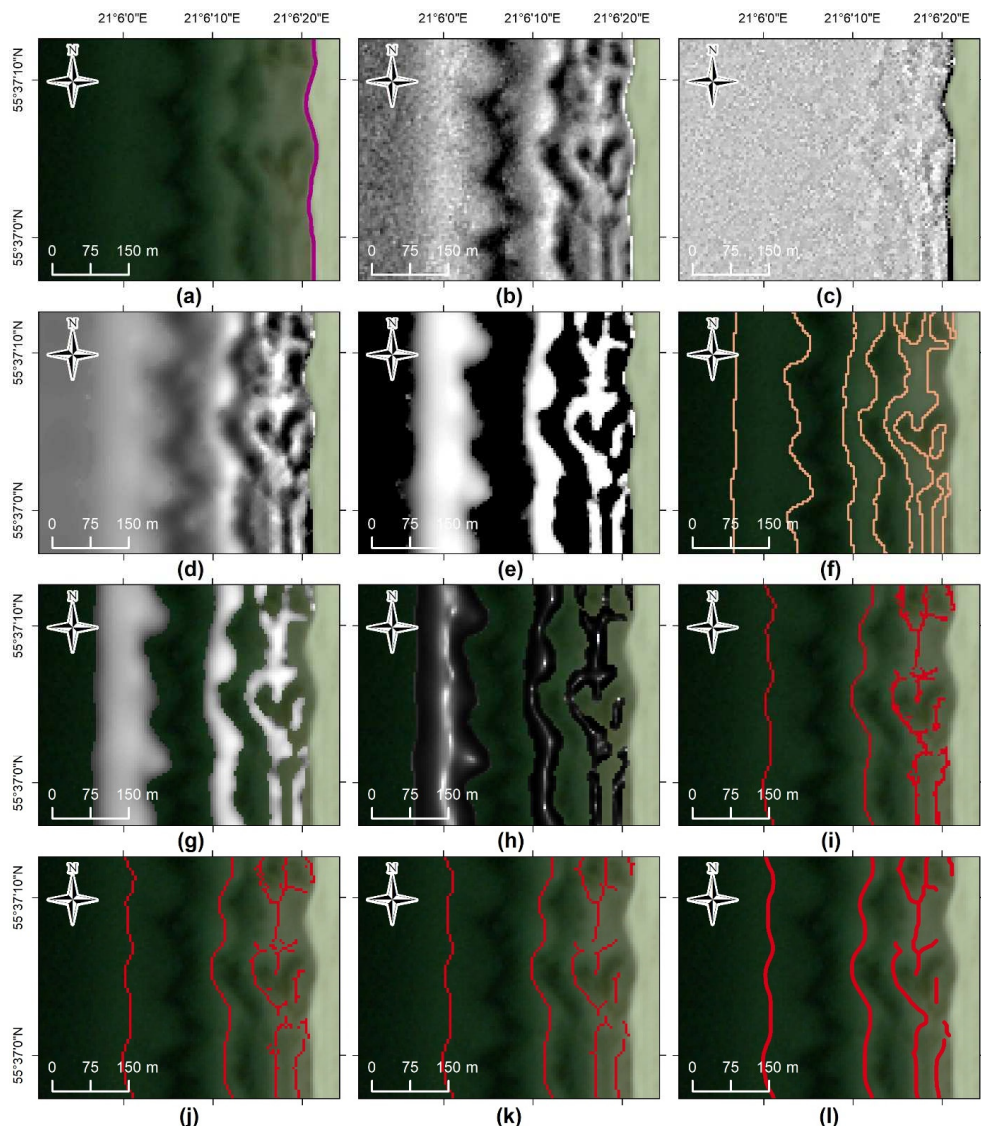


Figure 6. Examples of outputs at different stages of the proposed algorithm for PlanetScope imagery: (a) shoreline extracted after land-sea masking procedure; (b) multiscale RBPI Raster; (c) Curvature Raster; (d) Final RBPI-Curvature Raster; (e) Rescaled RBPI-Curvature Raster; (f) Bar Mask; (g) Final Bar Raster; (h) Bar-Slope Raster; (i) Primary Bar Crest Raster; (j) Secondary Bar Crest Raster; (k) Final Bar Crest Raster; (l) Final Bar Crest Polyline.

The multiscale RBPI and Curvature combination procedure:

1. The mean surface reflectance value for blue, green and red bands is calculated.
2. Mean surface reflectance raster of blue, green and red bands is used as an input for the second-order derivative (further curvature) calculation.
3. Curvature raster is clipped to the submerged part only and filtered with an adaptive median filter (Section 2.5). It reduces random multiplicative noise in curvature images

without oversmoothing of data. The result is saved as Curvature AMF Sea Raster (Figure 6c).

4. Values of the Curvature AMF Sea and multiscale RBPI rasters are standardized and summed as in Equation (8):

$$\text{RBPI}_{\text{stand}} + 0.3 \times \text{Curvature}_{\text{stand}} \quad (8)$$

where $\text{RBPI}_{\text{stand}}$ and $\text{Curvature}_{\text{stand}}$ denote standardized values of the multiscale RBPI and Curvature AMF Sea rasters, respectively. Combined multiscale RBPI and Curvature rasters are saved as the RBPI-Curvature raster.

Noise-induced segmentation and cross-shore differences in scale and distinctiveness of sandbars define the need to apply smoothing of different intensities to RBPI-Curvature raster in previously distinguished nearshore cross-shore sectors. To accomplish this, an Enhanced Lee filter (Section 2.5) with multiple window sizes (3×3 ; 5×5 ; 7×7 ; 11×11) is applied (Figure 5). At first, random multiplicative noise is reduced in the RBPI-Curvature raster with an adaptive median filter (Section 2.5), then an Enhanced Lee filter with 3×3 window is applied to the RBPI-Curvature raster after adaptive median filtering; 5×5 Enhanced Lee filter is applied to raster after 3×3 filtering, 7×7 after 5×5 and 11×11 after 7×7 to obtain rasters with increasing level of smoothing. As the offshore distance increases, the output of filtered RBPI-Curvature raster with a greater degree of smoothing is assigned to cross-shore distance-based nearshore sectors and combined into a single output (Figure 5). Finally, differences at edges of combined outputs are smoothed with Kuan filter (Section 2.5) with a 3×3 window. It was chosen because the Kuan filter does not categorize pixels as the Enhanced Lee filter (which better preserves edge sharpness) and gives the result with more naturally smoothed edges. The result after the filtering procedure is furthered referred to as Final RBPI-Curvature raster (Figure 6d).

To sink non-bar regions and to expose sandbars Final RBPI-Curvature raster is rescaled to scale from 1 to 1000 with MSLarge transformation function (Figure 7). MSLarge function brings out large values based on the mean and standard deviation of data. After transformation, deeper non-sandbar nearshore regions remain only as background with the same value, and higher regions of the nearshore bottom with sandbars preserve all range of values (non – sandbar region = 1; $1 < \text{sandbar region} \leq 1000$). Rescaled RBPI-Curvature raster values are converted to an integer, and a Majority filter with an 8-pixel neighbourhood is applied to remove the remaining small regions with a few isolated pixels to get a cleaner result. In this instance, if Rescaled RBPI-Curvature raster has remaining isolated pixels, they are replaced with background value because the majority filter replaces pixel value with mode if 5 out of 8 contiguous pixels have the same value. Rescaled RBPI-Curvature raster (Figure 6e) is the final output for the extraction of nearshore sandbars.

2.6.3. Extraction of Nearshore Sandbars

A rescaled RBPI-Curvature raster is used as an input for nearshore sandbar extraction. It is classified into two classes—sandbar and non-sandbar regions—with ISODATA unsupervised clustering. Classified raster is filtered with majority filter twice to remove remaining isolated pixels and to get a cleaner boundary of sandbars, and then the class with non-sandbar regions is set to no-data, and an integer raster with sandbars only is generated. It has remaining misclassified areas mostly outside the sandbar zone where surface reflectance values in the primary image were uneven due to noise signal, thin clouds, haze and heterogeneity of water surface. To remove misclassified regions, the sandbar raster is converted to a vector polygon layer, which is cleaned using selection operations with defined criteria based on the typical distance from the shoreline D_{off} and size of sandbars A in the study area. The details of the criteria are described below and in Figure 7.

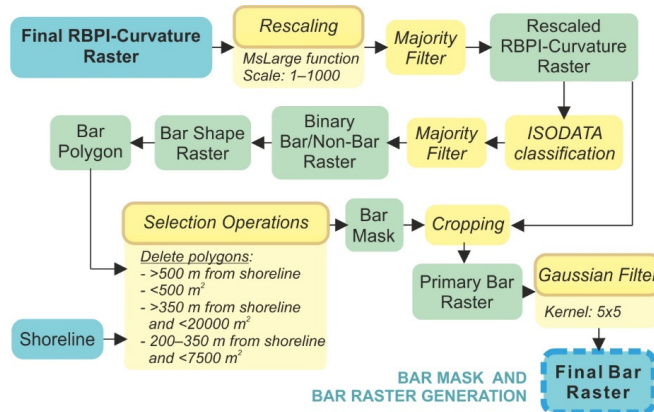


Figure 7. A flowchart of the sandbar extraction procedure.

The criteria to eliminate non-sandbar regions misclassified as sandbars:

1. $D_{off} > 500$ m (typically, the inner boundary of outer sandbars is within 500 m from the shoreline at least at one of its segments in the Curonian Spit)
2. $A < 500$ m^2
3. $D_{off} > 350$ m and $A < 20,000$ m^2
4. $200 < D_{off} < 350$ m and $A < 7500$ m^2 .

If a polygon satisfies at least one criterion, it is deleted as a non-sandbar. All remaining polygons are considered as sandbars and are saved as Bar Mask (Figure 6f). The rescaled RBPI-Curvature raster is clipped with Bar Mask and saved as Primary Bar Raster.

To smooth the Primary Bar Raster and to ensure the continuity of sandbar crests after the extraction Gaussian filter with a 5×5 kernel (Section 2.5) is applied. The result is saved as Final Bar Raster (Figure 6g). Additionally, the Slope was calculated for the Final Bar Raster, then inverted and saved as Bar-Slope Raster. The Slope is calculated as the maximum change in value over the distance between a pixel and its eight neighbours. It was not employed in further process, but it provides an output of extracted sandbars with clearly visible crestline (Figure 6h).

2.6.4. Extraction of Nearshore Sandbar Crests

Complex sandbar morphologies (crescentic shapes, rhythmic patterns, etc.) determines that sandbar crestlines might exhibit variable shapes and orientation relative to the shoreline: parallel, oblique or transverse. The typical approach to detect longshore sandbar crest locations with shoreline-perpendicular transects (e.g., [62]) might not identify all the variability of sandbar crestline shapes leading to undetected or incorrectly delineated crests that are not parallel to the shoreline. For better detection of sinuous crestlines, they are located in three directions: perpendicular to the shoreline and oblique to the shoreline (at 45° – 225° and 135° – 315° angles). Because the main shoreline direction in the study area is orientated from south to north, these directions correspond to West-East (W-E), North East–South West (NE-SW) and North West–South East (NW-SE) orientations.

In the crestline delineation procedure, maximum value pixels within local neighbourhoods defined by the rowing window in the Final Bar raster are considered as crests. Three local neighbourhoods, which represent perpendicular and oblique directions, are utilized (Figure 8):

1. A local neighbourhood with 5 pixels (25 m) orientated in the W-E direction;
2. An irregular local neighbourhood with 7 pixels (35 m) in the NE-SW direction (35 m in an oblique direction is equivalent to 25 m in a perpendicular direction of the same 25×25 m square neighbourhood);

3. An irregular local neighbourhood with 7 pixels (35 m) in the NW–SE direction.

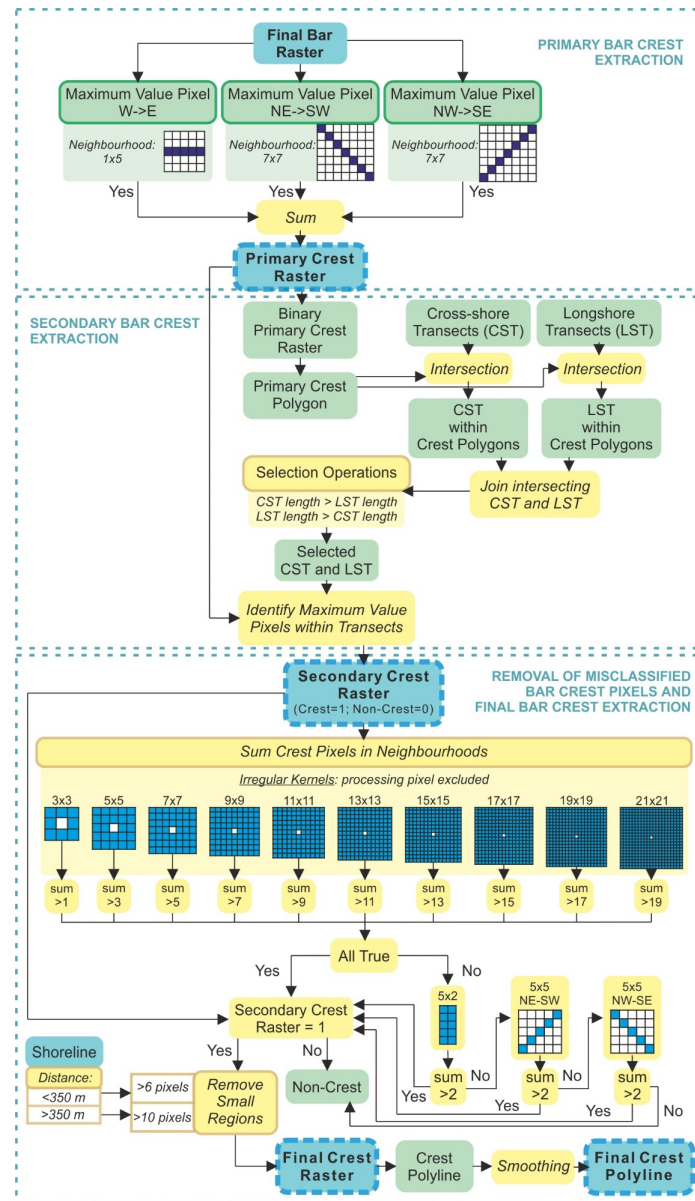


Figure 8. A flowchart of the sandbar crest extraction procedure: at first, the primary crest as maximum value pixels within three kernels are identified, then secondary crest with cross-shore/longshore transects is extracted, and the final bar crest is obtained after cleaning procedure with proximity-based filter.

If it is indicated that pixel value is equal to maximum within W–E, NE–SW, or NW–SE neighbourhood, it is considered as crest candidate. Identified maximum pixel values

within all three neighbourhoods are summed. Here, if the same pixel has maximum value within multiple neighbourhoods, it will be attributed with a higher value than pixels with maximum value within one neighbourhood. Raster with summed maximum pixel values within W–E, NE–SW and NW–SE directed neighbourhoods is considered the Primary Crest Raster (Figure 6i).

If maximum value pixels do not match within all local neighbourhoods, a crest wider than one pixel is generated in the Primary Crest Raster. To narrow crestlines to one pixel-wide maximum value pixels, secondary crests within crests candidate pixels in the Primary Crest Raster are determined using cross-shore (CST) and longshore (LST) transects. The procedure of secondary crest extraction is described below and in Figure 8.

The procedure for secondary crest extraction:

1. Primary Crest Raster is binarized and converted to polygon layer (Primary Crest Polygon).
2. Cross-shore (CST) and longshore (LST) transects with spacing equal to satellite image resolution (5 m) are created and intersected with Primary Crest Polygon.
3. Intersecting CST and LST within primary crest polygons are joined based on their spatial relationship.
4. Lengths (d) of pairs of intersecting CST (d_{CST}) and LST (d_{LST}) are compared: if $d_{CST} > d_{LST}$, it is considered that the main sandbar crest direction is orientated parallel to the shoreline, and CST is selected; if $d_{CST} < d_{LST}$, the main sandbar crest direction is orientated perpendicular to the shoreline, and LST is selected; if $d_{CST} = d_{LST}$, CST is selected. Selected CST and LST are merged into one layer. CST and LST lengths are equal when crests in Primary Crest Raster are one-pixel wide (in most instances), and CST/LST selection makes no difference because, in any case, the same pixel will be the maximum value pixel.
5. Maximum value pixels within selected CST and LST transects are identified as secondary crest pixels and exported to Secondary Crest Raster (Figure 6j).

The Secondary Crest Raster has remaining non-crest pixels misclassified as crests (usually sandbar boundary pixels or other redundant pixels/pixel regions). To distinguish them from actual crests, a crest cleaning algorithm is implemented. It is based on the understanding that the sandbar extends at least tens of meters, and one or a few isolated pixels cannot represent the sandbar crestline. It means that the crest pixel must have a certain number of neighbours also identified as crests. Local neighbourhoods of increasing size with the defined requirement for the number of neighbours to be crest pixels were used as a part of the crest cleaning algorithm. The details of the routine are described below and in Figure 8.

The routine for crest cleaning:

1. Square kernels with excluded centre (processing) pixels are used to quantify the number of neighbourhood pixels. Minimal kernel size is 3×3 pixels (15×15 m), and the maximum is 21×21 (105×105 m). Every kernel is expanded by 2 pixels until the maximum is reached. Crest values in the secondary crest raster are set to 1, so that sum of values in the kernel would be equal to the number of crest neighbours (Figure 8).
2. It is determined that in a neighbourhood of 3×3 pixels, processing crest pixel must have at least 2 crest neighbours (sum > 1). It means that within 8 neighbour pixels, at least 2 must be sandbar crests. When the kernel is expanded by 2 pixels, the requirement of the sum in the neighbourhood is also increased by 2 (Figure 8). The process is repeated until the maximum kernel is reached.
3. A pixel is identified as crest only if the requirement of the sum is fulfilled in all kernels, and it was previously identified as a crest pixel (value in secondary crest raster was equal to 1).
4. A defined filter sometimes is too aggressive and removes actual crest pixels, especially those at the beginning and at the end of the crestline or when the crest is sinuous. Thus, part of filtered pixels is restored with three kernels: 5×2 pixels square; 5 pixels

NE–SW and NW–SE directed (Figure 8). If the sum within at least one of three kernels is greater than 2, the pixel is restored as a crest pixel. If the pixel does not meet the criteria in all kernels, it is removed as a non-crest pixel.

5. After filtering, small regions with aggregated pixels remain misclassified as crests. They are removed based on the number of pixels aggregated into one continuous region (R). Defined criteria are split based on distance from shoreline (D_{off}): if $D_{off} < 350$ m, $R < 6$ pixels are removed; if $D_{off} > 350$ m, $R < 10$ pixels are removed. Distance criterion is set because near the shoreline sandbar morphologies of smaller-scale form, while outer sandbar exhibits much greater extents, so aggregated regions must be larger to be considered as crests.
6. After the removal of small regions, Final Crest Raster (Figure 6k) is created.
7. The Final Crest Raster is converted to a polyline layer. Polylines are smoothed with 20 m smoothing tolerance and exported as Final Crest Polyline (Figure 6l).

3. Results

3.1. Visual Assessment of Extracted Sandbars

The proposed method has been tested with 42 RapidEye and 103 PlanetScope images acquired in 2009–2020. Extracted sandbars and their crests were visually inspected to assess the quality of results and possible shortcomings of the designed algorithm. Figure 9 shows an example of a time series with derived boundaries and crests of nearshore sandbars. Typical inter-annual characteristics of cyclic behaviour and seasonal patterns of morphological development in multiple sandbar systems are apparent here.

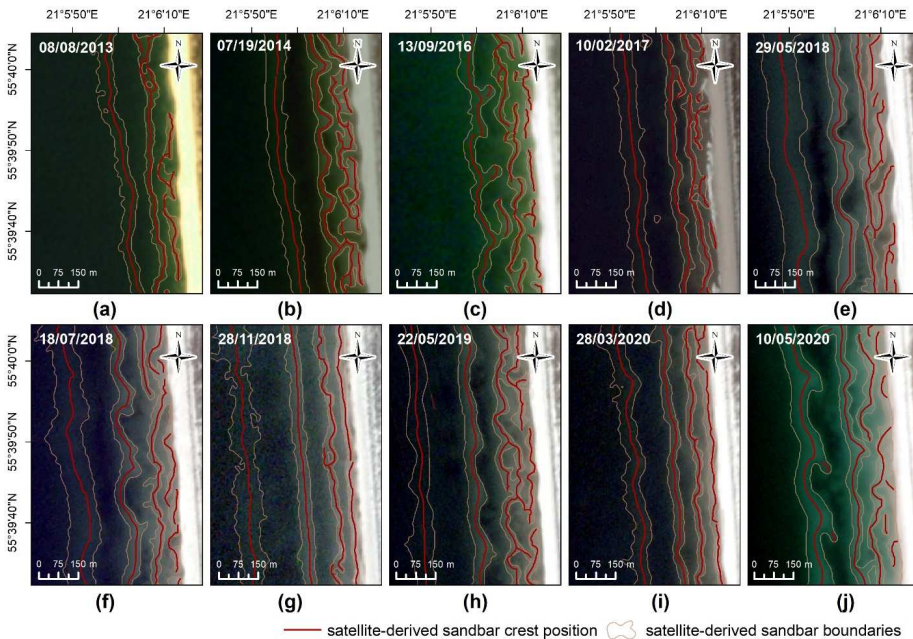


Figure 9. Time series of sandbar boundaries and crestlines delineated using the proposed algorithm in RapidEye (a–c) and PlanetScope (d–j) imagery. Typical characteristics of interannual and seasonal dynamics of multiple sandbar systems can be observed here: seaward migration (d–g) and decay (h) of the outer sandbar; fast development and seaward migration of the middle sandbar after the decay of the outer one (i,j); development of complex morphologies during the period of low wave energy (e,f,h,j) and straightening during the period of high wave energy (d,g,i).

Although the algorithm was designed for images with clear water and calm sea, the visual assessment showed that sea surface roughness caused by small waves has no significant impact on the result of satellite-derived sandbar crests. Visual observations revealed that capabilities to detect less distinctive sandbars in greater depths decrease if the transparency of the water column or atmosphere is decreased by turbulency of sediment, haze, thin clouds, or other phenomena.

3.2. Accuracy of Extracted Crestline Position

Six pairs of PlanetScope images and bathymetric surveys with 332 pairs of crest positions were compared to validate the proposed method (Figure 10a–c). PlanetScope-derived sandbar crest locations are in good agreement with in situ data: the total coefficient of determination (R^2) between measured and PlanetScope-derived sandbar crest distance from the shoreline was 0.999, ranging from 0.998 to 0.999 for individual dates. The root-mean-square error (RMSE) for all dates was 5.8 m, ranging from 4 to 9.7 m for individual dates (Figure 10b). For four out of six dates, RMSE was between 4 and 4.8 m, and only two dates showed errors larger than 5 m. The largest RMSE was for the image acquired on 26 June 2020, which had the largest time span between in situ and satellite data. Therefore, lower accuracy might be caused by changes in the sandbar system but not the algorithm itself.

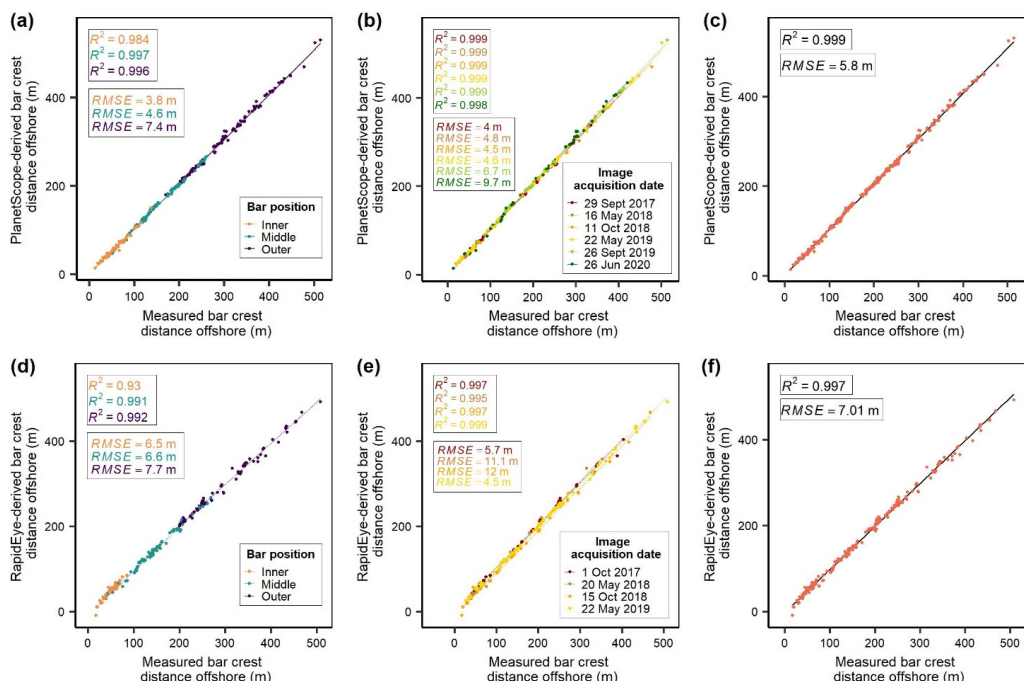


Figure 10. Correlation between measured and satellite-derived sandbar crest positions: (a–c) PlanetScope; (d,e) RapidEye. Column 1 (a,d) shows correlation for inner, middle and outer sandbars; column 2 (b,e) shows correlation for dates of image acquisition, column 3 (c,f) shows total correlation and root-mean-square-error for analysed sensors.

Four pairs of RapidEye images and available bathymetric surveys with 231 pairs of crest positions were compared to validate the proposed procedure for this sensor (Figure 10d–f). RapidEye-derived sandbar crest locations are in good agreement with in situ data with the total coefficient of determination (R^2) of 0.997, ranging from 0.995 to 0.999 for individual dates. The root-mean-square error (RMSE) for all dates was 7.01 m (Figure 10f). RMSE for two dates was between 4.5 and 5.7 m, and for the other two,

between 11.1 and 12 m (Figure 10e), showing large inconsistencies among accuracy of individual dates. Visual comparison of the PlanetScope image acquired on the same day as the bathymetric survey and the RapidEye image acquired on 20 May 2018, with a 4-day time span from in situ measurements revealed that the shape of sandbars has evolved during this period. Visual inspection of the PlanetScope image obtained on 11 October 2018 ($RMSE = 4.5$ m), RapidEye image obtained on October 15 ($RMSE = 12$ m), and crest points from a bathymetric survey performed on 15 October has shown that the RapidEye image was shifted landward from measured crest points and the PlanetScope image. These observations suggest that deviations of errors are rather caused by morphodynamics of sandbars and errors in image positional accuracy.

The $RMSE$ for inner, middle and outer sandbars in PlanetScope images was 3.8, 4.6 and 7.4, respectively (Figure 10a). The tendency of accuracy to increase as sandbar distance from shoreline decreases in RapidEye images remained similar as for PlanetScope sensor with $RMSE$ of 6.5, 6.6 and 7.7 for inner, middle and outer sandbars, respectively (Figure 10d). The largest $RMSE$ value for outer sandbar is because of the larger depth over their crests and the flat, wide shape of the crest itself, especially with the cases when outer sandbars are decaying.

The mean bias of sandbar distance offshore for PlanetScope and RapidEye sensors was 3.95 m and -2.71 m, respectively, meaning that sandbar distance from the shoreline in PlanetScope images was bias seaward and bias landward in RapidEye images. This tendency was evident for all individual dates. It suggests that data extracted from PlanetScope and RapidEye sensors in combination should be analysed with caution.

3.3. Accuracy of Extracted Shoreline Position

129 measured shoreline points were compared to PlanetScope-derived and 80 points to RapidEye-derived shoreline position to evaluate the accuracy of the proposed procedure for the shoreline extraction. The root-mean-square error ($RMSE$) for PlanetScope was 4.5 m, ranging from 0.2 to 7.7 m for individual dates. For RapidEye, the average $RMSE$ was 4.4 m, ranging from 0.8 to 6.5 m for individual dates. In images of both sensors, the shoreline was placed seaward from the measured position with a mean bias of 3.9 m and 3.4 m for PlanetScope and RapidEye, respectively. Seaward-directed displacement of satellite-derived shoreline position is often observed in optical remote sensing [53,90–93]. Here, the narrow range of the electromagnetic spectrum sampled by PlanetScope and RapidEye constellations with only near-infrared wavelengths outside the visible light region is one of the factors determining the accuracy of obtained shorelines. Inherent property of near-infrared wavelengths to sense concentrations of sediments and other constituents of water diminish the capability to discriminate water from land and contributes to the seaward displacement of satellite-derived shorelines.

4. Discussion

4.1. Strengths and Limitations

As research of nearshore sandbars is often limited by the data availability [61], the present study intends to develop an algorithm suitable to gather this data from satellite imagery using GIS techniques. The study suggests a new approach based on the Relative Bathymetric Position Index (RBPI) and a combination of data processing and filtering operations designed specifically for the purpose. The Bathymetric Position Index has been widely used with bathymetric datasets for various coastal and marine applications [94–103], including sandbar extraction in the bathymetric LiDAR dataset [26], but the idea of using this metric in remote sensing images without derived bathymetry to our knowledge has never been explored before. This article illustrates that with a newly designed methodology, RBPI is suitable to discriminate nearshore morphology in non-bathymetric remote sensing images. It is mainly possible because, similar to bathymetry digital elevation models, brighter and darker pixels in visible light spectrum bands of satellite imagery represent shallower and deeper nearshore areas.

The application of the proposed method in the Curonian Spit, the Baltic Sea demonstrates that, in combination with medium resolution satellite imagery, it can be used to study multiple nearshore sandbar systems. It is justified by the method design for a range of sandbar morphologies (straight and crescentic; longshore parallel and oblique), which cover most of the commonly observed nearshore sandbar types [5,11]. Therefore, if adjustments to site-specific parameters related to sandbar size and shoreline configuration are made, the proposed technique can be used to study these underwater features in other sandy environments.

Currently, only a few studies that analyse satellite-derived data with a focus on sandbar crest position exist [61,62]. Compared to other automated techniques, the major advantage of the proposed algorithm is that besides higher accuracy of crest locations, it provides outputs with an entire set of other information, including sandbar boundaries (Table 3). This enables the possibility to quantify width, length, area and the overall shape of sandbars in addition to the distance from the shoreline and the number of sandbars. The remaining missing sandbar characteristics are sand volume and water depth; therefore, possible extension of methodology could include derivation of nearshore bathymetry for evaluation of these parameters. With a set of in situ depth points, bathymetry could be derived using previously proposed techniques (e.g., [58,104,105]).

Table 3. A comparison of the proposed method to other automated and semi-automated methods of sandbar extraction in optical satellite imagery.

Reference	Main Methods	Outputs	Tested Satellite Sensors	Spatial Resolution of Tested Satellite Sensors	Sandbar Crest Position Accuracy	Software	Coastal Environment
Tätui and Constantin [62]	Peak detection in image-derived cross-shore profiles	Sandbar crests	Sentinel-2 MSI	10 m	$MAD = 6.22 \text{ m}$	R	Non-tidal, wave dominated
Roman-Rivera et al. [63]	Ruled-based object-based image classification	Sandbar boundaries	WorldView-2, 3, QuickBird	0.3–0.6 m	Not specified	ENVI	Microtidal
The proposed method	Multiscale RBPI, spatial statistics and filtering	Sandbar boundaries, sandbar crests, nearshore morphology, shoreline	PlanetScope, RapidEye, Landsat-8 OLI, Sentinel-2 MSI	3–30 m	$MAD = 3.42\text{--}5.05 \text{ m}$ (depending on sensor)	ArcGIS, R	Non-tidal, wave-dominated

Although the algorithm was implemented in the ArcGIS environment and many coastal researchers, managers and other stakeholders are familiar with it [106], the proposed technique uses general operations and functions which can be executed in other open-source GIS environments, including QGIS, GRASS GIS, SAGA GIS or using the R programming language.

Some aspects of the capabilities and limitations of the algorithm can be defined through its performance in the recognition and omission of sandbars compared to the ones identified in nearshore cross-shore profiles (Figure 11). Such assessment, based on images and in situ data, acquired under low wave energy (significant wave height 0–0.4 m) in a non-tidal coastal environment, exposes both shortcomings and superiorities of the satellite data over bathymetric surveys. One superiority emerges in very shallow waters where the algorithm enhances the detectability of inner sandbars when bathymetric measurements fail to locate them because of complicated navigation and echo-sounding errors in very shallow areas (<1 m) [107]. The algorithm demonstrates fine performance in sensing nearshore sandbars at least up to 6 m depth over their crest (Figure 11), including decaying outer sandbars with flat-topped crests. It is expected that the capability of the algorithm to

locate outer sandbars will diminish if more than one of the following constraints transpire: (1) water depth over sandbar crest is >6 m; (2) outer sandbar is decaying; (3) environmental factors limiting water transparency are evident. Limiting environmental factors include atmospheric conditions (clouds, haze), hydrodynamic conditions (breaking waves, rough sea surface) and water turbidity. Such conditions are more frequent in winter and autumn what determines lower temporal frequency and quality of data in those seasons. Limiting environmental factors act in two ways: decrease the accuracy of derived data and narrow down the range of water depth over sandbar crest when sandbars can be detected. The technique can still be applied if images do not contain breaking waves, wave foam and a high concentration of suspended material. Another limitation might be related to geopositional accuracy (<10 m) of imagery used in this study, which might be the cause of inaccuracies in sandbar position. Similar constraints were observed by previous studies, using other optical sensors: Tătui and Constantin [62] and Athanasiou et al. [61] observed omission of sandbars in Sentinel-2 and Landsat images caused by limited water column transparency and overlook of outer sandbars situated in the depth of 3 m in Sentinel-2 data [62]. However, the present study suggests that when none of the environmental constraints is present, the number of satellite-detected sandbars exceeds algorithm-related errors (Figure 11). It means that in some instances, satellite-derived data portray a better representation of nearshore bottom morphology.

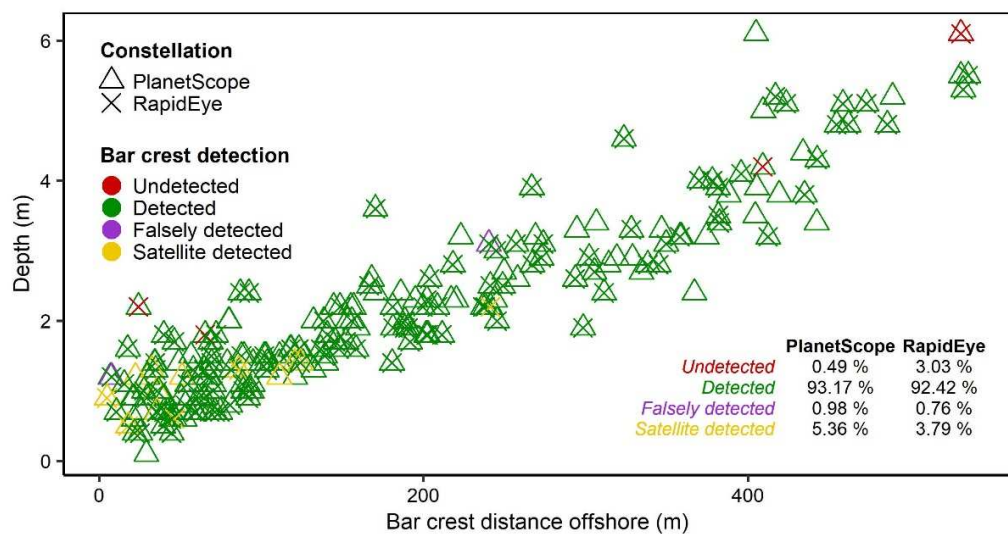


Figure 11. The ability of the algorithm to detect sandbars in PlanetScope and RapidEye images compared to measured data: undetected—sandbars visible in bathymetric cross-shore profile and undetected by the algorithm; detected—sandbars visible in bathymetric cross-shore profile and detected by the algorithm; falsely detected—non-existing sandbars, extracted by the algorithm; satellite detected—sandbars not-visible in cross-shore profiles, but identified by the algorithm.

Compared to the preferred optical remote sensing method to study sandbar behaviour video monitoring, the proposed technique provides data of lower temporal frequency and is not capable of working in full capacity under high wave energy (Section 2.5) as it was primarily designed for low wave energy conditions. However, in contrast to video monitoring, it extends possibilities of sandbar studies from local to regional or larger scale and in areas where sandbar data are not available.

4.2. Applicability to Sandbar Monitoring

To be able to use the proposed technique to monitor the behaviour of nearshore sandbars, the rate of sandbar dynamics must exceed possible errors. Previous studies have reported sandbar migration rates of 30–200 m/year [16,108–111], which implies the suitability of Planet’s imagery with an accuracy of the proposed technique (RMSE of 5.8–7 m) for monitoring of seasonal and inter-annual sandbar migration. With observed migration rates of 20–50 m/day during storms [38,110,112,113] and the current precision of the designed technique, it may be a low-cost solution to monitor short-term changes related to high-impact events. However, monitoring of moderate short-term changes is more complicated because of the possibility of misperceiving inaccuracies as an episodic sandbar migration or morphological evolution.

If placed into an automated workflow of analysis, the algorithm-derived satellite data could contribute to new insights into sandbar behaviour at multiple time scales and larger spatial extents or areas where sandbar data is unavailable. With conventional methods for acquiring sandbar data being time-consuming, expensive, or spatially limited [15,26], this study proves the feasibility of automatically derived satellite data as a valuable source of repetitive sandbar observations, which could provide necessary information for coastal research and management.

4.3. Applicability to Other Optical Sensors

The present study demonstrates the capability of the proposed method to derive sandbars and their crestlines in satellite images of 3–5 m spatial resolution. With slight modifications, this technique can be employed with other optical satellite sensors. To examine the potential of the method, it was tested with publicly available imagery of other medium-resolution satellites (Sentinel-2 MSI; Landsat-8 OLI). For Landsat-8, a panchromatic band (15 m) was used instead of multispectral bands (30 m). Images were upsampled, and the degree of spatial filtering was reduced. In Figure 12, it is illustrated that a modified version of the proposed method was capable of detecting sandbar crests precisely in Sentinel-2 and Landsat-8 images during low wave energy conditions. After comparison of 169 in situ crest points against crests derived from Sentinel-2 MSI (Figure 12c) and Landsat-8 OLI (Figure 12d) imagery, RMSE of nearly half a pixel has been found for both Sentinel-2 (4.5 m) and Landsat-8 (7.6 m) sensors. The results of Sentinel-2 and Landsat-8 validation suggest that using the proposed method sandbar crests in free satellite imagery of lower spatial resolution (10–15 m) may be detected with similar accuracy to higher spatial resolution imagery (3–5 m) of the commercial satellites used in this study.

The potential application of the proposed method has been also tested with Sentinel-2 MSI and Landsat-8 OLI imagery during medium–high wave energy conditions (Figure 13). After comparison of in situ crest positions with satellite-derived crest locations, RMSE of 18.9 m and 22.9 m has been found for Sentinel-2 MSI and Landsat-8 OLI, accordingly (Figure 13c,d). Although greater error might be partly caused due to a larger time-span between the acquisition of images and measurements, it shows that the accuracy of the proposed method drops significantly when medium and high energy breaking waves are present. It also should be noted that the proposed technique is capable of detecting sandbars if breaking waves are present over the sandbar crest or if the sandbar is visible through the water column. It was observed that during high wave energy conditions, the algorithm worked better in the northern part of the study area where the outer sandbar is found in 3–4 m water depth than in the southern part with an outer sandbar in 5–6 m depth.

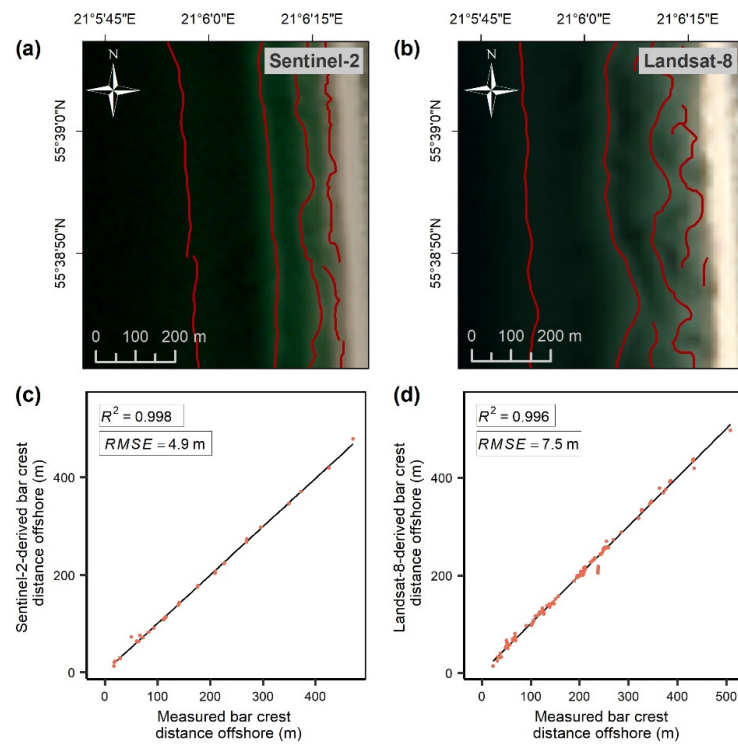


Figure 12. An example of sandbar crestlines delineated using the proposed method in Sentinel-2 MSI (a) and Landsat-8 OLI (b) images with a correlation of measured and extracted crest distance from the shoreline (c,d) during low wave energy conditions.

Future research could also focus on method application to aerial photography. If it contains spectral band in the infrared region which is required to extract underwater image part with sandbars or if different land-sea segmentation procedure based on panchromatic/visible light data is chosen (e.g., [114,115]), sandbars could be extracted from the data of both panchromatic and colour historical aerial photography, but additional research is required to evaluate the accuracy of such application.

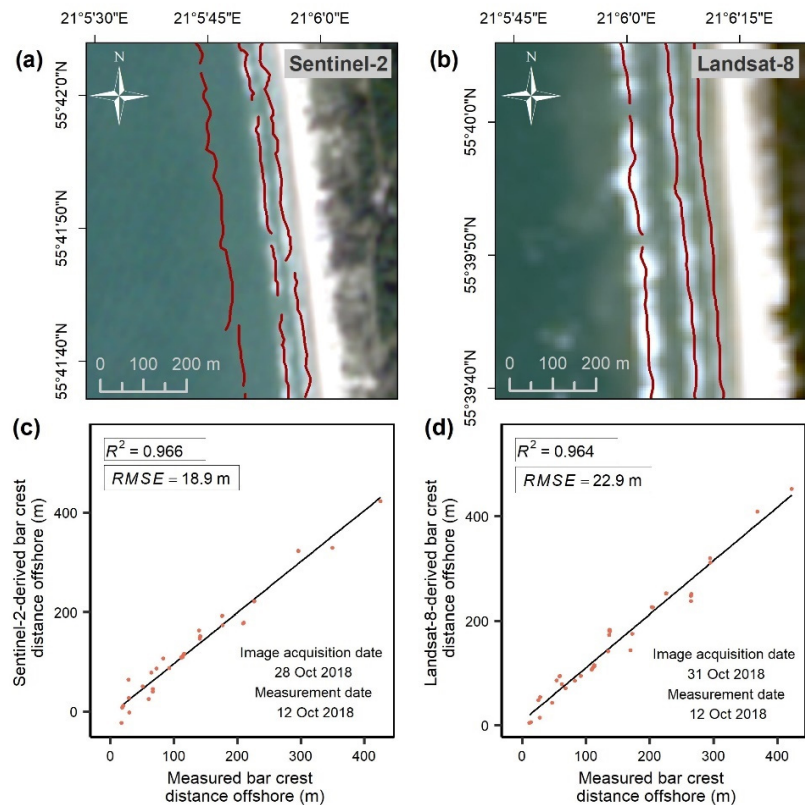


Figure 13. An example of sandbar crestlines delineated using the proposed method in Sentinel-2 MSI (a) and Landsat-8 OLI (b) images with a correlation of measured and extracted crest distance from the shoreline (c,d) during high wave energy conditions.

5. Conclusions

In this study, a novel methodological approach for the discrimination of nearshore sandbars in optical satellite imagery is designed. The proposed technique is a step-by-step workflow implementable in most GIS environments. In every step, an output providing new information about nearshore morphology is generated. After the implementation of the entire procedure, outputs with nearshore morphology, extracted sandbars, delineated sandbar crests and shorelines are acquired, providing a series of data required to study sandbar dynamics.

The capabilities of the new technique were demonstrated using a case study of the Curonian Spit, Baltic Sea. The accuracy of the method was assessed by comparing crest locations derived from PlanetScope and RapidEye images to in situ data of 6 bathymetric surveys. A strong agreement ($R^2 = 0.999$ and 0.997) between measured and derived sandbar crests was observed with an average RMSE of 5.8 and 7 m for PlanetScope and RapidEye sensors, accordingly.

The results suggest Planet's imagery as a source for monitoring nearshore sandbar behaviour in seasonal and inter-annual time scales. The versatility of the algorithm determines the high potential of its feasibility to other optical sensors, including Sentinel-2 MSI and Landsat-8 OLI, where sandbar crests were identified with an accuracy of half a pixel, and many sandy environments worldwide if proper modifications are made. Further research could fully validate the capabilities of the newly proposed algorithm.

to obtain sandbar morphology in other sandy nearshore regions and imagery of other satellite sensors.

The increasing availability of Earth observation imagery offers a free/low-cost alternative to traditional techniques for monitoring nearshore sandbars. This study demonstrates that in combination with an automated technique for data extraction, satellite images turn into a valid tool to observe sandbar morphology and dynamics. However, the utilization of satellite images is decided by the sensor quality (spatial and spectral resolution, signal-to-noise ratio), environmental conditions (water transparency, cloud cover, wave energy) and characteristics of the sandbar system itself (scales, depth, height of sandbars and distinctiveness of their crests). This study shows that satellite-derived sandbar data are most accurate during low wave energy conditions, and high wave energy results in significantly less accurate data. Future studies should seek to overcome constraints reducing the feasibility of satellite images to obtain sandbar morphology and to examine their full capacities to make new insights into sandbar behaviour.

Author Contributions: Conceptualization, R.J., L.J. and D.J.; methodology, R.J. and L.J.; validation, R.J.; formal analysis, R.J.; investigation, R.J., D.J., L.J., D.P. and G.Ž.; resources, L.J. and G.Ž.; data curation, R.J. and D.P.; writing—original draft preparation, R.J.; writing—review and editing, L.J., D.J., D.P. and G.Ž.; visualization, R.J.; supervision, D.J. All authors have read and agreed to the published version of the manuscript.

Funding: This research received no external funding.

Institutional Review Board Statement: Not applicable.

Informed Consent Statement: Not applicable.

Data Availability Statement: The data presented in this study are available on request from the corresponding author. The data are not publicly available due to the Data Use Agreement with Planet Labs.

Conflicts of Interest: The authors declare no conflict of interest.

References

- Price, T.D.; Ruessink, B.G.; Castelle, B. Morphological coupling in multiple sandbar systems—A review. *Earth Surf. Dyn.* **2014**, *2*, 309–321. [[CrossRef](#)]
- Cohn, N.; Ruggiero, P.; Ortiz, J.; Walstra, D.J. Investigating the role of complex sandbar morphology on nearshore hydrodynamics. *J. Coast. Res.* **2014**, *70*, 53–58. [[CrossRef](#)]
- Pape, L.; Ruessink, B.G. Multivariate Analysis of Nonlinearity in Sandbar Behavior. *Nonlinear Process. Geophys.* **2008**, *15*, 145–158. [[CrossRef](#)]
- Múnica, S.; Osorio, A.F.; Velásquez, J.D. Data-based methods and algorithms for the analysis of sandbar behavior with exogenous variables. *Comput. Geosci.* **2014**, *72*, 134–146. [[CrossRef](#)]
- Wijnberg, K.M.; Kroon, A. Barred beaches. *Geomorphology* **2002**, *48*, 103–120. [[CrossRef](#)]
- Larson, M.; Kraus, N.C. Temporal and spatial scales of beach profile change, Duck, North Carolina. *Mar. Geol.* **1994**, *117*, 75–94. [[CrossRef](#)]
- Di Leonardo, D.; Ruggiero, P. Regional scale sandbar variability: Observations from the U.S. Pacific Northwest. *Cont. Shelf Res.* **2015**, *95*, 74–88. [[CrossRef](#)]
- Yoshi, M.; Okada, M. Long-term field observations of multiple bar properties on an eroding coast. *J. Coast. Res.* **2011**, *64*, 860–864. [[CrossRef](#)]
- Short, A.D. Offshore Bars along the Alaskan Arctic Coast. *J. Geol.* **1975**, *83*, 209–221. [[CrossRef](#)]
- Van Enckevort, I.M.J.; Ruessink, B.G. Video observations of nearshore bar behaviour. Part 1: Alongshore uniform variability. *Cont. Shelf Res.* **2003**, *23*, 501–512. [[CrossRef](#)]
- Ribas, F.; Falqués, A.; Garnier, R. Nearshore Sand Bars on Western Mediterranean Beaches. In *Atlas of Bedforms in the Western Mediterranean*; Springer International Publishing: Cham, Switzerland, 2017; pp. 81–88.
- Van Enckevort, I.M.J.; Ruessink, B.G. Video observations of nearshore bar behaviour. Part 2: Alongshore non-uniform variability. *Cont. Shelf Res.* **2003**, *23*, 513–532. [[CrossRef](#)]
- Tătui, F.; Vespremeanu-Stroe, A.; Preoteasa, L. The correlated behavior of sandbars and foredunes on a nontidal coast (Danube Delta, Romania). *J. Coast. Res.* **2013**, *165*, 1874–1879. [[CrossRef](#)]
- Cohn, N.; Ruggiero, P.; De Vries, S.; Garcia-Medina, G. Beach Growth Driven by Intertidal Sandbar Welding. In Proceedings of the Coastal Dynamics, Helsingør, Denmark, 12–16 June 2017; pp. 12–16.

15. Román-Rivera, M.A.; Ellis, J.T. A synthetic review of remote sensing applications to detect nearshore bars. *Mar. Geol.* **2019**, *408*, 144–153. [[CrossRef](#)]
16. Ruessink, B.G.; Kroon, A. The behaviour of a multiple bar system in the nearshore zone of Terschelling, the Netherlands: 1965–1993. *Mar. Geol.* **1994**, *121*, 187–197. [[CrossRef](#)]
17. Grunnet, N.M.; Hoekstra, P. Alongshore variability of the multiple barred coast of Terschelling, The Netherlands. *Mar. Geol.* **2004**, *203*, 23–41. [[CrossRef](#)]
18. Grunnet, N.M.; Ruessink, B.G. Morphodynamic response of nearshore bars to a shoreface nourishment. *Coast. Eng.* **2005**, *52*, 119–137. [[CrossRef](#)]
19. Ruessink, B.G.; Wijnberg, K.M.; Holman, R.A.; Kuriyama, Y.; van Enckevort, I.M.J. Intersite comparison of interannual nearshore bar behavior. *J. Geophys. Res. C Ocean.* **2003**, *108*. [[CrossRef](#)]
20. Kuriyama, Y. Medium-term bar behavior and associated sediment transport at Hasaki, Japan. *J. Geophys. Res. C Ocean.* **2002**, *107*, 15-1–15-2. [[CrossRef](#)]
21. Wijnberg, K.M.; Terwindt, J.H.J. Extracting decadal morphological behaviour from high-resolution, long-term bathymetric surveys along the Holland coast using eigenfunction analysis. *Mar. Geol.* **1995**, *126*, 301–330. [[CrossRef](#)]
22. Short, A.D. Beach systems of the central Netherlands coast: Processes, morphology and structural impacts in a storm driven multi-bar system. *Mar. Geol.* **1992**, *107*. [[CrossRef](#)]
23. Aleman, N.; Robin, N.; Certain, R.; Vanroye, C.; Barusseau, J.; Bouchette, F. Typology of nearshore bars in the Gulf of Lions (France) using LiDAR technology. *J. Coast. Res.* **2011**, *64*, 721–725.
24. Aleman, N.; Robin, N.; Certain, R.; Anthony, E.J.; Barusseau, J.P. Longshore variability of beach states and bar types in a microtidal, storm-influenced, low-energy environment. *Geomorphology* **2015**, *241*, 175–191. [[CrossRef](#)]
25. Levoy, F.; Anthony, E.J.; Monfort, O.; Robin, N.; Bretel, P. Formation and migration of transverse bars along a tidal sandy coast deduced from multi-temporal Lidar datasets. *Mar. Geol.* **2013**, *342*, 39–52. [[CrossRef](#)]
26. Taramelli, A.; Cappucci, S.; Valentini, E.; Rossi, L.; Lisi, I. Nearshore Sandbar Classification of Sabaudia (Italy) with LiDAR Data: The FHyL Approach. *Remote Sens.* **2020**, *12*, 1053. [[CrossRef](#)]
27. Lippmann, T.C.; Holman, R.A. Quantification of Sand Bar Morphology: A Video Technique Based on Wave Dissipation. *J. Geophys. Res.* **1989**, *94*, 995–1011. [[CrossRef](#)]
28. Lippmann, T.C.; Holman, R.A. The Spatial and Temporal Variability of Sand Bar Morphology. *J. Geophys. Res.* **1990**, *95*, 575–586. [[CrossRef](#)]
29. Armaroli, C.; Ciavola, P. Dynamics of a nearshore bar system in the northern Adriatic: A video-based morphological classification. *Geomorphology* **2011**, *126*, 201–216. [[CrossRef](#)]
30. Bouvier, C.; Balouin, Y.; Castelle, B. Video monitoring of sandbar-shoreline response to an offshore submerged structure at a microtidal beach. *Geomorphology* **2017**, *295*, 297–305. [[CrossRef](#)]
31. Parlagreco, L.; Melito, L.; Devoti, S.; Perugini, E.; Soldini, L.; Zitti, G.; Brocchini, M. Monitoring for coastal resilience: Preliminary data from five Italian sandy beaches. *Sensors* **2019**, *19*, 1854. [[CrossRef](#)]
32. Angnuureng, D.B.; Almar, R.; Senechal, N.; Castelle, B.; Addo, K.A.; Marieu, V.; Ranasinghe, R. Shoreline resilience to individual storms and storm clusters on a meso-macrotidal barred beach. *Geomorphology* **2017**, *290*, 265–276. [[CrossRef](#)]
33. Ruessink, B.G.; Van Enckevort, I.M.J.; Kingston, K.S.; Davidson, M.A. Analysis of observed two- and three-dimensional nearshore bar behaviour. *Mar. Geol.* **2000**, *169*, 161–183. [[CrossRef](#)]
34. Konicki, K.M.; Holman, R.A. The statistics and kinematics of transverse sand bars on an open coast. *Mar. Geol.* **2000**, *169*, 69–101. [[CrossRef](#)]
35. Van Enckevort, I.M.J.; Ruessink, B.G.; Coco, G.; Suzuki, K.; Turner, I.L.; Plant, N.G.; Holman, R.A. Observations of nearshore crescentic sandbars. *J. Geophys. Res. C Ocean.* **2004**, *109*, C06028. [[CrossRef](#)]
36. Ribas, F.; Kroon, A. Characteristics and dynamics of surfzone transverse finger bars. *J. Geophys. Res. Earth Surf.* **2007**, *112*. [[CrossRef](#)]
37. Price, T.D.; Ruessink, B.G. State dynamics of a double sandbar system. *Cont. Shelf Res.* **2011**, *31*, 659–674. [[CrossRef](#)]
38. Almar, R.; Castelle, B.; Ruessink, B.G.; Senechal, N.; Bonneton, P.; Marieu, V. High-frequency video observation of two nearby double-barred beaches under high-energy wave forcing. *J. Coast. Res.* **2009**, *2009*, 1706–1710.
39. Parlagreco, P.; Archetti, L.; Simeoni, R.; Devoti, U.; Valentini, S.; Silenzi, A. Video-monitoring of a barred nourished beach. *J. Coast. Res.* **2011**, *64*, 110–114.
40. Contardo, S.; Symonds, G. Sandbar straightening under wind-sea and swell forcing. *Mar. Geol.* **2015**, *368*, 25–41. [[CrossRef](#)]
41. Splinter, K.; Harley, M.; Turner, I. Remote Sensing Is Changing Our View of the Coast: Insights from 40 Years of Monitoring at Narrabeen-Collaroy, Australia. *Remote Sens.* **2018**, *10*, 1744. [[CrossRef](#)]
42. Holman, R.A.; Stanley, J. The history and technical capabilities of Argus. *Coast. Eng.* **2007**, *54*, 477–491. [[CrossRef](#)]
43. Guedes, R.M.C.; Calliari, L.J.; Holland, K.T.; Plant, N.G.; Pereira, P.S.; Alves, F.N.A. Short-term sandbar variability based on video imagery: Comparison between Time-Average and Time-Variance techniques. *Mar. Geol.* **2011**, *289*, 122–134. [[CrossRef](#)]
44. Van de Lageweg, W.I.; Bryan, K.R.; Coco, G.; Ruessink, B.G. Observations of shoreline-sandbar coupling on an embayed beach. *Mar. Geol.* **2013**, *344*, 101–114. [[CrossRef](#)]
45. Nieto, M.A.; Garau, B.; Balle, S.; Simarro, G.; Zarruk, G.A.; Ortiz, A.; Tintoré, J.; Álvarez-Ellacuría, A.; Gómez-Pujol, L.; Orfila, A. An open source, low cost video-based coastal monitoring system. *Earth Surf. Process. Landf.* **2010**, *35*, 1712–1719. [[CrossRef](#)]

46. Rihouey, D.; Dugor, J.; Dailloux, D.; Morichon, D. Application of Remote Sensing Video Systems to Coastal Defence Monitoring. *J. Coast. Res.* **2009**, *II*, 1582–1586.
47. Murray, T.; Cartwright, N.; Tomlinson, R. Video-imaging of transient rip currents on the Gold Coast open beaches. *J. Coast. Res.* **2013**, *165*, 1809–1814. [CrossRef]
48. Andriolo, U.; Sánchez-García, E.; Taborda, R. Operational use of surfcam online streaming images for coastal morphodynamic studies. *Remote Sens.* **2019**, *11*, 78. [CrossRef]
49. Bracs, M.A.; Turner, I.L.; Splinter, K.D.; Short, A.D.; Lane, C.; Davidson, M.A.; Goodwin, I.D.; Pritchard, T.; Cameron, D. Evaluation of Opportunistic Shoreline Monitoring Capability Utilizing Existing “surfcam” Infrastructure. *J. Coast. Res.* **2016**, *32*, 542–554. [CrossRef]
50. Vos, K.; Harley, M.D.; Splinter, K.D.; Simmons, J.A.; Turner, I.L. Sub-annual to multi-decadal shoreline variability from publicly available satellite imagery. *Coast. Eng.* **2019**, *150*, 160–174. [CrossRef]
51. Feyisa, G.L.; Meilby, H.; Fensholt, R.; Proud, S.R. Automated Water Extraction Index: A new technique for surface water mapping using Landsat imagery. *Remote Sens. Environ.* **2014**, *140*, 23–35. [CrossRef]
52. Di, K.; Wang, J.; Ma, R.; Li, R. Automatic Shoreline Extraction from Highresolution IKONOS Satellite Imagery. In Proceedings of the ASPRS 2003 Annual Conference, Anchorage, AK, USA, 5 May 2003; pp. 1–4.
53. Almonacid-Caballer, J.; Sánchez-García, E.; Pardo-Pascual, J.E.; Balaguer-Beser, A.A.; Palomar-Vázquez, J. Evaluation of annual mean shoreline position deduced from Landsat imagery as a mid-term coastal evolution indicator. *Mar. Geol.* **2016**, *372*, 79–88. [CrossRef]
54. Guariglia, A.; Buonomassa, A.; Losurdo, A.; Saladino, R.; Trivigno, M.L.; Zaccagnino, A.; Colangelo, A. A multisource approach for coastline mapping and identification of shoreline changes. *Ann. Geophys.* **2006**, *49*, 295–304.
55. Wei, J.; Wang, M.; Lee, Z.; Briceño, H.O.; Yu, X.; Jiang, L.; Garcia, R.; Wang, J.; Luis, K. Shallow water bathymetry with multi-spectral satellite ocean color sensors: Leveraging temporal variation in image data. *Remote Sens. Environ.* **2020**, *250*, 112035. [CrossRef]
56. Lyzenga, D.R.; Malinas, N.P.; Tanis, F.J. Multispectral Bathymetry Using a Simple Physically Based Algorithm. *IEEE Trans. Geosci. Remote Sens.* **2006**, *44*, 2251. [CrossRef]
57. Manessa, M.D.; Haidar, M.; Hartuti, M.; Kresnawati, D.K. Determination of the best methodology for bathymetry mapping using SPOT 6 imagery: A study of 12 empirical algorithms. *Int. J. Remote. Sens.* **2017**, *14*, 127–136. [CrossRef]
58. Gabr, B.; Ahmed, M.; Marmoush, Y. PlanetScope and Landsat 8 Imageries for Bathymetry Mapping. *J. Mar. Sci. Eng.* **2020**, *8*, 143. [CrossRef]
59. Lafon, V.; De Melo Apoluceno, D.; Dupuis, H.; Michel, D.; Howa, H.; Froidefond, J.M. Morphodynamics of nearshore rhythmic sandbars in a mixed-energy environment (SW France): I. Mapping beach changes using visible satellite imagery. *Estuar. Coast. Shelf Sci.* **2004**, *61*, 289–299. [CrossRef]
60. Rodríguez-Martín, R.; Rodríguez-Santalla, I. Detection of Submerged Sand Bars in the Ebro Delta Using Aster Images. In *New Frontiers in Engineering Geology and the Environment*; Springer: Berlin, Germany, 2013; pp. 103–106. ISBN 42316715_16.
61. Athanasiou, P.; de Boer, W.; Yoo, J.; Ranasinghe, R.; Reniers, A. Analysing decadal-scale crescentic bar dynamics using satellite imagery: A case study at Anmok beach, South Korea. *Mar. Geol.* **2018**, *405*, 1–11. [CrossRef]
62. Tätili, F.; Constantin, S. Nearshore sandbars crest position dynamics analysed based on Earth Observation data. *Remote Sens. Environ.* **2020**, *237*, 111555. [CrossRef]
63. Román-Rivera, M.A.; Ellis, J.T.; Wang, C. Applying a rule-based object-based image analysis approach for nearshore bar identification and characterization. *J. Appl. Remote Sens.* **2020**, *14*, 044502. [CrossRef]
64. Kelpšaite, L.; Dailidiene, I. Influence of wind wave climate change on coastal processes in the eastern Baltic Sea. *J. Coast. Res.* **2011**, *64*, 220–224.
65. Jakimavičius, D.; Kriauciūnienė, J.; Šarauskienė, D. Assessment of wave climate and energy resources in the Baltic Sea nearshore (Lithuanian territorial water). *Oceanologia* **2018**, *60*, 207–218. [CrossRef]
66. Jarmalavičius, D.; Žilinskas, G.; Pupienis, D. Geologic framework as a factor controlling coastal morphometry and dynamics. Curonian Spit, Lithuania. *Int. J. Sediment. Res.* **2017**, *32*, 597–603. [CrossRef]
67. Wright, L.D.; Short, A.D. Morphodynamic variability of surf zones and beaches: A synthesis. *Mar. Geol.* **1984**, *56*, 93–118. [CrossRef]
68. Planet Team Planet Application Program Interface: In Space for Life on Earth. Available online: <https://api.planet.com/> (accessed on 9 May 2021).
69. Planet Planet Imagery Products Specifications. Available online: https://assets.planet.com/docs/Planet_Combined_Imagery_Product_Specs_letter_screen.pdf (accessed on 9 May 2021).
70. Sadeh, Y.; Zhu, X.; Dunkerley, D.; Walker, J.P.; Zhang, Y.; Rozenstein, O.; Manivasagam, V.S.; Chenu, K. Fusion of Sentinel-2 and PlanetScope time-series data into daily 3 m surface reflectance and wheat LAI monitoring. *Int. J. Appl. Earth Obs. Geoinf.* **2021**, *96*, 102260. [CrossRef]
71. Sadeh, Y.; Zhu, X.; Chenu, K.; Dunkerley, D. Sowing date detection at the field scale using CubeSats remote sensing. *Comput. Electron. Agric.* **2019**, *157*, 568–580. [CrossRef]
72. Houborg, R.; McCabe, M.F. A Cubesat enabled Spatio-Temporal Enhancement Method (CESTEM) utilizing Planet, Landsat and MODIS data. *Remote Sens. Environ.* **2018**, *209*, 211–226. [CrossRef]

73. Leach, N.; Coops, N.C.; Obrknezev, N. Normalization method for multi-sensor high spatial and temporal resolution satellite imagery with radiometric inconsistencies. *Comput. Electron. Agric.* **2019**, *164*, 104893. [[CrossRef](#)]
74. Kudela, R.M.; Hooker, S.B.; Houskeeper, H.F.; McPherson, M. The Influence of Signal to Noise Ratio of Legacy Airborne and Satellite Sensors for Simulating Next-Generation Coastal and Inland Water Products. *Remote Sens.* **2019**, *11*, 2071. [[CrossRef](#)]
75. Li, F.; Fan, J. Salt and Pepper Noise Removal by Adaptive Median Filter and Minimal Surface Inpainting. In Proceedings of the 2009 2nd International Congress on Image and Signal Processing, Tianjin, China, 17–19 October 2009; pp. 1–5.
76. Lopes, A.; Touzi, R.; Nezry, E. Adaptive speckle filters and scene heterogeneity. *IEEE Trans. Geosci. Remote Sens.* **1990**, *28*, 992–1000. [[CrossRef](#)]
77. Lee, J. Sen Digital Image Enhancement and Noise Filtering by Use of Local Statistics. *IEEE Trans. Pattern Anal. Mach. Intell.* **1980**, *2*, 165–168. [[CrossRef](#)] [[PubMed](#)]
78. Kuan, D.T.; Sawchuk, A.A.; Strand, T.C.; Chavel, P. Adaptive Noise Smoothing Filter for Images with Signal-Dependent Noise. *IEEE Trans. Pattern Anal. Mach. Intell.* **1985**, *7*, 165–177. [[CrossRef](#)] [[PubMed](#)]
79. McFeeters, S.K. The use of the Normalized Difference Water Index (NDWI) in the delineation of open water features. *Int. J. Remote Sens.* **1996**, *17*, 1425–1432. [[CrossRef](#)]
80. Xu, H. Modification of normalised difference water index (NDWI) to enhance open water features in remotely sensed imagery. *Int. J. Remote Sens.* **2006**, *27*, 3025–3033. [[CrossRef](#)]
81. Ghorai, D.; Mahapatra, M. Extracting Shoreline from Satellite Imagery for GIS Analysis. *Remote Sens. Earth Syst. Sci.* **2020**, *3*, 13–22. [[CrossRef](#)]
82. Newman, D.R.; Lindsay, J.B.; Cockburn, J.M.H. Evaluating metrics of local topographic position for multiscale geomorphometric analysis. *Geomorphology* **2018**, *312*, 40–50. [[CrossRef](#)]
83. Doumit, J.A. Multiscale Landforms Classification Based on UAV Datasets. *Sustain. Environ.* **2018**, *3*, 128. [[CrossRef](#)]
84. De Reu, J.; Bourgeois, J.; Bats, M.; Zwertyaegher, A.; Gelorini, V.; De Smedt, P.; Chu, W.; Antrop, M.; De Maeyer, P.; Finke, P.; et al. Application of the topographic position index to heterogeneous landscapes. *Geomorphology* **2013**, *186*, 39–49. [[CrossRef](#)]
85. Mokarram, M.; Roshan, G.; Negahban, S. Landform classification using topography position index (case study: Salt dome of Korsia-Darab plain, Iran). *Model. Earth Syst. Environ.* **2015**, *1*, 40. [[CrossRef](#)]
86. Liu, A. DEM-based Analysis of Local Relief. In *Advances in Digital Terrain Analysis*; Springer: Berlin, Germany, 2008; pp. 177–192.
87. Lecours, V.; Dolan, M.F.J.; Micallef, A.; Lucieer, V.L. A review of marine geomorphometry, the quantitative study of the seafloor. *Hydrod. Earth Syst. Sci.* **2016**, *20*, 3207–3244. [[CrossRef](#)]
88. Short, A.D.; Aagaard, T. Single and Multi-Bar Beach Change Models. *J. Coast. Res.* **1993**, *1*, 141–157.
89. Mascarenhas, V.; Keck, T. Marine Optics and Ocean Color Remote Sensing. In *YOUNMARES 8—Oceans Across Boundaries: Learning from Each Other*; Springer International Publishing: Cham, Switzerland, 2018; pp. 41–54.
90. Vos, K.; Splinter, K.D.; Harley, M.D.; Simmons, J.A.; Turner, I.L. CoastSat: A Google Earth Engine-enabled Python toolkit to extract shorelines from publicly available satellite imagery. *Environ. Model. Softw.* **2019**, *122*, 104528. [[CrossRef](#)]
91. Hagenaars, G.; de Vries, S.; Luijendijk, A.P.; de Boer, W.P.; Reniers, A.J.H.M. On the accuracy of automated shoreline detection derived from satellite imagery: A case study of the sand motor mega-scale nourishment. *Coast. Eng.* **2018**, *133*, 113–125. [[CrossRef](#)]
92. Kelly, J.T.; Gontz, A.M. Rapid Assessment of Shoreline Changes Induced by Tropical Cyclone Oma Using CubeSat Imagery in Southeast Queensland, Australia. *J. Coast. Res.* **2019**, *36*, 72. [[CrossRef](#)]
93. Pardo-Pascual, J.; Sánchez-García, E.; Almonacid-Caballer, J.; Palomar-Vázquez, J.; de los Santos, E.P.; Fernández-Sarría, A.; Balaguer-Beser, Á. Assessing the Accuracy of Automatically Extracted Shorelines on Mictrotidal Beaches from Landsat 7, Landsat 8 and Sentinel-2 Imagery. *Remote Sens.* **2018**, *10*, 326. [[CrossRef](#)]
94. Yamamoto, K.H.; Powell, R.L.; Anderson, S.; Sutton, P.C. Using LiDAR to quantify topographic and bathymetric details for sea turtle nesting beaches in Florida. *Remote Sens. Environ.* **2012**, *125*, 125–133. [[CrossRef](#)]
95. Dolan, M.F.J.; Grehan, A.J.; Guinan, J.C.; Brown, C. Modelling the local distribution of cold-water corals in relation to bathymetric variables: Adding spatial context to deep-sea video data. *Deep. Res. Part I Oceanogr. Res. Pap.* **2008**, *55*, 1564–1579. [[CrossRef](#)]
96. Lundblad, E.R.; Wright, D.J.; Miller, J.; Larkin, E.M.; Rinehart, R.; Naar, D.F.; Donahue, B.T.; Anderson, S.M.; Battista, T. A Benthic Terrain Classification Scheme for American Samoa. *Mar. Geod.* **2006**, *29*, 89–111. [[CrossRef](#)]
97. Goes, E.R.; Brown, C.J.; Araújo, T.C. Geomorphological Classification of the Benthic Structures on a Tropical Continental Shelf. *Front. Mar. Sci.* **2019**, *6*, 47. [[CrossRef](#)]
98. Lacharité, M.; Brown, C.J.; Gazzola, V. Multisource multibeam backscatter data: Developing a strategy for the production of benthic habitat maps using semi-automated seafloor classification methods. *Mar. Geophys. Res.* **2018**, *39*, 307–322. [[CrossRef](#)]
99. Pirtle, J.L.; Weber, T.C.; Wilson, C.D.; Rooper, C.N. Assessment of trawlable and untrawlable seafloor using multibeam-derived metrics. *Methods Oceanogr.* **2015**, *12*, 18–35. [[CrossRef](#)]
100. Monk, J.; Ierodiaconou, D.; Versace, V.L.; Bellgrove, A.; Harvey, E.; Ratray, A.; Laurendon, L.; Quinn, G.P. Habitat suitability for marine fishes using presence-only modelling and multibeam sonar. *Source Mar. Ecol. Prog. Ser.* **2010**, *420*, 157–174. [[CrossRef](#)]
101. Pearman, T.R.R.; Robert, K.; Callaway, A.; Hall, R.; Lo Iacono, C.; Huvenne, V.A.I. Improving the predictive capability of benthic species distribution models by incorporating oceanographic data—Towards holistic ecological modelling of a submarine canyon. *Prog. Oceanogr.* **2020**, *184*, 102338. [[CrossRef](#)]

102. Trzcinska, K.; Janowski, L.; Nowak, J.; Rucinska-Zjadacz, M.; Kruss, A.; von Deimling, J.S.; Pocwiardowski, P.; Tegowski, J. Spectral features of dual-frequency multibeam echosounder data for benthic habitat mapping. *Mar. Geol.* **2020**, *427*, 106239. [[CrossRef](#)]
103. Diesing, M.; Mitchell, P.J.; O'Keeffe, E.; Gavazzi, G.O.A.M.; Bas, T. Le Limitations of Predicting Substrate Classes on a Sedimentary Complex but Morphologically Simple Seabed. *Remote Sens.* **2020**, *12*, 3398. [[CrossRef](#)]
104. Poursanidis, D.; Traganos, D.; Chrysoulakis, N.; Reinartz, P. Cubesats allow high spatiotemporal estimates of satellite-derived bathymetry. *Remote Sens.* **2019**, *11*, 1299. [[CrossRef](#)]
105. Misra, A.; Vojinovic, Z.; Ramakrishnan, B.; Luijendijk, A.; Ranasinghe, R. Shallow water bathymetry mapping using Support Vector Machine (SVM) technique and multispectral imagery. *Int. J. Remote Sens.* **2018**, *39*, 4431–4450. [[CrossRef](#)]
106. Apostolopoulos, D.; Nikolakopoulos, K. A review and meta-analysis of remote sensing data, GIS methods, materials and indices used for monitoring the coastline evolution over the last twenty years. *Eur. J. Remote Sens.* **2021**, *54*, 240–265. [[CrossRef](#)]
107. Gao, J. Bathymetric mapping by means of remote sensing: Methods, accuracy and limitations. *Prog. Phys. Geogr.* **2009**, *33*, 103–116. [[CrossRef](#)]
108. Shand, R.D.; Bailey, D.G. A review of net offshore bar migration with photographic illustrations from Wanganui, New Zealand. *J. Coast. Res.* **1999**, *15*, 365–378.
109. Aagaard, T.; Kroon, A.; Hughes, M.G.; Greenwood, B. Field observations of nearshore bar formation. *Earth Surf. Process. Landf.* **2008**, *33*, 1021–1032. [[CrossRef](#)]
110. Melito, L.; Parlagreco, L.; Perugini, E.; Postacchini, M.; Devoti, S.; Soldini, L.; Zitti, G.; Liberti, L.; Brocchini, M. Sandbar dynamics in microtidal environments: Migration patterns in unprotected and bounded beaches. *Coast. Eng.* **2020**. [[CrossRef](#)]
111. Walstra, D.-J.; Wesselman, D.; van der Deijl, E.; Ruessink, G. On the Intersite Variability in Inter-Annual Nearshore Sandbar Cycles. *J. Mar. Sci. Eng.* **2016**, *4*, 15. [[CrossRef](#)]
112. van Son, S.; Lindenbergh, R.C.; de Schipper, M.A.; de Vries, S.; Duijnmaier, K. Monitoring bathymetric changes at storm scale. *PositionIT* **2010**, *9*, 59–65.
113. Ruessink, B.G.; Pape, L.; Turner, I.L. Daily to interannual cross-shore sandbar migration: Observations from a multiple sandbar system. *Cont. Shelf Res.* **2009**, *29*, 1663–1677. [[CrossRef](#)]
114. Ma, L.; Soomro, N.Q.; Shen, J.; Chen, L.; Mai, Z.; Wang, G. Hierarchical Sea-Land Segmentation for Panchromatic Remote Sensing Imagery. *Math. Probl. Eng.* **2017**, *2017*, 1–8. [[CrossRef](#)]
115. Paravolidakis, V.; Ragia, L.; Moirogiorgou, K.; Zervakis, M.E. Automatic coastline extraction using edge detection and optimization procedures. *Geosciences* **2018**, *8*, 407. [[CrossRef](#)]

II PUBLIKACIJA

Analysis of Interannual and Seasonal Nearshore Bar Behaviour Observed from Decadal Optical Satellite Data in the Curonian Spit, Baltic Sea

Janušaitė R., Jarmalavičius D., Jukna L., Žilinskas G., Pupienis D.

Remote Sensing, 2022, 14 (14): 3423.

DOI: <https://doi.org/10.3390/rs14143423>



Article

Analysis of Interannual and Seasonal Nearshore Bar Behaviour Observed from Decadal Optical Satellite Data in the Curonian Spit, Baltic Sea

Rasa Janušaitė ¹, Darius Jarmalavičius ^{1,*}, Laurynas Jukna ², Gintautas Žilinskas ¹ and Donatas Pupienis ¹

¹ Laboratory of Geoenvironmental Research, Nature Research Centre, 08412 Vilnius, Lithuania; rasa.janusaitė@gamtc.lt (R.J.); gintautas.zilinskas@gamtc.lt (G.Ž.); donatas.pupienis@gamtc.lt (D.P.)

² Institute of Geosciences, Vilnius University, 03101 Vilnius, Lithuania; laurynas.jukna@gef.vu.lt

* Correspondence: darius.jarmalavicius@gamtc.lt

Abstract: Long-term observations of nearshore bar behaviour are a vital component of coastal monitoring, management, and prediction. Optical satellite remote sensing enables the possibility of such observations over large spatial areas, but its full potential remains unexploited. This study assessed alongshore variability in cross-shore nearshore bar behaviour on a wave-dominated multi-bar coast of the Curonian Spit (south-eastern Baltic Sea) between 2011 and 2021, using satellite-derived bar data. Nearshore bars were extracted from a time series of PlanetScope and RapidEye satellite images with an automated GIS-based algorithm, previously proposed by the study authors. The cross-shore behaviour of a multiple bar system was analysed by adapting traditional bathymetry-based analysis techniques to satellite-derived data that included bar crestlines and images of multi-scale Relative Bathymetric Position Index (RBPI). The analysis was performed on 1071 shore-perpendicular transects. Multi-bar onshore and offshore migration rates were quantified on interannual and seasonal timescales. The results show that, on an interannual timescale, bars migrated offshore at rates up to 9.7 m/month, while the rates of onshore migration reached up to 11 m/month. During the months of low wave energy, bars moved offshore at rates up to 6.2 m/month, and during the months of high wave energy, up to 12.9 m/month. However onshore migration rates, during the months of low and high wave energy, reached up to 7.0 and 13.4 m/month, respectively. A complex empirical orthogonal function (CEO) analysis was performed on RBPI-derived cross-shore profiles, and cyclic offshore directed bar behaviour was examined. For the first time, the net offshore migration (NOM) cycle with bar cycle return periods of 1.8 to 13.5 years was investigated on the south-eastern Baltic Sea coast. Bar cycle return periods increased and rates of bar cross-shore migration decreased from north to south along the Curonian Spit. Similar nearshore bar behaviour regions were identified using clustering analysis based on quantified temporal and morphological characteristics of the bars. Factors controlling alongshore variability in bar cross-shore behaviour were determined. The study results suggest that small alongshore variations in nearshore hydrodynamics, caused by the local wave climate and its interplay with the shoreline orientation, determine the morphological and temporal variability of the multi-bar system in the Curonian Spit.



Citation: Janušaitė, R.; Jarmalavičius, D.; Jukna, L.; Žilinskas, G.; Pupienis, D. Analysis of Interannual and Seasonal Nearshore Bar Behaviour Observed from Decadal Optical Satellite Data in the Curonian Spit, Baltic Sea. *Remote Sens.* **2022**, *14*, 3423. <https://doi.org/10.3390/rs14143423>

Academic Editors: Cristina Ponte Lira and Ana Nobre Silva

Received: 2 June 2022

Accepted: 14 July 2022

Published: 16 July 2022

Publisher's Note: MDPI stays neutral with regard to jurisdictional claims in published maps and institutional affiliations.



Copyright: © 2022 by the authors. Licensee MDPI, Basel, Switzerland. This article is an open access article distributed under the terms and conditions of the Creative Commons Attribution (CC BY) license (<https://creativecommons.org/licenses/by/> 4.0/).

1. Introduction

Sandy coastal systems are characterised by submerged shore-parallel ridges, also known as nearshore bars, which form as a result of sedimentary processes in the surf zone. They are frequently observed as single or multiple bar systems in wave-dominated environments, ranging from non-tidal to macrotidal [1]. As the first line of coastal protection, bars are closely related to coastal stability, beach erosion, and shoreline position [2–4]. Bar

morphologies are portrayed by striking variability in their cross-shore and alongshore appearances [5,6].

In response to variability in the wave climate, bar cross-shore positions change over time [7–9]. Nearshore bars have been observed to respond to hydrodynamic forcing on a variety of timescales, from storm-related [10–12] to seasonal [13,14] and interannual [15–17]. The size of the bars appears to govern the dominant timescale [18].

On a storm-related timescale, the strong undertow induced by energetic wave conditions causes bars to migrate offshore [19]. Offshore bar migration rates of 1 m/day to 50 m/day have been reported during high-wave events [7,10,20]. Although rarely, onshore bar movement under storm conditions has also been observed [21,22].

On a seasonal timescale, seaward and landward bar movements are observed. Typically, periods of low-wave-energy conditions are associated with slow onshore bar movement, while periods of high-energy conditions are related to fast episodic offshore movements [13]. Seasonal variations in the bar position of up to 1 m/day and up to 1.2 m/day have been observed for landward and seaward migration, respectively [5,23].

On an interannual timescale, cyclic bar behaviour incorporating net offshore migration (NOM) has been observed at many sites worldwide [15,17,23–27] with several locations exhibiting net onshore migration [28,29]. During the interannual cross-shore migration cycles, bars generate near the shoreline, move offshore across the nearshore, and decay at the outer nearshore boundary [15]. NOM has been observed to last from a year [26] to nearly two decades [15,24,25,27,30–33]. At NOM sites, seaward bar migration rates of 20 to 200 m/year have been reported [15,24,32,34].

Most studies that analysed bar behaviour on storm-related, seasonal, or interannual timescales assessed the cross-shore movement of single, double, or triple bar systems and provided migration rates, mostly for the inner and outer bars only. Several studies attempted to quantify the cross-shore migration of bars on multiple timescales simultaneously [5,7,14,23], but such quantifications were completed only for limited alongshore lengths (<5 km).

Numerous studies used bathymetric [13,14,23,25,27,30,32,33,35,36] or remotely sensed data acquired by video monitoring systems [5,7,37] to determine the variability of bar cross-shore temporal and morphological characteristics. Only a very few of these studies focused on regions with alongshore lengths greater than tens [25,27] or hundreds of kilometres [17,35]. Recently, studies that used optical satellite imagery to detect nearshore bars emerged [38–42]. The methods proposed in these studies, when combined with Earth observation satellites, enable the possibility of studying bars over large spatial scales with a temporal frequency of days [43]. Since datasets with such spatiotemporal extents are unavailable for many sandy beaches worldwide, satellite remote sensing is a cost-effective alternative to state-of-the-art methods used to investigate bar behaviour. However, research involving the use of satellite images to investigate bars has not yet specifically focused on quantifying the cross-shore behaviour of bars.

The aim of this study is to assess the alongshore variability in interannual and seasonal bar cross-shore behaviour by adapting traditional analysis techniques to satellite-derived bar data using a case study of the multi-bar system, located along the Curonian Spit, south-eastern Baltic Sea. It is an extension of a previous study by Janušaitė et al. [39] who suggested a methodology to automatically extract nearshore bars from satellite images. Another study by Janušaitė et al. [2] proved that the medium-resolution satellite imagery used in this study is a powerful tool to study the phenomena of three-dimensional bar behaviour, particularly multi-bar switching, and its interplay with coastal evolution, whereas this study focuses on the analysis of two-dimensional bar behaviour. The motivation for this study is based on a paucity of studies focussing on: (1) the alongshore variability of cross-shore behaviour of bars in large spatial extents; (2) bar cross-shore behaviour in multi-bar systems with more than two or three bars; (3) quantification of cross-shore movement of bars and NOM using satellite-derived data; and (4) alongshore variability in bar cross-shore migration rates on multiple timescales. As an outcome of this study, we

provide a detailed methodology for using satellite-derived data to quantify the morphological and temporal characteristics of bars, including rates of cross-shore migration of bars on multiple timescales and NOM characteristics. The results are then demonstrated by analysing alongshore variability for the derived characteristics of the multi-bar system in the Curonian Spit and identifying nearshore regions with similar bar behaviour. We discuss the results by identifying factors influencing alongshore variability in bar dynamics and defining the limitations of this study.

2. Materials and Methods

2.1. Study Area

The research was undertaken in the Curonian Spit, located on the south-eastern coast of the Baltic Sea. The Curonian Spit is a 98-km-long sandy barrier, the territory of which is divided between the Republic of Lithuania and the Russian Federation. In this study, the 51-km-long Lithuanian part, stretching from the Klaipéda Strait in the northern end to the settlement of Nida in the south, is analysed (Figure 1).

The study area is a non-tidal (3.5–4.0 cm tidal range) environment with predominant wind-generated waves, alongshore currents, and net sediment transport directed from south to north. The Curonian Spit is predominantly exposed to a wave climate with waves approaching from westerly (NW, W, SW) directions [44,45] with an annual mean significant wave height of 0.52 m. Based on Copernicus Baltic Sea wave reanalysis data [46], monthly averaged significant wave heights from April to September range between 0.33 m and 0.55 m, while from October to March they vary between 0.60–0.84 m. During the strongest storms, when the wind speeds are close to or above the hurricane-force threshold, the wave height in the nearshore region reaches up to 5–6 m.

The subaerial beaches are composed of fine to medium sands. They are 30–65 m wide, with the widest at Smiltynė and the narrowest at Juodkrantė [47]. The beaches are bounded by a foredune ridge with high alongshore variability in height above mean sea level and sediment volume, determined as enclosed sand from the foredune toe to a point inland where the vertical variability are minimal. These characteristics range from $110\text{ m}^3/\text{m}$ at Juodkrantė to $2200\text{ m}^3/\text{m}$ at Smiltynė, and from 6 m at Juodkrantė to 16 m at Alksnynė [47].

The surf zone is characterised by a mean nearshore slope of 0.01 (up to 8 m depth) and features a multiple bar system with 2–5 bars. The morphologies of the bars vary from longshore straight to quasi-regular crescentic and shore-attached with shore-parallel or slightly oblique orientation (Figure 1C,D). Bars are composed of fine sand (0.1–0.25 mm), while troughs are made of coarser grain sizes ranging from fine to medium (0.25–0.5 mm) and coarse (0.5–1 mm) sands, sometimes with an admixture of shingle [48]. The development of most of the study area is governed by natural processes and only the northern end of the Curonian Spit is influenced by the Klaipéda port jetties [49]. Therefore, the approximately 300 m longshore section around Kopgalis lacks a well-developed bar system and was excluded from the analysis.

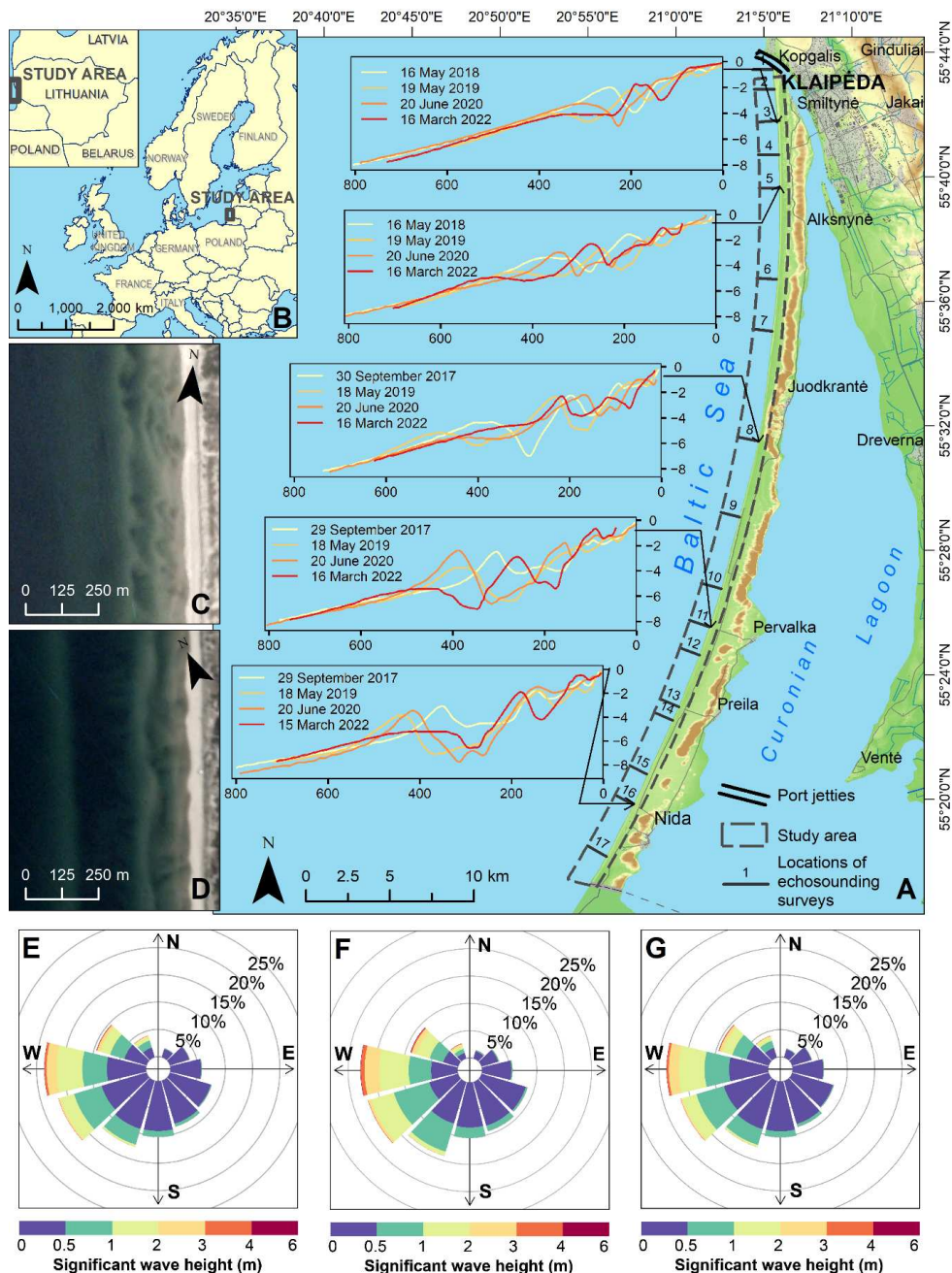


Figure 1. Configuration (A) and location (B) of the Curonian Spit (adapted from Janušaitė et al. [2,39]). Panels (C,D) contain PlanetScope images showing the typical bar morphologies at Smiltynė (C) and Nida (D). Panels (E–G) display wave roses of the Curonian Spit in 2011–2021, derived from the Copernicus Baltic Sea wave reanalysis data [46] for the entire year (E), high- (F) and low- (G) wave-energy seasons.

2.2. Data

The main data source for this study was multispectral images captured by the RapidEye and PlanetScope satellite constellations between 2011 and 2021 [50]. The RapidEye constellation consisted of five identical sensors that acquired images with five spectral bands (blue, green, red, red-edge, and near-infrared) at a 5-m spatial resolution every 5.5 days between 2008 and 2020. Since 2017, groups of individual CubeSats of the PlanetScope constellation have been acquiring images daily with four spectral bands (blue, green, red, and near-infrared) at a 3-m spatial resolution. To match the spatial resolution of RapidEye images, PlanetScope images were resampled at a 5-m resolution using bilinear interpolation. Images were selected based on three criteria: cloud cover of less than 20%, no visible wave breaking, and bars were visible. A total of 145 dates met the criteria. However, to maintain evenly spaced observations with a relatively low number of gaps, we decided to use monthly data, with the first available date of each month being chosen for analysis. The average difference between two consecutive observations was 2.3 months, but since the PlanetScope constellation was only launched in 2017, the available observations were unevenly distributed during the analysed period. Between 2011 and 2016, the difference between the two consecutive observations ranged from 1 to 10 months (on average, 3.4 months). Between 2017 and 2021, the difference between two consecutive observations varied from 1 to 5 months (on average, 1.6 months). In addition, the seasonal distribution of the available data was uneven, with most images captured between March and October and only a small number of images acquired between November and February, as the Curonian Spit rarely has cloud- and wave-free days during these months.

To determine the factors that influence the temporal characteristics of the nearshore bars, we used bathymetric and wave data. Bathymetric data were obtained from semi-annual echo-sounding surveys performed between 2017 and 2022 at 17 cross-shore locations along the study area (Figure 1A). Wave parameters for shallow nearshore waters were extracted from the hourly Baltic Sea wave reanalysis data with a spatial resolution of 2 km, provided by the Copernicus Marine Service [46].

2.3. Extraction and Preparation of Bar Data

We extracted bar data from satellite images following the approach proposed by Janušaitė et al. [39]. It is a multi-step algorithm that consists of four stages used to detect various morphological features for bar analysis: extracting the shoreline, calculating the multi-scale Relative Bathymetric Position Index (RBPI) with nearshore morphological features, identifying the bar boundaries, and deriving the positions of the bar crests within defined boundaries. RBPI is a signed metric of a local bathymetric position that indicates whether the pixel depth is higher or lower than the mean in the local neighbourhood, defined by the window size and normalised by the minimum and maximum values within the local neighbourhood [51]. We used surface reflectance of visible spectrum bands in the calculation of the RBPI as an indicator of shallower and deeper nearshore regions. The RBPI result is very similar to the bathymetry-derived perturbations except that the values do not match the true depth deviations. This enables the possibility to analyse bar behaviour without the necessity of expensive and time-intensive bathymetric surveys or implementation of bathymetry derivation algorithms.

The RBPI outputs were created by implementing a multi-scale approach that combines RBPI values in different-sized local neighbourhoods (3–39 pixels). Such an approach allows the identification of both smaller and larger bar morphologies, regardless of their distance from the shoreline. RBPI images, used as inputs for unsupervised classification and criteria-based selection operations, were employed to distinguish bar boundaries. Within these boundaries, bar crest locations were derived as maximum value pixels in shore-perpendicular and shore-oblique directions, then non-crest pixels were removed with a proximity-based filter. This approach to deriving bar crests, designed for variously oriented crests, is customised for diverse bar morphologies. The accuracy of the method was assessed by comparing satellite-derived crest positions with a bathymetry-derived

algorithm. It was determined that with this algorithm, bar crests were derived with an average root mean squared error (*RMSE*) of 5.8 and 7.0 m for PlanetScope and RapidEye sensors, accordingly. Between the inner and outer bars, the *RMSE* was between 3.8 m and 7.7 m [39]. To avoid the influence of possible errors on the results, we decided to exclude short-term changes in bar morphology from the analysis, and only seasonal and interannual bar behaviour were evaluated.

We conducted a further analysis of the cross-shore temporal and morphological characteristics of the bars using two satellite-derived outputs: RBPI images and bar crest positions. The traditional cross-shore profiling technique was applied, and 1071 shore-perpendicular profiles with 50-m alongshore spacing were employed for analysis. Two databases with bar characteristics were created: one with a monthly time series of RBPI cross-shore profiles at a 5-m spatial resolution and another with a monthly time series of bar distances from the shoreline, bar positions relative to the shoreline, and bar counts. The bar distance from the shoreline was defined as the distance from the mean shoreline of the intersection point between the bar crestline and the profiles. The mean shoreline was obtained from the time series of satellite-derived shorelines by identifying their mean position at each profile between 2011 and 2021. Positions relative to the shoreline, from first to fifth, were assigned to the bars, with the first bar being the seaward-most (outer) bar, the second being the second-seaward-most bar, etc. Figure 2 overviews the main data extraction and analysis steps of this study.

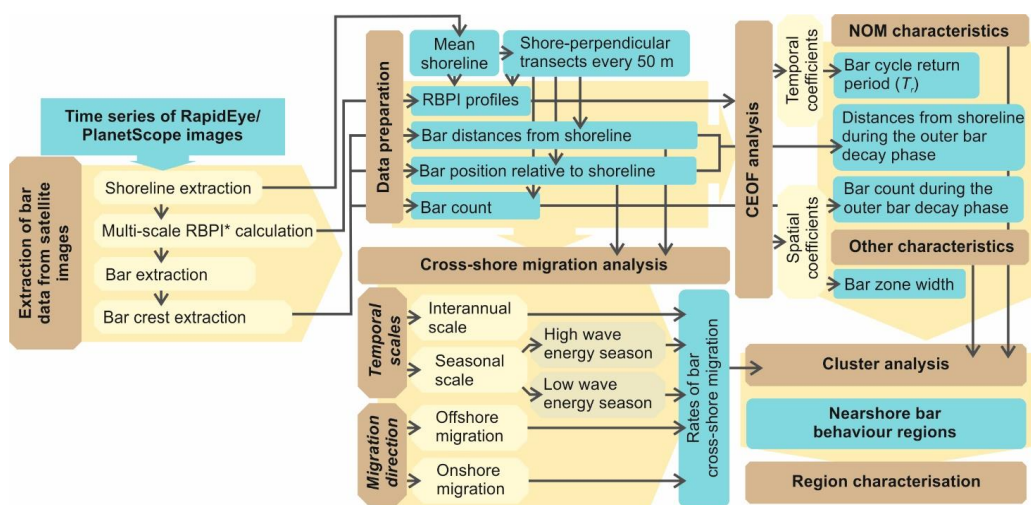


Figure 2. Flowchart describing the process of nearshore bar data extraction and analysis (RBPI*—Relative Bathymetric Position Index).

Bar data extraction, preparation, and further spatiotemporal analysis were performed in the R programming language or with ArcGIS Desktop 10.7.

2.4. Assessment of Interannual and Seasonal Migration Rates

We determined the rates of interannual and seasonal bar migration using the seasonal and interannual components of the time series of the bar distances from the shoreline for each cross-shore profile, as proposed by [5,23]. It was achieved in the following order: (1) an interannual component was obtained by computing a 12-month rolling mean of the time series of the bar distances from the shoreline; (2) the difference between the original time series of the bar distances from the shoreline and the interannual component was calculated; (3) a seasonal component was obtained by computing a 6-month rolling mean of

the difference, determined in point two; (4) interannual migration rates were computed as a temporal derivative of the interannual component; and (5) seasonal migration rates were computed as a temporal derivative of the sum of seasonal and interannual components. Positive rates of the interannual and seasonal bar migration, determined in steps four and five, were considered as the rates of offshore bar migration, while the negative rates were considered as the rates of onshore bar migration. A 6-month rolling mean was chosen to compute the seasonal component because two seasons were considered when evaluating seasonal bar migration: seasons of relatively low (April–September) and high (October–March) wave energy. Four seasons could be distinguished in the Curonian Spit, but because the availability of cloudless and wave-free satellite images in the winter months is limited, we decided to only use the two most important seasons, which are separated by the typical beginning and the end of the storm season. Seasonal bar migration rates were divided between these two periods of the year. Prior to the computation of the interannual and seasonal components, the bar distances from the shoreline were longshore averaged using a 500-m sliding window.

2.5. Assessment of Net Offshore Migration and Other Characteristics

Previous studies established the bar cycle return period (T_r)—a time between two successive bar decay events—as a core parameter describing progressive offshore bar behaviour [17,25,30–32]. Ruessink et al. [30] suggested a detailed methodology to extract T_r , along with the other geometric and temporal bar characteristics, via complex empirical orthogonal function analysis (CEOF) using cross-shore bathymetric profiles. Here, we adapted this CEOF-based methodology to non-bathymetric satellite-derived bar data.

Originally, the perturbation matrix is computed by subtracting the mean bathymetric profile from the original profile time series, and CEOF is performed on a complex matrix whose real part is the perturbation matrix and the imaginary part is the Hilbert transform of that matrix. In this study, the bathymetric perturbation matrix was replaced with that retrieved from the time series of RBPI profiles (Figure 3).

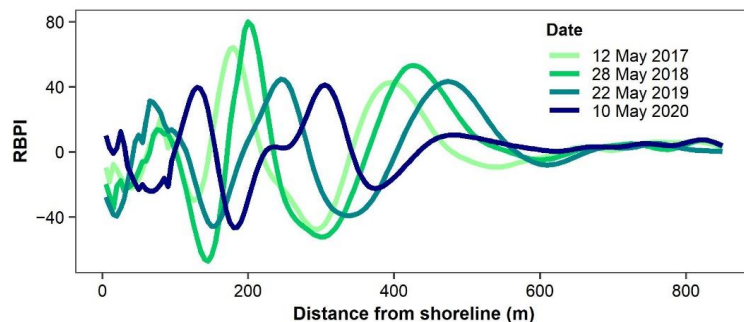


Figure 3. An example time series of filtered profiles of Relative Bathymetric Position Index (RBPI). The NOM pattern is clearly detectable in the time series.

Prior to CEOF analysis, the RBPI profiles were filtered with a fifth-order Butterworth low-pass filter and longshore averaged using a rolling mean with a 500-m window (Figure 3). A linear-weighted moving average was used to fill in missing values in the monthly RBPI time series with a moving average window equal to 4 (both sides left and right) (Figure 4B). To remove periodic noise introduced by longshore averaging and missing data filling, a fast Fourier transform filter was applied. The data were then smoothed using least asymmetric (la16) wavelets in a two-dimensional discrete wavelet transform (Figure 4C). A space-wide RBPI perturbation matrix was computed from the smoothed data, and CEOF was performed.

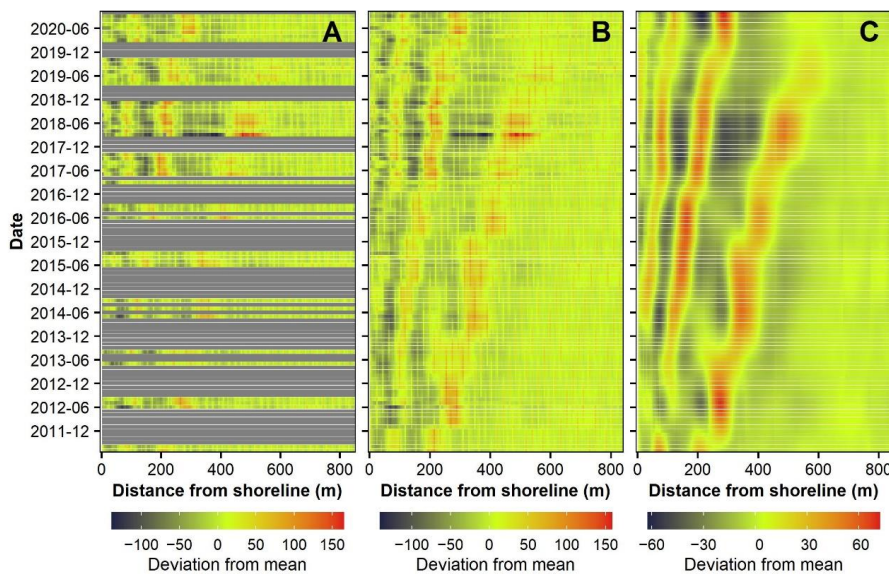


Figure 4. Space-time maps of perturbations in a single cross-shore profile of Relative Bathymetric Position Index (RBPI): (A) gappy monthly data (gaps are marked in grey); (B) data filled with a linear-weighted moving average; (C) data filtered with fast Fourier transform and discrete wavelet transform.

Similar to Ruessink et al. [30], T_r was computed from the third CEOF mode as the ratio between the 2π and the slope of the linear regression line between the unwrapped temporal phase and time. To identify the boundaries of the bar zone (W_{bz}), the spatial envelope of the bar amplitude (S) was extracted from the spatial CEOF coefficients. This shows the part of the profile where the bars were active. With a threshold $S = 0.35$, the landward and seaward limits of the barred part of the RBPI profile were defined.

Other NOM-related characteristics were computed using the database with bar distances from the shoreline. Outer bar distances from the shoreline during the decay phase of the NOM cycle ($X_{out-peak}$) were determined by identifying peak locations in a curve of a time series of the outer bar distances from the shoreline (X_{1st}). To locate the middle and inner bars during the decay phase of the outer bar, their distances from the shoreline for the dates of the $X_{out-peak}$ were extracted as $X_{mid-peak}$ and $X_{inn-peak}$, respectively. Table 1 lists all parameters used to assess the temporal and morphological characteristics of bars.

We compared the RBPI-derived cross-shore profiles with the bathymetry-derived profiles to illustrate the accuracy of the results and discuss the limitations of satellite-derived bar data in Section 4.3.

2.6. Definition of Nearshore Bar Behaviour Regions

We performed a cluster analysis to objectively separate alongshore nearshore regions that demonstrated similar patterns of bar morphology and behaviour. The clustering of cross-shore profiles included all parameters listed in Table 1. Although several clustering methods were tested, a hybrid approach combining agglomerative hierarchical and k-means clustering was selected and complete linkage was used as the agglomeration method. To identify multi-scale bar behaviour regions, clustering was performed on several levels. As a result, three-level clusters were distinguished, with two, four, and six clusters. The number of clusters was determined using the dendrogram of hierarchical clustering and several indices intended for choosing the optimal number of clusters. Six indices proposed two, three proposed four, and one proposed six as the optimal number of clusters.

Table 1. The abbreviations for the temporal and morphological parameters of the nearshore bars used in this study. The subscripts 1st, 2nd, 3rd, and 4th indicate if the parameter applies to the first, second, third, or fourth bar. Offshore and onshore bar migration rates were calculated in metres per month (m/mo).

Parameter	Abbreviation
Bar cycle return period	T_r
Bar distances from shoreline	$X_{1st}, X_{2nd}, X_{3rd}, X_{4th}$
Bar count (mode)	N_b
Bar zone width	W_{bz}
Rate of interannual offshore migration	$V_{off-1st}, V_{off-2nd}, V_{off-3rd}, V_{off-4th}$
Rate of interannual onshore migration	$V_{on-1st}, V_{on-2nd}, V_{on-3rd}, V_{on-4th}$
Rate of seasonal offshore migration (April–September)	$V_{off-low-1st}, V_{off-low-2nd}, V_{off-low-3rd}, V_{off-low-4th}$
Rate of seasonal onshore migration (April–September)	$V_{on-low-1st}, V_{on-low-2nd}, V_{on-low-3rd}, V_{on-low-4th}$
Rate of seasonal offshore migration (October–March)	$V_{off-high-1st}, V_{off-high-2nd}, V_{off-high-3rd}, V_{off-high-4th}$
Rate of seasonal onshore migration (October–March)	$V_{on-high-1st}, V_{on-high-2nd}, V_{on-high-3rd}, V_{on-high-4th}$
Maximum outer bar distance from shoreline at the decay phase	$X_{out-peak}$
Average middle bar distance from shoreline at the outer bar decay phase	$X_{mid-peak}$
Average inner bar distance from shoreline at the outer bar decay phase	$X_{inn-peak}$
Bar count at the outer bar decay phase	N_{b-peak}

3. Results

3.1. Morphological Characteristics of the Bar System

The multi-bar system of the study area displays a diverse alongshore configuration: the triple-bar system dominates in a major part of the Curonian Spit, especially to the south of Alksnyné, while to the north of Alksnyné, the triple-bar system alternates with the quadruple-bar system (Figure 5D). Therefore, the bar count mode (N_b) is three in 85.4% of the profiles, four in 13.0%, and two in 1.6%.

The first bar originates at 104–697 m distance from the shoreline (X_{1st} , IQR = 290–408 m). The mean crest position of the first bar is 349 m from the shoreline (Figure 5B). Along the Curonian Spit, the mean X_{1st} oscillates between 247 and 431 m, with the lowest mean X_{1st} at Smiltyné and the highest in the sector between southern Juodkranté and Pervalka. The crest position of the second bar (X_{2nd}) oscillates between 25 and 336 m (IQR = 123–186 m). It is located at $X_{2nd} = 156$ m on average (Figure 5B), but the mean X_{2nd} varies alongshore between 120 and 189 m, with minimum and maximum values in the same sectors as the first bar.

The third and fourth bars are located at $X_{3rd} = 1$ –208 m (IQR = 48–80 m) and $X_{4th} = 1$ –127 m (IQR = 22–45 m), respectively. The mean X_{3rd} and X_{4th} are 65 and 35 m, accordingly (Figure 5B). The mean crest position of the third and fourth bars decreases from north to south from 81 to 41 m and from 57 to 11 m, respectively. This is related to the fact that, due to the higher bar count in the north, the third bar is typically one of the middle bars, and in the south, it is typically an inner bar. The spacing between the bars increases with their distance from the shoreline. This kind of morphology corresponds to the typical bar distribution in multiple bar systems [1,52].

The average bar zone width (W_{bz}) for the Curonian Spit is 512.5 m, but it ranges alongshore between 340 m and 700 m. The alongshore non-uniformity of W_{bz} is the most evident to the south of Juodkranté, where the sectors of $W_{bz} = 400$ –600 m and $W_{bz} = 550$ –700 m alternate (Figure 5C).

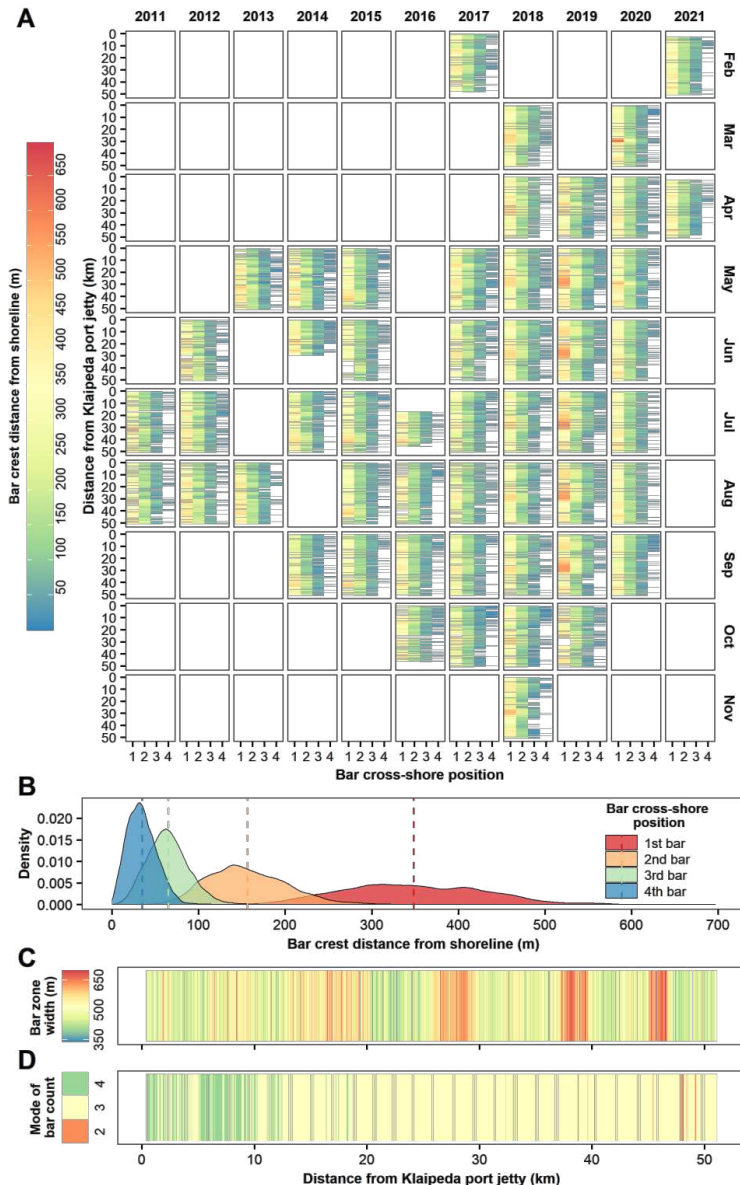


Figure 5. Morphological characteristics of the multi-bar system in the Curonian Spit: (A) alongshore variations in monthly bar distances from the shoreline by bar cross-shore position; (B) distribution of bar distances from the shoreline by bar cross-shore position; (C) alongshore variations in bar zone widths; (D) alongshore variations in bar count mode.

3.2. Interannual Bar Cross-Shore Migration

Both seaward- and landward-directed bar migration rates were computed for the interannual timescale. Depending on bar cross-shore and alongshore location, the time-averaged interannual offshore migration rates (V_{off}) varied between 0.1 and 9.7 m/mo, while the interannual onshore migration rates (V_{on}) ranged between 0.1 and 11.0 m/mo

(Figure 6A,B). Interannual migration rates were higher in the north of the study area than in the south. The boundary between faster and slower nearshore regions for seaward bar movement was at Juodkrantė, and for landward bar movement, it was at Pervalka (Figure 6A,B).

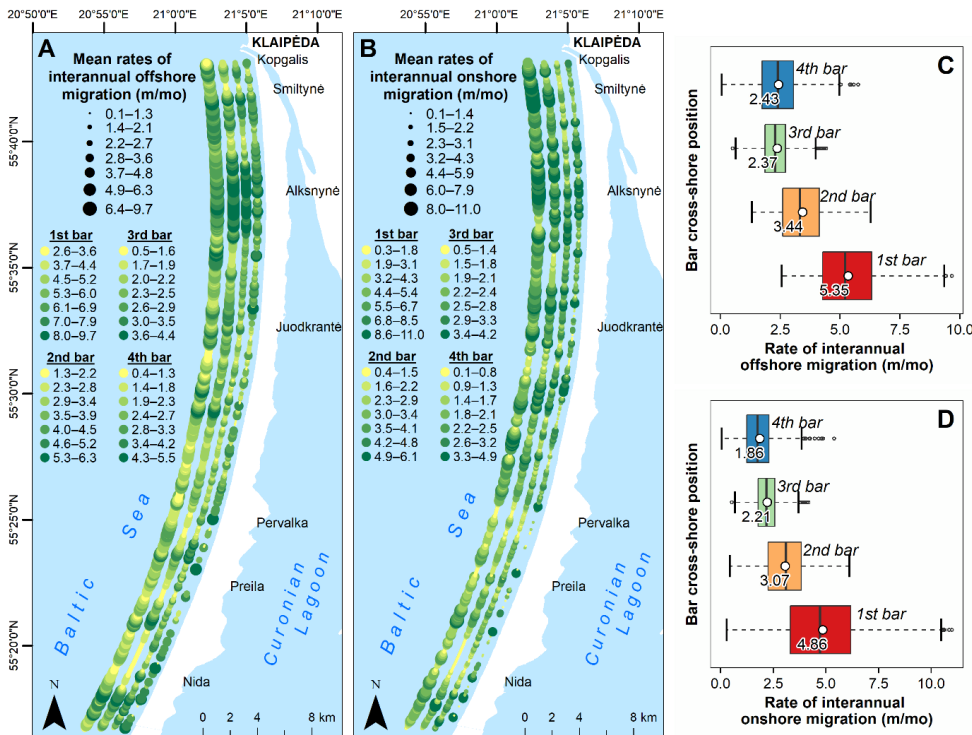


Figure 6. Alongshore variability in rates (m/month) of interannual offshore (A) and onshore (B) migration. The colour scale indicates mean interannual migration rates for different bar cross-shore positions (1st to 4th bar). It is set separately for each position and explained by the legend below the underlines. The 1st bar is depicted furthest from the shore and the 4th bar—closest. Boxplots illustrate the statistical distribution of interannual offshore (C) and onshore (D) migration rates by the cross-shore position of the bars.

The time-averaged V_{off} exceeded V_{on} in most profiles for all bar cross-shore positions: 60.2%, 64.4%, 59.4%, and 67.3% for the first, second, third, and the fourth bars, respectively. The first bar exhibited a higher V_{on} than V_{off} rates, mainly around Smiltynė, the northern part of Alksnynė, and south of Juodkrantė. Other bars demonstrated similar alongshore trends.

The first (outer) bar had the highest overall average of V_{off} and V_{on} ($V_{off} = 5.35$ m/mo, $V_{on} = 4.86$ m/mo) (Figure 6C,D). It moved fastest offshore and onshore in almost the entire study area (in 90.4% and 77.7% of the profiles). In the case of offshore migration, the first bar fell behind other bars only on short random nearshore sectors, while in the case of onshore migration, it was shortly surpassed by the second bar in the north and by the second to fourth bars in the south. The overall average rates of V_{off} and V_{on} for the second bar were 3.44 m/mo and 3.07 m/mo, respectively (Figure 6C,D). The third and fourth bars demonstrated a similar overall average V_{off} ($V_{off} = 2.37$ m/mo and 2.43 m/mo) and V_{on} ($V_{on} = 2.21$ and 1.86 m/mo) rates. Together, they were the slowest offshore and onshore migrating bars along a major part of the Curonian Spit (in 91.6% and 80.8% of the profiles).

In the north, between Kopgalis and Juodkrantė, the fourth bar dominated as the slowest bar in landward-directed migration and alternated with the third bar as the slowest in the seaward migration. In the south, the third bar was the slowest in the seaward migration and alternated with the fourth and second bars as the slowest in the landward migration.

3.3. Seasonal Bar Cross-Shore Migration

3.3.1. Low-Wave-Energy Season

In the low-wave-energy season, comprising the months between April and October, ranges of time-averaged offshore ($V_{off-low}$) and onshore (V_{on-low}) migration rates were similar: 0.1–6.2 m/mo and 0.1–7.0 m/mo, respectively, depending on bar cross- and alongshore positions (Figure 7A,B). In the north, between Kopgalis and Juodkrantė, bars exhibited higher rates of $V_{off-low}$ and V_{on-low} than in the rest of the study area. The rapid northern sector was characterised by the fastest part around Smiltynė and the slowest part around Alksnynė.

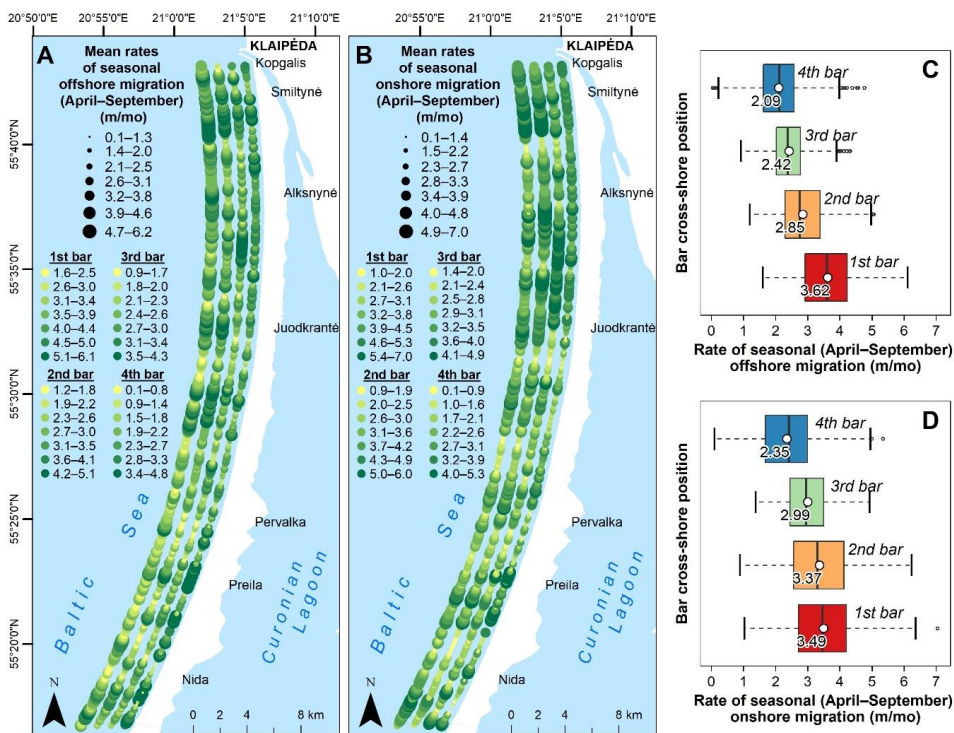


Figure 7. Alongshore variability in rates (m/month) of seasonal offshore (A) and onshore (B) migration in April–September. The colour scale indicates seasonal migration rates in April–September for different bar cross-shore positions (1st to 4th bar). It is set separately for each position and explained by the legend below the underlines. The 1st bar is depicted furthest from the shore and the 4th bar—closest. Boxplots illustrate the statistical distribution of the seasonal offshore (C) and onshore (D) migration rates by the cross-shore position of the bars.

The time-averaged V_{on-low} exceeded $V_{off-low}$ in a slightly larger portion of the Curonian Spit for the second to fourth bars: in 54.6% of the profiles for the second bar, 54.1% for the third, and 57.4% for the fourth. However, for the first bar, time-averaged rates of V_{on-low} were lower than $V_{off-low}$ in 64.5% of the profiles. For the second to fourth bars,

V_{on-low} exceeded $V_{off-low}$ the most between Alksnyné and Juodkranté. For the first bar, the $V_{off-low}$ was higher than V_{on-low} the most around Alksnyné.

The overall average $V_{off-low}$ ($V_{off-low} = 3.62$ m/mo) was the highest for the first bar (Figure 7C), which was fastest-moving in the majority of the profiles (71.5%). The overall averages of $V_{off-low}$ for the second, third, and fourth bars were 2.85 m/mo, 2.42 m/mo, and 2.09 m/mo, respectively (Figure 7C). On the contrary, the global averages of V_{on-low} for the first and second bars were more similar (3.37–3.49 m/mo), while the third and fourth bars exhibited lower overall average rates of V_{on-low} (2.35–2.99 m/mo) (Figure 7D). In terms of V_{on-low} , the first and the second bars were the fastest in more than three quarters of the profiles. The first was the fastest around Juodkranté and between Preila and Nida, the second around Smiltyné and Alksnyné, and in the rest of the study area, the fastest bars alternated without a consistent pattern. The fourth bar was the slowest in over a half of the profiles in both, V_{on-low} and $V_{off-low}$, most evidently in the central sector of the study area. In the case of $V_{off-low}$, it alternated with the second and third bars in another half of the profiles, and with the first and third bars in the case of V_{on-low} .

3.3.2. High-Wave-Energy Season

During the high-wave-energy season, comprising the months between October and March, the ranges of time-averaged offshore ($V_{off-high}$) and onshore ($V_{on-high}$) migration rates were similar: 0.1–12.9 m/mo and 0.1–13.4 m/mo, respectively, depending on bar cross- and alongshore positions (Figure 8A,B). Globally, bars in the north exhibited higher time-averaged rates of $V_{off-high}$ and $V_{on-high}$ than bars in the south. For the first bar, the highest offshore and onshore migration rates were observed between Smiltyné and Alksnyné, while other bars seemed to be faster between Alksnyné and Juodkranté (Figure 8A,B).

The time-averaged $V_{off-high}$ exceeded $V_{on-high}$ in the major part of the Curonian Spit for the first (in 64.5% of profiles) bar, but for other cross-shore positions, $V_{on-high}$ was higher than $V_{off-high}$ in the larger share of profiles (53.5–57.4%).

The global average rates of $V_{off-high}$ depended on the bar cross-shore position, with the first bar demonstrating the highest average rate of 6.56 m/mo, and the fourth bar exhibiting the lowest average rate of 2.47 m/mo (Figure 8C). The first bar showed the highest rates of $V_{off-high}$ in 77.2% of the study area and dominated as the fastest almost along the entire study area except for the sector around Juodkranté, where the second bar often surpassed the first bar. Together, the fourth and the third bars displayed the lowest rates of $V_{off-high}$ in 85.0% of the study area. Between Kopgalis and Pervalka, the fourth bar dominated as the slowest bar, whereas, in the remainder of the study area, the third bar was the slowest, occasionally alternating with other bars.

Analogous to the low wave energy season, the overall average rates of $V_{on-high}$ were relatively similar for the first and the second bars (4.65–5.5 m/mo), while the third and the fourth bars demonstrated lower average rates of $V_{on-high}$ (2.69–3.37 m/mo) (Figure 8D). Together, the first and second bars showed the highest rates of $V_{on-high}$ in 83.0% of the profiles, whereas the third and the fourth bars displayed the lowest rates of $V_{on-high}$ in 71.9% of profiles. The first bar dominated as the fastest in the major part of the Curonian Spit, except for the sector around Juodkranté, where it was surpassed by the second bar. Between Kopgalis and Juodkranté, the fourth bar emerged as the slowest in $V_{on-high}$, and in the rest of the Curonian Spit, it alternated with the second and the third bars.

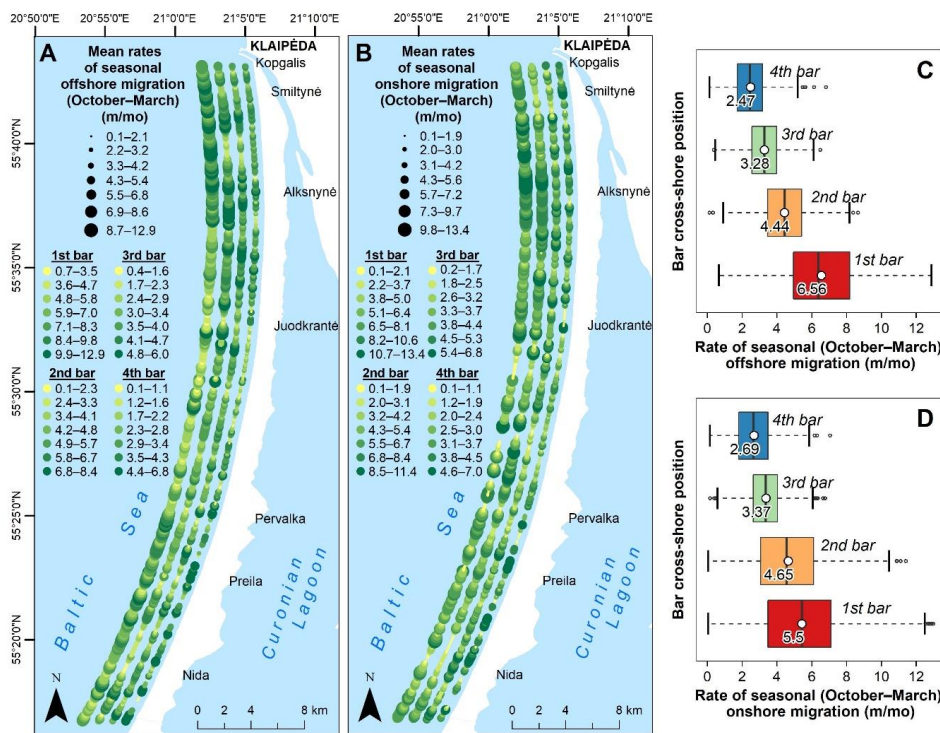


Figure 8. Alongshore variability in seasonal bar offshore (A) and onshore (B) migration rates (m/month) from October to March. The colour scale indicates mean seasonal migration rates in October–March for different bar cross-shore positions (1st to 4th bar). It is set separately for each position and explained by the legend below the underlines. The 1st bar is depicted furthest from the shore and the 4th bar—closest. Boxplots on the right illustrate the statistical distribution of the seasonal offshore (C) and onshore (D) migration rates by the cross-shore position of the bars.

3.4. Comparison of Bar Cross-Shore Migration on Seasonal and Interannual Timescales

Figure 9 shows cross comparisons of bar migration rates on timescales discussed in the previous sections. It shows that, during the months of high wave energy, the rates of seasonal migration in the first bar exceeded the rates of interannual migration in the larger part of the Curonian Spit (in 71.6% of the profiles for offshore and 59.4% for onshore migration). However, the rates of seasonal migration of the first bar during the months of low wave energy were lower than the rates of interannual migration in most of the Curonian Spit (in 92.1% of the profiles for offshore and 65.8% for onshore migration).

The offshore migration trends of other bars were similar: rates of seasonal displacements during the months of high wave energy exceeded the rates of interannual migration in most of the Curonian Spit (in 56.0–81.2% of the profiles), but the rates of interannual migration were higher than the seasonal rates during the months of low wave energy. The onshore migration rates for the second to fourth bars, on the other hand, were slightly different: the seasonal migration rates during the months of high wave energy exceeded the rates during the months of low wave energy in 58.6–73.1% of the profiles, and the seasonal rates during the months of low wave energy were higher than the rates of interannual onshore migration in 61.7–84.6% of the profiles. These results indicate that seasonal variations in bar cross-shore position during the high-wave-energy season account for the largest

share of the cross-shore variability of the bars. This also implies that the largest share of bar cross-shore behaviour in the Curonian Spit is governed by high-wave-energy events.

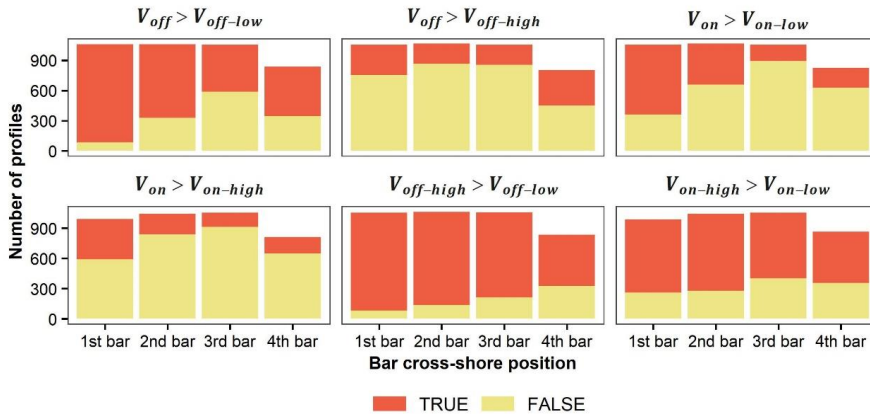


Figure 9. Comparison of bar cross-shore migration rates on different timescales. The orange in the figure indicates the number of cross-shore profiles where the average migration rates on the timescale on the left side of the greater-than sign exceeded the rates on the timescale on the right side; pale yellow indicates where the right side exceeded the left side.

With the increasing distance from the shoreline, the share of profiles, where the average seasonal migration rates exceeded the rates of the interannual bar movements, decreased slightly. This shows that, with the increasing distance from the shoreline, the seasonal cross-shore variability of the bars decreased slightly compared to the interannual variability.

3.5. Net Offshore Migration (NOM)

On an interannual timescale, bars in the Curonian Spit display a progressive offshore-directed cyclic behaviour, first described on the Dutch coast [15], and then followed by observations at many other sites worldwide [17,23–26]. Consistent with the Dutch model, bars in the Curonian Spit generate near the shoreline and subsequently move seaward and landward at rates described in the previous sections. On a multi-annual scale, bars migrate net offshore across the surf zone until they finally decay at the seaward limit of the nearshore. A time period, separating two consecutive bar decay events, is defined by the bar cycle return period (T_r), estimated from the third complex mode as a result of the CEOF analysis. The average estimated T_r in the Curonian Spit was 6.7 years. However, bar cycle return periods highly varied alongshore, ranging from 1.8 years in the north to 13.5 years in the south (Figure 10).

Bars between Kopgalis and Juodkrantė demonstrated shorter-than-average return periods (1.8–5.3 years), while from southern Juodkrantė to Nida, T_r was longer than average (7–13.5 years) (Figure 10). Around the southern Juodkrantė, the return periods greatly varied and ranged from 4.3 to 9.6 years (Figure 10). During the study period, the 3.5 km-long southernmost nearshore sector showed no evident NOM-like behaviour, hence T_r was not estimated here.

The outer bars decayed located at $X_{out-peak} = 255\text{--}696\text{ m}$ ($\bar{X}_{out-peak} = 472\text{ m}$). They degenerated at positions furthest from the shoreline between 20 and 30 km from the Klaipėda port jetty ($\bar{X}_{out-peak} = 552\text{ m}$) and decayed closest to the shoreline at the northern end of the study area ($\bar{X}_{out-peak} = 357\text{ m}$). On the dates of $X_{1st} = X_{out-peak}$, middle (second) and inner bars were located at $X_{mid-peak} = 121\text{--}331\text{ m}$ ($\bar{X}_{mid-peak} = 208\text{ m}$) and $X_{inn-peak} = 41\text{--}258\text{ m}$ ($\bar{X}_{inn-peak} = 67\text{ m}$).

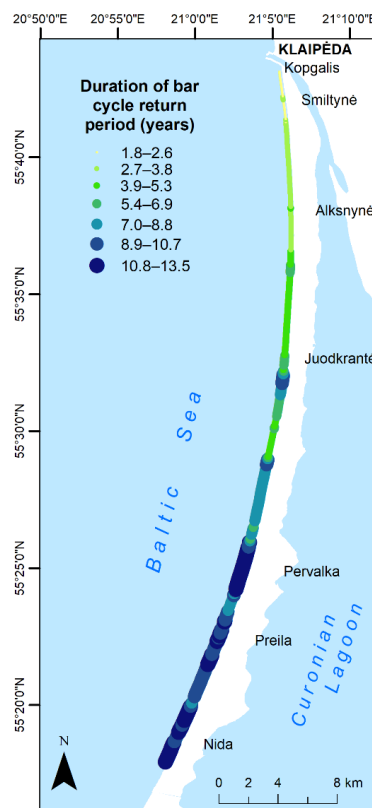


Figure 10. Alongshore variability in the bar cycle return periods (T_r).

3.6. Similar Nearshore Bar Behaviour Regions

Wijnberg and Terwindt [53] introduced the concept of large-scale coastal behaviour (LSCB) regions, in which bars exhibit similar patterns of cross-shore temporal and morphological characteristics. The LSCB regions were based on changes in profile shape and cross-shore position determined from the long-term bathymetric dataset. Similarly, we sought to identify alongshore nearshore regions, which demonstrated similar features of bar cross-shore behaviour based on a cluster analysis of 36 satellite-derived characteristics of the multiple bar system at three spatial scales. Because of the differences in the nature of methodology, we refer to them as large-scale (L1), mid-scale (L2), and small-scale (L3) nearshore bar behaviour (NBB) regions. Identified NBB regions and their mean characteristics are given in Figure 11.

At the large-scale level, two NBB regions (L1-1 and L1-2) mainly divided the study area into southern (L1-2) and northern (L1-1) parts (Figure 11B). In the northern part, the average bar return periods were twice as short as in the southern part (4.3 and 9.0 years), bars exhibited higher rates of interannual and seasonal migration, nearshore contained a higher number of bars, narrower bar zone, and outer bars located closer to the shoreline (Figure 11A).

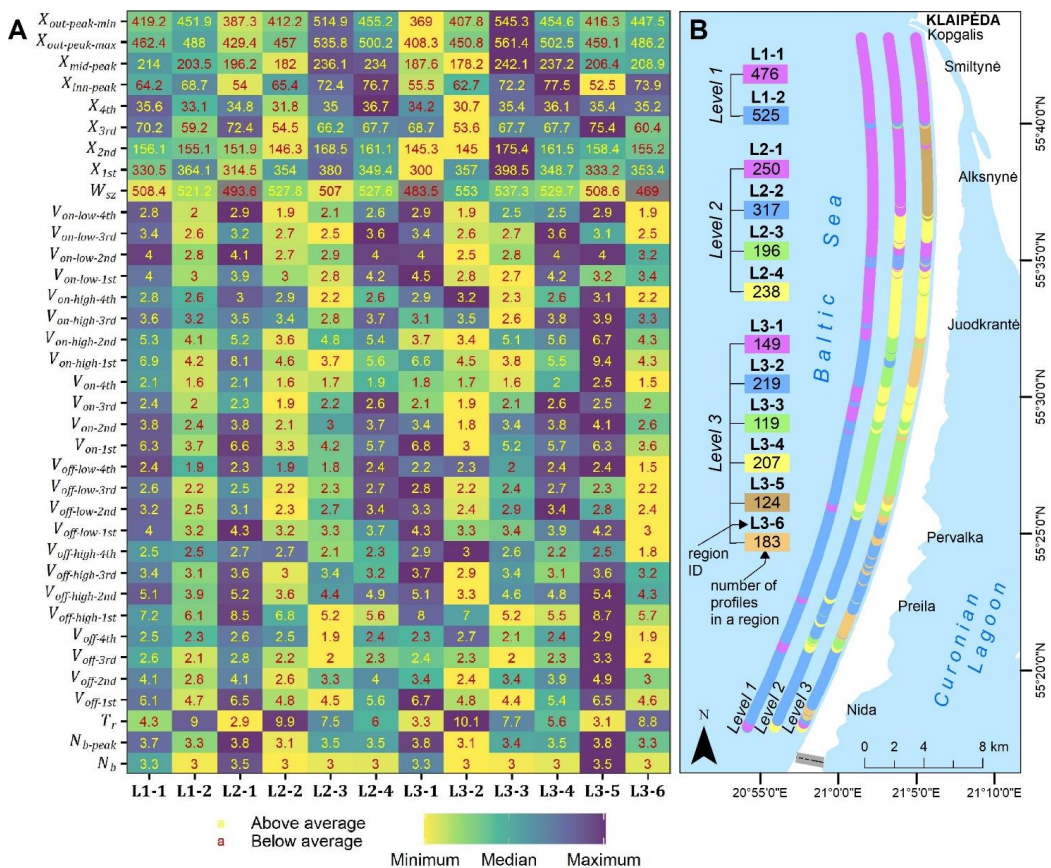


Figure 11. Large- (Level 1, L1), middle- (Level 2, L2), and small (Level 3, L3)-scale nearshore bar behaviour (NBB) regions in the Curonian Spit: (A) mean temporal and morphological bar characteristics in NBB regions; (B) location of the NBB regions.

At the mid-scale level, four NBB regions (L2-1, L2-2, L2-3, and L2-4) were distinguished (Figure 11B). The central part of the study area emerged as L2-3 and L2-4 regions, separating the northern (L2-1) and southern (L2-2) parts. The cross-shore profiles that belonged to the faster northern sector (L1-1) at the large-scale level are attributed to the L2-3 region, and those belonging to the slower southern sector (L1-2) are assigned to the L2-4 region. Located closer to the north, the L2-4 region featured characteristics that were more similar to the northern NBB region (L2-1), while L2-3 was more similar to the southern NBB region (L2-2). However, in the L2-4 region, the bars demonstrated lower rates of interannual and seasonal offshore migration than in the L2-1 region. Meanwhile, bars in the L2-3 region exhibited lower rates of interannual offshore and seasonal onshore migration, but higher rates of interannual onshore and seasonal offshore migration than in the L2-2 region. In the northern (L2-1), central (L2-4 and L2-3), and southern NBB regions, the average return periods were 2.9, 6.0, 7.5, and 9.9 years, respectively. Bars in both central NBB regions (L2-3 and L2-4) were located further from the shoreline than in the southern (L2-2) and northern regions (L2-1) (Figure 11A).

At the smallest-scale level, six NBB regions (L3-1, L3-2, L3-3, L3-4, L3-5, and L3-6) were distinguished (Figure 11B). The fast northern NBB region (L2-1) was divided into L3-1 and L3-5 regions. The bars showed average return periods of just over 3 years in

both small-scale northern NBB regions, but in the L3-1 region, the second to fourth bars were located relatively close to the shoreline, and in the L3-5 region, bars exhibited higher than the average distances from the shoreline (Figure 11A). Bars in L3-1 demonstrated mostly high rates of seasonal and average interannual migration rates. In contrast, the bars in L3-5 showed average-to-high seasonal migration rates and very high interannual migration rates, suggesting that the interannual timescale is more important in L3-5 and that the seasonal scale plays a more important role in L3-3. At this level, the L3-6 region emerged as a discontinuous NBB region incorporating two narrow sectors assigned with cross-shore profiles from the central L2-3 and southern L2-2 regions (Figure 11B). Bars in L3-6 demonstrated low rates of interannual and seasonal onshore migration and very low rates of seasonal offshore migration. The inner bar system in the L3-6 region was located closer to the shoreline than in the surrounding regions, while the outer bar system was located at the average distances from the shoreline (Figure 11). Although it was not among the clustering characteristics, it was previously observed that bars in locations of L3-6 often tend to switch [2], and this type of behaviour results in different bar characteristics than in the surrounding regions.

4. Discussion

4.1. General Patterns of Bar Cross-Shore Behaviour

Quantitative analysis of bar cross-shore migration shows that bars in the Curonian Spit migrated at rates up to 11.0 m/mo on an interannual timescale and up to 13.4 m/mo on a seasonal timescale. On an interannual timescale, the time-averaged offshore bar migration rates exceeded the rates of onshore bar migration, suggesting that bars in the Curonian Spit are gradually moving offshore over the years and display NOM-like behaviour, observed on many multi-barred coasts [7,15,17,24–27].

The cross-shore migration rates of the bars depended on their cross-shore position, with the first (outer) bar demonstrating the highest rates, while the fourth bar exhibited the lowest rates. While this pattern observed in the Curonian Spit is consistent with several other microtidal coasts [5,7], there are also documented cases of different distributions of migration speeds between bar cross-shore positions [54,55]. In the non-tidal setting of the Curonian Spit, wave action is the main driver that causes bar movements. As waves approach the shoreline, wave energy dissipation increases with each more shoreward located bar; therefore, the outer bar is exposed to the highest wave energy, resulting in its fastest motion [56]. The cross-shore mobility of the second to fourth bars, especially directed seaward, is also limited by the position of the outer bar.

On the seasonal timescale, the outer bar moved faster offshore during the months of high wave energy and displayed similar off- and on-shore migration rates during the months of low wave energy, while other bars moved faster onshore during the months of low wave energy and displayed similar off- and on-shore migration rates during the months of low wave energy. The seasonal variations in the cross-shore positions of the bars during the high wave energy season were the highest, implying that the largest share of bar cross-shore behaviour in the Curonian Spit is governed by the energetic wave conditions in the months between October and March. The breaking of high waves during these months induces a strong offshore-directed undertow, causing rapid bar offshore migration [10,19], which mostly contributes to the gradual interannual offshore migration. The seasonal offshore migration during the less energetic months between April and September was mostly slower than the interannual migration, suggesting that processes during these months do not significantly influence offshore bar movement on an interannual timescale. For the second to fourth bars, seasonal onshore migration during the months of both high and low wave energy exceeded interannual onshore migration, hence hydrodynamic processes in these two seasons appear to be important for onshore migration on an interannual timescale. For the outer bar, however, only rates of onshore migration during months of energetic wave conditions exceeded the interannual migration. The reason for this might be that the outer bar is often too deep to be affected by nearshore

hydrodynamics during the months of low wave energy. Therefore, its onshore movement on an interannual timescale is mostly governed by onshore migration during the months of high wave energy.

In the Curonian Spit, the rates of bar cross-shore movements may also have been affected by the three-dimensional behaviour of the bars. During bar switching episodes, which frequently occur in the Curonian Spit, the cross-shore positions of the bars change significantly [2]. Similarly, bars in the Curonian Spit often develop irregular crescentic or sinuous shapes visible in satellite imagery; the development of these shapes may also be the cause of the landward bar movements at the bar horns and seaward bar movements at the bays, especially during the months of low wave energy, when the formation of such shapes is most probable [6,57].

4.2. Factors Determining the Alongshore Variability of Morphological and Temporal Characteristics of Bars

The study results show high alongshore variability in bar cycle return periods (T_r), migration rates, and bar morphology. The duration of the bar cycle return period increases, while bar migration and bar count rates decrease from north to south along the Curonian Spit. This is reflected in the large-scale NBB regions identified in this study, which divided the Curonian Spit into faster northern and slower southern sectors (Figure 11). Previous studies on multi-barred coasts have suggested that alongshore variations in T_r and bar migration are related to the depth range of the bar zone [25,30], nearshore slope [31], bar size, or the width of the bar zone [24,25]. To identify possible factors determining such variations at the current study site, a linear regression analysis was performed between T_r , time-averaged bar migration rates (V_{on} , V_{off} , V_{on-low} , $V_{off-low}$, $V_{on-high}$, $V_{off-high}$), bar zone morphological (bar zone width (W_{bz}), volume (S_{bz})), depth range (D_{bz}), depth at the seaward limit of the bar zone (D_{sea}), bar count (N_b), the total number of observed bar switching episodes (N_{switch})) and environmental parameters (overall mean significant wave height (H_w), mean significant wave height in April–September (H_{w-low}) and October–March (H_{w-high}), mean wave period (T_w), mean deviation of wave direction from a shore-perpendicular angle (α_w), and shoreline compass angle ($\alpha_{shoreline}$)).

A strong statistically significant ($p < 0.05$) linear correlation was observed between bar cycle return periods and depth-related (D_{bz} , D_{sea}), bar-size-related (W_{bz} , S_{bz}), and wave-related (α_w , H_w , H_{w-high} , H_{w-low} , T_w) parameters in the Curonian Spit (Figure 12A). A moderate correlation coefficient was found between T_r and $\alpha_{shoreline}$, N_b , N_{switch} . Time-averaged bar migration rates had a negative linear relationship with T_r -increasing parameters, but the correlation was weaker than with T_r and, in some cases, statistically insignificant (Figure 12A).

In general, these findings show that, in a wider and deeper bar zone with larger volume bars, T_r is longer and bars move slower than in a narrower and shallower bar zone with smaller volume bars but a greater number of bars. Ruessink et al. [30] found that T_r increases by 4 years when D_{bz} increases by 1 m. Here, similar results were found with an increase of 3.7 years/m, implying that a similar rule applies to both tidal and non-tidal environments.

With higher waves, longer wave periods, and waves propagating more obliquely with respect to the shoreline, the bar return periods also tend to be prolonged, although the alongshore variations of H_w and T_w in the Curonian Spit are relatively low (≈ 0.4 m and ≈ 0.6 s) (Figure 4B).

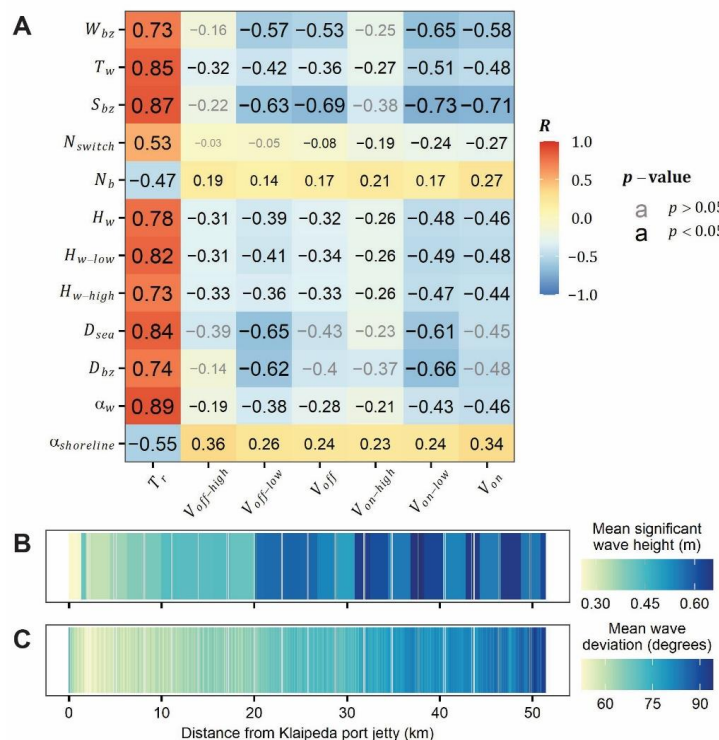


Figure 12. The relationship between temporal bar characteristics and environmental variables (A). Numbers in black indicate statistically significant correlation rates (with 95% confidence), and numbers in grey indicate statistically insignificant rates. The size of the number shows the magnitude of the correlation. Panels (B,C) display alongshore variability in the mean significant wave height (B) and the mean deviation of wave direction from the shore-normal angle (C) in the Curonian Spit in 2011–2021.

How these parameters affect the alongshore variability of bar dynamics is determined by the prevalent hydrodynamic processes and their interaction with the shoreline orientation. Predominant wind directions from west and south–west [45] and the shifting of the shoreline orientation from SW-NE to S-N (Figure 1A) cause a more oblique wave incidence angle southward of the study area (Figure 4C). Oblique waves cause stronger longshore currents, and in combination, they produce stronger longshore sediment transport in the southern part of the Curonian Spit than in the northern part between Alksnynė and Kopgalis, where cross-shore sediment transport prevails. The longshore distribution of sand grain fractions in the Curonian Spit supports the assumption of stronger longshore sediment transport to its southern part [58].

Generally, larger S_{bz} , W_{bz} , H_w , and α_w with a steeper nearshore slope are observed in the southern large-scale NBB region than in the northern region (Table 2). It is well-known that oblique wave energy, frequently observed in the southern NBB region, straightens longshore bars [59–61]. Therefore, the nearshore morphology results in well-pronounced bars with deeper continuous troughs. Higher waves activate greater amounts of sediment at greater depths, resulting in the formation of larger volume bars. Bars with a larger volume respond more slowly to wave forcing than smaller bars [62]; therefore, specific wave conditions may have to last longer for bars to change. Additionally, it was estimated that bars migrate cross-shore at a maximum rate under shore-normal wave incidence [63]. As a result, larger bar volumes and waves with high angles of incidence reduce the cross-shore

mobility of bars, leading to longer T_r , and slower bar motion in the southern NBB region. On the contrary, from Koggalis to Alksnyné, where cross-shore sediment transport prevails, the bars are smaller with better-pronounced crescentic morphologies, resulting in a shorter T_r and faster bar motion in the northern NBB region. Analogous dependencies of bar temporal and environmental characteristics are observed in mid- and small-scale NBB regions (Figure 11; Table 2). These results suggest that small alongshore variations in nearshore hydrodynamics, caused by local wave climate and its interaction with the shoreline orientation, decide the morphological and temporal characteristics of the multi-bar system in the Curonian Spit. This is also evident in the identified NBB regions, whose boundaries are mostly located where shoreline orientation shifts (Figure 11B). The importance of the interaction between shoreline orientation and local wave climate in decadal bar evolution was also recently observed on a single-bar microtidal coast [36].

Table 2. Mean values of the environmental and bar zone variables for the nearshore bar behaviour regions (clusters).

Level	Cluster	D_{sea}	D_{bz}	S_{bz}	$\alpha_{shoreline}$	α_w	N_{switch}	H_w	H_{w-low}	H_{w-high}	T_w
L1	L1-1	5.46	4.47	301.57	271.50	63.00	1.00	0.42	0.33	0.53	2.07
	L1-2	6.58	5.32	471.25	197.36	76.79	1.43	0.60	0.47	0.74	2.34
L2	L2-1	4.95	4.15	246.29	319.83	58.63	0.00	0.35	0.27	0.45	1.97
	L2-2	6.80	5.57	505.14	197.91	77.31	1.60	0.59	0.46	0.72	2.33
	L2-3	6.04	4.68	386.54	196.00	75.50	1.00	0.63	0.49	0.78	2.36
	L2-4	6.29	5.00	393.71	190.95	70.29	2.67	0.53	0.42	0.67	2.24
L3	L3-1	4.76	3.95	233.39	314.58	59.50	0.48	0.37	0.28	0.46	1.98
	L3-2	6.80	5.64	507.20	202.54	79.13	2.47	0.59	0.47	0.72	2.33
	L3-3	5.98	4.66	393.33	192.91	72.09	0.65	0.54	0.42	0.66	2.27
	L3-4	6.29	5.00	393.71	187.67	67.61	0.93	0.49	0.38	0.62	2.19
	L3-5	6.74	4.95	297.86	287.80	60.17	0.00	0.41	0.31	0.52	2.05
	L3-6	6.29	4.88	423.33	198.91	74.26	1.06	0.57	0.45	0.71	2.30

4.3. Accuracy and Limitations of Satellite-Derived Temporal Characteristics of Bars

This study suggests a methodology to analyse cross-shore morphology and dynamics of bars solely based on optical satellite data as an alternative to resource-intensive bathymetric surveys or other state-of-the-art remote sensing techniques such as video monitoring. Previous studies have proven satellite-derived bar positions to be an accurate measure of bar morphology [38–40,42]. However, clouds, haze, and water turbidity, all of which limit water clarity, have a significant impact on the quality of satellite-derived data. Nonetheless, the nearly daily frequency of satellite observations helps to select only good-quality data (cloud- and wave-free) for the monthly observations required for the proposed analysis mechanism, especially between March and October. The Curonian Spit, on the other hand, rarely has cloudless and wave-free days between November and February. Because there are only a few bar observations during these months, the seasonal characteristics of bars in the high-wave-energy season are mostly based on observations from March and October. Moreover, the analysis only covers from 2011 to 2021, which is three years less than the maximum estimated T_r in the study area, and thus may not fully reflect the variability of the multi-bar system, where $T_r > 10$ years.

The algorithm used to derive bar data was found to be better at detecting inner-bar morphologies in the shallowest nearshore regions (depths < 1 m), where echo-sounding techniques tend to fail, but it can overlook decaying bars at depths greater than 6 m [39]. This means that the outer bar may decay sooner from a satellite-derived RBPI profile than from a bathymetric profile, resulting in a shorter satellite-derived bar life span. Though it may cause the location of the bar decay to shift shoreward, the bar cycle return period, which indicates the time between two successive bar decay events, should remain precise. Figure 13 illustrates that RBPI-derived perturbations are less pronounced on the outer bar and more pronounced on the inner and middle bars than bathymetry-derived perturbations.

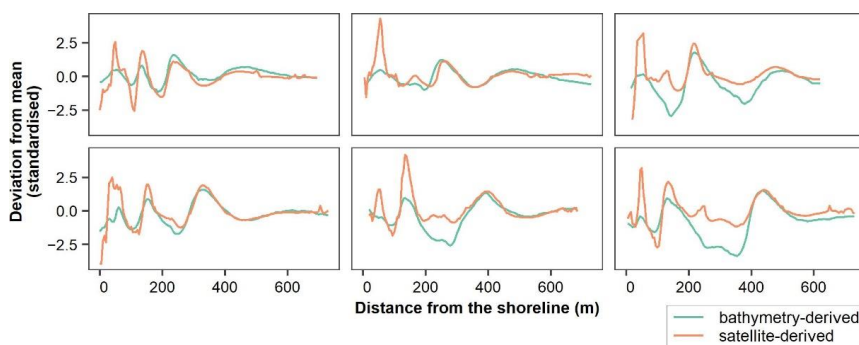


Figure 13. Cross-shore profiles of bathymetry-derived and RBPI-derived perturbations (values were standardised for comparison) at different alongshore locations in the Curonian Spit. Bathymetric surveys were conducted on the 19 May 2019, and a satellite image was acquired on the 22 May 2019.

5. Conclusions

This study examines intra-site variations in the cross-shore morphological and temporal characteristics of a multiple bar system on a 51-km-long sandy barrier, using satellite-derived data. The study suggests a methodology for the analysis of bar cross-shore behaviour solely based on satellite imagery, without the need for in situ measurements. This proves that RBPI-derived data can be treated in a similar way to the traditional cross-shore bathymetric profiles.

A triple–quadruple-bar system with a well-known multi-annual progressive offshore-directed cyclic behaviour was observed at the study site. Bar cycle return periods ranging from 1.8 to 13.5 years were estimated along with NOM phase-related bar characteristics. To our knowledge, this is the first time NOM-like behaviour that has been documented on the south-eastern coast of the Baltic Sea, showing that this model of multi-annual bar behaviour is also applicable in this region and demonstrating the potential of satellite remote sensing in the exploration of the bars in coastal regions that are understudied. Seaward and landward migration of the first to fourth bars was quantified on interannual and seasonal timescales, showing that bars exhibited the highest migration rates on a seasonal timescale during the months of high wave energy. Cross-shore migration rates depended on the cross-shore position of the bars, with the outer bar migrating fastest, as observed on several other microtidal coasts. The interannual offshore migration of the bars outpaced onshore migration, while the seasonal offshore migration exceeded onshore migration for the outer bar only.

In general, bar cycle return periods increased and migration rates decreased from north to south in the study area. This is exemplified by the identified nearshore bar behaviour regions, which, at the largest scale, subdivide the Curonian Spit into faster northern and slower southern regions. Strong significant correlation rates were found between the temporal characteristics of the bars and the variables whose values increase southward of the Curonian Spit, including bar zone depth, bar size, wave height, and wave obliquity. The study results suggest that the interaction between shoreline orientation and small alongshore differences in nearshore hydrodynamics determines the alongshore variability of the morphological and temporal characteristics of the nearshore bars.

The study expands the knowledge of the large-extent cross-shore behaviour of multi-bar systems with more than two or three bars on the non-tidal coasts and illustrates the capabilities of optical satellite remote sensing in the field of nearshore morphodynamics. Nearshore bar systems on other tideless and microtidal coasts could be explored, using the combination of satellite imagery and analysis mechanism, proposed in this study. This could lead to new insights into nearshore bar behaviour, particularly at sites previously overlooked due to an absence of bar data.

Author Contributions: Conceptualization, R.J. and L.J.; methodology, R.J.; formal analysis, R.J.; investigation, R.J., D.J., L.J., D.P. and G.Ž.; resources, L.J. and G.Ž.; data curation, R.J. and D.P.; writing—original draft preparation, R.J.; writing—review and editing, D.J. and L.J.; visualization, R.J.; supervision, D.J. All authors have read and agreed to the published version of the manuscript.

Funding: This research received no external funding.

Data Availability Statement: The data presented in this study are available on request from the corresponding author. The data are not publicly available due to the Data Use Agreement with Planet Labs.

Conflicts of Interest: The authors declare no conflict of interest.

References

- Wijnberg, K.M.; Kroon, A. Barred beaches. *Geomorphology* **2002**, *48*, 103–120. [[CrossRef](#)]
- Janušaitė, R.; Jarmalavičius, D.; Pupienis, D.; Žilinskas, G.; Jukna, L. Nearshore sandbar switching episodes and their relationship with coastal erosion at the Curonian Spit, Baltic Sea. *Oceanologia* **2021**, *in press*. [[CrossRef](#)]
- Phillips, M.S.; Harley, M.D.; Turner, I.L.; Splinter, K.D.; Cox, R.J. Shoreline recovery on wave-dominated sandy coastlines: The role of sandbar morphodynamics and nearshore wave parameters. *Mar. Geol.* **2017**, *385*, 146–159. [[CrossRef](#)]
- Van de Lageweg, W.I.; Bryan, K.R.; Coco, G.; Ruessink, B.G. Observations of shoreline-sandbar coupling on an embayed beach. *Mar. Geol.* **2013**, *344*, 101–114. [[CrossRef](#)]
- Van Enckevort, I.M.J.; Ruessink, B.G. Video observations of nearshore bar behaviour. Part 1: Alongshore uniform variability. *Cont. Shelf Res.* **2003**, *23*, 501–512. [[CrossRef](#)]
- Van Enckevort, I.M.J.; Ruessink, B.G.; Coco, G.; Suzuki, K.; Turner, I.L.; Plant, N.G.; Holman, R.A. Observations of nearshore crescentic sandbars. *J. Geophys. Res. C Ocean.* **2004**, *109*, C06028. [[CrossRef](#)]
- Melito, L.; Parlagreco, L.; Perugini, E.; Postacchini, M.; Devoti, S.; Soldini, L.; Zitti, G.; Liberti, L.; Brocchini, M. Sandbar dynamics in microtidal environments: Migration patterns in unprotected and bounded beaches. *Coast. Eng.* **2020**, *161*, 103768. [[CrossRef](#)]
- Hsu, T.J.; Elgar, S.; Guza, R.T. Wave-induced sediment transport and onshore sandbar migration. *Coast. Eng.* **2006**, *53*, 817–824. [[CrossRef](#)]
- Hoefel, F.; Elgar, S. Wave-Induced Sediment Transport and Sandbar Migration. *Science* **2003**, *299*, 1885–1887. [[CrossRef](#)]
- Gallagher, E.L.; Elgar, S.; Guza, R.T. Observations of sand bar evolution on a natural beach. *J. Geophys. Res. Ocean.* **1998**, *103*, 3203–3215. [[CrossRef](#)]
- Sallenger, A.H.; Holman, R.A.; Birkemeier, W.A. Storm-induced response of a nearshore-bar system. *Mar. Geol.* **1985**, *64*, 237–257. [[CrossRef](#)]
- Ostrowski, R.; Pruszak, Z.; Zeidler, R.B. Multi-scale nearshore & beach changes. In Proceedings of the Coastal Engineering Conference, Auckland, New Zealand, 2–6 December 1991; Volume 2, pp. 2101–2116.
- Vidal-Ruiz, J.A.; Ruiz de Alegria-Arzaburu, A. Variability of sandbar morphometrics over three seasonal cycles on a single-barred beach. *Geomorphology* **2019**, *333*, 61–72. [[CrossRef](#)]
- Larson, M.; Kraus, N.C. Temporal and spatial scales of beach profile change, Duck, North Carolina. *Mar. Geol.* **1994**, *117*, 75–94. [[CrossRef](#)]
- Ruessink, B.G.; Kroon, A. The behaviour of a multiple bar system in the nearshore zone of Terschelling, The Netherlands: 1965–1993. *Mar. Geol.* **1994**, *121*, 187–197. [[CrossRef](#)]
- Shand, R.D.; Bailey, D.G. A review of net offshore bar migration with photographic illustrations from Wanganui, New Zealand. *J. Coast. Res.* **1999**, *15*, 365–378.
- Aleman, N.; Certain, R.; Robin, N.; Barusseau, J.P. Morphodynamics of slightly oblique nearshore bars and their relationship with the cycle of net offshore migration. *Mar. Geol.* **2017**, *392*, 41–52. [[CrossRef](#)]
- Ruessink, B.G.; Pape, L.; Turner, I.L. Daily to interannual cross-shore sandbar migration: Observations from a multiple sandbar system. *Cont. Shelf Res.* **2009**, *29*, 1663–1677. [[CrossRef](#)]
- Elgar, S.; Gallagher, E.L.; Guza, R.T. Nearshore sandbar migration. *J. Geophys. Res. Ocean.* **2001**, *106*, 11623–11627. [[CrossRef](#)]
- Almar, R.; Castelle, B.; Ruessink, B.G.; Senechal, N.; Bonneton, P.; Marie, V. High-frequency video observation of two nearby double-barred beaches under high-energy wave forcing. *J. Coast. Res.* **2009**, *2009*, 1706–1710.
- Houser, C.; Greenwood, B. Onshore migration of a swash bar during a storm. *J. Coast. Res.* **2007**, *23*, 1–14. [[CrossRef](#)]
- Aagaard, T.; Nielsen, J.; Greenwood, B. Suspended sediment transport and nearshore bar formation on a shallow intermediate-state beach. *Mar. Geol.* **1998**, *148*, 203–225. [[CrossRef](#)]
- Plant, N.G.; Holman, R.A.; Freilich, M.H.; Birkemeier, W.A. A simple model for interannual sandbar behavior. *J. Geophys. Res. Ocean.* **1999**, *104*, 15755–15776. [[CrossRef](#)]
- Shand, R.D.; Shepherd, M.J.; Bailey, D.G. An inter-site comparison of net offshore bar migration characteristics and environmental conditions. *J. Coast. Res.* **1999**, *15*, 750–765.
- Tătui, F.; Vespremeanu-Stroe, A.; Ruessink, B.G. Alongshore variability of cross-shore bar behavior on a nontidal beach. *Earth Surf. Processes Landf.* **2016**, *41*, 2085–2097. [[CrossRef](#)]

26. Kuriyama, Y. Medium-term bar behavior and associated sediment transport at Hasaki, Japan. *J. Geophys. Res. Ocean.* **2002**, *107*, 15-1–15-12. [[CrossRef](#)]
27. Yuhi, M.; Okada, M. Long-term field observations of multiple bar properties on an eroding coast. *J. Coast. Res.* **2011**, *64*, 860–864. [[CrossRef](#)]
28. Aagaard, T.; Davidson-Arnott, R.; Greenwood, B.; Nielsen, J. Sediment supply from shoreface to dunes: Linking sediment transport measurements and long-term morphological evolution. *Geomorphology* **2004**, *60*, 205–224. [[CrossRef](#)]
29. Anthony, E.J.; Vanhee, S.; Ruz, M.H. Short-term beach-dune sand budgets on the north sea coast of France: Sand supply from shoreface to dunes, and the role of wind and fetch. *Geomorphology* **2006**, *81*, 316–329. [[CrossRef](#)]
30. Ruessink, B.G.; Wijnberg, K.M.; Holman, R.A.; Kuriyama, Y.; van Enckevort, I.M.J. Intersite comparison of interannual nearshore bar behavior. *J. Geophys. Res. C Ocean.* **2003**, *108*, 3249–3260. [[CrossRef](#)]
31. Walstra, D.-J.; Wesselman, D.; van der Deijl, E.; Ruessink, G. On the Intersite Variability in Inter-Annual Nearshore Sandbar Cycles. *J. Mar. Sci. Eng.* **2016**, *4*, 15. [[CrossRef](#)]
32. Grunnet, N.M.; Hoekstra, P. Alongshore variability of the multiple barred coast of Terschelling, The Netherlands. *Mar. Geol.* **2004**, *203*, 23–41. [[CrossRef](#)]
33. Aleman, N.; Robin, N.; Certain, R.; Barousseau, J.-P.; Gervais, M. Net offshore bar migration variability at a regional scale: Inter-site comparison (Languedoc-Roussillon, France). *J. Coast. Res.* **2013**, *165*, 1715–1720. [[CrossRef](#)]
34. Aagaard, T.; Kroon, A.; Greenwood, B.; Hughes, M.G. Observations of offshore bar decay: Sediment budgets and the role of lower shoreface processes. *Cont. Shelf Res.* **2010**, *30*, 1497–1510. [[CrossRef](#)]
35. Di Leonardo, D.; Ruggiero, P. Regional scale sandbar variability: Observations from the U.S. Pacific Northwest. *Cont. Shelf Res.* **2015**, *95*, 74–88. [[CrossRef](#)]
36. Gijsman, R.; Ruessink, B.G.; Visscher, J.; Schlurmann, T. Observations on decadal sandbar behaviour along a large-scale curved shoreline. *Earth Surf. Processes Landf.* **2021**, *46*, 490–503. [[CrossRef](#)]
37. Masselink, G.; Austin, M.; Scott, T.; Poate, T.; Russell, P. Role of wave forcing, storms and NAO in outer bar dynamics on a high-energy, macro-tidal beach. *Geomorphology* **2014**, *226*, 76–93. [[CrossRef](#)]
38. Tátui, F.; Constantin, S. Nearshore sandbars crest position dynamics analysed based on Earth Observation data. *Remote Sens. Environ.* **2020**, *237*, 111555. [[CrossRef](#)]
39. Janušaitė, R.; Jukna, L.; Jarmalavičius, D.; Pupienis, D.; Žilinskas, G. A Novel GIS-Based Approach for Automated Detection of Nearshore Sandbar Morphological Characteristics in Optical Satellite Imagery. *Remote Sens.* **2021**, *13*, 2233. [[CrossRef](#)]
40. Román-Rivera, M.A.; Ellis, J.T.; Wang, C. Applying a rule-based object-based image analysis approach for nearshore bar identification and characterization. *J. Appl. Remote Sens.* **2020**, *14*, 044502. [[CrossRef](#)]
41. Do, J.D.; Jin, J.-Y.; Jeong, W.M.; Lee, B.; Kim, C.H.; Chang, Y.S. Observation of nearshore crescentic sandbar formation during storm wave conditions using satellite images and video monitoring data. *Mar. Geol.* **2021**, *442*, 106661. [[CrossRef](#)]
42. Athanasiou, P.; de Boer, W.; Yoo, J.; Ranasinghe, R.; Reniers, A. Analysing decadal-scale crescentic bar dynamics using satellite imagery: A case study at Anmok beach, South Korea. *Mar. Geol.* **2018**, *405*, 1–11. [[CrossRef](#)]
43. Román-Rivera, M.A.; Ellis, J.T. A synthetic review of remote sensing applications to detect nearshore bars. *Mar. Geol.* **2019**, *408*, 144–153. [[CrossRef](#)]
44. Kelpšaitė, L.; Dailiūtė, I.; Soomere, T. Changes in wave dynamics at the south-eastern coast of the Baltic Proper during 1993–2008. *Boreal Environ. Res.* **2011**, *16*, 220–232.
45. Jakimavičius, D.; Kriaucūnienė, J.; Šarauskienė, D. Assessment of wave climate and energy resources in the Baltic Sea nearshore (Lithuanian territorial water). *Oceanologia* **2018**, *60*, 207–218. [[CrossRef](#)]
46. EU. Copernicus Marine Service Information Baltic Sea Wave Hindcast. Available online: https://resources.marine.copernicus.eu/product-detail/BALTICSEA_REANALYSIS_WAV_003_015/INFORMATION (accessed on 18 May 2022). [[CrossRef](#)]
47. Jarmalavičius, D.; Pupienis, D.; Žilinskas, G.; Janušaitė, R.; Karaliunas, V. Beach-foredune sediment budget response to sea level fluctuation: Curonian Spit, Lithuania. *Water* **2020**, *12*, 583. [[CrossRef](#)]
48. Janušaitė, R.; Jukna, L. Morphology of Curonian Spit Nearshore Zone Bars. *Ann. Geogr.* **2017**, *50*, 3–20.
49. Žilinskas, G.; Janušaitė, R.; Jarmalavičius, D.; Pupienis, D. The impact of Klaipėda Port entrance channel dredging on the dynamics of coastal zone, Lithuania. *Oceanologia* **2020**, *62*, 489–500. [[CrossRef](#)]
50. Planet Team. Planet Application Program Interface: In Space for Life on Earth. Available online: <https://api.planet.com/> (accessed on 9 May 2021).
51. Newman, D.R.; Lindsay, J.B.; Cockburn, J.M.H. Evaluating metrics of local topographic position for multiscale geomorphometric analysis. *Geomorphology* **2018**, *312*, 40–50. [[CrossRef](#)]
52. Short, A.D. Beach systems of the central Netherlands coast: Processes, morphology and structural impacts in a storm driven multi-bar system. *Mar. Geol.* **1992**, *107*, 103–132. [[CrossRef](#)]
53. Wijnberg, K.M.; Terwindt, J.H.J. Extracting decadal morphological behaviour from high-resolution, long-term bathymetric surveys along the Holland coast using eigenfunction analysis. *Mar. Geol.* **1995**, *126*, 301–330. [[CrossRef](#)]
54. Larson, M.; Kraus, N.C. Dynamics of longshore bars. In Proceedings of the Coastal Engineering Conference, Venice, Italy, 4–9 October 1992; Volume 2, p. 2219.
55. Goulart, E.S.; Calliari, L.J. Medium-term morphodynamic behavior of a multiple sand bar beach. *J. Coast. Res.* **2013**, *165*, 1774–1779. [[CrossRef](#)]

56. Alexander, P.S.; Holman, R.A. Quantification of nearshore morphology based on video imaging. *Mar. Geol.* **2004**, *208*, 101–111. [[CrossRef](#)]
57. Wright, L.D.; Short, A.D. Morphodynamic variability of surf zones and beaches: A synthesis. *Mar. Geol.* **1984**, *56*, 93–118. [[CrossRef](#)]
58. Žilinskas, G.; Jarmalavičius, D. Interrelation of morphometric parameters of the submarine shore slope of the Curonian Spit, Lithuania. *Baltica* **2007**, *20*, 46–52.
59. Garnier, R.; Falqué, A.; Calvete, D.; Thiébot, J.; Ribas, F. A mechanism for sandbar straightening by oblique wave incidence. *Geophys. Res. Lett.* **2013**, *40*, 2726–2730. [[CrossRef](#)]
60. Gu, Z.; Zhang, C.; Zheng, J. Influences of wave forcing and morphological variability on the evolution of a double-sandbar system. *Proc. Inst. Mech. Eng. Part M J. Eng. Marit. Environ.* **2016**, *230*, 467–480. [[CrossRef](#)]
61. De Swart, R.L.; Ribas, F.; Simarro, G.; Guillén, J.; Calvete, D. The role of bathymetry and directional wave conditions on observed crescentic bar dynamics. *Earth Surf. Processes Landf.* **2021**, *46*, 3252–3270. [[CrossRef](#)]
62. Smit, M.W.J.; Reniers, A.J.H.M.; Ruessink, B.G.; Roelvink, J.A. The morphological response of a nearshore double sandbar system to constant wave forcing. *Coast. Eng.* **2008**, *55*, 761–770. [[CrossRef](#)]
63. Dubarbier, B.; Castelle, B.; Marie, V.; Ruessink, G. Process-based modeling of cross-shore sandbar behavior. *Coast. Eng.* **2015**, *95*, 35–50. [[CrossRef](#)]

III PUBLIKACIJA

The impact of Klaipėda Port entrance channel dredging on the dynamics of coastal zone, Lithuania

Žilinskas G., **Janušaitė R.**, Jarmalavičius D., Pupienis D.

Oceanologia, 2020, 62, 489–500.

DOI: <https://doi.org/10.1016/j.oceano.2020.08.002>



Available online at www.sciencedirect.com

ScienceDirect

journal homepage: www.journals.elsevier.com/oceanologia



ORIGINAL RESEARCH ARTICLE

The impact of Klaipėda Port entrance channel dredging on the dynamics of coastal zone, Lithuania

Gintautas Žilinskas, Rasa Janušaitė, Darius Jarmalavičius, Donatas Pupienis*

Nature Research Centre, Institute of Geology and Geography, Vilnius, Lithuania

Received 20 May 2020; accepted 3 August 2020

Available online 15 August 2020

KEYWORDS

Southern Baltic;
Sediment transport;
Port jetties;
Entrance channel
dredging

Summary Dredging entrance channels to ports on open littoral drift seashores often causes major morphological changes to the shoreline. This study aims to assess the impact of dredging the Port of Klaipėda's entrance channel and the construction of the jetties on the coastal zone. Based on an analysis of cartographic material collected between 1835 and 2017, and on field data (bathymetric surveys and cross-shore profile levelling), changes to the coastal zone in the area nearest to the port were evaluated. The dominant longshore sediment transport on the Lithuanian nearshore runs from south to north. Thus, based on established patterns, intensive accretion could have been expected to take place on the southern side of the port jetties and erosion on their northern side. However, in the case of the Port of Klaipėda, in the area nearest to the port on the updrift side of the port jetties, where accretion would have been expected to take place, the nearshore depth increased throughout the 20th century (when the length and configuration of the jetties did not change). The shoreline shifted landward instead of moving further out to sea. The present study shows that the intensive dredging of the entrance channel caused nearshore and shore erosion on the updrift side of the port jetties, even while a sufficient sediment load was being transported by the longshore drift.

© 2020 Institute of Oceanology of the Polish Academy of Sciences. Production and hosting by Elsevier B.V. This is an open access article under the CC BY-NC-ND license (<http://creativecommons.org/licenses/by-nc-nd/4.0/>).

* Corresponding author at: Nature Research Centre, Institute of Geology and Geography, Akademijos str. 2, LT-08412 Vilnius, Lithuania.

E-mail addresses: gintautas.zilinskas@gamtc.lt (G. Žilinskas), rasha.janusaita@gamtc.lt (R. Janušaitė), darius.jarmalavicius@gamtc.lt (D. Jarmalavičius), donatas.pupienis@gamtc.lt (D. Pupienis).

Peer review under the responsibility of the Institute of Oceanology of the Polish Academy of Sciences.



Production and hosting by Elsevier

<https://doi.org/10.1016/j.oceano.2020.08.002>

0078-3234/© 2020 Institute of Oceanology of the Polish Academy of Sciences. Production and hosting by Elsevier B.V. This is an open access article under the CC BY-NC-ND license (<http://creativecommons.org/licenses/by-nc-nd/4.0/>).

1. Introduction

The depth of ports is an important factor with regard to competition in container shipping. In order to accommodate the largest cargo carriers, port water areas must be dredged to remove excess sediments (Demir et al., 2004; HELCOM, 2015; Mohanty et al., 2012; Žaromskis, 2008).

The fact that nearshore dredging causes shore erosion has been known for a long time (Blackman, 1951; Kojima et al., 1986; McLoughlin, 2000; Shaw, 1978; Simons and Hollingham, 2001; Šuškýj et al., 1987; Work et al., 2004). The impact of dredging on the shoreline usually depends directly on the distance between the shoreline and the dredging site, the depth of the dredged pit and the amount of extracted marine sediments (Marine Habitat Committee, 2000).

An overview of the processes taking place in the dredging environment and the results of laboratory investigations and numerical modelling are given in Demir et al. (2004). It was determined that offshore dredging has both a direct and indirect impact on the coastal zone. According to Demir et al. (2004), the amount of erosion is in proportion to the amount of dredged sediments if the depth of the pit is smaller than the depth of closure. When the dredging pit is beyond the limits of the depth of closure, dredging has no direct impact on the shore. Wave field changes that are predetermined by changes in the bottom relief are regarded as an indirect impact (Demir et al., 2004). The sediment transport models change depending on changes in the wave energy's alongshore distribution.

The impact of port dredging on the state of the adjacent shores is not as easily determined when entrance channels are protected by jetties and when water and sediment transport takes place between a river delta or estuary and the sea via a channel (Healy et al., 2002; Kudale, 2010; Mohanty et al., 2012; Tsinker, 2004). The influence of the Klaipėda Port jetties on the state of the adjacent coastal area has been analyzed in a number of studies (Knaps, 1965; Pupienis et al., 2013; Žaromskis and Gulbiškės, 2016; Žaromskis, 2008; Žilinskas, 1998). These studies focused on the impact of the port jetties and emphasized coastal zone erosion processes on the downdrift side. The impact of entrance channel dredging on the coastal zone was not taken into consideration.

The aim of the present study is to show the impact of entrance channel dredging on the adjacent shore and to prove that its intensive dredging and cleaning have caused coastal erosion on the updrift side of the port jetty even while a sufficient sediment load was being transported by the along-shore drift.

2. Study area and methods

The Port of Klaipėda is located in the south-western part of the Baltic Sea across the Klaipėda Strait (Figure 1). It is the northernmost ice-free port (even in the coldest winters) in the East Baltic. At present, the water area of the port (6.5 km^2) covers almost the entire Klaipėda Strait. The length of the water area is approximately 11.5 km, and its width ranges between 3 m at the port gates in the north and 1350 m in the southern part of the Strait. The average depth

of the entrance channel is 15.2–15.5 m and the average depth of the navigation channel near most of the quays is 14.5 m.

The number of stormy days (with a wind velocity of over 15 m/s) per year is between 50 and 60. Storms usually occur in the autumn and winter. The wind velocity during storms reaches 25–28 m/s, while during extreme storms it can even reach 30–40 m/s. The maximal recorded wave height on the nearshore exceeded 6 m and the maximal sea level rise reached 185 cm. The most frequent storm wind directions are south-westerly (35.6%) and westerly winds (24.3%) (Kriauciūnienė et al., 2006). Up to 57.7% of the waves on the Lithuanian shoreline are from a westerly direction: SW, W and NW (Jakimavičius et al., 2018). The high volumes of river runoff into the Curonian Lagoon (about $23 \text{ km}^3/\text{yr}$) are responsible for outflowing currents dominating the Klaipėda Strait (80% of the surface and 60% of the near-bottom currents). The water level in the Lagoon is on average 12 cm above sea level. The average velocity of the outflowing currents is 0.3–0.4 m/s. During spring tides, this velocity can reach 2 m/s. Inflowing currents develop in W, NW and N storm wind conditions. As the tide-ebb amplitude on the south-eastern Baltic coast only reaches 3.5–4.0 cm (Jarmalavičius et al., 2020), the wind-generated waves, the south to north alongshore sediment transport (Žilinskas et al., 2018) and the aeolian processes (Jarmalavičius et al., 2019) are the main beach-forming agents on the Lithuanian shore. The Baltic sea level rise on the Lithuanian shore ($0.16 \pm 0.02 \text{ cm}/\text{yr}$) has so far not had any noticeable impact on the shoreline's dynamics (Jarmalavičius et al., 2017).

The impact of dredging the Klaipėda Port entrance channel on the shore zone was analyzed using charts during a number of years, in 1835, 1845, 1878, 1910, 1993, 1955, 1961, 1991, 1998, 2003 and 2017. Also used were bathymetric plans of the port (1:10 000 and 1:5 000), material that had accumulated in the Klaipėda Port archives, and measurements taken on the shore and nearshore. The investigation area included approximately 1500 m-long sectors on both sides of the port jetties to 15 m isobaths (the data before the 20th century was collected to 10 m isobaths).

A bathymetric survey was carried out in 2017 using a Humminbird Helix 9 SI GPS multibeam echo sounder on both sides of the port jetties. Morphological investigations of the shore in the Klaipėda Port sector (3000 m-long sectors on both sides of the port) have been carried out since 1995. Cross-profiles of the coast are levelled (using a TOPCON GTS 229 electronic tachometer) once a year in the first week of May in calm weather (fair weather) conditions and when the sea level is close to the mean long-term average (Jarmalavičius et al., 2012). Shoreline dynamics and nearshore bathymetry changes for different periods are analyzed using ArcMap 10.7 software.

3. Results

Before the port jetties were constructed, the depth of the Klaipėda Strait was maintained by outflowing spring tidal waters from the Curonian Lagoon. The dominant depth was 5 m. The tidal waters from the Lagoon transported sediments of varying composition (mud, aleurite and sand).

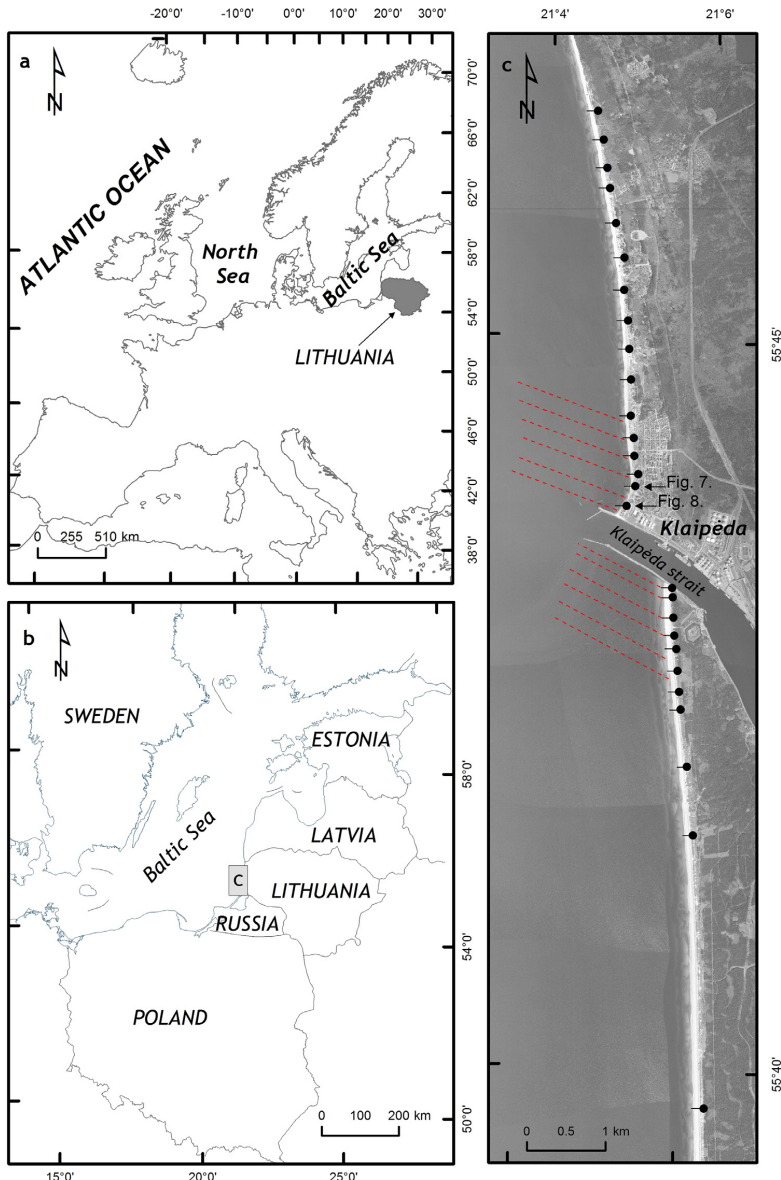


Figure 1 Study area. Black dots indicate locations of cross-shore levelling, red dotted lines – locations of nearshore cross-section measurements.

These sediments, as well as sediments transported by the sea from south to north, form three bars: southern, central and northern. At the end of the 18th century and the beginning of the 19th century (Figure 2), an intensive accumulation of sand took place at the distal end of the Curonian Spit. Between 1796 and 1820, the distal end shifted approximately 640 m northward (Veit, 1821), i.e. 8.5 m per year on average. The pressure of the water flowing

out of the Curonian Lagoon and onto the mainland shore due to the extension of the Curonian Spit caused the mainland shore to erode. Between 1796 and 1820, the mainland shore retreated by 180 m (Veit, 1821), i.e. by 7.2 m per year. In 1773, 1784, 1797 and 1801, in order to protect the entrance channel from silting, wooden piles with stone fillings were embedded at the distal end of the Curonian Spit.

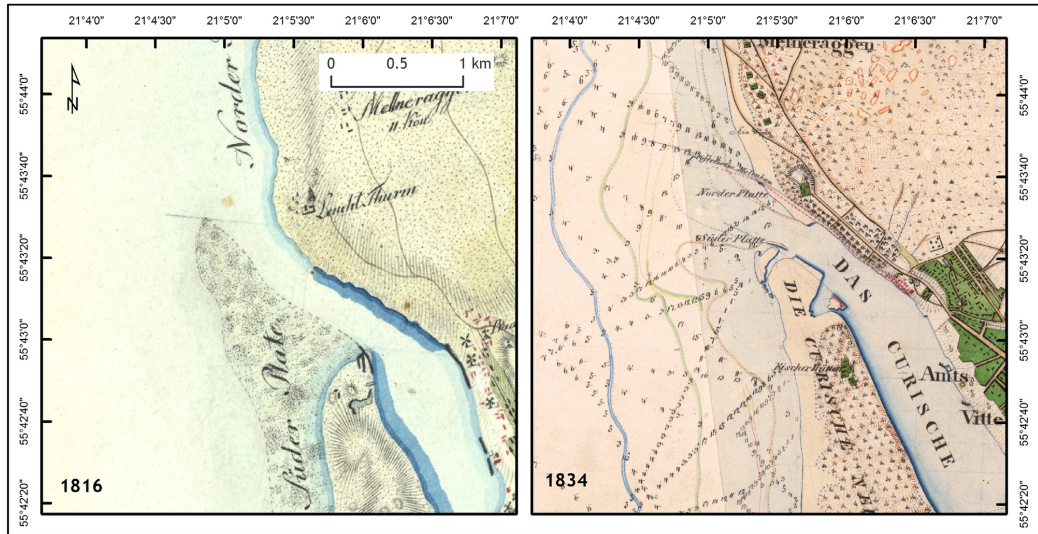


Figure 2 The Klaipėda Strait before the beginning of port jetties construction in 1816 and 1834.

However, during and even after the end of the construction work, the jetties were destroyed over and again by strong storms or spring tides (Žilinskas, 1998). Only a 152 m-long jetty, constructed in 1806 and stretching approximately 46 m out to sea (Figure 3a), was not destroyed (Veit, 1921). After 10 years, due to a rapid accumulation of sand, this jetty became part of the shore and by 1821 it was totally covered with sand. Sand flowing into the Klaipėda Strait impeded navigation.

The analysis of the Klaipėda Port jetties and entrance channel deepening impact on adjacent coastal environments was split into three specific periods: 1834–1902; 1902–2000; 2000–2017.

3.1. Construction of the port jetties (1834–1902)

In 1834, in order to ensure favourable conditions for navigation and to stop the erosion of the Klaipėda Strait's mainland shore, the construction of the northern jetty was started (Figure 3). The finished (1878) jetty was 1158 m in length. The construction of a new southern jetty was started in 1847 50–60 m to the north of the jetty built in 1806 (Figure 3). The construction work finished in 1902. The new jetty was 1227 m in length.

The jetties acted as barriers against sediment drift; the northern and southern bars verged onto the shore, and on the nearshore on both sides of the jetties (at a depth of 0–3 m) intensive accumulation took place. However, at depths below 3 m, isobath bed erosion set in (Figure 4). Part of the central bar shifted out to sea due to intensified outflows from the Curonian Lagoon after the jetties were constructed. The remaining part was removed while the navigation channel was being dredged. At the end of the 19th century, the maintained depth in the entrance channel was 6 m (Figure 5). Due to the inefficient mechanics of the time,

the annual amounts of dredged material did not usually exceed several thousand cubic metres (Hagen, 1885).

During the construction work, the shoreline in the adjacent sectors migrated rapidly in a seaward direction (Figures 3–4, Table 1). Large-scale changes took place alongside the jetties in particular. Further to the north or south of the jetties, these displacements were consistently less noticeable.

Between 1835 and 1878, the shoreline near the northern jetty (at a distance of 50 m) migrated 544 m in a seaward direction. Moving northward at distances of 250 m, 500 m, 750 m, 1000 m and 1250 m from the jetty, the shoreline's displacements toward the sea were 403, 265, 211, 144 and 122 metres, respectively. A similar pattern of shoreline dynamics within the same timespan could be seen in the area along the southern jetty. 50 m from the jetty, the shoreline migrated by 422 m. Further from the jetty, at distances of 250 m, 500 m, 750 m, 1000 m and 1250 m, the displacements were 284, 173, 120, 76 and 58 m, respectively.

Between 1835 and 1978, the mainland shore's area 1300 m from the northern jetty increased by approximately 326 000 m² and the Curonian Spit shore's area increased by just 169 000 m² at the same distance from the southern jetty. During the same timespan, two circumstances were responsible for the rapid seaward migration of the shoreline beyond the updrift northern jetty and for the increase in the land area being almost as twice as large as on the side of the southern jetty:

- The construction of the southern jetty only started in 1847, i.e. 13 years later than the construction of the northern jetty, behind which the shoreline had migrated markedly seaward during this timespan (Figure 3).
- Until the beginning of the 20th century, the dredged sand from the port had been dumped behind the northern jetty at shallow depths, causing an accumulation of sand

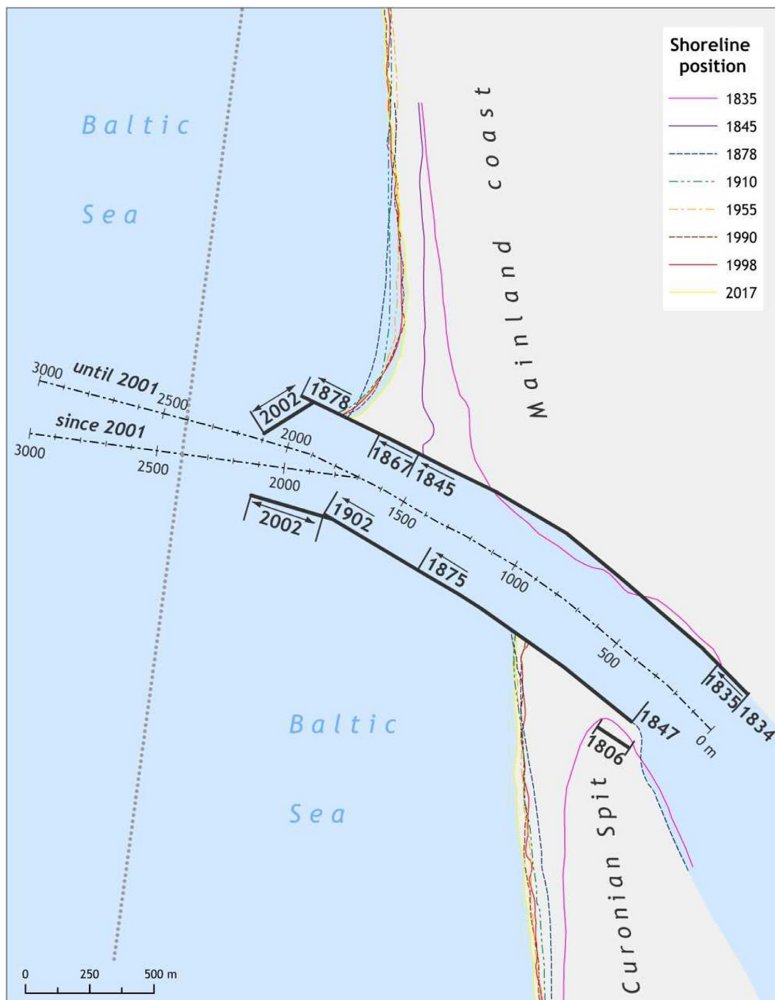


Figure 3 The stages of construction of the Port of Klaipėda's jetties and shoreline dynamics during the period 1835–2017. The dashed-dotted line indicates the fairway axis. The dotted line indicate nearshore depth dynamics showed in Figure 9. The scheme was compiled based on R. Knaps's data (1965): 1835, 1845, 1878, and on those of the authors: 1910, 1955, 1990, 1998, 2017.

on the shore. Later, when it was observed that some of the sand dumped behind the northern jetty had returned to the navigation channel, the dredged sand was dumped 10–20 m farther from the port at depths of 20–25 m from 1963 and 25–35 m from 1994.

The accumulation of large amounts of sand on the shore caused wide beaches (65–85 m) to form. In order to stop the intensive blowing of sand toward the town on the mainland shore and into the Curonian Lagoon, foredune ridge formation was started in as early as the first half of the 19th century (Musset, 1916). At the beginning of the 20th century, the foredune height beyond the northern jetty ranged from 3.8 m at a distance of 50 m from the jetty to 10.5 m

at a distance of 1620 m (Figure 6a). Even larger amounts of sand accumulated beyond the southern jetty: the height of the foredune ridge 50 m from the jetty was 6.0 m and at a distance of 1750 m it even reached 13.1 m (Figure 6b).

The maximal seaward shift of the shoreline on both sides of the jetties almost coincided with the end of the construction work (Figure 3).

3.2. Intensive dredging of the entrance channel (1902–2000)

Throughout the 20th century, the length and configuration of the port jetties remained the same (Figures 3, 4a–b). They were only heightened, widened and repaired. How-

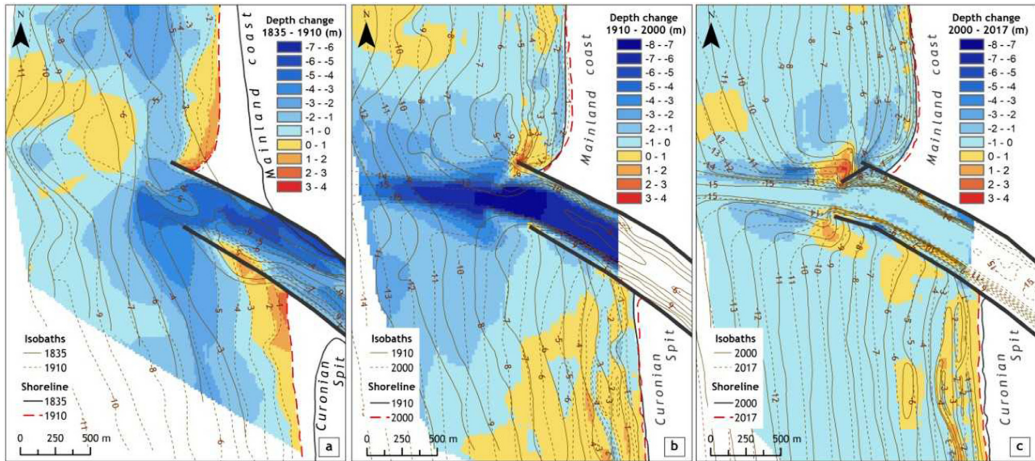


Figure 4 The coastal zone dynamics during the period 1835–2017. The positive depth change values indicate accumulation and the negative values indicate erosion.

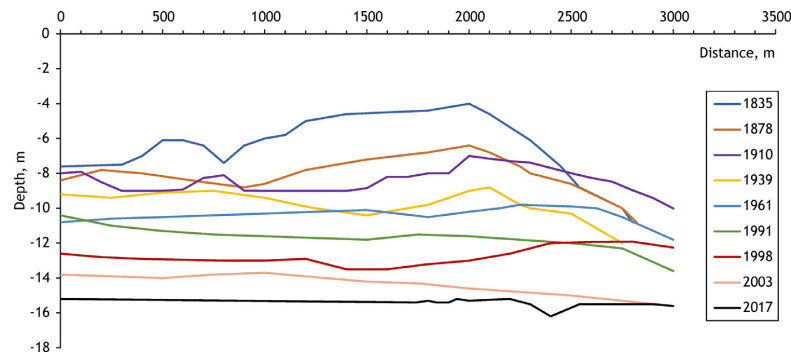


Figure 5 Depth dynamics along the fairway axis of the entrance channel from the start of Klaipėda Port construction to these days. The profile location is shown in [Figure 3](#).

Table 1 Shoreline dynamics (m/yr) in 1835–2017 at both sides of the Klaipėda Port jetties.

Period	Shoreline displacement, m/year					
The distance from jetty, m	1835–1878	1878–1910	1910–1955	1955–1990	1990–2004	2004–2017
Northern jetty	1250	2.83	0.22	0.40	1.09	0.39
	1000	3.35	0.91	-0.62	-0.14	0.38
	750	4.91	-0.09	-0.87	-0.29	-1.69
	500	6.16	-0.72	-0.69	-0.71	-1.94
	250	9.37	-1.22	-0.24	-0.43	-2.43
	50	12.7	0.38	-0.22	-0.46	-1.95
Southern jetty	50	9.81	0.22	-0.09	-1.29	-0.21
	250	6.61	0.84	-0.09	-0.46	-0.37
	500	4.02	0.81	0.27	-0.12	2.45
	750	2.79	1.41	0.36	0.17	-0.12
	1000	1.77	1.72	0.58	0.29	2.20
	1250	1.35	1.13	0.82	0.23	1.96

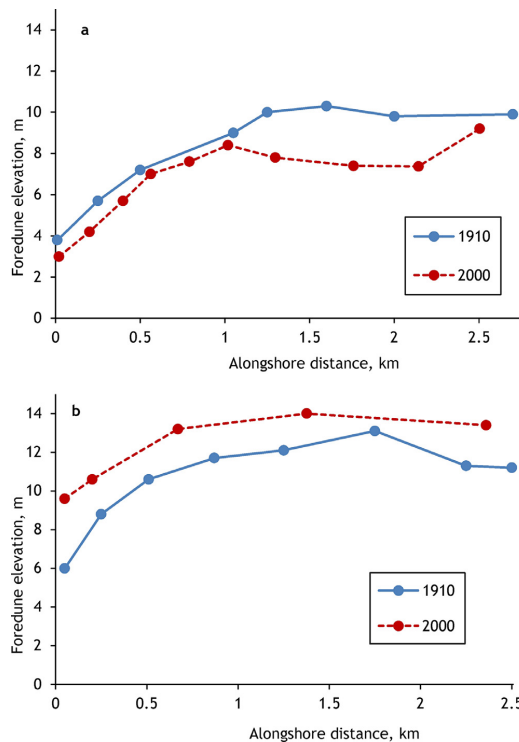


Figure 6 Dynamics of the foredune height in 1910–2000: a – northward, b – southward from the jetties.

ever, this timespan was marked by particularly significant changes in the parameters of the entrance channel. Since the beginning of the 20th century, efforts have been made to maintain a depth of 6 m in the entrance channel. In 1927, the depth was increased to 6.5 m, in 1928 to 8 m and in 1939 to 9.5 m. During and after the Second World War (1941–1958), the dredging works were irregular and the depth of the entrance channel varied from 6 to 8 m (Žilinskas, 1998). In 1958, regular dredging was resumed and in 1962 the depth reached 11 m and the channel was completely straightened for the first time. In order to accommodate ships with the deepest drafts, the dredging work continued: in 1974, the depth of the entrance channel had already reached 12 m, in 1986 it was 12.5 m and in 1997 it was 14.5 m (Figure 5).

The channel was simultaneously deepened and widened. Before the 20th century, judging from the bathymetric plans, the width of the entrance channel meandering between the bars ranged from 20 to 35 m. At the beginning of the 20th century it was 30–50 m. Between 1928 and 1939, the maintained width of the channel was 50 m, from 1945 it was 80 m, from 1957 it was 100 m and from 1997 it was 130 m. Beginning in 1960, in order to compensate for the rapid filling in of the channel during storms, the slopes of the channel were formed with smaller angles and sediment traps were constructed beyond the port gates. The entrance channel was widened to almost 260 m along an approximately 200 m sector beyond the port

gates. This wider cross-section of the navigation channel reduced the speed of the currents in the sediment traps along the channel and moderated any sudden changes in depth.

Deepening and widening the entrance channel increased the amount of dredged soil at the same time. Between 1930 and 1960, up to 100 000 m³/yr of soil was removed to maintain a depth of 8–9 m (Žaromskis and Gulbinskas, 2016). On average, approximately 210 000 m³/yr of soil had to be removed to maintain a depth of 10.5–11.0 m (1960–1970) and approximately 330 000 m³/yr to maintain a depth of 12–13 m (1970–1997). Based on data from the Klaipėda Port archives, between 1950 and 2000 over 10 million m³ of sediment was removed from the channel during the deepening and widening work.

It should be noted that the internal water area of the port was deepened and expanded at the same time the navigation channel was being deepened and widened. As a result, transitory coarse-grained sediment from the rivers and Curonian Lagoon accumulated in the inner water area of the port, and since the 1980s this has not had any effect on the filling in of the navigation channel (Gulbinskas, 1999; Mėžinė et al., 2019). At present, silt (0.01–0.0 mm) and clay (<0.01 mm) particles dominate the lagoon water (Remeikaitė-Nikienė et al., 2018).

In the 20th century, with the increasing amounts of dredged sediment, widening the entrance channel and dumping the dredged sand at greater depths in the water area adjacent to the entrance channel also increased. The nearshore erosion also increased significantly (Figure 4b). A comparison of the morphometric data from the bathymetric plans from 1910 and 2000 showed that during this timespan, while the entrance channel was being deepened and widened, approximately 3.7 million m³ of sediment was removed (the sediment removed during cleaning was not included). Due to sea bottom erosion, the nearshore to the north of the entrance channel has lost 1.3 million m³ of sediment and to the south 1.8 million m³.

The shallowing of the sea bottom (since the 1990s) at the distal end of the northern jetty can be explained by shipwrecks. On November 21 1981, a 170 m-long tanker from Gibraltar named "Globe Asimi" crashed at the distal end of the northern jetty, broke into two parts and sank. On September 25 1988 during a fierce storm, a German freighter named "Rudolf Breitscheid" (142.2 m long) crashed and sank in almost the same place. These ships are lying on the sea bottom (with their upper parts protruding a few metres above the surface) almost parallel to the shore along the northern jetty in a south-north direction and act as a barrier against the waves, thus creating the right conditions for the accumulation of sediment.

Ever since the jetties were finished, the shoreline on either side of them has been retreating (Figure 3). Near the northern jetty, a bay has developed with its central part at a distance of 500 m from the jetty (Figures 3, 4b). It is interesting to note that there was also maximal shore erosion 500 m from the downdrift side of a jetty in Gopalpur Port on the east coast of India (Mohanty et al., 2012). Between 1910 and 1990, the average rate of shoreline retreat in the central part of the bay was 0.63 m/yr (Table 1). Shoreline erosion took place in a sector stretching 1 km north of the jetty. In this sector, approximately 45.2 thousand m² of land

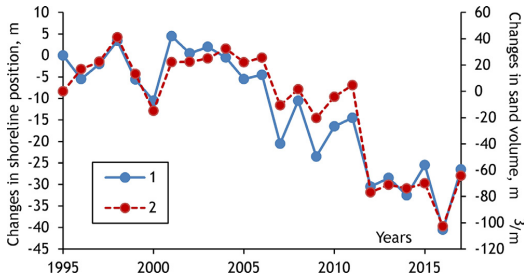


Figure 7 The shoreline dynamics (1) and the volume of sand (2) at a distance of 500 m north of the jetty during the period 1995–2017. The positive values indicate shoreline accretion and the amount of accumulated sand, and the negative values indicate shoreline erosion and the amount of eroded sand. The profile location is shown in Figure 1.

was washed away. During the analyzed timespan, the spatial position of the shoreline further to the north remained stable or even migrated slightly out to sea. This shoreline retreat has markedly changed the shore's morphology. The average width of the beach decreased from 60–75 m in 1910 to 35–45 m in 2000. Due to these narrow beaches, storms could reach and erode the foredune ridges. In the sector closest to the jetty, the foredune ridge has disappeared altogether (Figure 6a).

The last decade of the 20th century and the beginning of the 21st century can be viewed as an exception. During this timespan, the spatial position of the shoreline stabilized and in some places even moved out to sea. This phenomenon can be explained by the impact of the above-mentioned shipwrecks on hydro-lithodynamic processes. In 1995 work got underway to salvage the shipwrecks. The final wrecks were removed in 2005 and precisely at that time the shoreline retreat resumed and its intensity increased (Figure 7, Table 1).

South of the jetties, in the sector closest (250–300 m) to the jetties, the shoreline retreated throughout the 20th century (Figures 3, 4b, Table 1). In this sector, approximately 13.1 thousand m³ of land has washed away. Further to the north, the shoreline has been migrating seaward (with small fluctuations caused by extreme storms) since the port was first built. On the southern side of the port jetties, the changes to the beach width have not been as significant: from 65–75 m in 1910 to 40–60 m in 2000 within a 250–300 m-long sector. Further to the south, the beach width has remained almost unchanged (Žilinskas et al., 2001). The height of the foredune ridge has increased along the entire sector, but its spatial position in the 250 m-long sector closest to the southern jetty has changed (Figure 6b). As the shoreline has retreated (Figure 3) the foredune ridge has eroded. Some of the sand has washed away out to sea and some has been blown further to the leeward side of the foredune. Beyond this shore sector (Figures 3, 4b), where the dynamic trend of the shoreline changes (the shoreline's regression is replaced by transgression), not only has the height of the foredune ridge increased, but between 1910 and 2000 a new ridge developed 40–50 m from the foredune ridge closer to the sea. Its height in 2000 was 5–6 m (Žilinskas et al., 2001).

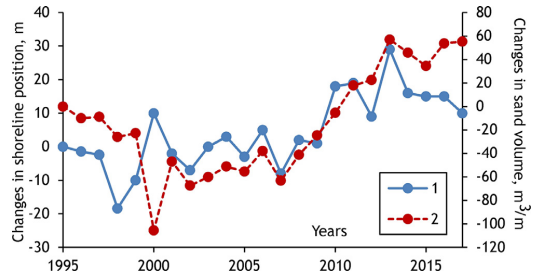


Figure 8 The shoreline dynamics (1) and the volume of sand (2) at a distance of 200 m north of the jetty during the period 1995–2017. The positive values indicate shoreline accretion and the amount of accumulated sand, and the negative values indicate shoreline erosion and the amount of eroded sand. The profile location is shown in Figure 1.

3.3. Reconstruction of the port jetties (2000–2017)

In 2001–2002, the jetties were lengthened (the northern one by 205 m and the southern one by 278 m), turning them SW. The port gates were narrowed in order to slow down the filling in of the entrance channel at the distal end of the jetties. The direction of the fairway axis was also changed (Figure 3). The entrance channel was deepened to 15.5 m, and to 16.2 beyond the port gates (Figure 5). The width of the entrance channel reached 150 m in 2004. Moreover, the slopes of the channel were made twice as flat (1:1, tgα = 0.166) as before (1:3, tgα = 0.333) in order to prevent the rapid filling in of the entrance channel during storms. In 2001–2002, new sediment traps approximately 200 m long and 125 m wide (on both sides of the channel) were dug around 200 m from the ends of the lengthened jetties.

Although relatively little time (15 years) has passed since the jetties were reconstructed, it is evident (Figure 4c) that the nearshore to the north of the deepened entrance channel and beyond the northern jetty has also deepened. A rather intensive accumulation of sediment has been observed at the end of the northern jetty. This is related to the ongoing filling in of the pits that were left after the shipwrecks were salvaged. Moreover, while the northern jetty was being lengthened, the northern sediment trap was filled in. After the jetties were lengthened, the retreat of the shoreline (av. 2.5 m/yr) beyond the northern jetty intensified (Figures 3, 7; Table 1). The foredune ridge along a 450 m sector stretching from the jetty was completely washed away.

After the jetties were reconstructed, there was an increase in the depth of seabed south of the deepened entrance channel, while on the adjacent nearshore an accumulation of sediment was also observed (Figure 4c). The shallowing of the nearshore affected the shoreline's dynamic trend (Figure 8).

Since around 2004, the shoreline has been migrating seaward (at a rate of approximately 1.5 m/yr) (Table 1). These changes could have been predetermined by a few factors: mitigated wave impact after lengthening the jetty and turning it westward, a smaller nearshore slope angle and filling in the former sediment traps. Moreover, in 2013, over

Table 2 Dynamics of the nearshore slope (up to a depth of 8 m) at both sides of Klaipėda Port jetties in 1835–2017.

Year	Nearshore slope ($\text{tg}\alpha$)					
	1835	1910	1955	2000	2017	1835–2017
The distance from jetty, m						
Northern jetty	1250	—	—	0.1000	0.0109	—
	1000	—	—	0.0086	0.0102	—
	750	0.0054	0.0087	0.0089	0.0088	0.0097
	500	0.0049	0.0087	0.0076	0.0081	0.0094
	250	0.0054	0.0076	0.007	0.0086	0.0121
	50	0.0057	0.008	0.0072	0.0104	0.0163
Southern jetty	50	0.0029	0.0065	0.0066	0.0082	0.0082
	250	0.0038	0.006	0.0061	0.0074	0.0075
	500	0.004	0.0059	0.0062	0.0074	0.0075
	750	0.0046	0.0057	0.0061	0.0071	0.0074
	1000	0.0047	0.0063	0.0062	0.0072	0.0073
						0.0026

3000 m³ of sand was poured onto the beach along a 150 m sector. Presumably, the shoreline's advance is a temporary phenomenon related to the above-mentioned circumstances. The 2018–2020 data show the shoreline retreating in the sector under consideration.

On generalizing the above investigation results, it can be stated that between 1834 and 1902, and between 2000 and 2017, morphological changes to the coastal zone were caused by the construction and reconstruction of the port jetties. Between 1902 and 2000, when the spatial positions of the jetties remained stable, there was a significant impact on the morphological changes in the port environment from deepening, widening and cleaning the entrance channel.

4. Discussion

The intensive expansion of ports on open littoral drift seashores that started in the 19th century is considered one of the most dramatic human interventions in coastal processes (Port Engineering II., 1990). It was determined that port jetties and breakwaters had a profound effect on the natural equilibrium of shore zones. An area of accretion forms on the updrift side of port jetties and an area of erosion on their downdrift side (Bakker, 1968; Bruun, 1995; Johnson, 1957; Komar, 1976; Kudale, 2010; Mohanty et al., 2012). These processes also are characteristic of south-eastern Baltic ports: Władysławowo in Poland (Szmytkiewicz et al., 2000), Baltijsk in Russia's Kaliningrad Region (Babakov and Chuburenko, 2019), and Liepaja and Ventspils in Latvia (Eberhards and Lapinskas, 2008).

Alongshore sediment transport from south to north dominates the Lithuanian shore (Knaps, 1965; Krek et al., 2016; Ostrowski et al., 2014; Pupienis et al., 2017; Žilinskas et al., 2018). This has been proven by investigations into the impact of the hydrotechnical constructions to the north of the Port of Klaipėda (there are no dredging works in their environment). Intensive accretion has taken place on the updrift (southern) side and erosion on the downdrift (northern) side of Palanga pier, which is located 22 km north of the Port of Klaipėda (built in 1878) (Žilinskas et al., 2010) and the unfinished Port of Šventoji (construction started in 1924)

(Kriauciūnienė et al., 2013), which is located 34 km from the Port of Klaipėda.

Shore zone erosion had already set in by the end of the 19th century to the north of the finished northern jetty in the Port of Klaipėda (Figures 3–4, Table 1). The changes in the coastal zone fully match the classic model of coastal zone development when alongshore sediment transport is disturbed by jetties (Bruun, 1995; Johnson, 1957; Komar, 1976; Kudale, 2010). In the case of the Port of Klaipėda, the course and development of the processes taking place on the northern side of the jetties caused a bay to be formed. Its development was evaluated by applying a mathematical function, namely a parabolic bay equation (Pupienis et al., 2013). On the other hand, discriminating between the effects of dredging and downdrift on the down-drift side of the port is quite a complicated task.

Meanwhile, on the updrift side of the jetties, where accretion was expected to take place, sediment barely accumulated on the nearshore after finishing the southern jetty. Moreover, in the nearest shore sector the shoreline did not migrate out to sea and even retreated inland (Figures 3–4, Table 1). Based on the investigation results (section 3), we can assume that these changes were predetermined by intensive cleaning of the entrance channel in the 20th century.

In contrast to the downdrift side of the jetties, erosion on their updrift side did not set in immediately after the end of the southern jetty's construction (Table 1). During the first half of the 20th century, when the amount of sediment dredged from the entrance channel was 100 thousand m³ yr, some of the lost sediment was compensated for by alongshore sediment transport. During the second half of the 20th century, when the amount of dredged sediment reached 330 thousand m³ yr, the alongshore sediment transport was unable to compensate for these losses.

This time lag is natural: at first, while the entrance channel was being deepened and widened, the sediment was replenished from the adjacent nearshore zone; therefore, the changes to the nearshore were not immediate. These processes are reflected by the slope angle dynamics across (Table 2) and along the nearshore (Figure 9).

Investigations into different underwater quarries on the northern nearshore of the Black Sea have also shown that

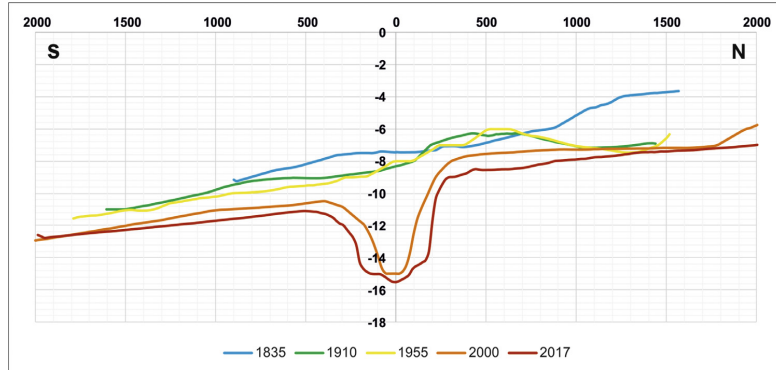


Figure 9 Nearshore depth dynamics at a distance of 400 m from the port gates in 1835–2017. Abscissa “0” on the fairway axis of entrance channel in 2001 (Figure 3).

the impact of dredging pits on the shore becomes evident only 3–4 years after the beginning of dredging works. In some cases, the impact on the shore only becomes apparent after 8 years such as, for example, in the Saxon Spit (the western part of the Crimean Peninsula) or 10 years as in Yalta Bay (the southern part of the Crimean Peninsula) (Šuiský et al., 1987). Presumably for this reason, M. R. Philips (2008), who investigated the nearshore in South Wales (Port Eynon and Horton Beach for 6 years and Port Penarth for 5 years), failed to establish any causality between seabed dredging and beach erosion.

Dredging the entrance channel causes changes in the wave field. Due to the wave divergence in the entrance channel, the wave height there decreases (Environmental Impact..., 2019). However, outside the entrance channel the wave refraction pattern changes along with the decrease in depth. The refraction tends to turn the waves away from the pit (Demir et al., 2004, Treloar, 1986). In the nearshore adjacent to the channel, due to the waves' convergence, the wave height increases. Bottom sediments driven by the waves settle to the bottom of the channel under the influence of gravity (Žilinskas, 1998). The bottom erosion of the nearshore adjacent to the entrance channel is also affected by the longshore sediment transport. The velocity of the longshore current is significantly reduced due to the greater depth of the entrance channel (Environmental Impact..., 2019). Therefore, sediments being transported along the shore settle in the channel. The sediment deficit increases in the coastal zone near the port, as the sediments dredged from the entrance channel are dumped in the Baltic Sea's deep water zone (Pupienis and Žilinskas, 2005).

During storms, the wave field at greater nearshore depths is subject to weaker transformations in the surf zone. Therefore, waves that are less reduced in height and that have more energy reach the shore (Brampton and Evans, 1998; Maa et al., 2001; Work, 2004). The wave set-up and the width of washed out beaches during storms are in direct dependence on the wave height (Žilinskas, 1994–1995). Therefore, the deepening of the nearshore causes the shore to erode. Investigations into the Port of Klaipėda environment have shown that intensive deepening of the

entrance channel caused nearshore and shore erosion on the updrift side of the jetty, even when a sufficient sediment load was being transported by the alongshore drift.

A reconstruction of the Port of Klaipėda' entrance channel and jetties is planned to take place in 2020; therefore, negative changes to the coastal zone are expected in the future, including a more rapid retreat of the shoreline (Environmental Impact..., 2019). Based on the results of wave height modelling for westerly winds of different speeds (Environmental Impact ..., 2019; Jakimavičius et al., 2018), it is estimated that in the case of winds with a speed of 15 m/s coming from a SW and W direction, there would be significant increases in the wave height at the port gate of 0.03 and 0.66 m, respectively. For winds coming from a NW direction, the wave height would decrease by 0.51 m. For winds with a speed of 20 m/s coming from a SW and W direction, the wave height would be expected to increase by 0.80 m and 1.67 m, respectively. For winds coming from a NW direction, the wave height would decrease by 0.97 m. These estimated increases in wave height for SW and W winds would lead to significant changes to the shoreline that would not be compensated for, even by the lower wave heights for the NW winds. According to the results of the wave height modelling (Environmental Impact..., 2019), the recurrence of winds with speeds over 10 m/s coming from a SW and W direction could reach 23.6% and 23.2%, respectively, i.e., they would be more frequent than winds coming from a NW direction (11.2%). Based on the shoreline modelling (Environmental Impact..., 2019), after the reconstruction of the Port of Klaipėda's jetties and entrance channel, the shoreline could retreat along a 50 m section on both sides of the jetties by 0.8 m/yr to the south and 1.3 m/yr to the north, respectively. A comparison of the modelled 2007–2013 shoreline dynamics with those of 1910–1990 showed the shoreline's average rate of retreat would increase to 0.11 m/yr to the south and 0.92 m/yr to the north. The modelling results confirmed the hypothesis that the erosion of the coastal zone near the Port of Klaipėda is related to the dredging of the entrance channel.

One way of mitigating the coastal zone erosion on the updrift side of the jetty would be nearshore and beach

nourishment using sand dredged from the entrance channel (Žilinskas, 1998). The previous nourishment of the nearshore at Giruliai (Karaliūnas et al., 2020; Žilinskas et al., 2003) and of the beach at Palanga (Pupienis et al., 2014; Žilinskas et al., 2008) proved and ensured the stability of the coastal sections. Also, sand dredged from the entrance channel could be used to form a sandbar along the shore (Žilinskas et al., 2010). However, as noted by Staniszewska et al. (2016), to ensure coastal zone protection from erosion, the amount of sediment used for coastal nourishment should be significantly increased.

5. Conclusion

Due to dredging works in coastal zones, lithodynamic systems lose some sediment, thus causing sediment deficiencies on the nearshore. Meanwhile, the energy potential of waves remains the same or even increases due to weaker wave transformation in surf zones. Coastal erosion intensifies. In other words, natural systems attempt to compensate for sediment loss in their coastal zones and to restore a state of equilibrium. Investigations into the Port of Klaipėda environment have shown that intensive deepening and cleaning of the entrance channel caused nearshore and shore erosion on the updrift side of the port jetty, even when the sediment load transported by the alongshore sediment drift is sufficient.

Acknowledgments

This research did not receive any specific grant from funding agencies in the public, commercial, or not-for-profit sectors. We are grateful to both reviewers for the helpful comments on an earlier version of this manuscript.

References

- Babakov, A.N., Chuburenko, B.V., 2019. The Structure of the Net Alongshore Sediment Transport in the Eastern Gulf of Gdańsk. *Water Res.* 46 (4), 515–529, <https://doi.org/10.1134/S0097807819040031>.
- Bakker, W.T., 1968. The Dynamics of Coast with a Groin System. Proc. 11th Conf. Coast. Eng. 492–517.
- Blackman, B., 1951. Dredging at Inlets on Sandy Coasts. Proc. 1st Conf. Coast. Eng., 169–174.
- Brampton, A.H., Evans, C.D.R., 1998. Regional seabed sediment studies and assessment of marine aggregate dredging. *CIRIA Rep. C505*, London, 28–32.
- Bruun, P., 1995. The Development of Downdrift Erosion. *J. Coast. Res.* 11 (4), 1242–1257, <http://www.jstor.org/stable/4298427>.
- Demir, H., Otay, E.N., Work, P.A., Börökçi, O.S., 2004. Impacts of Dredging on Shoreline Change. *J. Waterway, Port, Coast., Ocean Eng.* 130 (4), 170–178, [https://doi.org/10.1061/\(ASCE\)0733-950X\(2004\)130:4\(170\)](https://doi.org/10.1061/(ASCE)0733-950X(2004)130:4(170)).
- Eberhards, G., Lapinskis, J., 2008. Processes on the Latvian Coast of the Baltic Sea. *Atlas*. Riga, 64 pp.
- Environmental Impact Assessment of Klaipeda State Seaport External and Internal Entrance Chanal Improvement (Dredging and Distribution), Southern and Northern Breakwater Reconstruction (Construction) and Part of the Curonian Spit Slope Reinforcement and Southern Port Gate Construction Environmental Impact Assessment., 2019. Sweco Lietuva, Vilnius, 905 pp., https://www.sweco.lt/contentassets/b18af075b8484f838a58090c1df73b55/2019-02-26-pav-ataskaita_sweco-www.pdf.
- Gulbinskas, S., 1999. Anthropogenic impact and geological processes in the Baltic Sea. In: *Lietuvos moksłas*, Vilnius, 338–355.
- Hagen, L.H., 1885. Die Seehafen in der Provinzen Preussen. II. Der Hafen zu Memel, Berlin, 133 pp.
- Healy, T., Stephens, S., Blacka, K., Gorman, R., Cole, R., Beamsley, B., 2002. Port redesign and planned beach renourishment in a high wave energy sandy-muddy coastal environment, Port Gisborne, New Zealand. *Geomorphology* 48, 163–177, [https://doi.org/10.1016/S0169-555X\(02\)00180-0](https://doi.org/10.1016/S0169-555X(02)00180-0).
- HELCOM, 2015. Guidelines for Management of Dredged Material at Sea. HELCOM, Helsinki, 39 pp.
- Jakimavičius, D., Kriauciūnienė, J., Šarauskienė, D., 2018. Assessment of wave climate and energy resources in the Baltic Sea nearshore (Lithuanian territorial water). *Oceanologia* 60 (2), 207–218, <https://doi.org/10.1016/j.oceano.2017.10.004>.
- Jarmalavičius, D., Pupienis, D., Žilinskas, G., Janušaitė, R., Karaliūnas, V., 2020. Beach-Foredune Sediment Budget Response to Sea Level Fluctuation. *Curonian Spit, Lithuania. Water* 12 (2), 583, 1–12, <https://doi.org/10.3390/w12020583>.
- Jarmalavičius, D., Pupienis, D., Žilinskas, G., Karaliūnas, V., Jukná, L., 2019. The development and stability of beach-dune system on the wave-dominated coast: A case study of the Curonian Spit, Lithuania. *Aeolian Res.* 41, 100542. 1–7, <https://doi.org/10.1016/j.aeolia.2019.100542>.
- Jarmalavičius, D., Satkūnas, J., Žilinskas, G., Pupienis, D., 2012. Dynamics of beaches of Lithuanian coast (the Baltic Sea) for the period 1993–2008 based on morphometric indicators. *Env. Earth Sci.* 65 (6), 1727–1736, <https://doi.org/10.1007/s12665-011-1152-3>.
- Jarmalavičius, D., Žilinskas, G., Pupienis, D., Kriauciūnienė, J., 2017. Subaerial beach volume change on a decadal time scale: the Lithuanian Baltic Sea coast. *Zeitschrift für Geomorph* 61 (2), 149–158, <https://doi.org/10.1127/zfg/2017/0441>.
- Johnson, J.W., 1957. Littoral Drift Problem at Shoreline harbors. *J. Waterways and Harbors Division, ASCE* 83 (WW1) 1211-1–1211-37.
- Karaliūnas, V., Jarmalavičius, D., Pupienis, D., Janušaitė, R., Žilinskas, G., Karlonienė, D., Malvárez, G., Navas, F. (Eds.), 2020. Shore nourishment impact on coastal landscape transformation: An example of the Lithuanian Baltic Sea coast. *Global Coastal Issues of 2020. J. Coas. Res.* 95 (SI), 840–844, <https://doi.org/10.2112/SI95-163.1>.
- Klaps, R.B., 1965. Sediment transport along the southeastern Baltic Sea coast. *Tech. Rep. 104*, Latgipprom, Riga, 16 pp.
- Kojima, H., Ijima, T., Nakamura, T., 1986. Impact of offshore dredging on beaches along the Genkai Sea, Japan. In: *Proc. 20th Int. Conf. on Coast. Eng. ASCE*, New York, 1281–1295.
- Komar, P.D., 1976. *Beach Processes and Sedimentation*. Prentice-Hall Inc, New Jersey, 429 pp.
- Krek, A., Stont, Z., Ulyanova, M., 2016. Alongshore bedload transport in the south eastern part of the Baltic Sea under changing hydroeteorological conditions. *Reg. Stud. Mar. Sci.* 7, 81–87, <https://doi.org/10.1016/j.rsma.2016.05.011>.
- Kriauciūnienė, J., Gailiušis, B., Kovalenkovienė, M., 2006. Peculiarities of sea wave propagation in the Klaipėda Strait. *Lithuanica Baltica* 19 (1), 20–29.
- Kriauciūnienė, J., Žilinskas, G., Pupienis, D., Jarmalavičius, D., Gailiušis, B., 2013. Impact of Šventoji port jetties on coastal dynamics of the Baltic Sea. *J. Env. Eng. Land. Manag.* 21 (2), 114–122, <https://doi.org/10.3846/16486897.2012.695736>.
- Kudale, M.D., 2010. Impact of port development on the coastline and the need for protection. *Ind. J. Geo-Mar. Sci.* 39 (4), 597–604, <http://nopr.niscair.res.in/handle/123456789/10808>.
- Maa, J.P.-Y., Hobbs III, C.H., Hardaway Jr, C.S., 2001. A Criterion for

- Determining the Impact on Shorelines Caused by Altering Wave Transformation.** *J. Coast. Res.* 17 (1), 107–113.
- Marine Habitat Committee, 2000. Report of the working group on the effects of extraction of marine sediments on the marine ecosystem. Rep. No. ICES CM 2000/E:07, Gdańsk, Poland, 49 pp.
- McLoughlin, L.C., 2000. Shaping Sydney Harbour: Sedimentation, dredging and reclamation 1788–1990s. *Aust. Geogr.* 31 (2), 183–208, <https://doi.org/10.1080/713612246>.
- Mėžinė, J., Ferrarin, C., Vaiciūtė, D., Idzelytė, R., Zemlys, P., Umgieser, G., 2019. Sediment Transport Mechanisms in a Lagoon with High River Discharge and Sediment Loading. *Water* 11 (10), 1–24, <https://doi.org/10.3390/w11101970>.
- Mohanty, P.K., Patra, S.K., Bramha, S., Seth, B., Pradhan, U., Behera, B., Mishra, P., Panda, U.S., 2012. Impact of groins on beaches morphology: a case study near Gopalpur port, east coast of India. *J. Coast. Res.* 28 (1), 132–142, <https://doi.org/10.2112/JCOASTRES-D-10-00045.1>.
- Müssel, M., 1916. Untersuchungen über die Erfolge der Dunenarbeiten auf der Kurischen Nehrung, Memel, 32 pp.
- Ostrowski, R., Pruszak, Z., Babakov, A., 2014. Condition of southeastern Baltic Sea shores and methods of protecting them. *Archives of Hydro-Engineering and Environmental Mechanics* 61 (1–2), 17–37, <https://doi.org/10.1515/heem-2015-0002>.
- Phillips, M.R., 2008. Beach erosion and marine aggregate dredging: a question of evidence? *Geograph. J.* 174 (4), 332–343, <https://www.jstor.org/stable/40205253>.
- Pupienis, D., Žilinskas, G., 2005. Specific features of morphodynamic processes in the dumps of the Lithuanian offshore. *Baltica* 18 (1), 29–37.
- Pupienis, D., Buynevich, I., Ryabchuk, D., Jarmalavičius, D., Žilinskas, G., Fedorovič, J., Kovaleva, O., Sergeev, A., Cichoń-Pupienis, A., 2017. Spatial patterns in heavy-mineral concentrations along the Curonian Spit coast, southeastern Baltic Sea. *Estuar. Coast. Shelf Sci.* 195, 41–50, <https://doi.org/10.1016/j.ecss.2016.08.008>.
- Pupienis, D., Jarmalavičius, D., Žilinskas, G., Fedorovič, J., 2014. Beach nourishment experiment in Palanga, Lithuania. In: Green, A.N., Cooper, J.A.G. (Eds.), *Proceedings 13th International Coastal Symposium* (Durban, South Africa), *J. Coas. Res.*, 70(SI), 490–495.
- Pupienis, D., Jonuškaitė, S., Jarmalavičius, D., Žilinskas, G., 2013. Klaipėda port jetties impact on the Baltic Sea shoreline dynamics, Lithuania. *J. Coast. Res.* 65(SI), 2167–2172, <https://doi.org/10.2112/SI65-366.1>.
- Remeikaitė-Nikienė, N., Garnaga-Budré, G., Lujanienė, G., Jokšas, K., Stankevičius, A., Malejovas, V., Barisevičiutė, R., 2018. Distribution of metals and extent of contamination in sediments from the south-eastern Baltic Sea (Lithuanian zone). *Oceanologia* 60 (2), 193–206, <https://doi.org/10.1016/j.oceano.2017.11.001>.
- Shaw, J.R., 1978. Coastal response at Point Pelee, Lake Erie. *Rep. Symp. Tech. Environ. Speciecon. And Regul. Aspects Coast. Zone Manag.* San-Francisco 3, 1937–1953.
- Simons, R., Hollingham, S., 2001. Marine aggregate dredging: A review of current procedures for assessing coastal processes and impact at the coastline. *Tech. Rep. No HYD10401, Civil Environ. Eng. Dept., Univ. College London, London*, 81 pp.
- Šuiský, J.D., Vychovanec, G.B., Pedan, G.S., 1987. Results of investigations of the impact of underwater sand dredging on the dynamics of the shores of the Black Sea dynamics. In: Vašutinskaja, L.G. (Ed.). In: *Prirodnyje osnovy beregozaschity*. Moskva, Nauka, 68–82.
- Szmytkiewicz, M., Biegowski, J., Kaczmarek, L.M., Okroj, T., Ostrowski, R., Pruszak, Z., Rozynsky, G., Skaja, M., 2000. Coastal line changes nearby harbour structures: comparative analysis of one-line models versus field data. *Coast. Eng.* 40, 119–139.
- Staniszewska, M., Boniecka, H., Cykowska, H., 2016. Dredging works in the Polish open sea ports as an anthropogenic factor of development of sea coastal zones. *Bulletin of the Maritime Institute in Gdańsk* 31 (1), 173–180, <https://doi.org/10.5604/12307424.1223959>.
- Treloar, P.D., 1986. Spectral wave refraction under the influence of depth and current. *Coast. Eng.* 9, 439–452, [https://doi.org/10.1016/0378-3839\(86\)90007-4](https://doi.org/10.1016/0378-3839(86)90007-4).
- Tsinker, G.P., 2004. *Port Engineering*. John Wiley and Sons Inc, USA, 882 pp.
- Veit, H.K., 1821. *Beschreibung des Memelschen Hafens und der daselbst angelegten Werke, nebst einem Situations Plane*. In: *Beiträge zur Kunde Preussens*, 4. Königsberg, 458–516.
- Work, P.A., Fehrenbacher, F., Voulgaris, G., 2004. Nearshore Impacts of Dredging for Beach Nourishment. *J. Waterway, Port, Coast., Ocean Eng.* 130, 303–311, [https://doi.org/10.1061/\(ASCE\)0733-950X\(2004\)130:6\(303\)](https://doi.org/10.1061/(ASCE)0733-950X(2004)130:6(303)).
- Žaromskis, R., 2008. *Baltic Sea Ports*. Vilnius University, Vilnius, 432 pp.
- Žaromskis, R., Gulbinskas, S., 2016. Changes of Baltic Sea nearshore bottom relief in the vicinity of Klaipėda harbour during the 20th century. *Geologija. Geografija* 2 (3), 135–150.
- Žilinskas, G., 1998. The peculiarities of shoreline dynamics in the impact zone of Klaipėda port. *Geografijos metraštis* 31, 99–109.
- Žilinskas, G., 1994. Set-up in the surf zone. *Geografijos metraštis* 28, 235–255.
- Žilinskas, G., Jarmalavičius, D., Minkevičius, V., 2001. *Eolian processes on the marine coast*. GI, Vilnius, 284 pp.
- Žilinskas, G., Jarmalavičius, D., Pupienis, D., 2003. The influence of nourishment of nearshore sediment supplies on the coast. *Geografijos metraštis* 36 (1), 89–100.
- Žilinskas, G., Jarmalavičius, D., Pupienis, D., 2018. The influence of natural and anthropogenic factors on grain size distribution along the southeaster Baltic spits. *Geol. Q.* 62 (2), 375–384, <http://dx.doi.org/10.7306/gq.1413>.
- Žilinskas, G., Pupienis, D., Jarmalavičius, D., 2010. Possibilities of regeneration of Palanga coastal zone. *J. Env. Land. Manag.* 18 (2), 95–10, <http://doi:10.3846/jejm.2010.11>.

IV PUBLIKACIJA

**Nearshore sandbar switching episodes and their relationship with
coastal erosion at the Curonian Spit, Baltic Sea**

Janušaitė R., Jarmalavičius D., Pupienis D., Žilinskas G., Jukna L.
Oceanologia, 2021.

DOI: <https://doi.org/10.1016/j.oceano.2021.11.004>

Available online at www.sciencedirect.com

ScienceDirect

journal homepage: www.journals.elsevier.com/oceanologia

Nearshore sandbar switching episodes and their relationship with coastal erosion at the Curonian Spit, Baltic Sea

Rasa Janušaitė^{a,*}, Darius Jarmalavičius^a, Donatas Pupienis^a,
Gintautas Žilinskas^a, Laurynas Jukna^b

^a Laboratory of Geoenvironmental Research, Nature Research Centre, Vilnius, Lithuania

^b Institute of Geosciences, Vilnius University, Vilnius, Lithuania

Received 30 August 2021; accepted 22 November 2021

Available online xxx

KEYWORDS

Nearshore
morphodynamics;
Multiple sandbar
system;
Storms;
Sand volume;
Lithuania

Abstract The longshore realignment of nearshore sandbars is a morphodynamic phenomenon of multiple sandbar systems that has been known about for several decades. However, it is unknown how switching-related nearshore changes influence the evolution of subaerial beaches. This study aims to define the relationship between sandbar switching episodes and the dynamic state of the beach-foredune system along the Curonian Spit coast (Baltic Sea) using decadal satellite-derived and beach profiling data. To define this connection, sandbar switching locations, sandbar cross-shore positions, shoreline positions, and sand volume changes in the beach-foredune system were assessed on interannual and storm-related time scales. Twenty-seven sandbar switching episodes were observed with an average duration of 14.3 months. Most of the switching episodes occurred at preferred locations, coinciding with breaking points of different shoreline orientations where oblique waves and longshore currents prevailed. Shoreline retreat at an average rate of -14.2 m was observed within most of the sandbar switching zones. During major storm events, the average rate of erosion within the sandbar switching zones was significantly higher than the rate outside them. On an interannual time scale, a moderate average rate of erosion was observed within the sandbar switching zones compared to a small accretion rate outside them. Additional case studies of coastal evolution within the

* Corresponding author at: Laboratory of Geoenvironmental Research, Nature Research Centre, Akademijos Str. 2, 08412, Vilnius, Lithuania.
E-mail address: rasa.janusaite@gamtc.lt (R. Janušaitė).

Peer review under the responsibility of the Institute of Oceanology of the Polish Academy of Sciences.



Production and hosting by Elsevier

<https://doi.org/10.1016/j.oceano.2021.11.004>

0078-3234/© 2021 Institute of Oceanology of the Polish Academy of Sciences. Production and hosting by Elsevier B.V. This is an open access article under the CC BY-NC-ND license (<http://creativecommons.org/licenses/by-nc-nd/4.0/>).

Please cite this article as: R. Janušaitė, D. Jarmalavičius, D. Pupienis et al., Nearshore sandbar switching episodes and their relationship with coastal erosion at the curonian spit, Baltic Sea, Oceanologia, <https://doi.org/10.1016/j.oceano.2021.11.004>

switching zones indicated well-correlated rates of switching-determined outer sandbar positions, shoreline positions, and sand volume on the beach and foredune during the switching episodes. The results of this study could be important for the identification of erosional hot spots and coastal prediction.

© 2021 Institute of Oceanology of the Polish Academy of Sciences. Production and hosting by Elsevier B.V. This is an open access article under the CC BY-NC-ND license (<http://creativecommons.org/licenses/by-nc-nd/4.0/>).

1. Introduction

The magnitude and occurrence of coastal erosion are spatiotemporally variable and controlled by complex natural and anthropogenic factors (Stive et al., 2002). In sandy environments, natural factors include wave climate, sea-level fluctuations, coastal orientation, and antecedent or nearshore morphology (Del Río et al., 2013; Stive et al., 2002). The key feature characterising the latter is nearshore sandbars. Various studies have aimed to determine links between the dynamics of nearshore sandbars and subaerial beaches on a range of temporal scales: from long-term and middle-term (Aagaard et al., 2004; McNinch, 2004; Splinter et al., 2018; Stive et al., 1997; Tătui et al., 2013; Umeda et al., 2018; Yuhi and Umeda, 2018), to short-term and storm-related (Castelle et al., 2015, 2007; Kuznetsova and Saprykina, 2019). They related the short-term and mid-term variability of shoreline and sediment volume on subaerial beaches to the cyclic variability of sandbar systems during net offshore migration (NOM) (Parlagreco et al., 2019; Shand et al., 2006; Yuhi et al., 2016; Yuhi and Umeda, 2018); observed beach sediment supply from sandbar welding (Aagaard et al., 2004; Cohn et al., 2017) and coupled shoreline and sandbar behaviour (Balouin et al., 2013; Gijssman et al., 2021; Pruszak et al., 2008; Quartel et al., 2008; Ruessink et al., 2007; Van de Lageweg et al., 2013); documented the role of nearshore sandbars in the formation of coastal erosion spots during storm events (Castelle et al., 2019, 2015, 2007; Harley et al., 2009; Thornton et al., 2007) and post-storm shoreline recovery (Brooks et al., 2017; Phillips et al., 2017). Although a considerable amount of research has been devoted to understanding connections between subaerial beaches and subaqueous sandbars, there are still many unknowns about these interactions.

At the end of the last century sandbar switching as a feature of multiple sandbar system behaviour was observed (Shand and Bailey, 1999; Wijnberg and Wolf, 1994). It involves longshore sandbars becoming discontinuous and on their discontinuous side attaching to a landward or seaward sandbar (Shand, 2003; Shand et al., 2001). A sandbar switching period consisting of interrelated sandbar switches is referred to as a sandbar switching episode (Shand et al., 2001). The longshore area of a sandbar switching episode extends from several hundred meters to a few kilometres, and is referred to as a transitional zone (Aleman et al., 2017; Shand et al., 2001; Wijnberg and Wolf, 1994) or, in this study, a sandbar switching zone.

Sandbar realignment has been observed in video observations, bathymetric datasets, aerial photography, and LiDAR data on microtidal and mesotidal coasts (Aleman et al.,

2017; Bouvier et al., 2017; Ojeda et al., 2008; Shand, 2003; Shand et al., 2001; Walstra et al., 2016; Wijnberg et al., 2007; Wijnberg and Wolf, 1994). The current knowledge about sandbar switching episodes can be summarised as follows: 1) naturally, they seem to be caused by shore-oblique high energy events and strong longshore currents if longshore differences in the sandbar morphology are present (Aleman et al., 2017; Shand et al., 2001); 2) they may be triggered by alongshore variability related to shoreface nourishment or underwater coastal engineering structures (Bouvier et al., 2017; Ojeda et al., 2008; Vermaas et al., 2017; Wijnberg et al., 2007); 3) sandbar switching locations may be persistent or non-persistent (Walstra et al., 2016); 4) persistent switching locations are transitional zones between multiple sandbar systems exhibiting different characteristics of the NOM cycle (Walstra et al., 2016); 5) sandbar switching zones migrate alongshore at a rate of between tens and hundreds of meters per month (Shand et al., 2001; Wijnberg and Wolf, 1994); 6) sandbar switches may be shoreward propagating (migrating from outer-middle sandbar switches to middle-inner ones) or stationary (Shand et al., 2001); 7) sandbar switching is not a seasonal phenomenon and its effect on nearshore morphodynamic system lasts for several seasons (Wijnberg et al., 2007). A sandbar switching episode is associated with significant changes in sandbar cross-shore and longshore positions, which affects the nearshore flow field and may cause changes in coastal evolution. However, interactions between these transitional zones in the subaqueous and subaerial domains have never been studied to the best of our knowledge.

In this study, sandbar switching is explored as being one of the factors determining interannual and storm-induced coastal erosion. The primary aim of this study is to define the relationship between sandbar switching episodes and the evolution of subaerial beaches in a non-tidal wave-dominated environment on the Lithuanian part of the Curonian Spit coast (South-Eastern Baltic Sea). To achieve this, the occurrence and persistence of sandbar switching on the Curonian Spit are determined. Satellite-derived shoreline changes in the coastal areas of sandbar switching are assessed and the relationship between sandbar switching and sand volume on a subaerial beach is defined on interannual and storm-related time scales.

2. Material and methods

2.1. Study area

The Curonian Spit is a sandy barrier in the South-Eastern Baltic Sea, stretching for 98 km from the Sambia Peninsula

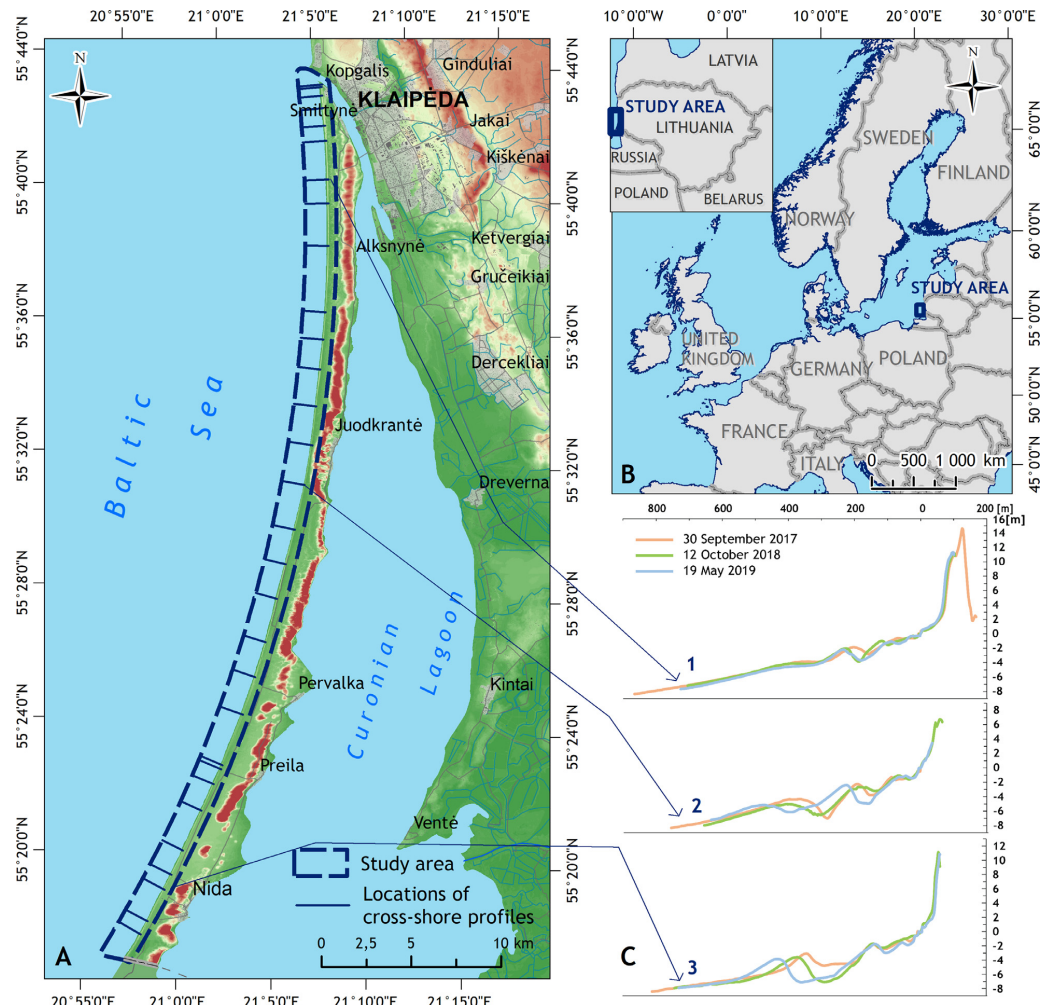


Figure 1 The study area in the Lithuanian part of the Curonian Spit configuration with the locations of the topographic surveys (A), the location of the study area (B), and examples of coastal cross-shore profiles (C).

to the Klaipėda Strait. The 51 km-long northern part of the Curonian Spit, from the Klaipėda port jetty to the Lithuanian state border, was analysed in this study (Figure 1). The Curonian Spit coast is a non-tidal wave-dominated environment. Waves approaching from westerly directions (North-West, South-West, West) are dominant on the nearshore of the Curonian Spit. The annual mean wave height at Klaipėda is 0.5–1 m (Kelpšaitė and Dailidienė, 2011). The wave climate on the nearshore of the Curonian Spit is seasonal, with a mean wave height of 0.76 and 0.85 m in winter and autumn, and 0.56 and 0.62 m in spring and summer (Jakimavičius et al., 2018). The morphology of the study area mostly results from natural coastal evolution, but the development of the northern end of the Curonian Spit is influenced by the Klaipėda port jetty (Žilinskas et al., 2020).

The subaerial section of the Curonian Spit coast is characterised by sandy beaches, composed of fine and medium sand, and bordered by a foredune ridge. The beaches are 30–80 m wide and the foredune height ranges from 6 to 16 m (Figure 1c) (Jarmalavičius et al., 2017; Žilinskas et al., 2018). The underwater slope of the Curonian Spit consists of a multiple sandbar system with 2–5 longshore sandbars. The width of the sandbar zone from the shoreline to the lower limit of the seaward outer sandbar slope varies from 250 to 750 m. The nearshore slope ($\tan \beta$) in the sandbar zone is 0.009–0.014. The northern part of the study area is characterised by the smallest sandbars, and the lowest sandbar zone width, slope, and depth (Figure 1c). The southern part of the study area is characterised by the largest sandbars, a wider sandbar zone, a higher nearshore slope, and a

greater depth ([Figure 1c](#)). The multiple sandbar system on the nearshore of the Curonian Spit exhibits various types of morphologies, from longshore straight to crescentic (mostly irregular) and shore-attached.

2.2. Field and satellite data

In this study, a combination of multispectral satellite imagery and cross-section beach profiling surveys for the period 2009–2021 was used to assess morphological changes in the nearshore and subaerial beach.

The beach profiling was performed at 30 fixed cross-shore profiles ([Figure 1a](#)) every April–May using the Topcon HiPer SR Global Navigation Satellite System (GNSS) with a vertical accuracy of 0.015 m. The beach profiling data were used to evaluate interannual sand volume changes on the beach and foredune. Surveys to evaluate storm-induced sand volume changes were carried out within a week after a storm event when the weather had calmed down and the water level had dropped.

42 RapidEye (for the period 2009–2016) and 103 PlanetScope (for the period 2016–2021) images were employed for the shoreline extraction and identification of the sandbar switching phenomenon. RapidEye is a constellation of five identical push-broom satellite sensors that acquired five-band (Blue, Green, Red, Red-Edge, Near-Infrared) imagery with a spatial resolution of 5 m every 5.5 days during the period 2009–2020. PlanetScope is a constellation of approximately 130 satellites that has acquired four-band (Blue, Green, Red, Near-Infrared) imagery daily with a spatial resolution of 3 m since 2016. In this study, atmospherically and geometrically corrected (to < 10 m RMSE positional accuracy) RapidEye Level 3A and PlanetScope Level 3B products were used ([Planet, 2021](#); [Planet Team, 2017](#)).

To identify sandbar switching locations during major storm events that occurred before the launch of the Rapid-Eye constellation, imagery of Landsat-4 and Landsat-5 Thematic Mapper (TM) was used. The Landsat 4–5 TMs are multispectral satellite sensors that collected seven-band (spectral range 450–1250 nm) imagery with a spatial resolution of 30 m and a temporal resolution of 16 days during the period 1982–2012. Landsat Level-2 surface reflectance products were used in this study ([USGS, 1998](#)).

The presence of sandbar switching during storm events was identified using satellite images from the last and first available dates when the sandbar morphology was clearly visible before and after the storm events. The time between the storm and image acquisition date ranged from 4 to 11 days for storm Laura and from 45 to 75 days for storm Felix. Because the average duration of a sandbar switching episode on the Curonian Spit is 435 days, sandbar switching was considered to be present during a storm event if it was observed before and after the storm.

2.3. Identification and definition of sandbar switching zones

Every satellite image for the period 2009–2021 was inspected visually and sandbar switching zones were localised manually. Sandbar switching zone was defined as a nearshore area stretching in an alongshore direction 500 m

to the north and 500 m to the south of the point where the sandbar joined another seaward or landward-located sandbar ([Figure 2a](#)). If switching occurred between multiple sandbars, a distance of 500 m was calculated from the northernmost and southernmost joins ([Figure 2b](#)). The defined sandbar switching zone covered the area where the morphology of the sandbar system was affected by the switching. The first observation, last observation, duration, position of the switched sandbars, and switching type were fixed for each switching zone. The image acquisition date, when a sandbar was observed to be connected to another sandbar for the first time was considered to be the first observation; the image acquisition date when a sandbar join was visible for the last time was considered to be last observation. Switches involving outer and middle sandbars were analysed in this study; switches involving inner sandbars only were ignored due to the complexity of the inner nearshore morphology and their small influence on the characteristics of the overall sandbar system. The position of the outer sandbar was assessed to be the distance of the outer sandbar crest from the mean shoreline. Changes in the distance of the outer sandbar from the mean shoreline was considered to be one of the characteristics that showed switching-induced changes in the sandbar system. Sandbar crests were delineated from the PlanetScope and RapidEye images using an automated procedure, described in [Janušaitė et al. \(2021\)](#), with an average root mean square error (RMSE) of 5.8 and 7 m, respectively.

2.4. Determination of subaerial beach characteristics

An automated algorithm was designed for the shoreline extraction from the satellite images used in this study. The Normalized Difference Water Index (NDWI) ([McFeeters, 1996](#)) was calculated for the images and was used as input for the ISODATA unsupervised classification in combination with a near-infrared band to classify the images into land or sea (for the detailed procedure see [Janušaitė et al., 2021](#)). The boundary between land and sea was considered to be shoreline. Using this method, the shorelines were derived with an average RMSE of 4.4 m.

Shoreline-perpendicular transects were generated along the study area every 25 meters to evaluate changes in the shoreline position. The shoreline position, fixed one year before the first observation of a sandbar switching episode, was used as a starting point to calculate the shoreline change rate for a specific date. Every procedure involving satellite images was performed in the ArcGIS 10.7 environment.

The annual sand volume changes were calculated for the beach and foredune from the cross-shore profiles by comparing two successive years. To evaluate the impact of storms, the last cross-shore profiles before a storm were compared to those, measured after the storm. The sand volume in the cross-shore profiles was defined as an area enclosed by the beach and foredune surface and a horizontal line from the shoreline to the foredune landward toe. The mean of the annual and post-storm sand volume change rate in the profiles inside and outside the sandbar switching zones was compared using a two-sample t-test and the me-

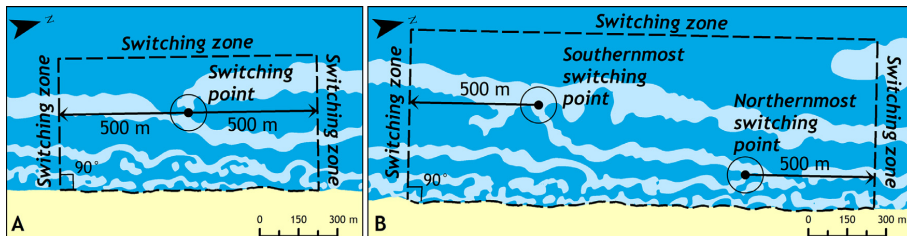


Figure 2 Definition of sandbar switching zone boundaries: A – a case of a switching zone with a single switch within its boundaries; B – a case of a switching zone with multiple switches within its boundaries.

Table 1 Duration of sandbar switching episodes on the Curonian Spit.

Type of switching episode	Number of observations	Duration of switching episode [months]				
		Average	Median	25–75%	Min	Max
Permanent switch	12	18.0	13	8.0–25.5	2	49
Temporary switch	11	9.3	6	5.0–15.0	2	26
Temporary connection	4	17.3	12	8.8–31.0	8	37
Total	27	14.3	11	6–18	2	49

dian of the annual and post-storm sand volume change rate was compared using an unpaired two-sample Wilcoxon test.

3. Results

3.1. Sandbar switching zones

3.1.1. Temporal and morphological characteristics

For the period 2009–2021, 27 sandbar switching episodes were observed on the Curonian Spit with an average duration of 14.3 months (Table 1). The majority of these sandbar switching episodes appeared after a stormy winter season and lasted for at least one season until the next winter. 14 switching episodes occurred between the outer and middle sandbars (outer-middle sandbar switch), 1 between the outer and inner (outer-inner sandbar switch), and 12 between multiple sandbars (outer-middle, middle-inner sandbar switch).

Three types of sandbar switching were observed: permanent switch, temporary switch, and temporary connection (Figure 3). A permanent switch is defined as a switch that occurs when a sandbar joins another seaward or landward located sandbar, takes its position, and continues to develop in that position (Figure 3a). A temporary switch is when a sandbar takes the place of another sandbar, but after some time returns to its primary position (Figure 3b). A temporary connection is when a sandbar joins another landward or seaward-located sandbar but switching does not occur (Figure 3c). Permanent and temporary switches were the most common types during the analysed period (Table 1).

3.1.2. Spatial characteristics

Between 2009 and 2021, the switching zones were distributed unevenly along the Curonian Spit (Figure 4). After completion, the switching episodes reoccurred in the

same or a close-by location. This property allows approximate stretches to be distinguished where sandbar switching is typically absent and present along the Curonian Spit nearshore: no switching episodes were typically observed in the northern section of the study area; the northernmost switching zone was observed to the south of Alksnynė (13.5–14.5 km from the Klaipėda port jetty); the second was observed to the south of Juodkrantė (21 km from the Klaipėda port jetty); the third was observed in the area between 26 and 28 km from the Klaipėda port jetty; the fourth was observed to the north or south of Pervalka (32–36 km from the Klaipėda port jetty), the fifth was observed at Preila (38.5 km from the Klaipėda port jetty); the sixth was observed to the north of Nida (42.5–43.5 km from the Klaipėda port jetty); the seventh was observed in the southern part of Nida (47.5 km from the Klaipėda port jetty) (Figure 4). Switching episodes also occurred in other locations, but they were not spatially recurrent. Figure 4a shows that the majority of the recurrent sandbar switching locations on the Curonian Spit were observed in locations where the orientation of the mean shoreline for the period 2009–2021 was changing.

3.2. Shoreline changes in the sandbar switching zones

Shoreline retreat at an average rate of −14.2 m occurred in 25 (out of 27) sandbar switching zones, which were observed during the period 2009–2021. The average length of the shoreline retreat area in the switching zones was 554.6 m and the average area of the shoreline retreat was 12.8 m²/m. Figure 5 shows the shoreline change characteristics in different sandbar switching zones on the dates of maximum shoreline retreat.

Several scenarios of shoreline behaviour were observed in the sandbar switching zones:

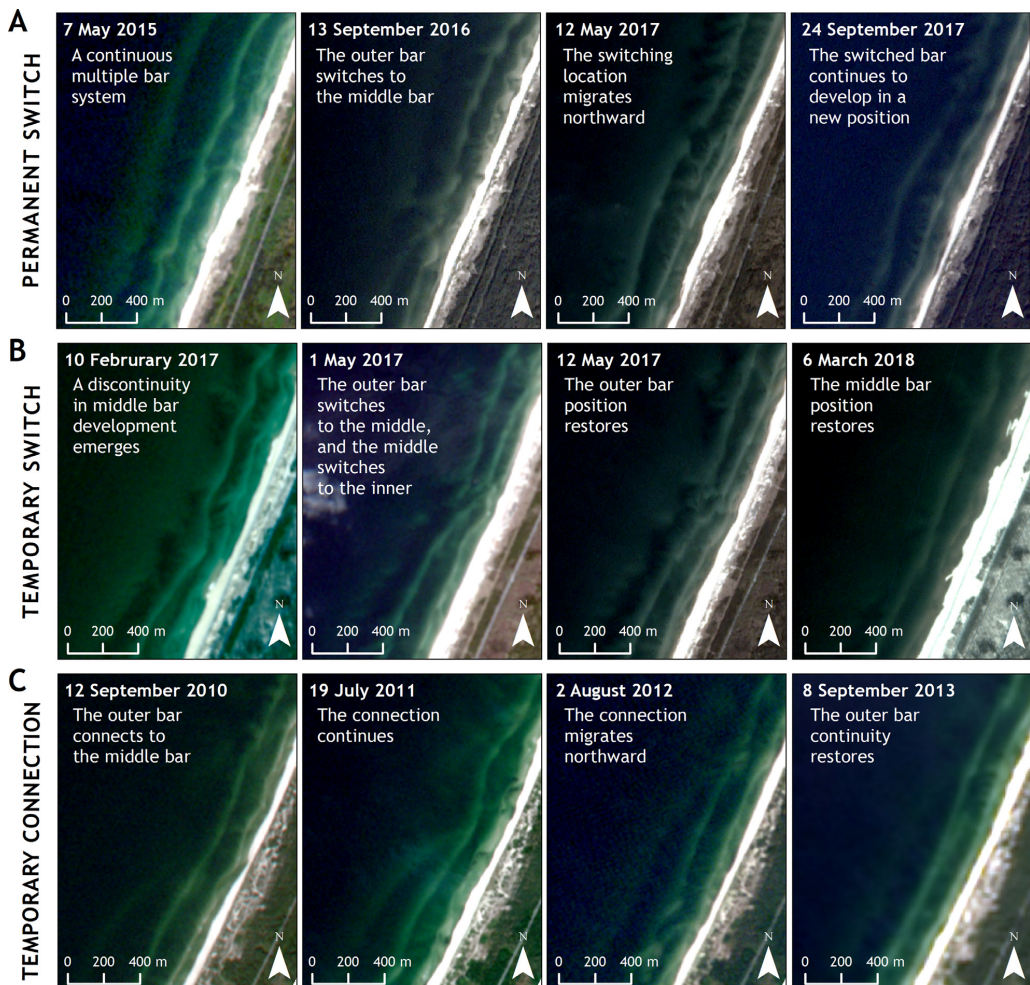


Figure 3 Examples of three different sandbar switching types on the Curonian Spit and their evolution. The evolution of the same switching type is represented by a horizontal sequence of images.

- 1) **Erosion scenario (E).** The shoreline retreated throughout the entire sandbar switching zone. The E scenario was observed in 15 sandbar switching zones where shoreline retreat zone was between 285 and 1258 m in length (646 on average). The average shoreline retreat area for the E scenario was $15.5 \text{ m}^2/\text{m}$.
- 2) **Accretion-erosion-accretion scenario (A-E-A).** The shoreline retreated in the middle part of the sandbar switching zone and advanced or remained stable in the northern and southern parts of the switching zone. The A-E-A scenario was observed in 6 sandbar switching zones where the middle shoreline retreat zone was between 196 and 696 m in length (343 m on average), and the sum length of the outer shoreline advance zones was between 233 and 944 m (546 on average). The average shoreline re-

treat and shoreline advance areas were $6.7 \text{ m}^2/\text{m}$ and $17.8 \text{ m}^2/\text{m}$, respectively.

- 3) **Accretion-erosion scenario (A-E).** The shoreline retreated in the northern or southern parts of the sandbar switching zone and advanced or remained stable in the remaining part. The A-E scenario was observed in 2 sandbar switching zones where the shoreline retreat and advance zones were equal to 443 and 233 m in length on average. The average shoreline retreat and advance areas were 16 and $9.5 \text{ m}^2/\text{m}$, respectively.
- 4) **Erosion-accretion-erosion scenario (E-A-E).** The shoreline retreated in a major part of the sandbar switching zone with a small middle section remaining stable or advancing. The E-A-E scenario was observed in 2 sandbar switching zones where the outer retreat zones and mid-

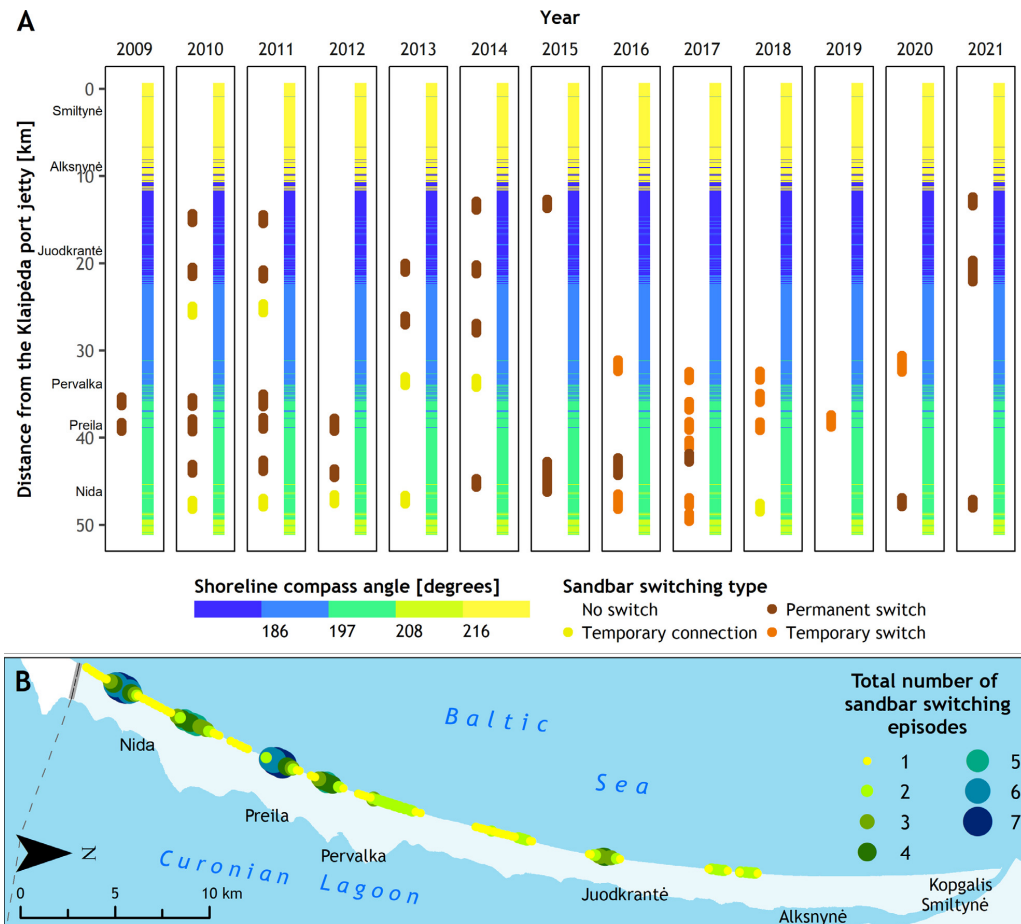


Figure 4 Spatial distribution of the sandbar switching zones on the Curonian Spit in 2009–2021: A – shoreline orientation and locations of sandbar switching zones by year. The sandbar switches tended to occur at the breaking points of different shoreline orientations. The shoreline orientation was calculated as a compass angle of mean shoreline position, which was divided into equal transects with a spacing of 25 m. B – spatial distribution of the total reoccurrence of sandbar switching episodes.

dle advance zone were 612 and 115 m in length on average, respectively. The average shoreline retreat area was $8.2 \text{ m}^2/\text{m}$, and the average shoreline advance area was $6.6 \text{ m}^2/\text{m}$.

3.3. Sand volume changes in the sandbar switching zones

3.3.1. Interannual sand volume change

During the period 2009–2021, 319 topographic cross-shore profiles were measured, with 30 in the sandbar switching zones. The average sand volume change in the beach-foredune system was $3.2 \text{ m}^3/\text{m}$ (0.6%) and $-3.5 \text{ m}^3/\text{m}$ (-0.8%) at profiles outside and within the sandbar switching zones, respectively (Figure 6). According to the t-test results, the averages of the cubic sand volume change at pro-

files with and without sandbar switches were significantly different with 95% confidence ($p < 0.05$) (Figure 6b). However, the averages of the percentage sand volume change in the beach-foredune system at profiles with and without sandbar switches were strongly influenced by the outliers, and an average comparison resulted in no significant results (Figure 6). To overcome the influence of the outliers, the medians of the interannual sand volume change were compared using a Wilcoxon test. Both the median of the percentage sand volume change and the median of the cubic sand volume change, at profiles with and without sandbar switches, were significantly different with 95% confidence ($p < 0.05$) (Figure 6). The significantly different average and median rates of sand volume change at locations within and outside sandbar switching zones suggest that the sandbar switching was related to higher coastal erosion rates than

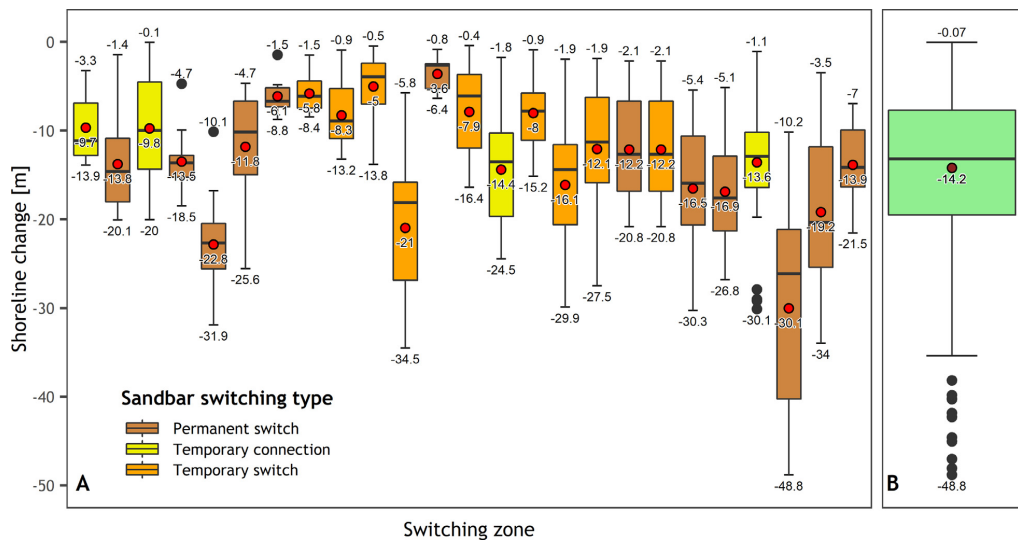


Figure 5 Boxplots defining the shoreline retreat characteristics within each sandbar switching zone in order of switching occurrence (from the earliest (left) to the latest (right)) (A) and combined for all the switching zones (B). The shoreline retreat characteristics were assessed for the transects located within the shoreline retreat area with 25 m spacing on the date of maximum shoreline retreat.

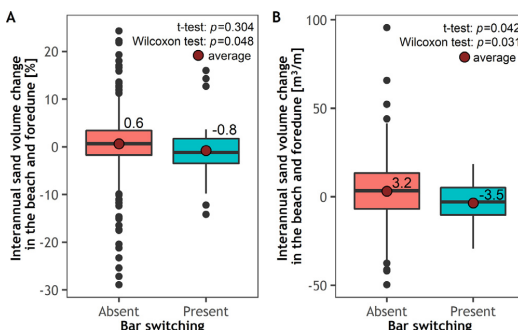


Figure 6 Comparison of the sand volume changes in the coastal cross-shore profiles when sandbar switching was absent or present. A – percentage of sand volume change; B – sand volume change in m^3/m .

locations outside the switching zones where accretion and dynamic equilibrium are dominant.

3.3.2. Sand volume change during major storms

During the last two decades, four major storms with wind speed exceeding the hurricane-force threshold ($\geq 32.6 \text{ m/s}$) have hit the coast of the Curonian Spit: Anatol in 1999, Erwin in 2005, Felix in 2015, and Laura in 2020. The main characteristics of winds, water levels, and changes in sand volume during the most destructive storms are summarised in Table 2. Only storms Anatol, Felix, and Laura were considered in this study because, during storm Erwin, the coast of the Curonian Spit gained 3.3 m^3/m of sand due to the high

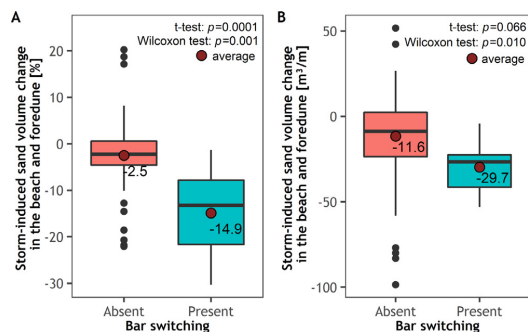


Figure 7 Comparison of the sand volume changes in the coastal cross-shore profiles during major storms when sandbar switching was absent or present. A – percentage of sand volume change; B – sand volume change in m^3/m .

sediment supply from the southern part of the Curonian Spit (Kaliningrad oblast) and no considerable damage was done.

Eight sandbar switching episodes were observed at the locations of the topographic cross-shore profiles before major storm events (2 before Anatol, 3 before Felix, and 3 before Laura). The average rate of sand volume change in the beach-foredune system after major storm events was $-11.6 \text{ m}^3/\text{m}$ (-2.5%) and $-29.7 \text{ m}^3/\text{m}$ (-14.9%) at profiles outside and within the sandbar switching zones, respectively (Figure 7). According to the t-test results, the averages of the cubic sand volume change at profiles with and without switches were not significantly different ($p=0.066$)

Table 2 The main characteristics of major storms on the Curonian Spit.

Storm	Date	Mean maximal wind speed [m/s]	Gust wind speed [m/s]	Prevailing wind direction	Water level [m]	Sand volume change [m ³ /m]
Anatol	4 December 1999	25	45.0	SW–SWS	+1.65	-35.7
Erwin	8–9 January 2005	25	33.0	W–WSW	+1.54	+3.3
Felix	11 January 2015	25	32.6	WSW	+1.37	-7.7
Laura	12 March 2020	28	36.4	W	+1.73	-2.0

(Figure 7b). One reason for this is that the result was influenced by sediment availability. The highest rate of erosion during the storm events was observed at profiles in the northern part of the study area with the largest sediment budget and where no sandbar switching was typically observed (Figure 4). For this reason, the percentage average sand volume changes were compared. The percentage averages of the sand volume change at profiles with and without switches were significantly different, with 95% confidence ($p<0.05$) (Figure 7a). According to a Wilcoxon test, the medians of the sand volume change were significantly different with 95% confidence ($p<0.05$) in both cases (percentage and cubic) (Figure 7).

3.4. Case studies of different coastal change scenarios

3.4.1. A case of erosion during a calm period

In this case, a sandbar switching episode occurred between 28 May 2008 and 2 August 2012 at the Preila rescue station. Multiple switches were observed in this sandbar switching zone. The episode occurred when the distance from the shoreline of the outer sandbar became discontinuous along-shore (Figure 8a). In 2009, the outer sandbar joined the middle sandbar, and the middle sandbar joined the inner sandbar. In 2010–2012, the outer sandbar joined migrated north and the northern segment of the disconnected outer sandbar migrated south, while the distance between them decreased. In 2013, the discontinuous ends of the outer sandbar merged and continuity was restored in the sandbar system.

Two cross-shore profiles of interannual topographic surveys are located in this switching episode zone (Figure 8a). The coastal evolution in these profiles largely coincided with the evolution of switching episodes. Before the switching episode, the beach and foredune at profile 1 exhibited stability, then during the period 2008–2012, the beach and foredune experienced severe erosion with a sediment loss of 30–40 m³/m per year (Figure 8c). After continuity was restored in the sandbar system, the accretion on the beach and foredune set in with a sediment gain of up to 20 m³/m per year. Since 2016, coastal development has stabilised and dynamic equilibrium has set in. During the period of coastal instability (2009–2016), the correlation coefficient R between the sand volume change in the beach and foredune and the change in the distance from the shoreline of the outer sandbar was 0.78 ($p<0.05$). The switching location migrated north towards profile 2 (Figure 8b) and erosion at this profile started a year later with a sediment loss

of 15–25 m³/m per year (Figure 8d). In 2013, accretion processes began at a rate of 10–20 m³/m per year. A period of large amount of accretion continued until 2016, when the development of the beach and foredune stabilised. During the period of coastal instability, correlation coefficient R between the sand volume change in the beach and foredune and the change in the distance from the shoreline of the outer sandbar was 0.48 ($p<0.05$). Changes in the shoreline and outer sandbar positions were in close agreement at profile 2 during the switching episode ($R=0.85$, $p<0.05$) (Figure 8f).

3.4.2. A case of erosion-accretion-erosion during a calm period

In this case, the switching episode occurred between 18 April 2019 and 5 October 2019. Temporary switches between outer-middle and middle-inner sandbars were observed when the outer and middle sandbars became discontinuous longshore and joined landward located sandbars. One cross-shore profile of interannual topographic surveys is located within this sandbar switching zone (Figure 9, profile 5). In 2018–2019, the year when a sandbar switching zone formation occurred, and in 2019–2020, the year when a sandbar switching episode occurred, the sand volume in the beach-foredune system for this profile decreased by over 20 m³/m/y. In 2020–2021, the year after the sandbar switching episode ended, profile 5 gained 29.1 m³/m of sand (Figure 9e).

The shoreline change within this sandbar switching zone was variable: the northern (profile 3) and southern parts (profile 5) of the switching zone suffered from shoreline retreat, and the middle part of 124 m (profile 4) underwent shoreline advance (Figure 9). On the date of maximum shoreline retreat, the area of shoreline erosion was 11.1 m²/m with maximum and average shoreline retreat rates of 27.5 and 13.01 m, respectively. At profile 5, a decrease in the outer sandbar distance from the shoreline was followed by the highest shoreline recession within the switching zone (Figure 9d). The outer sandbar position at profiles 3 and 4 was quasi-stable during the switching episode, but at profile 3 the shoreline retreated, while at profile 4 the shoreline advanced at a rate of up to 12 m (Figure 9b, c). After the sandbar switching episode, the shoreline at profiles 3 and 5 started to recover. Correlation coefficient R between the shoreline change and the change in the outer sandbar distance from the shoreline in this zone was 0.59 ($p<0.05$) (Figure 9f).

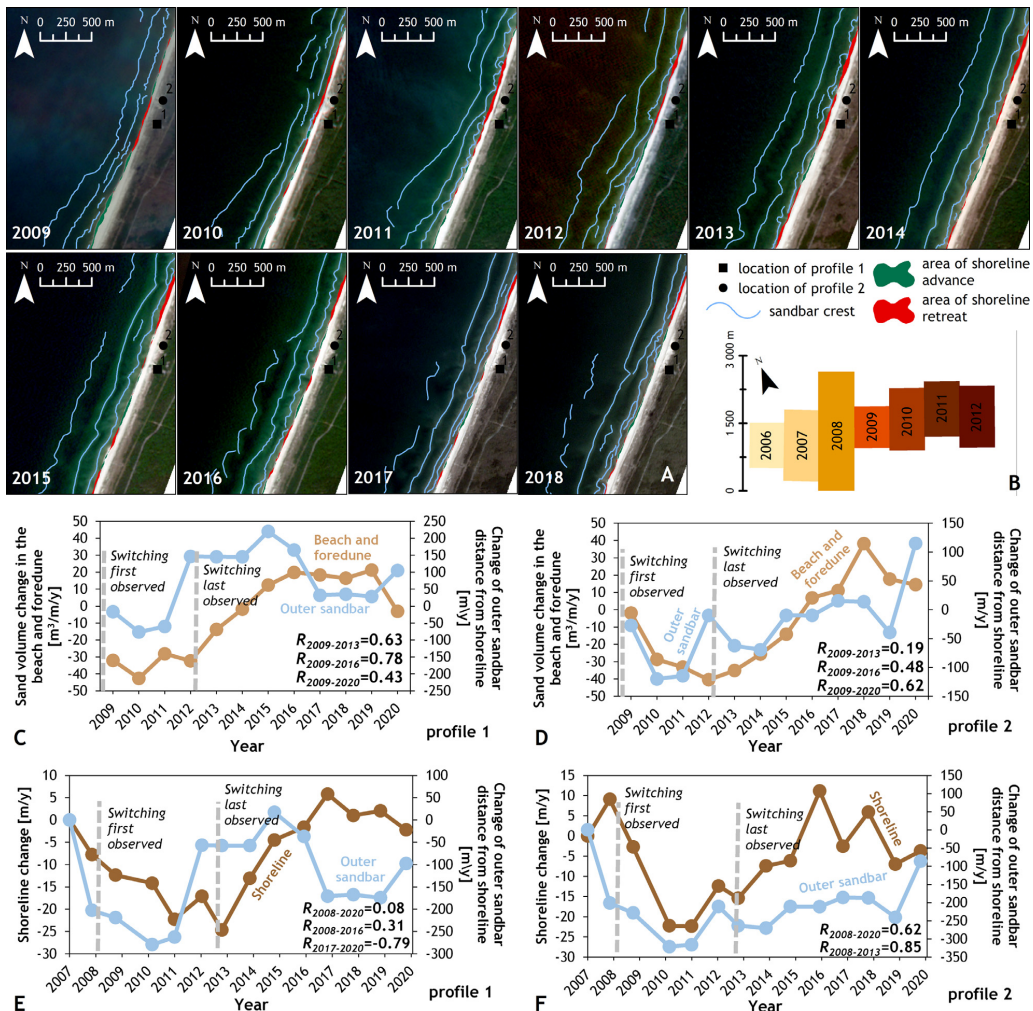


Figure 8 The coastal development during the sandbar switching episode at Preila: A – changes in the sandbar position; B – migration and length change of a sandbar switching zone; C, D – changes in the beach and foredune volume and outer sandbar distance from the shoreline at profiles 1 and 2; E, F – shoreline changes and change in the outer sandbar distance from the shoreline at profiles 1 and 2.

3.4.3. A case of erosion with storm influence

In this case, a sandbar switching episode occurred between 6 September 2014 and 6 October 2015. Here, a full switch between the outer and middle sandbars was observed. The switching episode occurred when the outer sandbar was split, and the northern segment of the disconnected outer sandbar joined the middle sandbar. During the switching episode, the southern end of the disconnected outer sandbar slowly decayed (Figure 10a).

During the switching episode, the Curonian Spit coast was hit by storm Felix (11 January 2015); therefore, this case represents switching-related coastal changes during storm events. In this case, two adjacent cross-shore profiles are

analysed (profiles 6 and 7) (Figure 10). Both profiles experienced highly contrasting storm-induced changes. Profile 6, which was within the sandbar switching zone during storm Felix, lost $28.6 \text{ m}^3/\text{m}$ of sand. Profile 7, which was outside the sandbar switching zone during storm Felix, gained $51.7 \text{ m}^3/\text{m}$ of sand. During the overall period affected by the sandbar switching episode (2014–2016), profile 6 lost $51.1 \text{ m}^3/\text{m}$ of sand while profile 7 gained $55.3 \text{ m}^3/\text{m}$. Almost identical rates of coastal erosion and accretion at profiles 6 and 7 suggest that the eroded sand within the sandbar switching zone was redistributed outside it, around the location of profile 7. The sand volume change within this switching zone was well correlated with

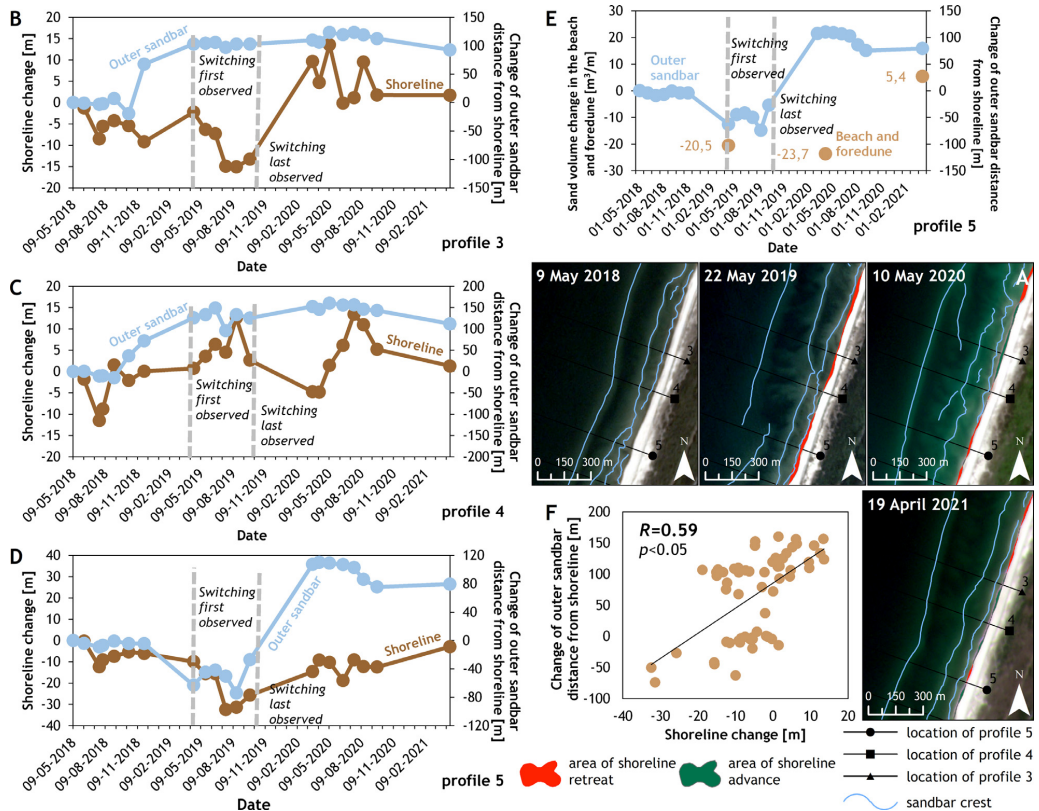


Figure 9 The coastal development during one of the sandbar switching episodes: A – changes in the sandbar position before, during, and after the switching episode; B – change of shoreline and outer sandbar position at profile 3; C – at profile 4, D – at profile 5; E – sand volume change in the beach-foredune system and outer sandbar position change at profile 5; F – the relationship between the changes in the shoreline and outer sandbar position at profiles 3, 4 and 5.

the switching-related changes of the outer sandbar cross-shore position ($R=0.86$, $p<0.05$) (Figure 10d). The shoreline position changes at profiles 6 and 7 were less consistent with the changes in the sandbar position ($R=0.49$, $p<0.05$) (Figure 10d).

4. Discussion

In this study, the sandbar switching phenomenon in multiple sandbar systems and its relation to beach-foredune system changes are analysed by using decadal data from satellite imagery and topographic surveys. On the Curonian Spit, sandbar switching episodes are observed from 13 km from the Klaipėda port jetty and further to the south in quasi-stable locations (in most cases) where they tend to reoccur multiple times. A set of specific hydrodynamic conditions and specific antecedent morphology (discontinuity in longshore sandbar development) is necessary for the formation of sandbar switches (Shand et al., 2001; Walstra et al., 2016; Wijnberg and Wolf, 1994). Due to the north-eastern

coastal orientation and the predominant south-westerly wind and wave direction (Jakimavičius et al., 2018), cross-shore sediment transport is dominant in the northern part of the Curonian Spit (Žilinskas et al., 2018), resulting in no observed sandbar switches; with the changing shoreline orientation to northern-southern and south-western, the longshore currents become stronger and the longshore sediment transport prevails where sandbar switches are typically observed. This result is consistent with previous studies suggesting that switching formation requires obliquely incident wave events and strong longshore currents (Aleman et al., 2017; Shand et al., 2001).

Apart from the oblique waves and strong longshore currents, the main cause of sandbar switching formation is an alongshore discontinuity in the sandbar system development (Aleman et al., 2017; Shand et al., 2001; Walstra et al., 2016) which is determined by alongshore differences in the hydrodynamic and morphodynamic conditions. Therefore, the ideal conditions for sandbar switching to occur would be transitional zones where different hydrodynamic and morphodynamic conditions collide. Differences in shoreline

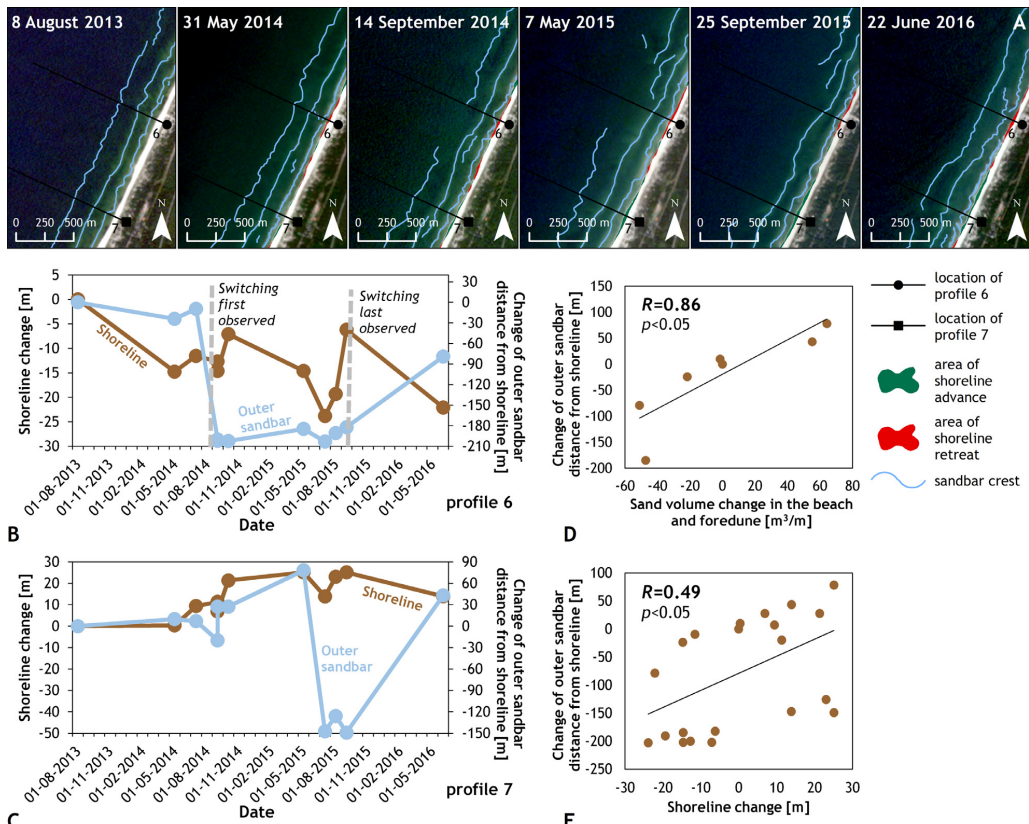


Figure 10 The coastal development during sandbar switching episode and storm Felix (profile 6 represents development within the switching zone; profile 7 – outside the switching zone): A – changes in the sandbar position; B – changes in the shoreline and outer sandbar position at profile 6; C – changes in the shoreline and outer sandbar position at profile 7; D – relationship between the changes in sand volume on the beach and foredune, and changes in the outer sandbar position at profiles 6 and 7; E – relationship between the changes in the shoreline and outer sandbar positions at profiles 6 and 7.

orientation are one of the factors causing the formation of such transitional zones. The results of this study demonstrate that transitional zones between predominant shoreline compass angle coincide with typical locations of sandbar switching formation (Figure 4a).

On the basis of the above described, the essential conditions for the occurrence of sandbar switching episodes would be locations where the breakpoint of different shoreline orientations and shore-oblique waves with associated longshore currents coincide. The described complex of conditions could be used to identify potential locations where sandbar switches occur. In Figure 11, the shoreline compass angle and averaged deviation of wave propagation angle from the shore-normal angle, calculated for longshore stretches of 1 km for the period between 2009 and 2020, are used as the independent variables in the logistic regression model for the prediction of sandbar switching locations. Using both metrics, a sandbar switching location can be predicted with McFadden's pseudo R^2 of 0.57. However,

using the deviation of wave direction only, R^2 is 0.54. This suggests that the contribution of shoreline direction to the accuracy of the model is minor, and the direction of wave propagation is more important for the prediction of sandbar switching formation.

Although it has been almost three decades since the longshore realignment of nearshore sandbars was observed and identified for the first time (Shand et al., 2001; Wijnberg and Wolf, 1994), the way this phenomenon affects the development of subaerial beaches has never been studied before. In this study, the emergence of coastal erosion within sandbar switching zones, including a decrease in sand volume in a beach-foredune system and shoreline retreat on interannual and storm-related time scales, was observed for the first time. This shows that the longshore realignment of nearshore sandbars plays an important role in the development of a beach-foredune system. The causes of this connection could be twofold: 1) switching-related changes in sandbar morphology affect the overall nearshore flow field

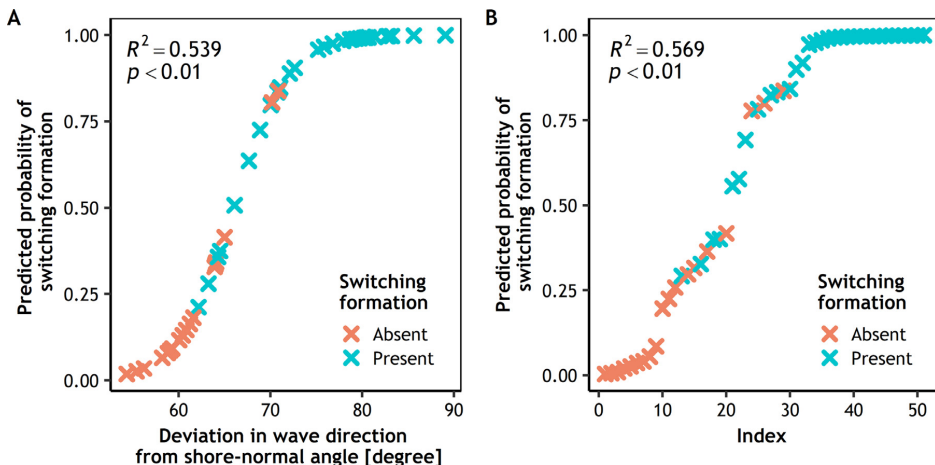


Figure 11 Logistic regression model for the sandbar switching formation: A – model with a deviation in wave direction from a shore-normal angle as the independent variable; B – model with a change in the shoreline compass angle and deviation in wave direction from a shore-normal angle as independent variables. The colour in the figure indicates the observed values (true) and the point locations indicate the predicted probability of sandbar switching formation. The R^2 value was calculated as McFadden-pseudo-R-squared.

and disturb the usual sediment exchange between the beach and nearshore; 2) sandbar switching zones are often related to the local diminishing in width of the nearshore sandbar zone (e.g., when the outer sandbar splits and connects to the landward sandbar). Nearshore sandbars act as natural barriers, dissipating wave energy (Dubarbier et al., 2015; Fernández-Mora et al., 2015; Plant et al., 2001; Price et al., 2014); when this barrier disappears or the sandbar zone diminishes, the portion of dissipated wave energy decreases and the portion of wave energy which reaches the coastline increases near the location of the diminished sandbar zone, thus causing increased rates of local coastal erosion. This assumption is based on case studies of sandbar switching zones, showing strong and moderate agreement between changes in shoreline position, changes in sand volume in the beach-foredune system, and changes in the outer sandbar position during sandbar switching episodes. Additional observations on other non-tidal and microtidal sandy beaches with multiple sandbar systems, exhibiting patterns of sandbar realignment, could confirm the relation between the sandbar switching episodes and coastal erosion observed along the Curonian Spit coast and should seek to identify the exact causes of this connection.

5. Conclusions

The present study analyses the switching-related morphodynamic behaviour of multiple sandbar system and its connection to changes in a shoreline and beach-foredune system on the Curonian Spit, located along the South-Eastern Baltic Sea coast. It is determined that sandbar switches on the Curonian Spit prefer quasi-stable locations where sandbar switching episodes are repeatedly observed. These preferred locations coincide with transitional zones between

different prevailing shoreline compass angles and oblique wave energy. Typical sandbar switching episode lasts for over a year or longer and affect the nearshore flow field from seasonal to interannual time scales.

The emergence of coastal erosion processes within sandbar switching zones was observed in this study. On an interannual time scale, the beach and foredune experienced a small average rate of erosion during the sandbar switching episodes compared to locations outside the sandbar switching zones, which exhibit a small average rate of accretion. On a storm-related time scale, a higher average rate of beach and foredune erosion was observed within the sandbar switching zones than at locations outside those zones. During the switching episodes, the shoreline typically retreats landward and recovers after a sandbar switching episode. It is hypothesised that increased coastal erosion at switching locations could be related to an imbalance in the typical sediment exchange between the beach and nearshore, and a local diminishing of the sandbar zone both caused by sandbar switching-induced changes in the nearshore morphology and nearshore flow field. This assumption is partly confirmed by case studies of coastal development within sandbar switching zones, demonstrating that the position of the outer sandbar is well correlated with the shoreline and beach-foredune volume changes during sandbar switching episodes: when the distance from the shoreline of the outer sandbar decreases, the beach dynamic state moves towards erosion. The relationship between sandbar switching and coastal erosion has been observed and assessed for the first time, no previous studies analysing the morphodynamic connection between sandbar switching zones and subaerial domain exist. Therefore, further studies should seek to confirm this relationship and identify the processes behind it.

The results of this study reveal the importance of the sandbar switching phenomenon in coastal development and suggest that the identification of potential sandbar switching locations could be used to find potential coastal erosion hot spots. Also, the study results imply that sandbar switching zones are characterised by a high variability of coastal changes. This observation could be important for coastal prediction.

Declaration of Competing Interest

The authors declare that they have no known competing financial interests or personal relationships that could have appeared to influence the work reported in this paper.

Acknowledgments

This research did not receive any specific grant from funding agencies in the public, commercial, or non-profit sectors. The authors wish to thank Viktoras Karaliūnas (Nature Research Centre, Lithuania) for the technical support and two anonymous reviewers for their useful suggestions.

References

- Aagaard, T., Davidson-Arnott, R., Greenwood, B., Nielsen, J., 2004. Sediment supply from shoreface to dunes: Linking sediment transport measurements and long-term morphological evolution. *Geomorphology* 60, 205–224. <https://doi.org/10.1016/j.geomorph.2003.08.002>.
- Aleman, N., Certain, R., Robin, N., Barusseau, J.P., 2017. Morphodynamics of slightly oblique nearshore bars and their relationship with the cycle of net offshore migration. *Mar. Geol.* 392, 41–52. <https://doi.org/10.1016/j.margeo.2017.08.014>.
- Balouin, Y., Tesson, J., Gervais, M., 2013. Cuspate shoreline relationship with nearshore bar dynamics during storm events – field observations at Sete beach, France. *J. Coast. Res.* 65, 440–445. <https://doi.org/10.2112/SI65-075.1>.
- Bouvier, C., Balouin, Y., Castelle, B., 2017. Video monitoring of sandbar-shoreline response to an offshore submerged structure at a microtidal beach. *Geomorphology* 295, 297–305. <https://doi.org/10.1016/j.geomorph.2017.07.017>.
- Brooks, S.M., Spencer, T., Christie, E.K., 2017. Storm impacts and shoreline recovery: Mechanisms and controls in the southern North Sea. *Geomorphology* 283, 48–60. <https://doi.org/10.1016/j.geomorph.2017.01.007>.
- Castelle, B., Marieu, V., Bujan, S., Bujan Alongshore-Variable Beach, S., Changes, D., 2019. Alongshore-Variable Beach and Dune Changes on the Timescales from Days (Storms) to Decades Along the Rip-dominated Beaches of the Gironde Coast, SW France. *J. Coast. Res.* SI 88, 157–171. <https://doi.org/10.2112/SI88-012.1>.
- Castelle, B., Marieu, V., Bujan, S., Splinter, K.D., Robinet, A., Sénechal, N., Ferreira, S., 2015. Impact of the winter 2013–2014 series of severe Western Europe storms on a double-barred sandy coast: Beach and dune erosion and megacusp embayments. *Geomorphology* <https://doi.org/10.1016/j.geomorph.2015.03.006>.
- Castelle, B., Turner, I.L., Ruessink, B.G., Tomlinson, R.B., 2007. Impact of storms on beach erosion: Broadbeach (Gold Coast, Australia). *J. Coast. Res.* 50, 534–539.
- Cohn, N., Ruggiero, P., De Vries, S., García-Medina, G., 2017. Beach growth driven by intertidal sandbar welding. In: *Coastal Dynamics*, 2017, 12–16 Helsingør.
- Del Río, L., Gracia, F.J., Benavente, J., 2013. Shoreline change patterns in sandy coasts. A case study in SW Spain. *Geomorphology* 196, 252–266. <https://doi.org/10.1016/j.geomorph.2012.07.027>.
- Dubarbier, B., Castelle, B., Marieu, V., Ruessink, G., 2015. Process-based modeling of cross-shore sandbar behavior. *Coast. Eng.* 95, 35–50. <https://doi.org/10.1016/j.coastaleng.2014.09.004>.
- Fernández-Mora, A., Calvete, D., Falqués, A., De Swart, H.E., 2015. Onshore sandbar migration in the surf zone: New insights into the wave-induced sediment transport mechanisms. *Geophys. Res. Lett.* 42, 2869–2877. <https://doi.org/10.1002/2014GL063004>.
- Gijssman, R., Ruessink, B.G., Visscher, J., Schlurmann, T., 2021. Observations on decadal sandbar behaviour along a large-scale curved shoreline. *Earth Surf. Process. Landforms* 46, 490–503. <https://doi.org/10.1002/esp.5041>.
- Harley, M.D., Turner, I.L., Short, A.D., Ranasinghe, R., 2009. An empirical model of beach response to storms–SE Australia. In: *19th Australasian Coastal and Ocean Engineering Conference 2009 and the 12th Australasian Port and Harbour Conference 2009, Coasts and Ports, 2009*, 589–595.
- Jakimavičius, D., Kriauciūnienė, J., Šarauskienė, D., 2018. Assessment of wave climate and energy resources in the Baltic Sea nearshore (Lithuanian territorial water). *Oceanologia* 60, 207–218. <https://doi.org/10.1016/j.oceano.2017.10.004>.
- Janušaitė, R., Jukna, L., Jarmalavičius, D., Pupienis, D., Žilinskas, G., 2021. A Novel GIS-Based Approach for Automated Detection of Nearshore Sandbar Morphological Characteristics in Optical Satellite Imagery. *Remote Sens* 13, 2233. <https://doi.org/10.3390/rs13112233>.
- Jarmalavičius, D., Žilinskas, G., Pupienis, D., 2017. Geologic framework as a factor controlling coastal morphometry and dynamics. *Curonian Spit, Lithuania. Int. J. Sediment Res.* 32, 597–603. <https://doi.org/10.1016/j.ijsrc.2017.07.006>.
- Kelpšaitė, L., Dailidienė, I., 2011. Influence of wind wave climate change on coastal processes in the eastern Baltic Sea. *J. Coast. Res.* 64, 220–224.
- Kuznetsova, O., Saprykina, Y., 2019. Influence of Underwater Bar Location on Cross-Shore Sediment Transport in the Coastal Zone. *J. Mar. Sci. Eng.* 7, 55. <https://doi.org/10.3390/jmse7030055>.
- McFeeters, S.K., 1996. The use of the Normalized Difference Water Index (NDWI) in the delineation of open water features. *Int. J. Remote Sens.* 17, 1425–1432. <https://doi.org/10.1080/014311690849714>.
- McNinch, J.E., 2004. Geologic control in the nearshore: Shore-oblique sandbars and shoreline erosional hotspots, Mid-Atlantic Bight, USA. *Mar. Geol.* <https://doi.org/10.1016/j.margeo.2004.07.006>.
- Øjeda, E., Ruessink, B.G., Guillen, J., 2008. Morphodynamic response of a two-barred beach to a shoreface nourishment. *Coast. Eng.* 55, 1185–1196. <https://doi.org/10.1016/j.coastaleng.2008.05.006>.
- Parlagreco, L., Melito, L., Devoti, S., Perugini, E., Soldini, L., Zitti, G., Brocchini, M., 2019. Monitoring for Coastal Resilience: Preliminary Data from Five Italian Sandy Beaches. *Sensors* 19, 1854. <https://doi.org/10.3390/s19081854>.
- Phillips, M.S., Harley, M.D., Turner, I.L., Splinter, K.D., Cox, R.J., 2017. Shoreline recovery on wave-dominated sandy coastlines: the role of sandbar morphodynamics and nearshore wave parameters. *Mar. Geol.* 385, 146–159. <https://doi.org/10.1016/j.margeo.2017.01.005>.
- Planet, 2021. Planet Imagery Products Specifications [WWW Document]. URL https://assets.planet.com/docs/Planet_Combined_Imagery_Product_Specs_letter_screen.pdf (accessed 5.9.21).

- Planet Team, 2017. Planet Application Program Interface: In Space for Life on Earth [WWW Document]. URL <https://api.planet.com/> (accessed 5.9.21).
- Plant, N.G., Freilich, M.H., Holman, R.A., 2001. Role of morphologic feedback in surf zone sandbar response. *J. Geophys. Res. Ocean.* 106, 973–989. <https://doi.org/10.1029/2000JC00144>.
- Price, T.D., Ruessink, B.G., Castelle, B., 2014. Morphological coupling in multiple sandbar systems – A review. *Earth Surf. Dyn.* <https://doi.org/10.5194/esurf-2-309-2014>.
- Pruszak, Zbigniew, Różyński, Grzegorz, Szmytkiewicz, Piotr, Pruszak, Z, Różyński, G, Szmytkiewicz, P, 2008. Megascale rhythmic shoreline forms on a beach with multiple bars. *Oceanologia* 50, 183–203.
- Quartel, S., Kroon, A., Ruessink, B.G., 2008. Seasonal accretion and erosion patterns of a microtidal sandy beach. *Mar. Geol.* 250, 19–33. <https://doi.org/10.1016/j.margeo.2007.11.003>.
- Ruessink, B.G., Coco, G., Ranasinghe, R., Turner, I.L., 2007. Coupled and noncoupled behavior of three-dimensional morphological patterns in a double sandbar system. *J. Geophys. Res. Ocean.* 112. <https://doi.org/10.1029/2006JC003799>.
- Shand, R.D., 2003. Relationships between episodes of bar switching, cross-shore bar migration and outer bar degeneration at Wanganui, New Zealand. *J. Coast. Res.* 19, 157–170.
- Shand, R.D., Bailey, D.G., 1999. A review of net offshore bar migration with photographic illustrations from Wanganui, New Zealand. *J. Coast. Res.* 15, 365–378.
- Shand, R.D., Bailey, D.G., Shepherd, M.J., 2001. Longshore realignment of shore-parallel sand-bars at Wanganui, New Zealand. *Mar. Geol.* 179, 147–161. [https://doi.org/10.1016/S0025-3227\(01\)00223-7](https://doi.org/10.1016/S0025-3227(01)00223-7).
- Shand, R.D., Hesp, P.A., Shepherd, M.J., 2006. Beach Cut In Relation To Net Offshore Bar Migration Characteristics of Beach Cut. *J. Coast. Res.* 2004, 334–340.
- Splinter, K.D., Gonzalez, M.V.G., Oltman-Shay, J., Rutten, J., Holman, R., 2018. Observations and modelling of shoreline and multiple sandbar behaviour on a high-energy meso-tidal beach. *Cont. Shelf Res.* 159, 33–45. <https://doi.org/10.1016/j.csr.2018.03.010>.
- Stive, M.J.F., Aarninkhof, S.G.J., Hamm, L., Hanson, H., Larson, M., Wijnberg, K.M., Nicholls, R.J., Capobianco, M., 2002. Variability of shore and shoreline evolution. *Coast. Eng.* 47, 211–235. [https://doi.org/10.1016/S0378-3839\(02\)00126-6](https://doi.org/10.1016/S0378-3839(02)00126-6).
- Stive, M.J.F., Guillen, J., Capobianco, M., 1997. Bar migration and duneface oscillation on decadal scales. In: Proceedings of the 25th Coastal Engineering Conference 1996, 2884–2896. <https://doi.org/10.1061/9780784402429.223>.
- Tătăru, F., Vespremeanu-Stroe, A., Preoteasa, L., 2013. The correlated behavior of sandbars and foredunes on a nontidal coast (Danube Delta, Romania). *J. Coast. Res.* <https://doi.org/10.2112/si16-317.1>.
- Thornton, E.B., MacMahan, J., Sallenger, A.H., 2007. Rip currents, mega-cusps, and eroding dunes. *Mar. Geol.* 240, 151–167. <https://doi.org/10.1016/j.margeo.2007.02.018>.
- Umeda, S., Yuhi, M., Karunaratna, H., 2018. Seasonal to Decadal Variability of Shoreline Position on a Multiple Sandbar Beach. *J. Coast. Res.* 85, 261–265. <https://doi.org/10.2112/si85-053.1>.
- USGS, 1998. USGS EROS Archive - Landsat Archives - Landsat 4-5 Thematic Mapper (TM) Level-1 Data Products. <https://doi.org/10.5066/P9IAKXOV>
- Van de Lageweg, W.I., Bryan, K.R., Coco, G., Ruessink, B.G., 2013. Observations of shoreline-sandbar coupling on an embayed beach. *Mar. Geol.* 344, 101–114. <https://doi.org/10.1016/j.margeo.2013.07.018>.
- Vermaas, T., Elias, E., Van Der Spek, A., Hoogland, R., 2017. Time-dependent effects of nourishments on shoreface bar behaviour. In: *Coastal Dynamics*, 2017, 862–869 Helsingør.
- Walstra, D.-J., Wesselman, D., van der Deijl, E., Ruessink, G., 2016. On the Inter-site Variability in Inter-Annual Nearshore Sandbar Cycles. *J. Mar. Sci. Eng.* 4, 15. <https://doi.org/10.3390/jmse4010015>.
- Wijnberg, K.M., Aarninkhof, S.G.J., Spanhoff, R., 2007. Response of a shoreline sand wave to beach nourishment. In: *Proceedings of the 30th Coastal Engineering Conference 2006*. World Scientific Publishing Company, 4205–4217. https://doi.org/10.1142/978981270954_0353.
- Wijnberg, K.M., Wolf, F.C.J., 1994. Three-dimensional behaviour of a multiple bar system. In: *Proceedings of Coastal Dynamics'94*. ASCE, 59–73.
- Yuhi, M., Matsuyama, M., Hayakawa, K., 2016. Sandbar Migration and Shoreline Change on the Chirihama Coast, Japan. *J. Mar. Sci. Eng.* 4, 40. <https://doi.org/10.3390/jmse4020040>.
- Yuhi, M., Umeda, S., 2018. Characteristics of Systematic Migrations of Multiple Sandbars and Related Cross-Shore Sediment Transport at Chirihama and Adjacent Coasts, Japan. *J. Coast. Res.* 85, 231–235. <https://doi.org/10.2112/si85-047.1>.
- Žilinskas, G., Janušaitė, R., Jarmalavičius, D., Pupienis, D., 2020. The impact of Klaipėda Port entrance channel dredging on the dynamics of coastal zone, Lithuania. *Oceanologia* 62, 489–500. <https://doi.org/10.1016/j.oceano.2020.08.002>.
- Žilinskas, G., Jarmalavičius, D., Pupienis, D., 2018. The influence of natural and anthropogenic factors on grain size distribution along the southeastern Baltic spits. *Geol. Q.* 62, 375–384. <https://doi.org/10.7306/gq.1413>.

Vilniaus universiteto leidykla
Saulėtekio al. 9, III rūmai, LT-10222 Vilnius
El. p. info@leidykla.vu.lt, www.leidykla.vu.lt
bookshop.vu.lt, journals.vu.lt
Tiražas 17 egz.